

THE FAR ULTRAVIOLET AURORA OF GANYMEDE

INAUGURAL-DISSERTATION

zur

Erlangung des Doktorgrades
der Mathematisch-Naturwissenschaftlichen Fakultät
der Universität zu Köln

vorgelegt von

Fabrizio-Michele Musacchio

aus Velbert

Köln 2016

Berichtersteller: Prof. Dr. Joachim Saur
(Gutachter) Prof. Dr. Bülent Tezkan

Tag der mündlichen Prüfung: 12. Januar 2017

Abstract

The far ultraviolet (FUV) aurora on Jupiter's largest moon, Ganymede, is characterized by two distinct ovals in the northern and southern hemisphere, which have been investigated by several campaigns of the *Hubble Space Telescope* (HST) in the past two decades (e.g., Hall et al. (1998), Feldman et al. (2000) and McGrath et al. (2013)). The aurora is generated by electron-impact dissociative excitation of atomic and molecular oxygen in Ganymede's tenuous atmosphere. The most likely acceleration mechanism for the high energetic electrons triggering the auroral emission are field aligned electric currents (FAC) accelerating electrons along the open-closed magnetic field lines boundary (OCFB) of Jupiter's and Ganymede's magnetic field towards the moon's atmosphere (Eviatar et al. 2001a). This acceleration mechanism is consistent with the locations of the observed ovals being close to the intersection lines of the OCFB, predicted by numerical modeling, with Ganymede's atmosphere (Feldman et al. 2000; Eviatar et al. 2001a; McGrath et al. 2013). The compression of Ganymede's mini-magnetosphere due to the impinging Jovian magnetospheric plasma flow on the upstream side shifts the OCFB and accordingly the auroral ovals to elevated planetographic latitudes (between 40° and 55°) on the trailing side (Neubauer 1998; Feldman et al. 2000; McGrath et al. 2013). On the downstream side, the mini-magnetosphere is stretched which shifts the OCFB to lower latitudes (between 10° and 30°) on the leading side. Furthermore, the aurora on Ganymede is expected to be time-variable since the moon is exposed to the time-periodic plasma and magnetic field of Jupiter's magnetosphere. The influence of periodically changing local plasma conditions on the morphology and brightness of Ganymede's aurora has not been analyzed yet. In this thesis we systematically analyze the spatial structure and the temporal variability of Ganymede's FUV auroral ovals as a function of its time-variable magnetospheric environment. We analyze spectral images obtained between 1998 and 2011 by the *Space Telescope Imaging Spectrograph* (STIS) on-board of HST. The observations cover the satellite at eastern and western elongation, observing Ganymede's leading and trailing side. The observations also cover various magnetic latitudes of Ganymede within the Jovian plasma sheet. As a result of our study, we find both, asymmetries in the spatial distribution of auroral brightness on the observed moon disk and temporal varia-

tions correlated to Ganymede's changing position relative to the Jovian current sheet. We find a hemispheric dichotomy of the total disk averaged brightness between the leading side (95.4 ± 2.1 R) and the trailing side (67.2 ± 2.9 R), i.e., the plasma downstream side is significantly brighter than the plasma upstream side. Furthermore, the Jupiter-facing side of the moon disk is brighter than the anti-Jovian side by a factor of 1.81 ± 0.06 on the leading side and by a factor of 1.41 ± 0.14 on the trailing side, indicating local inhomogeneities in the current systems associated with the generation of the aurora. We demonstrate, that the auroral brightness is clearly correlated to Ganymede's position relative to the Jovian current sheet, as we see an increased brightness on the leading side and a decrease of brightness on the trailing side, when Ganymede is inside the current sheet compared to elevated magnetic latitudes. At the same time, the auroral ovals shift on the leading side towards Ganymede's planetographic equator by an average of $4.1^\circ \pm 0.7^\circ$ latitude, and on the trailing side towards the poles by an average of $2.9^\circ \pm 1.5^\circ$ latitude when Ganymede is at the center of the current sheet. The brightness variations and the ovals' movements are a response to the changing local plasma conditions inside the current sheet as Ganymede's mini-magnetosphere is exposed to a stronger interaction with the Jovian magnetospheric plasma. By calculating the center between the northern and southern oval we are able to derive further constraints on the orientation of Ganymede's magnetic equator. We find that Ganymede's dipole magnetic moment is oriented further westward at approximately 47° ($+58^\circ/-43^\circ$) planetographic west-longitude compared to previous estimates. Finally, by analyzing the amount, the size and structure, and the longitudinal distribution of bright auroral spots along the ovals, we find that the occurrence of the spots is rather randomly than systematically ordered, which might be due to the intermittent magnetic reconnection at Ganymede's upstream side (Eviatar et al. 2001a).

Zusammenfassung

Das im fernen ultravioletten Wellenlängenbereich (*far ultraviolet*, kurz: FUV) sichtbare Polarlicht des größten Mondes Jupiters, Ganymed, zeichnet sich durch seine beiden Polarlichtovale in der Nord- und Südhemisphäre des Mondes aus. Das Polarlicht bei Ganymed wurde in den vergangenen zwei Jahrzehnten mit zahlreichen Kampagnen des *Hubble* Weltraumteleskops (*Hubble Space Telescope*, kurz: HST) untersucht (z.B. in Hall et al. (1998), Feldman et al. (2000) and McGrath et al. (2013)). Das Polarlicht entsteht durch dissoziative Elektronenstoßanregung atomaren und molekularen Sauerstoffs in Ganymeds dünner Atmosphäre. Der wahrscheinlichste Beschleunigungsmechanismus für die hochenergetischen Elektronen, die die Polarlichtemission anregen, sind feldparallele elektrische Ströme (*field aligned currents*, kurz: FAC), die die Elektronen entlang der Grenzfläche zwischen offenen und geschlossenen Magnetfeldlinien Ganymeds und Jupiters (*open-closed magnetic field lines boundary*, kurz: OCFB) in Richtung der Atmosphäre Ganymeds beschleunigen (Eviatar et al. 2001a). HST Beobachtungen bestätigten, dass die Lage der Polarlichtovale mit der durch numerische Modellierungen theoretisch berechneten Schnittlinie der OCFB mit Ganymeds Atmosphäre nahezu übereinstimmt (Feldman et al. 2000; Eviatar et al. 2001a; McGrath et al. 2013). Ganymeds Mini-Magnetosphäre ist dem ständigen Strom von Plasma aus der Jupiter-Magnetosphäre ausgesetzt, wodurch die Mini-Magnetosphäre auf der angeströmten Seite, die zugleich Ganymeds orbital hinterher hinkende Hemisphäre ist (in Folge als *Rückseite* des Mondes bezeichnet), komprimiert wird (Neubauer 1998). Auf der abgeströmten Seite, die zugleich Ganymeds orbital führende Hemisphäre ist (in Folge als *Vorderseite* des Mondes bezeichnet), wird die Mini-Magnetosphäre gestreckt. Kompression und Streckung der Mini-Magnetosphäre bewirken, dass die OCFB und damit auch die Polarlichtovale auf der Rückseite Ganymeds zu höheren Breiten (zwischen 40° und 55°) und auf der Vorderseite zu niedrigeren Breiten (zwischen 10° und 30°) verschoben sind (Feldman et al. 2000; McGrath et al. 2013). Ferner unterliegt das Polarlicht auf Ganymed zeitlichen Variationen, da der Mond dem zeitlich variablen Plasma und Magnetfeld Jupiters ausgesetzt ist. Da der Einfluss zeitlich veränderlicher, lokaler Plasmabedingungen auf die Morphologie und die Helligkeit von Ganymeds Polarlichtern noch nicht hinreichend untersucht wurde, untersu-

chen wir in der hier vorgelegten Doktorarbeit systematisch die räumliche Struktur und zeitliche Variabilität von Ganymeds Polarlichtovalen im fernen ultravioletten Wellenlängenbereich als Funktion der zeitlich veränderlichen magnetosphärischen Umgebung des Mondes. Dazu analysieren wir einen großen Satz von spektroskopischen Bildern, die mit dem *Space Telescope Imaging Spectrograph* (kurz: STIS) an Bord von HST im Zeitraum von 1998 bis 2011 aufgenommen wurden. Die Beobachtungen decken Ganymed bei östlicher als auch bei westlicher Elongation und damit die Vorder- und Rückseite des Mondes ab. Ebenfalls decken die Beobachtungen Ganymed bei verschiedenen magnetischen Breiten innerhalb der Plasmaschicht Jupiters ab. Als Ergebnis unserer Studie beobachten wir sowohl Asymmetrien in der räumlichen Verteilung der Polarlichthelligkeiten auf der Mondscheibe als auch zeitliche Variationen dieser Helligkeiten als Funktion von Ganymeds wechselnder Lage bezüglich der Stromschicht. Wir erkennen eine Dichotomie der gemittelten Scheibenhelligkeit zwischen der Mondvorderseite (95.4 ± 2.1 R) und der Mondrückseite (67.2 ± 2.9 R), d.h. die vom Plasma abgeströmte Seite ist signifikant heller als die vom Plasma angeströmte Seite. Außerdem ist der Teil der Mondscheibe, der dem Jupiter zugewandt ist, auf der Mondvorderseite um den Faktor 1.81 ± 0.06 und auf der Mondrückseite um den Faktor 1.41 ± 0.14 heller als der Teil der Mondscheibe, der dem Jupiter abgewandt ist, was auf lokale Inhomogenitäten im Stromsystem, das mit der Entstehung der Polarlichter verknüpft ist, hinweist. Die Polarlichthelligkeiten sind eindeutig mit der Lage Ganymeds bezüglich der Stromschicht Jupiters verknüpft, was sich in einem Anstieg der Helligkeit auf der Mondvorderseite und einem Abfall der Helligkeit auf der Mondrückseite zeigt, wenn Ganymed von hohen magnetischen Breiten in die Stromschicht eintritt. Gleichzeitig verschiebt sich die Lage der Ovale auf der Mondvorderseite um durchschnittlich $4.1^\circ \pm 0.7^\circ$ planetographischer Breite hin zum planetographischen Äquator Ganymeds und auf der Mondrückseite um durchschnittlich $2.9^\circ \pm 1.5^\circ$ planetographischer Breite hin zu den Polen Ganymedes, wenn sich Ganymed in der Stromschicht befindet. Sowohl die Variationen der Helligkeiten als auch das Wandern der Polarlichtovalen sind eine Reaktion auf veränderte lokale Plasmaeigenschaften innerhalb der Stromschicht, wo Ganymeds Mini-Magnetosphäre einer stärkeren Wechselwirkung mit dem magnetosphärischen Plasma Jupiters ausgesetzt ist. Durch die Berechnung der Mittelpunkte zwischen den Nord- und Südpolarlichtovalen sind wir darüber hinaus in der Lage, weitere Randbedingungen für die Berechnung der Orientierung von Ganymeds magnetischem Äquator abzuleiten. Unsere Berech-

nungen ergeben eine im Vergleich zur vorangegangenen Abschätzungen westlicher orientierte Lage von Ganymeds Dipolmoment bei etwa 47° ($+58^\circ/-43^\circ$) planetographischer Länge. Am Ende unserer Studie untersuchen wir das Auftreten heller Polarlichtflecken entlang der Polarlichtovale hinsichtlich ihrer Anzahl, Größe, Form und Verteilung als Funktion planetographischer Länge. Wir entdecken ein vielmehr zufälliges als systematisches Auftreten der Polarlichtflecken, was möglicherweise durch die diskontinuierlich erfolgende Rekonnektion von magnetischen Feldlinien auf der angeströmten Seite der Mini-Magnetosphäre hervorgerufen wird.

Contents

1	Introduction	1
1.1	Purpose of this thesis	7
1.2	Structure of this dissertation	8
2	Ganymede and the discovery of its aurora	9
2.1	Ganymede and the Jovian System	10
2.1.1	Ganymede's surface structure, interior composition, and subsurface ocean	10
2.1.2	Atmosphere	17
2.1.3	Ganymede's intrinsic magnetic field and magnetospheric environment	20
2.2	Ganymede's aurora	27
2.2.1	Discovery of Ganymede's FUV aurora	27
2.2.2	Previous modeling of the aurora and comparison with the observations	34
2.3	Summary	38
3	Observations and data processing	41
3.1	Selecting HST campaigns	42
3.2	Processing of HST/STIS data	46
3.2.1	fit-files and background subtraction	49
3.2.2	Locating the Ganymede disk on the detector	51
3.2.3	Flux conversion	59
3.2.4	Modeling reflected solar light	61
3.2.5	Generating spectral images	65
3.2.6	Error propagation	70
3.2.7	Flux integration	71
3.2.8	Spot detection method	74
4	Results	79
4.1	Ganymede's albedo in the FUV range	80
4.2	Spectral images and general morphology of Ganymede's FUV aurora	82

4.3	Total disk averaged brightness	85
4.3.1	Hemispheric brightness asymmetries	85
4.3.2	Magnetic latitude dependency of total disk averaged brightness	88
4.3.3	Off-Limb emission and comparison with the emission on the moon disk	90
4.3.4	Abundance of atomic and molecular oxygen in Ganymede's atmosphere from 1356/1304 Å brightness ratios	91
4.3.5	General on-disk distribution of auroral brightness	94
4.4	Latitudinal distribution of auroral brightness	97
4.4.1	Separating oval and rest-disk emission	101
4.4.2	Brightness synchronicity between the northern and southern oval	104
4.4.3	Location of the auroral ovals	104
4.4.4	Symmetry study of the northern and southern oval	109
4.4.4.1	Comparing ϑ_c to the planetographic equator	110
4.4.4.2	Comparing ϑ_c to the magnetic equator	113
4.5	Longitudinal distribution of brightest spots	116
4.5.1	Occurrence of bright spots	118
4.5.2	Longitudinal distribution of the centroids of the spots	120
4.5.3	Summary	123
5	Summary and Conclusions	125
	List of Figures	135
	List of Tables	139
	References	141
	Supplementary Material	159
S1	List of abbreviations	160
S2	List of quantities and units	161
S3	Trace drift calibration for the 52X2 aperture	162
S4	Spectral images of OI λ 1304 Å	163
S5	Comparison of total disk averaged brightnesses and brightnesses derived by the anuli integration	164

S6	Gaussian fit results for latitudinal anuli integrated brightness peaks in three longitudinal regions on the moon disk	165
S7	Effective error of Section 4.4.4	166
S8	Resulting reduced χ^2 of Section 4.4.4	167
S9	USGS surface map	168
Permissions for external material used in this thesis		171
Danksagung		177
Versicherung		179
	Teilpublikationen / Publications	180

Introduction

In this chapter we briefly introduce into the subject of this thesis, the aurora on Jupiter's largest moon, Ganymede. We explain the motivation for our study and present the structure of the thesis.

In 1621, Galileo Galilei (1564-1624) witnessed a great auroral outburst in Venice, Italy, which marks one of the first recorded observations of auroral emission in Central Europe (Falck-Ytter and Torbjorn 1999). Five years earlier, Galilei and his student Mario Guiducci (1585-1646) published an essay in 1616, in which the term *aurora borealis* is used for the first time to describe the polar lights on the northern hemisphere¹ (Siscoe 1978). The term is a combination of the name of the Roman goddess of dawn, *aurora*, and the Greek name for the north wind, *boreas*. The polar lights on the southern hemisphere are called *aurora australis*, as *australis* is the Latin name for the south wind. Today, the term *aurora* is commonly used to describe the polar lights.

About one decade prior to his aurora observations, on January 7, 1610, Galilei made one of his first observations of the night sky with his newly invented optical instrument, the telescope. He observed Jupiter which was accompanied by three bright dots strung on a line going through the planet. He originally considered these dots as stars and sketched them together with Jupiter on a notepad (Barker 2004). Excerpts of these sketches are shown in Figure 1. During the following days, Galilei continued observing Jupiter and sketched the accompanying "stars". He noticed that the observed bright dots kept their alignment on a line through Jupiter, but moved from day to day (panels 2 and 3 in Figure 1) and from hour to hour (not shown in the figure). On January 13, 1610, Galilei saw a fourth star appearing. He continued his observations until March 2, 1610, and concluded that the bright dots, which continued to change their positions relative to each other but always remained close to Jupiter, must be planetary bodies orbiting around Jupiter (Barker 2004).

Galilei published his findings in *Sidereus Nuncius* in 1610 (Galilei 1610), which was dedicated to his Grand Duke Cosimo de' Medici and, therefore, he called the newly discovered moons of Jupiter the *Medicean planets* I, II, III and IV. This nomenclature was used for centuries until they had been renamed to the *Galilean satellites* *Io*, *Europa*, *Ganymede* and *Callisto*, the Greek names of the lovers of the Roman god *Jupiter* (Marazzini 2005). Today, we know that the Galilean satellites are the four largest moons of Jupiter among numerous small-sized and irregular moons.

¹Galilei and Guiducci used the Italian term *boreale aurora*. It was the French scientist Pierre Gassendi (1592-1655) who introduced the Latin term *aurora borealis* for the first time in 1621 (Falck-Ytter and Torbjorn 1999).

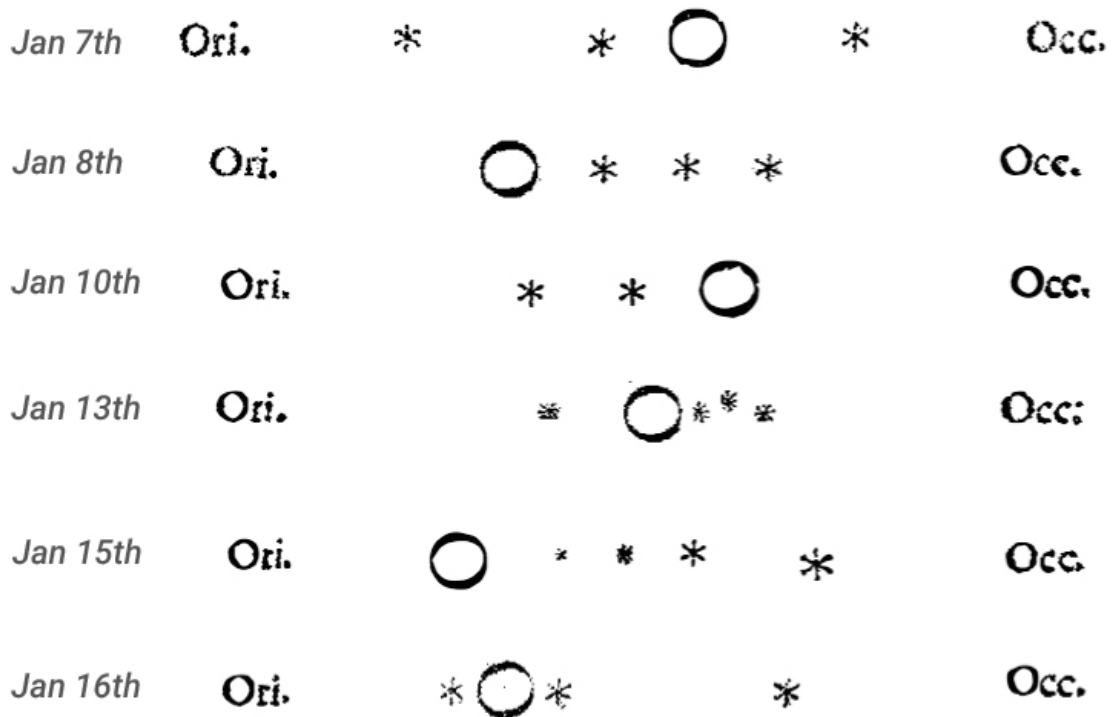
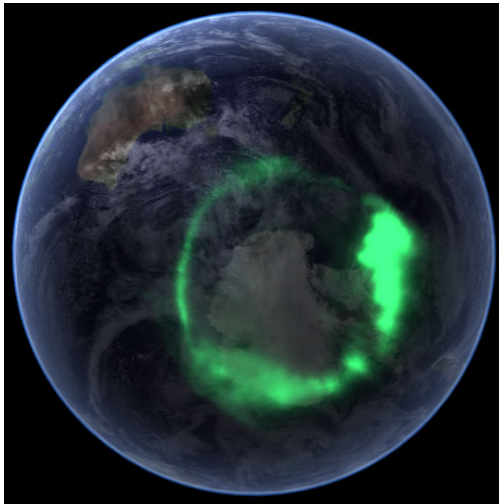


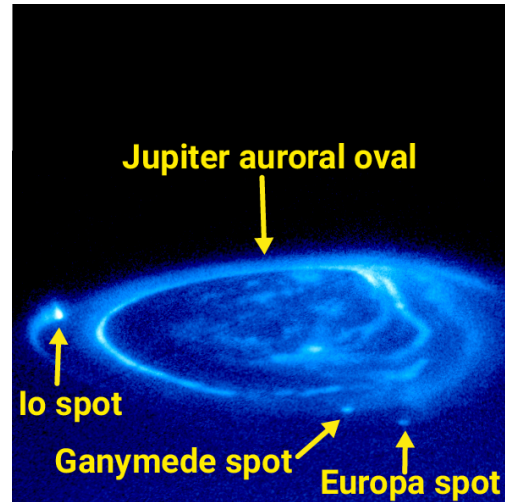
Figure 1 – Galileo Galilei’s sketches of Jupiter (circle) and the Galilean satellites (stars) made in Januar 1610. “Ori.” (abbreviation for the Latin word *orient*) means East and “Occ.” (*occident*) West. Each panel is taken from Galilei (1610) and is enhanced in contrast and brightness.

The homemade telescope of Galileo Galilei was a groundbreaking invention at that time and a milestone in the development of optical instruments. Of course, the accuracy of telescopes has been steadily improved over the years and centuries. Today, we are able to observe the Galilean satellites with a higher resolution than at Galilei’s time. With advanced spectrographs aboard space telescopes like the *Hubble Space Telescope* (HST) we are able to observe targets at wavelengths beyond the visible light. Due to the improvements of optical-spectroscopic instruments over the past decades, we discovered that the auroral outburst seen by Galilei in 1621 is not an exclusive phenomenon at Earth. Auroral emission also occurs at other planetary bodies in our solar system such as Jupiter (see, e.g., Clarke et al. (2004) and Figure 2B), Saturn (see, e.g., Kurth et al. (2009)) or Uranus (see., e.g., Lamy et al. (2012) and Figure 2C). The most recent observation of auroral emission on a brown dwarf (Hallinan et al. 2015; Kao et al. 2016) is the first detection of aurora on an extrasolar object outside of our solar system.

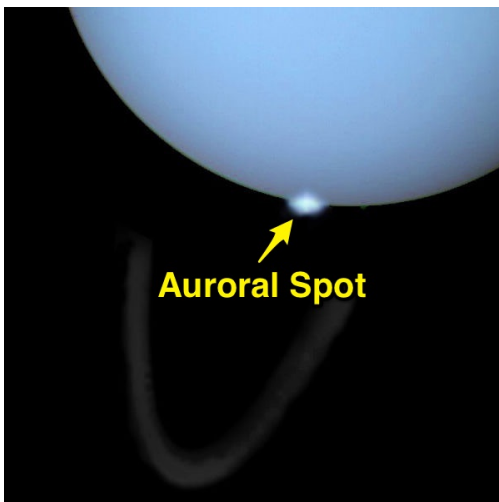
Even though the aurorae of all these planetary bodies describe the same physical phenomenon, they differ from body to body in morphology, i.e., in location,



A Aurora australis at Earth: UV false-colour image observed by the satellite *IMAGE* and overlaid on an image at visible wavelengths (NASA 2005).



B Aurora at Jupiter: FUV auroral oval observed with HST (NASA 1998).



C Aurora at Uranus: Composite image of HST aurora observations at visible and ultraviolet wavelengths, *Voyager 2* photographs of Uranus' disk at visible wavelengths, and *Gemini Observatory* observations of the Uranus' ring system at infrared wavelengths. (NASA 2012).



D Aurora at Ganymede: The two FUV auroral ovals at frontal view on Ganymede's plasma downstream side, observed with HST (McGrath et al. (2013), excerpt from their figure 2).

Figure 2 – Auroral ovals at Earth (A), Jupiter (B), Uranus (C) and Ganymede (D). Note that additionally to the main oval at Jupiter the so-called footprints (indicated as "spots" in the image) of the Galilean satellites are also visible, caused by magnetic flux tubes which connect Jupiter's ionosphere to the moons. The two FUV auroral ovals at Ganymede go around the moon's north and south pole as they do at Earth, but at lower planetographic latitudes.

extension and shape, in brightness and in their generation processes (compare the panels in Figure 2). Today, our understanding of the physical processes of auroral phenomena is still incomplete. Generally speaking, an aurora is a light display which occurs when charged particles hit the atmosphere of a celestial body. At Earth, auroral emission mostly occurs above 60° latitude on the northern and southern hemisphere (Figure 2A). Originating as a stream of plasma particles from the sun, the solar wind interacts with the Earth's magnetosphere. The magnetosphere is the region around a planetary body which is controlled by the body's magnetic field. The interaction leads to an acceleration of charged particles (electrons and ions). These particles propagate along Earth's magnetic field lines towards the atmosphere where they collide with neutral atoms and molecules (mostly oxygen and nitrogen). Due to the collisions, the atmospheric particles get excited and, after a short time, they deenergize which results in the emission of light. This emission of light is being called *aurora*.

In principal, three components are necessary to trigger an aurora: a *generator for acceleration*, *accelerated charged particles* and a *neutral atmosphere*. At Earth, the acceleration is driven by the interaction between the solar wind and Earth's magnetic field. Another example for solar wind triggered aurora is Mars. Mars possesses no global magnetic field but has only multiple magnetic field spots distributed over the southern hemisphere. These spots are correlated with magnetized material in the crust of the planet. In 2004, the ESA mission *Mars Express* discovered auroral emission in the far ultraviolet wavelength range (FUV) coinciding with the magnetic field spots. Although the acceleration process is still unclear, it was thought to be energetic solar wind electrons which propagate along the Martian magnetic field lines colliding with neutral gas of the Martian atmosphere (Leblanc and Chicarro 2008). However, ten years later in 2014, the NASA mission *MAVEN* observed auroral emission for the first time on the northern hemisphere (Phillips 2015; Brown et al. 2015). It is unclear how the solar wind interacts with the Martian atmosphere under the lack of magnetic fields on that hemisphere, but the observed aurora in that region indicates a direct interaction of solar wind particles with the neutral atmosphere.

The aurora on Jupiter demonstrates that the solar wind interaction is not a necessary condition to auroral emission. At Jupiter, the energy of the solar wind is

weaker than at Earth and the Jovian magnetic field strength is much stronger² (Khurana et al. 2004). Since the observed aurora of Jupiter is a hundred times more energetic and ten times brighter compared to the aurora at Earth (Clarke et al. 2004), a different acceleration process has to be present. Unlike Earth's magnetosphere, Jupiter's magnetosphere is not dominated by the solar wind interaction but by the planet's super fast rotation period of ~ 10 h. Jupiter's intrinsic magnetic field and the magnetospheric plasma roughly corotate with this rotation period at the inner part of the magnetosphere ($< 10 R_J$, where $R_J = 71,492$ km is the radius of Jupiter). At the middle part of the magnetosphere ($10-40 R_J$) this corotation breaks down since Jupiter's ionosphere can not transport sufficient angular momentum to the outflowing plasma. A radial current system develops to maintain (quasi) corotation (Khurana et al. 2004). These radial currents accelerate electrons into the Jovian ionosphere and generate auroral ovals around both poles of Jupiter (Khurana et al. (2004); Figure 2B). This is an almost continuous process and nearly independent of the time-variable solar wind activity.

Auroral emission is not only confined to planets and their dense atmospheres, though. Aurora has been observed also on the Galilean satellites. Embedded within the Jovian magnetosphere, the velocity of the corotating Jovian magnetospheric plasma is much higher than the orbital velocity of the satellites. The magnetospheric plasma impinges the satellites and their tenuous, neutral atmospheres, triggering the auroral emission. The morphology and brightness of the aurora is individual for each planet and for each satellite. They depend on the local planet- or moon-plasma interaction as well as on the composition of their atmospheres. Studying their aurora is therefore a valuable diagnostic tool for exploring their magnetospheric environment and atmospheres. In this thesis, we study the morphology and brightness of the aurora on Ganymede, the largest Galilean satellite. The aurora on Ganymede shares several key features with the aurora on Earth, but there are also huge differences between the bodies besides the size and the internal composition. Both bodies have two distinct auroral ovals aligned around their north and south poles (compare Figure 2A and D; Hall et al. (1998); Feldman et al. (2000); McGrath et al. (2013)). Unlike at Earth, where the auroral ovals can be also observed at visible wavelengths, the auroral ovals at Ganymede have been detected only in the far ultraviolet range until now. Ano-

²e.g., the equatorial magnetic field strength at Earth lies around 30,000 nT and at Jupiter at 400,000 nT (Khurana et al. 2004).

ther particularity of Ganymede is that it is the only moon known so far having its own magnetic field (Kivelson et al. 1996). This magnetic field is strong enough to maintain a region of closed magnetic field lines shielding the moon from the Jovian magnetic field and plasma flow in which Ganymede is embedded. This *mini-magnetosphere* can roughly be compared with Earth's magnetosphere which is embedded within the solar wind. But as the Jovian magnetospheric plasma flow is sub-Alfvénic and sub-sonic, the corotating plasma can interact directly with Ganymede's mini-magnetosphere without being modified by a bow shock, which usually forms upstream of a planetary magnetosphere like at Earth (Jia et al. 2008). Therefore, Ganymede's mini-magnetosphere roughly forms a cylindrical shape, while Earth's magnetosphere exhibits a bullet-like shape.

1.1 Purpose of this thesis

In the past decades, we gained a basic understanding of Ganymede's aurora by several spacecraft missions and HST observations discussed by several authors. The focus of this thesis is the further investigation of Ganymede's aurora under its time-varying components. A common feature of all Galilean satellites is that their orbital plane and the Jovian magnetospheric equator are tilted by $\sim 10^\circ$ due to the misalignment of Jupiter's rotation and dipole axis. As the Jovian magnetic field corotates with the planet's synodic rotation period of 10.5 hours, Ganymede changes its position relative to the magnetic equator within 5.25 hours and transits through the current sheet, a thin layer with increased plasma density in the magnetic equatorial plane. Above and below the current sheet, Jupiter's magnetic field orientation changes. Inside the current sheet, Ganymede is exposed to increased plasma density and thermal pressure compared to outside of the current sheet (Kivelson et al. 1997; Khurana et al. 2004). However, the influence of these periodically changing local plasma conditions on the morphology and brightness of Ganymede's aurora has not been analyzed yet. We therefore analyze sets of HST campaigns which consecutively observe Ganymede's transit from high elevated magnetic latitudes towards the current sheet. Due to the asymmetry of Ganymede's magnetosphere on the plasma upstream and downstream side, we compare the auroral brightness on the upstream and downstream side separately at different positions of Ganymede within the Jovian plasma sheet. We analyze

if and how the location of the ovals varies depending on Ganymede's magnetic latitude. We also analyze the symmetry between the northern and southern oval in order to derive further constraints on the orientation Ganymede's magnetic dipole moment. Finally, we investigate the patchiness of the auroral emission along the ovals in order to investigate any possible correlation between the occurrence of bright auroral spots and the intermittence of the magnetic reconnection on the upstream side of Ganymede's mini-magnetosphere.

1.2 Structure of this dissertation

First, we give in Chapter 2 a brief overview of the basic parameters of Ganymede such as the moon's orbital, surface and interior parameters as well as its intrinsic magnetic field and magnetospheric environment. We provide all information necessary to get a basic understanding for the subsequent discussion of Ganymede's aurora. We present the first observations of the aurora and discuss several theoretical works explaining the generation process of Ganymede's aurora. In Chapter 3, we introduce the HST data sets used in our analysis, the criteria for choosing them and how they are processed. We then present and discuss the results of our study in Chapter 4. Finally, we summarize our main findings conclusions and give a short outlook of possible further studies in Chapter 5.

Ganymede and the discovery of its aurora

In this chapter, we present all previous observations and modeling of Ganymede's aurora, which are relevant for the purpose of this thesis. First, we briefly introduce key properties of Ganymede regarding its interior and surface composition, its atmosphere, and its subsurface ocean. We provide all necessary key features for a basic understanding of Ganymede's magnetospheric environment including a description of Ganymede's intrinsic magnetic field. In the second part of this chapter, we discuss the discovery and all previous spectroscopic observations of the aurora on Ganymede. At the end of this chapter, we present works by several authors which theoretically describe the excitation process of Ganymede's aurora.

2.1 Ganymede and the Jovian System

In the past decades, Ganymede, as well as the Jovian system, have been investigated by several space missions including short time surveys during stop-over flybys, e.g., the *Pioneer* (1973/1974) and *Voyager* (1979) missions, as well as long time surveys. By far the longest in-situ observations were obtained by the *Galileo* spacecraft (1989-2003) which entered the Jovian system on December 7, 1995 and orbited Jupiter and the Galilean satellites for almost eight years. In the following, we present basic facts about Ganymede and its environment obtained by these space missions (supplemented by ground based observations or observations during flybys of other spacecrafts).

2.1.1 Ganymede's surface structure, interior composition, and subsurface ocean

Ganymede is by far the largest moon of the Galilean satellites. Basic orbital and physical parameters of Jupiter and the Galilean satellites are summarized in Table 1 (Bagenal et al. 2004). Having a radius of $R_G = 2,634$ km, Ganymede not only is the largest moon among all moons of our solar system (e.g., Earth's Moon has a radius of $1,737$ km = $0.65 R_G$) but is even larger than the innermost planet Mercury, which has a radius of $2,440$ km (= $0.93 R_G$). Being tidally locked, Ganymede takes 7 days, 3 hours and 42.6 minutes for a full rotation around Jupiter. Preceded by Io and Europa and followed by Callisto, Ganymede is the third of the Galilean satellites and orbits Jupiter with a low inclination $\ll 1^\circ$ at an average distance of $\sim 1,070,400$ km or ~ 15 Jupiter radii (1 Jupiter radius $R_J = 71,492$ km). The orbital velocity of Ganymede is 11 km/s and the eccentricity of Ganymede's orbit, 1.5×10^{-3} , is very small.

Table 1 – Orbital and physical parameters of Jupiter and the Galilean satellites. (Bagenal et al. 2004)

body	radius ^{a)} [km]	mass [kg]	distance ^{b)} to Sun/Jupiter	orbital period	avg. orbital velocity	<i>i</i> ^{c)}	rotation period
Jupiter	$R_J = 71,492$	1.9×10^{27}	5.2 AU ^{d)}	11.7 yr	13.1 km/s	1.3°	9.93 h
Io	$R_I = 1,822$	8.9×10^{22}	5.9 R_J	1.8 d	17.3 km/s	0.1°	syn. ^{e)}
Europa	$R_E = 1,561$	4.8×10^{22}	9.4 R_J	3.6 d	13.7 km/s	0.5°	syn. ^{e)}
Ganymede	$R_G = 2,634$	1.5×10^{23}	15.0 R_J	7.2 d	10.9 km/s	0.2°	syn. ^{e)}
Callisto	$R_C = 2,401$	1.1×10^{23}	26.3 R_J	16.7 d	8.2 km/s	0.2°	syn. ^{e)}

a) equatorial radius

b) average between apo- and pericenter

c) inclination relative to the ecliptic (for Jupiter) and Jupiter's equatorial plane (for the moons)

d) 1 AU = 1 Astronomical Unit = 149,597,870.7 km

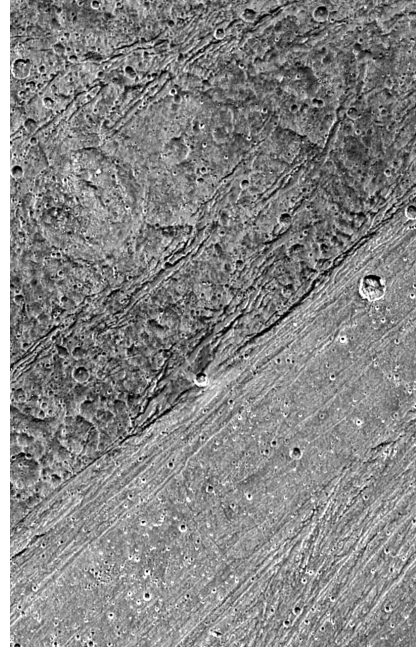
e) synchronous rotation, i.e., tidally locked

Surface and albedo

The surface temperature varies between 70 K on the nightside and 152 K on the dayside. The average surface temperature is 110 K (Orton et al. 1996; Delitsky and Lane 1998). Ganymede's surface consists mostly of frozen water but also contains minor components of carbon and sulfur dioxide (CO₂, SO₂) as well as organic compounds (McCord et al. 1998; Pappalardo et al. 2004). Most characteristic for Ganymede's surface is its division into two major terrain types. Forty percent of the surface is a relatively old and dark terrain, while the rest consists of younger and brighter terrain (Showman and Malhotra 1999; Pappalardo et al. 2004). Figure 3A shows a composite image of Ganymede's trailing hemisphere. The false color image is a composition of images at different wavelengths taken by the *Solid State Imaging* system (SSI) on board the *Galileo* spacecraft and enhances the contrast between the dark and bright terrain. The dark terrain is geologically very old and highly cratered, indicated by the white dots in Figure 3A and 4. It contains clays and organic materials which darkens the water ice in that terrain (Pappalardo et al. 2004). Estimated from the crater density, the dark terrain is approximately four billion years old (Zahnle et al. 1998). The bright terrain is less cratered and relatively smooth. Observations by the *Galileo* spacecraft indicate that the craters in the bright area have been smoothed out due to resurfacing, which indicates that this terrain is geologically younger than the dark ter-



A False color image of Ganymede's trailing hemisphere centered at 306° west-longitude (North is at the top). The image is a composition of green, violet, and micrometer filtered images taken on March 29, 1998 by the Solid State Imaging system on board the *Galileo* spacecraft.



B A 25×10 km cut-out of the trailing hemisphere (306° west-longitude and -14° latitude, North is on the right side), showing parts of Nicholson Regio (top, dark terrain) and Harpagia Sulcus (bottom, bright terrain).

Figure 3 – Surface of Ganymede: Global view of Ganymede's trailing hemisphere (A) and a zoom on Ganymede's surface structure (B). (Pappalardo et al. 2004, supplementary material)

rain (Pappalardo et al. 2004). The bright terrain is also characterized by arrays of grooves and ridges (Pappalardo et al. 1998). Figure 3B shows the harsh contrast between the dark and bright terrain. Shown is a 25×10 km² cut-out of Ganymede's trailing hemisphere that contains parts of *Nicholson Regio* (top, dark terrain) and *Harpagia Sulcus* (bottom, bright terrain) (Pappalardo et al. 2004). The two specific regions are also indicated in Figure 4 (see blue text annotations). The mechanism for the formation of the grooved terrain is still unclear. Tectonic activity is supposed as the main heating mechanism, but also cryovolcanism might have played a role for the formation of Ganymede's surface structure (Pappalardo et al. 1998, 2004).

The mosaic of high- and mid-resolving images from the *Voyager* 1 and 2 and the *Galileo* missions in Figure 4 provides a global view of Ganymede's surface in the

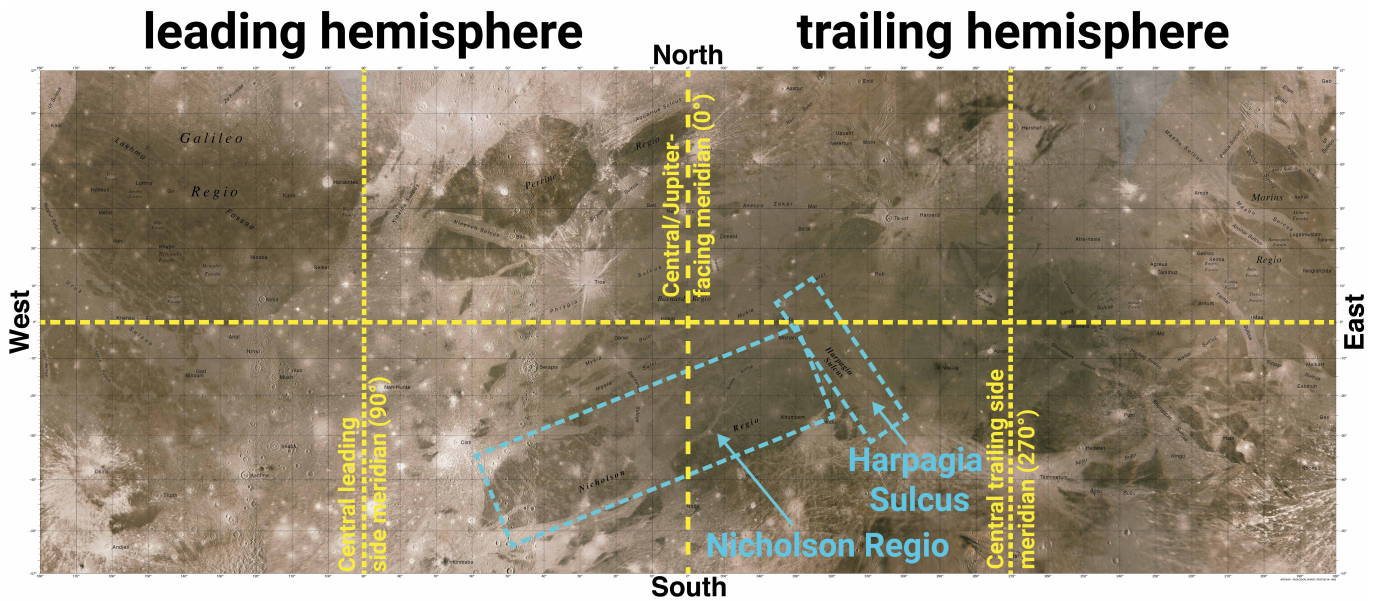


Figure 4 – Mosaic of high- and mid-resolving photographs from *Galileo* and *Voyager* 1 and 2, mercator projected on a sphere of Ganymede’s radius for planetographic latitudes up to $\pm 56^\circ$ (modified; for further processing details read USGS (2003)). The planetographic central/ 0° longitude is defined by the Jupiter-facing meridian (thick vertical dashed yellow line). Leading and trailing hemispheres are also indicated. Names of regions on this map are approved by the International Astronomical Union (IAU). A larger version of this image is available in Figure 53 in Appendix S9. (USGS 2003)

latitudinal band between $\pm 56^\circ$ (USGS 2003). The brightness of each individual image is adjusted to provide a seamless composite image at visible wavelength range. We have modified the original image from USGS (2003) by adding additional annotations. We indicate the central Jupiter-facing meridian, which defines the 0° planetographic longitude. The image uses the planetographic west-longitude system, i.e., the longitude is counted in clockwise direction. Unless otherwise indicated, we use this definition for Ganymede’s planetographic coordinate system throughout this work. The orbital leading and trailing hemisphere as well as their corresponding central meridian, i.e., 90° and 270° longitude, are also indicated. In this broad overview of Ganymede’s surface, we see that the leading side seems to be brighter than the trailing side. Pappalardo et al. (2004, and references therein) created a global map of Ganymede’s albedo at the visible wavelength of 5600 \AA ($1 \text{ \AA} = 10^{-1} \text{ nm}$), shown in Figure 5. The authors derived a synthetic light curve (solid line) from *Voyager* and *Galileo* observations and adjusted it in order to fit various observations from ground-based¹ telescope observations (circles

¹i.e., Earth-based

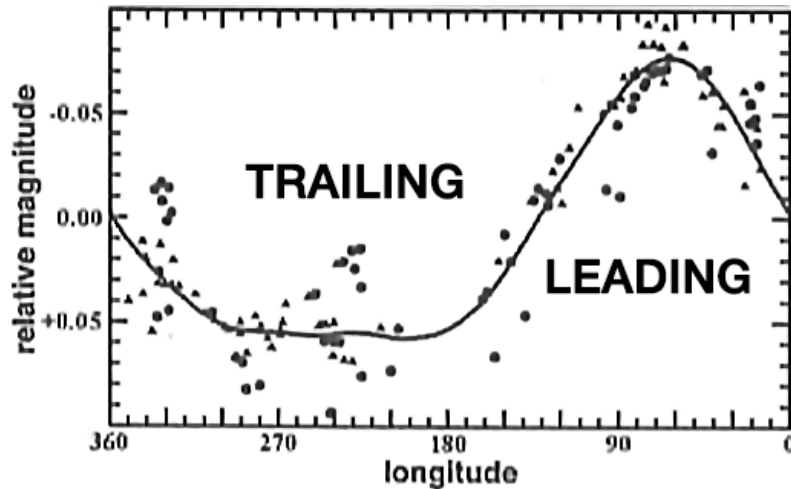


Figure 5 – Albedo map of Ganymede at 5600 Å (visible light). A synthetic light curve (solid line, derived from *Voyager* and *Galileo* observations) is adjusted to various telescope observations (circles and triangles). (Pappalardo et al. (2004, their figure 16.24) and references therein)

and triangles). The light curve confirms a hemispheric albedo dichotomy for that wavelength range. Similar to Europa, the reflectance is higher on the leading side than on the trailing side (Calvin et al. 1995; Pappalardo et al. 2004). A possible explanation for the dichotomy could be an enhanced reservoir of SO_2 on the trailing side (Domingue et al. 1996, 1998; Pappalardo et al. 2004).

Polar caps

As frozen ice particles scatter light at shorter wavelengths, the violet enhancements at the poles in Figure 3A are possibly caused by Ganymede's frosty polar caps (Pappalardo et al. 2004). On average, Ganymede's polar caps have a very vast latitudinal extension as they extend down to 40° latitude, at some locations they can even reach 25° latitude (compared to Earth: e.g., Cologne lies at 50° north latitude). There are different theories about the origin of Ganymede's polar caps. The most common explanation is an enhanced bombardment of the surface by plasma particles due to Ganymede's intrinsic magnetic field, which has been discovered by the *Galileo* mission (Kivelson et al. 1996; Khurana et al. 2007). The surface sputtering leads to a redistribution of water molecules and frozen particles can migrate into the colder areas of the polar region (Khurana et al. 2007).

Interior composition

Even though Ganymede's surface is dominated by frozen water (50–90%, Showman and Malhotra (1999), Pappalardo et al. (2004)), its density of 1.936 g cm^{-3} suggests a nearly equal portion of ice and rocky material for Ganymede as a whole (Showman and Malhotra 1999). Ganymede has a mass of $1.482 \cdot 10^{23} \text{ kg}$ (Showman and Malhotra 1999). This is only 0.025 times the mass of Earth but nearly twice the mass of the Moon. Although Ganymede is slightly larger than Mercury, its mass is only half of that of Mercury. Ganymede's moment of inertia, derived from observations during close flybys by the *Galileo* spacecraft, is with $C/MR^2 = 0.3105 \pm 0.0028$ the smallest measured value for a solid body in our solar system (Anderson et al. 1996; Showman and Malhotra 1999). For example, Earth has a moment of inertia of $C/MR^2=0.3307$ and Mercury $C/MR^2=0.346$. A moment of inertia lower than 0.4³ indicates an increasing density with increasing depth. The model for Ganymede's interior by Bland et al. (2008), where Ganymede is differentiated into three different layers, is so far the best explanation for the measured moment of inertia. As shown in Figure 6, this model includes a central iron sulfide (FeS) core, a silicate mantle, and an outer layer of mostly frozen water. In order to sustain the intrinsic magnetic field, Showman and Malhotra (1999) suggest the existence of a metallic core and Anderson et al. (1996) and Schubert et al. (1996) propose that the radius of such a core lies between 0.15 and 0.5 R_G . In the Bland et al. (2008) model, the core has a radius of 700 km and consists of an outer solid mantle and a liquid inner core. The surrounding silicate mantle has a thickness of 1020 km. The outer layer, with a thickness of 914 km, consists of water shells of different types of ice⁴ and possibly one (Schubert et al. 2004) or more layers (Vance et al. 2014) of liquid water oceans of unknown thickness and depth. Possible heating sources of a subsurface ocean on Ganymede are tidal forces and the orbital resonance of Ganymede with Europa (1:2) and Io (1:4) (Showman et al. 1997). According to the model by Bland et al. (2008), the subsurface ocean must have a minimum thickness of 22 km. In contrast, Kivelson et al. (2002) derive a minimum thickness of 10 km from their magnetic field model. The depth of the ocean is assumed to lie between 150 and 170 km beneath the icy

²C: polar moment of inertia of the body; M: mass of the body; R: mean radius of the body.

³ $C/MR^2 = 0.4$ is the moment of inertia of a sphere with uniformly density distribution.

⁴In Figure 6, two different types of ice are indicated: crystalline ice (ice I) and high pressure ice (HP ice). Ice is classified according to its temperature and pressure, which defines the phase state of the ice.

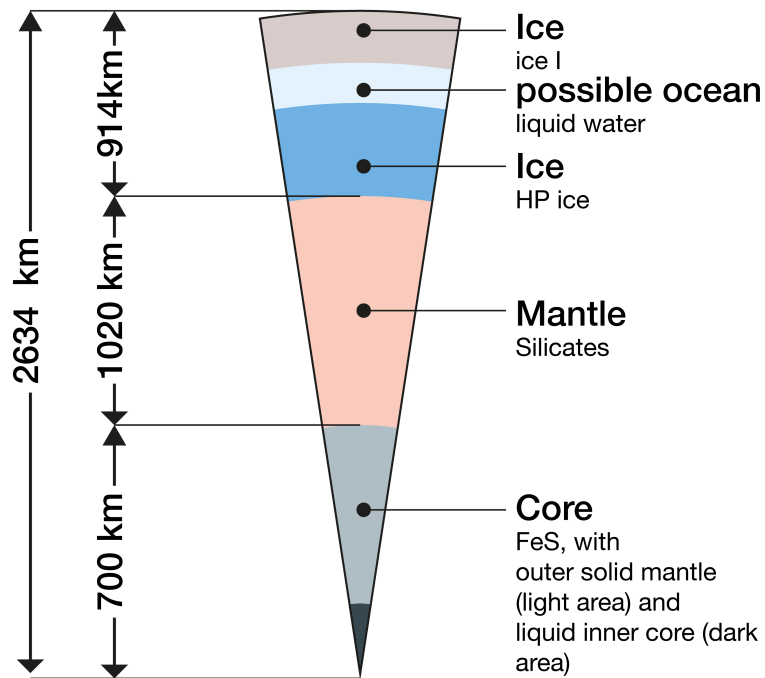


Figure 6 – Sketch of Ganymede’s interior composition according to a three-layer model by Bland et al. (2008).

surface Kivelson et al. (2002). We discuss Ganymede’s subsurface ocean in the following section in more detail.

Subsurface ocean

First indications of a subsurface ocean at Ganymede were found by Kivelson et al. (2002) who analyzed magnetic field measurements taken by the *Galileo* spacecraft. However, the interpretations of these magnetometer data are not conclusive, i.e., they can be explained with two different models for Ganymede’s internal magnetic field at the same time (Saur et al. 2015). The first model includes a dynamo dipole field with additional quadrupole moments. The second model includes a dynamo dipole field with an induced field within a saline subsurface ocean. In the second model, preferred by Kivelson et al. (2002), the time-variable component of Jupiter’s magnetic field at Ganymede’s orbit is responsible for the induction in the electrically conductive subsurface ocean. The major disadvantage of the reported magnetometer measurements is the fact that they were taken during several flybys and the individual flyby trajectories are not identical. Therefore, it is not possible to distinguish between spatial variations and temporal

variations, i.e., between magnetic moments of higher order or induction effects in a subsurface ocean. As a consequence, the magnetic field measurements alone are ambiguous and they rather suggest than prove the existence of an ocean at Ganymede.

Saur et al. (2015) use a different approach to verify the existence of the ocean. They analyzed the response of Ganymede's auroral ovals to the time-varying component of the Jovian magnetospheric field in Ganymede's vicinity. They used temporally and spatially resolved HST observations of Ganymede's auroral ovals which do not suffer from the mentioned ambiguity of the magnetometer measurements. As sketched in Figure 7, in the absence of an ocean, Jupiter's time-variable magnetic field would cause an oscillation of the auroral ovals by $5.8^\circ \pm 1.3^\circ$ (Saur et al. 2015). Saur et al. (2015) showed that the observed amplitude of the oscillation is only $2.0^\circ \pm 1.3^\circ$. As a conductive subsurface ocean partly compensates Jupiter's time-variable fields through electromagnetic induction, Saur et al. (2015) relate the reduced oscillation to the induction in a saline subsurface ocean within Ganymede. At the same time, when induction signals at Ganymede are present, the inferred quadrupole coefficients of Ganymede's dynamo field must be particularly small (Kivelson et al. 2002; Christensen 2015; Saur et al. 2015). This is the first conclusive proof of a subsurface ocean by measuring the location of the auroral ovals on a solar system body. Prior to Saur et al. (2015), Roth et al. (2014b) found potential evidence for a subsurface ocean at Europa, i.e., they found erupting water vapor plumes at the moon's surface, also by using spectroscopic HST observations⁵. Saur et al. (2015) also suggest that Ganymede's ocean lies between 150 and 250 km beneath the surface or, alternatively, its top edge lies at a maximum depth of 330 km.

2.1.2 Atmosphere

First indications for an atmosphere at Ganymede come from stellar experiment observation by Carlson et al. (1973). The authors estimate an atmospheric surface pressure of around $1 \mu\text{bar}$ ⁶. Observations by the *Voyager Ultraviolet Science*

⁵As the magnetospheric configuration and properties at Europa are different compared to Ganymede, Roth et al. (2014b) used a different approach: They detected water vapor plumes above the limb of the observed disk of Europa. For more details, please read Roth et al. (2014b, a) and Roth et al. (2016).

⁶1 microbar = 0.1 Pascal (Pa) = 0.1 N m^{-2}

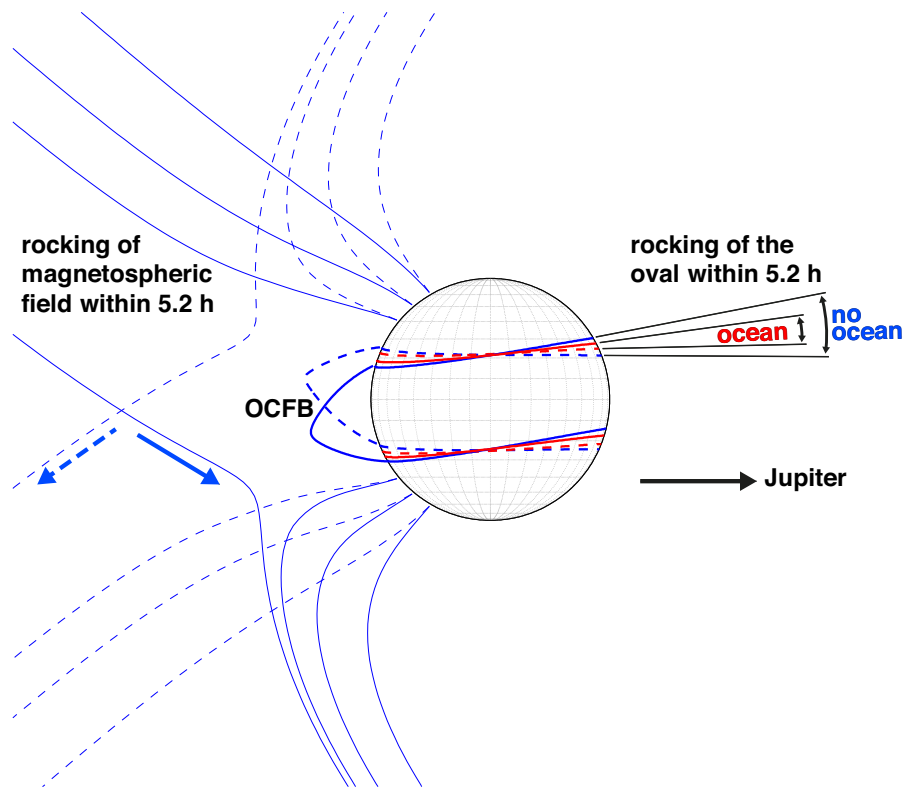


Figure 7 – Sketch of the “rocking” auroral ovals at Ganymede taken from Saur et al. (2015, their figure 1). Within 5.25 hours, Ganymede transits from above to below the Jovian current sheet and experiences a change of orientation of the Jovian magnetospheric field (simplified, blue thin lines). Shown is the case when Ganymede is above (dashed lines) and below the current sheet (solid lines), respectively. The auroral ovals, whose location coincide with the location of the open-closed field line boundary (OCFB, further details see Section 2.1.3), respond to this time-varying magnetic field by a “rocking”, i.e., an oscillation of the ovals. Without induction in a subsurface ocean this oscillation is stronger (blue lines) than with induction (red lines) as the induction in an ocean partly compensates Jupiter’s time-variable field.

telescope (UVS) five years later could not confirm an atmosphere and placed an upper limit on the surface pressure. This value is five times lower in magnitude than the value suggested by Carlson et al. (1973) and corresponds to a surface particle number density of $1.5 \times 10^9 \text{ cm}^{-3}$ (Broadfoot et al. 1981). Around two decades later, Hall et al. (1998) finally find new evidence for an atmosphere on Ganymede from spectroscopic *Hubble Space Telescope Goddard High Resolution Spectrograph* (HST/GHRS) observations. Hall et al. (1998) observe emission at the FUV wavelengths at $\text{OI } \lambda 1304 \text{ \AA}$ and $\text{OI } \lambda 1356 \text{ \AA}$ (Figure 13) which is associated to an airglow of atomic oxygen. The excitation of this airglow, in turn, is associated with dissociation of neutral molecular oxygen by electron impact, indicating that a tenuous neutral oxygen atmosphere must be present at Ganymede.

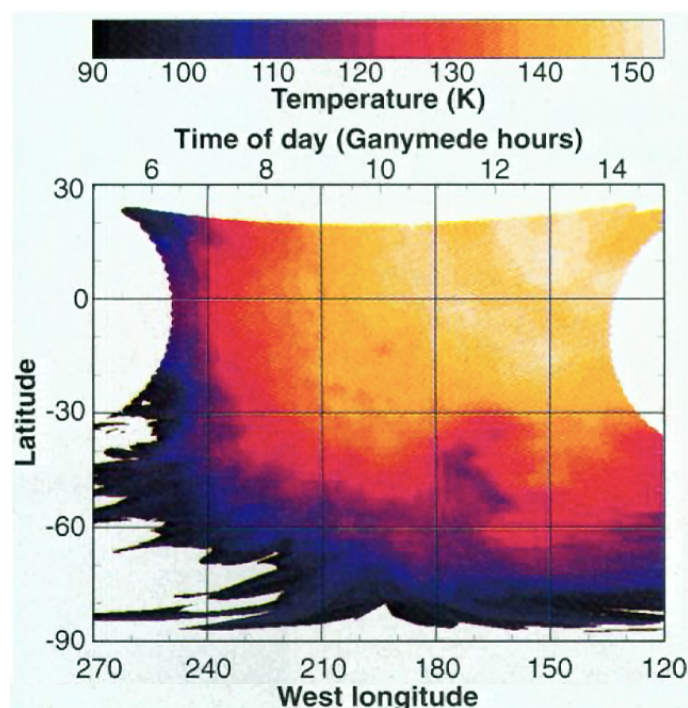


Figure 8 – Heating map of Ganymede’s dayside from Orton et al. (1996, their figure 1; reprinted with permission from AAAS, see Appendix S9 for further details). Top axis is in Ganymede local time (e.g., 12 h = local noon), bottom axis is in planetographic west-longitude. y -axis is in planetographic latitudes. Color coded is the temperature range from 90 to 150 K.

Implied from the intensity ratio of the two oxygen lines, this atmosphere predominantly consists of molecular O_2 (Hall et al. 1998). Hall et al. (1998) calculate an O_2 column density lying between 10^{14} and 10^{15} cm^{-2} .

Two sources for Ganymede’s atmosphere are suggested: sublimation and sputtering of the frozen water on the surface (Eviatar et al. 2001b; Turc et al. 2014). Sublimation is predominant in the region around the sub-solar point, i.e., the equatorial and tropical region on the dayside. Here, water vapor and hydroxyl (HO) are able to survive in the atmosphere (Eviatar et al. 2001b). Since this region is shielded from magnetospheric energetic electrons by closed field lines of Ganymede’s magnetic field, photodissociation is the main process for splitting the water molecules into hydrogen and oxygen (Budzien et al. 1994; Eviatar et al. 2001b). The volatile hydrogen escapes the atmosphere due to the low energy, which is required to escape from Ganymede’s surface (Eviatar et al. 2001b). The heavier oxygen remains gravitationally bound to Ganymede, forming the atmosphere. Atomic oxygen is created by photodissociation of O_2 molecules (86%) and H_2O (14%) (Eviatar et al. 2001b). In the polar region and on the nightside,

the temperatures are too low for sublimation (Eviatar et al. 2001b; Turc et al. 2014) as shown in Figure 8 (taken from Orton et al. (1996)). The heating map for Ganymede's dayside in Figure 8 shows a vast temperature gradient from ~ 150 K around the subsolar point to ~ 90 K at higher latitudes and in the pre-dawn region (Orton et al. 1996). O_2 , H_2 and H are produced by sputtering of surface water ice in the magnetospheric unprotected polar region, i.e., the region of open magnetic field lines without magnetospheric shielding effects (Bar-Nun et al. 1985; Eviatar et al. 2001b). Sputtered water vapor and OH recondense at once in the low temperature region at the poles and nightside. The hydrogen (atomic and molecular) escapes rapidly, again due to the low escape velocity required at Ganymede. Only molecular oxygen can survive in gaseous state at temperatures above 80 K (Johnson 1996) forming the atmosphere in these colder regions (Eviatar et al. 2001b).

The two different atmospheric production processes lead to a strong atmospheric dichotomy between polar and subsolar equatorial regions (Turc et al. 2014). This atmospheric dichotomy also impacts Ganymede's ionosphere. The existence of an ionosphere at Ganymede is implied by its indigenous, neutral atmosphere as neutral oxygen (atomic and molecular) gets ionized by magnetospheric energetic electrons and solar extreme ultraviolet (EUV) radiation (Paranicas et al. 1999; Eviatar et al. 2001b). Eviatar et al. (2001b) report that the ionosphere is dominated by molecular oxygen ions in the polar and by atomic oxygen ions in the equatorial region. In addition to the ionospheric plasma outflow, i.e., an outflow of oxygen ions at the polar caps, Eviatar et al. (2001b) expect an oxygen corona above the limb of Ganymede from neutral, (low) excited oxygen atoms escaping the polar cap region. A corona of escaping hydrogen has been already detected by Feldman et al. (2000) with the *Space Telescope Imaging Spectrograph* (STIS) on board of HST. Feldman et al. (2000) actually confirmed the previous discovery of a Lyman- α emission from a hydrogen exosphere by Barth et al. (1997) from *Galileo* UVS observations.

2.1.3 Ganymede's intrinsic magnetic field and magnetospheric environment

One major finding of the *Galileo* mission regarding Ganymede is the discovery of the intrinsic magnetic field of the moon (Kivelson et al. 1996). So far, Gany-

mede is the only known moon which possesses its own permanent magnetic field embedded within a planetary magnetosphere. The magnetic field is strong enough to shield Ganymede from the Jovian magnetic field and a so-called *mini-magnetosphere* develops. In the following, we briefly describe the individual components of Ganymede's magnetic field and its interaction with the surrounding Jovian magnetic field.

Discovery and main characteristics

From magnetic field measurements by the *Galileo* spacecraft during the six close flybys at Ganymede, *G1*⁷, *G2*, *G7*, *G8*, *G28* and *G29*, from 1996 to 2000, Ganymede's magnetic field topology has been analyzed at significant different locations in the magnetospheric environment of the moon. In first-order, Ganymede's magnetic field can be approximated by a dipole magnetic field (Kivelson et al. 1996, 1998) with an equatorial field strength of 719 nT⁸ (Kivelson et al. 2002). The magnetic moment of the dipole is tilted by 176°, i.e., the magnetic north pole lies in the southern hemisphere and is rotated by -24° planetographic west-longitude (Kivelson et al. 2002). Higher moments, e.g., quadrupole moments are very small compared to the dipole moment (Kivelson et al. 2002).

Shortly after the discovery of Ganymede's magnetic field, Kivelson et al. (1996) developed a first-order approximation of the magnetic field topology at Ganymede. Adopted by Neubauer (1998), this simplified model is shown in Figure 9. It consists of a vacuum-superposition of Ganymede's magnetic dipole field and the ambient Jovian background magnetic field (both fields are oriented in anti-parallel direction). Even though this model neglects the local plasma interaction and internal induced fields, it demonstrates very well the different magnetospheric regions emerging at Ganymede. *Region I* is defined by the closed magnetic field lines starting and ending in the ionosphere of Jupiter. Open field lines at the poles connect Ganymede with the Jovian ionosphere and define *Region II*. Finally, *Region III* is defined by the region of closed Ganymedean field lines around Ganymede's equator, i.e., they start and end on Ganymede. The open-closed field line boundary (OCFB), sometimes also called *separatrix*, separates the individual regions from each other.

⁷the number refers to the orbit of the close flyby at Ganymede

⁸1 Tesla (T) = 1 kg s⁻² A⁻¹

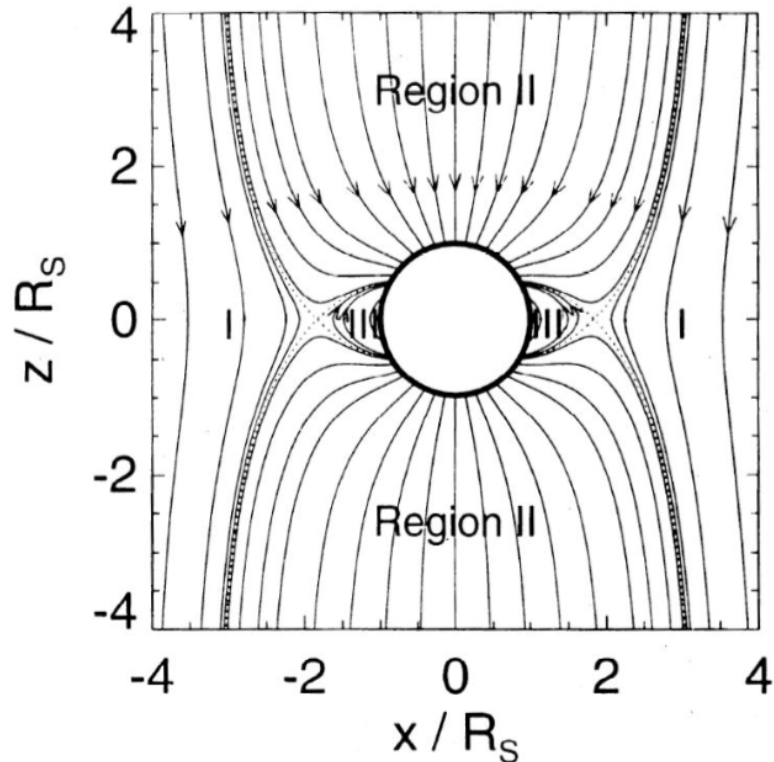


Figure 9 – First-order approximation of the magnetic field topology at Ganymede (taken from Neubauer (1998)): A vacuum-superposition of a parallel Ganymedean dipole magnetic field and ambient Jovian background magnetic field. Viewing geometry see Figure 10. R_S is the radius of Ganymede. Region I to III indicate the region of closed field lines originating and ending on Jupiter (I), open field lines connecting Ganymede with the Jovian ionosphere (II) and closed Ganymedean field lines (III), respectively.

As the background magnetic field of Jupiter at Ganymede's orbit with 120 nT is low compared to Ganymede's equatorial field strength, Ganymede's intrinsic magnetic field is strong enough to carve out space in the Jovian magnetosphere, creating a so-called *mini-magnetosphere* around Ganymede with a diameter between 4 to 5 R_G (Kivelson et al. 1998; Neubauer 1998). In agreement with Ganymede's oxygen atmosphere (see Section 2.1.2), the main ion species of this mini-magnetosphere are O^+ and O_2^{+9} (Eviatar et al. 2001b). At Ganymede's magnetic equator, both, the Jovian and Ganymedean magnetic field, are oriented in anti-parallel direction and magnetic reconnection might occur at points where both fields intersect (Neubauer 1998).

On its orbit around Jupiter, Ganymede always remains in the Jovian magnetos-

⁹The low latitude region is dominated by O^+ , while in the polar cap region the main ion species are O^+ and O_2^+ (Eviatar et al. 2001b).

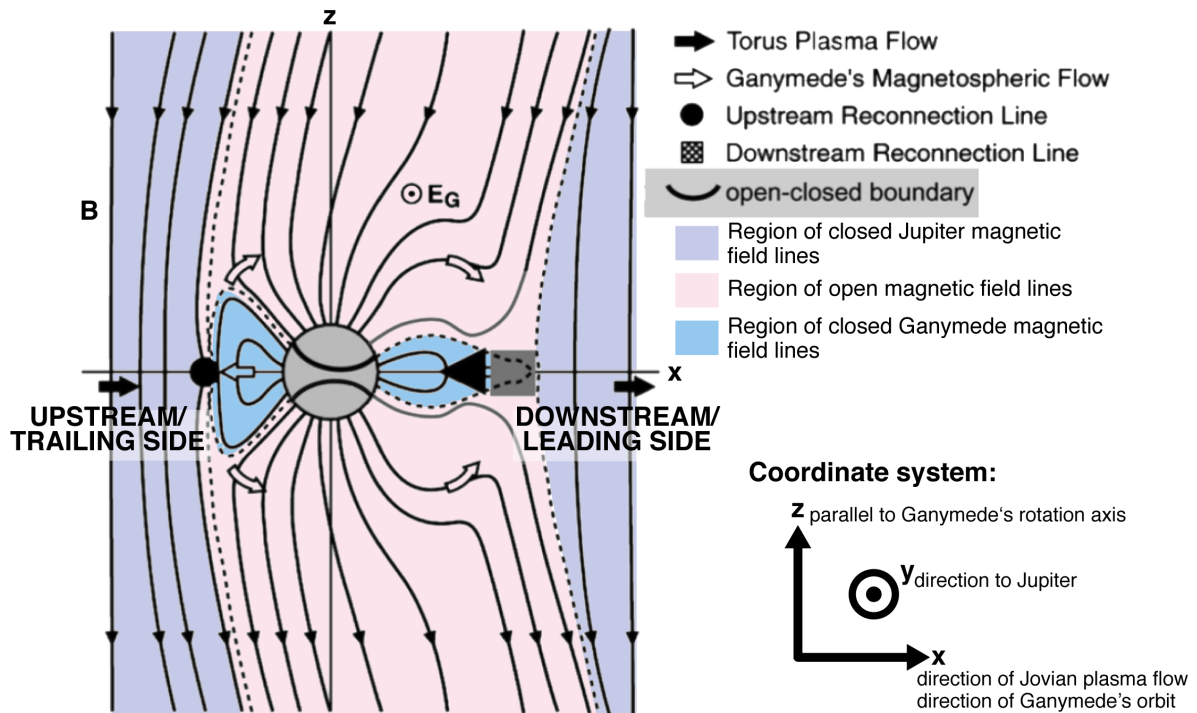


Figure 10 – Schematic view of Ganymede's magnetic field taken from Kivelson et al. (2004, their figure 21.4, modified), viewing onto the two-dimensional plane which contains the Jovian plasma flow and Ganymede's orbital trajectory (x -direction) and Ganymede's rotation axis (z -direction). The view points into the direction towards Jupiter (y -direction, not shown here, see coordinate system definition for further details). Indicated are the three different magnetic field lines regions: closed field lines originating and ending on Jupiter (violet), open field lines connecting Ganymede with the Jovian ionosphere (red) and closed Ganymede field lines starting and ending on Ganymede (blue). The open-closed field boundary (OCFB, dashed line) separates the individual regions from each other. The OCFB's intersection with Ganymede's surface/ionosphere is sketched as the two thick curves on the moon disk.

phere. Furthermore, Ganymede is exposed to the steady flow of the Jovian magnetospheric plasma. At Ganymede's orbit, the plasma flow slightly sub-corotates with the Jovian magnetic field with a flow velocity of 150 km/s which is much higher than Ganymede's orbital velocity of 11 km/s (Kivelson et al. 1998, 2002; McGrath et al. 2013). Hence, Ganymede is constantly overtaken by the bulk plasma flow. The plasma impinges the upstream side, i.e., Ganymede's trailing hemisphere, and distorts the dipolar shape of Ganymede's magnetosphere. This forms the bullet-like shape which can be observed for many other planetary magnetospheres in the solar system like at Earth, where the solar wind hits and distorts Earth's magnetosphere in the same way. Unlike at Earth, where the incoming plasma flow is super-sonic, the bulk plasma flow at Ganymede is sub-sonic and no bow shock

forms on the upstream side. Under these circumstances, Ganymede's magnetosphere has a more cylindrical shape rather than the typical bullet-like shape.

In addition to the simple vacuum-superposition shown in Figure 9, Figure 10 shows Ganymede's magnetic field environment under the influence of the impinging plasma flow. We have modified this figure from Kivelson et al. (2004, their figure 21.4) and indicated the three different magnetospheric regions from above with colors: closed Jovian magnetic field lines (violet shaded area), open field lines connecting Ganymede with Jupiter's ionosphere (red) and the region of closed Ganymedeian field lines (blue). The plasma flow velocity is in x -direction and the z -axis contains Ganymede's rotation axis. The viewer looks into the direction towards Jupiter (see coordinate system definition in that figure for a better understanding). The OCFB is indicated by the dashed line. The OCFB's intersection with Ganymede's surface is sketched as the two thick curves on the moon disk. The points of reconnection are actually points where two separatrices intersect (indicated by a black circle and square in that figure). In a three-dimensional interpretation, the reconnection points form a ring surrounding Ganymede (Neubauer 1998; Duling et al. 2014). Figure 10 also demonstrates the influence of an additional magnetic field due to the plasma interaction (Kopp and Ip 2002; Ip and Kopp 2002; Jia et al. 2009b). On the upstream side, this additional magnetic field is oriented anti-parallel to the ambient Jovian magnetic field and counteracts the background field, i.e., it weakens the background magnetic field. Due to the slight weakening of the background magnetic field, Ganymede's intrinsic field becomes more effective and is able to expand the mini-magnetosphere on the upstream side. This expansion leads to a shifting of the OCFB towards higher latitudes on Ganymede. On the downstream side, the opposite is the case and the mini-magnetosphere gets stretched into the plasma flow direction and hence the OCFB shifts down towards lower planetographic latitudes.

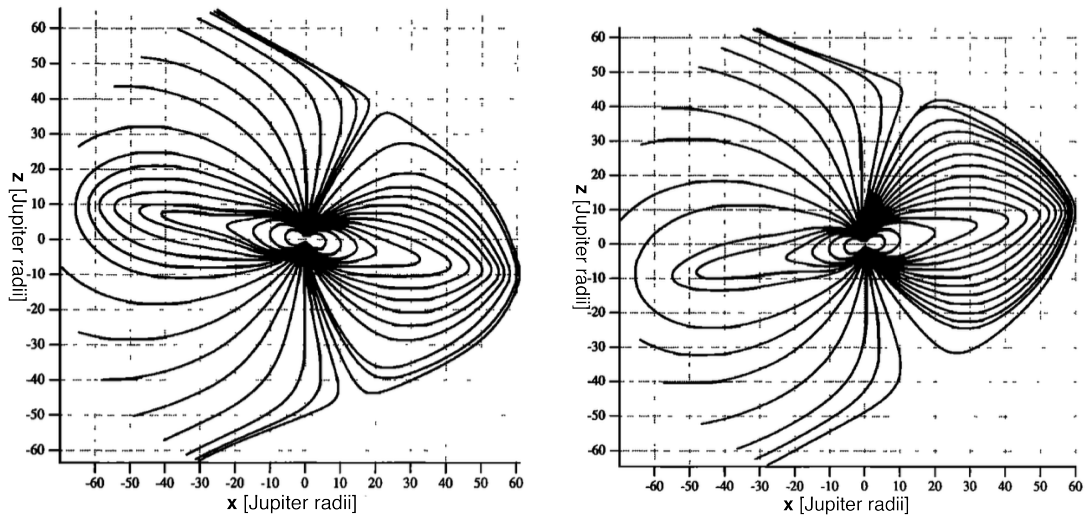
Origin of the intrinsic magnetic field

Overall, Ganymede's magnetic field consists of a superposition of the satellite's intrinsic magnetic field, the Jovian background field, the induced field in a subsurface ocean (see Chapter 2.1.1), and the magnetic field due to the local plasma interaction. Ganymede's magnetosphere and its interaction with the local plasma has been modeled by several authors, e.g., Kivelson et al. (2002), Kopp and Ip

(2002), Ip and Kopp (2002), Paty and Winglee (2004), Jia et al. (2008), Jia et al. (2009b) and Duling et al. (2014). These theoretical works were able to reproduce and explain the *Galileo* magnetic field measurements. In contrast, the origin of the measured Ganymede magnetic field is still controversially discussed. For example, Cray and Bagenal (1998) suggest remanent ferromagnetism hold in an outer layer which is enriched with iron-bearing minerals and magnetite. The source of this remanent ferromagnetism would be Jupiter's magnetic field in the past, when Ganymede was closer at Jupiter, or a paleomagnetic field originating from a dynamo which would have become inactive today. On the other hand, due to the measured weak quadrupole moments, Kivelson et al. (2002) suggest a convectively driven dynamo in Ganymede's liquid iron-sulfide (FeS) core (Figure 6). Additional contribution to the dynamo driven magnetic field comes from the so-called iron snow (Zhan and Schubert 2012; Christensen 2015). On top of the core, liquid iron crystallizes as the core temperature decreases below the melting temperature of iron. The solidified iron becomes heavier than the surrounding liquid iron and sulfur and sinks down to deeper core regions. At deeper core regions, the temperature increases and the iron snow remelts again and enriches the core fluid with iron, driving compositional convection (Christensen 2015).

Variability of the magnetospheric environment

The Jovian magnetic field can be described in a first-order approximation as a dipole magnetic field (Krupp et al. 2004). Its dipole moment is tilted by 9.6° relative to the rotation axis. A simplified representation of the Jovian magnetospheric field lines is shown in Figure 11 after the model by Engle (1992). Shown is the periodic variation of the Jovian magnetic field orientation relative to Jupiter's equatorial plane within 10.5 hours, the synodic rotation period of Jupiter. This global model of the Jovian magnetosphere includes a thin current sheet layer constrained to the dipole magnetic equator (not shown in the figure). The current sheet (CS), also called plasma sheet, is a layer of magnetospheric plasma which is constrained to the magnetic equator due to centrifugal forces from the corotating plasma (Khurana 1997; Khurana et al. 2004). However, Engle (1992)'s model does not include hinging and delaying of the current sheet due to internal and external forces on the Jovian magnetic field configuration (Khurana et al. 2004). Figure 12 shows a more realistic geometry of the current sheet after Khurana et al. (2004).



A Magnetic dipole axis tilted 10° towards the sun.

B Magnetic dipole axis tilted 10° away from the sun.

Figure 11 – Two-dimensional noon-midnight plane (positive x -direction points towards the sun) of Jovian magnetic field lines after Engle (1992, their figures 2 and 3) for two different magnetic field orientations relative to Jupiters rotation axis/equatorial plane.

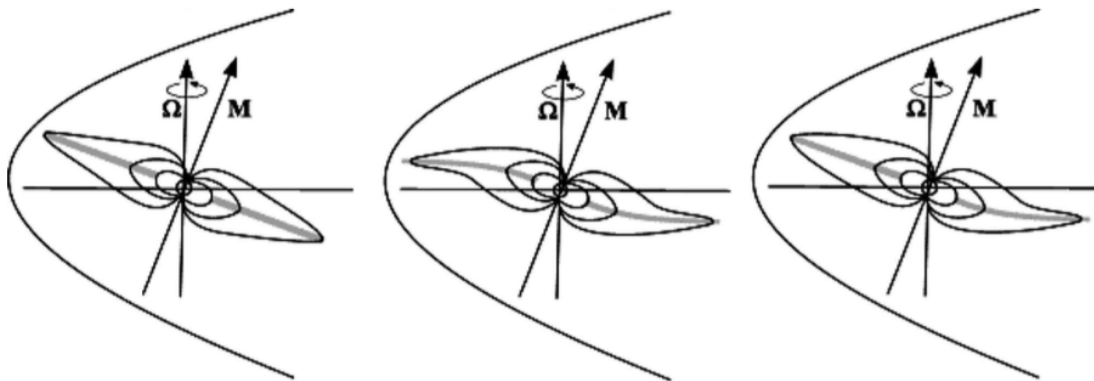


Figure 12 – Schematic view of the Jovian current sheet (CS) after Khurana et al. (2004, their figure 24.5) for three different magnetic field configurations. Left: CS as a rigid disk constrained to the dipole magnetic equator, Center: CS hinged by stresses due to the magnetospheric plasma, Right: CS hinged due to solar wind forcing on the night side.

Due to the very low eccentricity, Ganymede nearly orbits in Jupiter's equatorial plane. But due to the tilt of the Jovian magnetic field, Ganymede changes its position relative to the current sheet every 5.25 hours, i.e., Ganymede transits from above to below the Jovian current sheet. During this transit, Ganymede experiences a change of the Jovian magnetic field lines orientation as well as changing local plasma conditions. Correspondingly, the configuration of the Ganymedean

mini-magnetosphere varies with the periodically varying orientation of the Jovian background field (Kivelson et al. 1998; Kopp and Ip 2002; Ip and Kopp 2002; Jia et al. 2008, 2009b; Saur et al. 2015). This periodic variation is sketched for selected magnetic field lines in Figure 7 and is discussed in Section 2.1.1. The simplified magnetic field in Figure 7 contains Ganymede's intrinsic magnetic field, the Jovian time-variable background field, induction in a subsurface ocean, and a simplified proxy for the magnetic field due to the plasma interaction (Saur et al. 2015). Figure 17 also shows Ganymede's magnetic field configuration for different background field orientations according to the MHD model of Kopp and Ip (2002),

2.2 Ganymede's aurora

In the previous section, we presented main aspects and facts regarding Ganymede which are required to understand the moon's aurora. Here, we present the first and subsequent observations of the FUV aurora at Ganymede. We also discuss theoretical models by several authors, who analyzed the aurora and gave possible explanations for the underlying generation processes of the aurora.

2.2.1 Discovery of Ganymede's FUV aurora

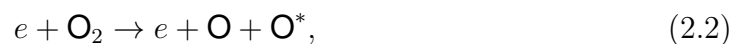
The first observation of Ganymede's aurora was made by the *Hubble Space Telescope* (HST), which orbits Earth within ~ 96 minutes at an altitude of around 560 km. First evidence for auroral emission was found in the mid-1990s: together with the discovery of Ganymede's tenuous oxygen atmosphere, Hall et al. (1998) detected a non-uniform spatially distributed FUV emission in the north and south polar regions of Ganymede. Hall et al. (1998) analyzed spectral observations taken with the HST *Goddard High Resolution Spectrograph* (HST/GHRS) in 1996 (HST campaign ID 6758, principal investigator (PI): Doyle Hall), where Ganymede's trailing hemisphere and both hemispheres of Europa have been observed in the FUV range. The resulting one-dimensional spectra are shown in Figure 13. The top panel of that figure shows the spectrum of Ganymede (thin line, taken on

June 21, 1996¹⁰), plotted together with the modeled solar spectrum according to the day of the observation. Three distinct peaks at OI $\lambda 1304 \text{ \AA}$, CII $\lambda 1335 \text{ \AA}$ and OI $\lambda 1356 \text{ \AA}$ clearly stand out of the observed spectrum. After subtraction of the solar spectrum (not shown in the figure), only the peaks at 1304 \AA and 1356 \AA remain, originating from Ganymede's atmosphere (Hall et al. 1998). The carbonic CII $\lambda 1335 \text{ \AA}$ emission is part of the reflected solar spectrum and vanishes after the subtraction. The Lyman- α emission at HI $\lambda 1216 \text{ \AA}$ has a flattened emission shape in the spectra (not shown in Figure 13), which indicates a uniform hydrogen airglow at Ganymede. In contrast, the two double peaks at the oxygen lines (more pronounced at OI $\lambda 1356 \text{ \AA}$) indicate a non-uniformly distributed oxygen airglow. Hall et al. (1998) constrain oxygen airglow to the polar regions extending between 40° to 50° planetographic latitude. At Europa instead, after subtracting the reflected solar light, a (more or less) uniform, single-peak emission pattern remains at OI $\lambda 1356 \text{ \AA}$, which indicates a global oxygen airglow at that moon.

The observation and analysis of Hall et al. (1998) delivered additional evidence to previous *Galileo* findings for an oxygen atmosphere as well as first indications for auroral emission at Ganymede. According to Section 2.1.2, Ganymede's atmosphere contains both atomic and molecular oxygen, where the molecular form is the dominant one. The detected emission is, however, emitted from atomic oxygen (Hall et al. 1998). Electron-impact excitation as defined by Equation 2.1,



as well as electron-impact dissociative excitation given by Equation 2.2,



are according to Hall et al. (1998) the two¹¹ most probable generation processes

¹⁰The day of observation coincides with the week of the first Ganymede encounter by the *Galileo* spacecraft (Hall et al. 1998).

¹¹A third possible process based on a model including resonance scattering is discussed in Hall et al. (1998).

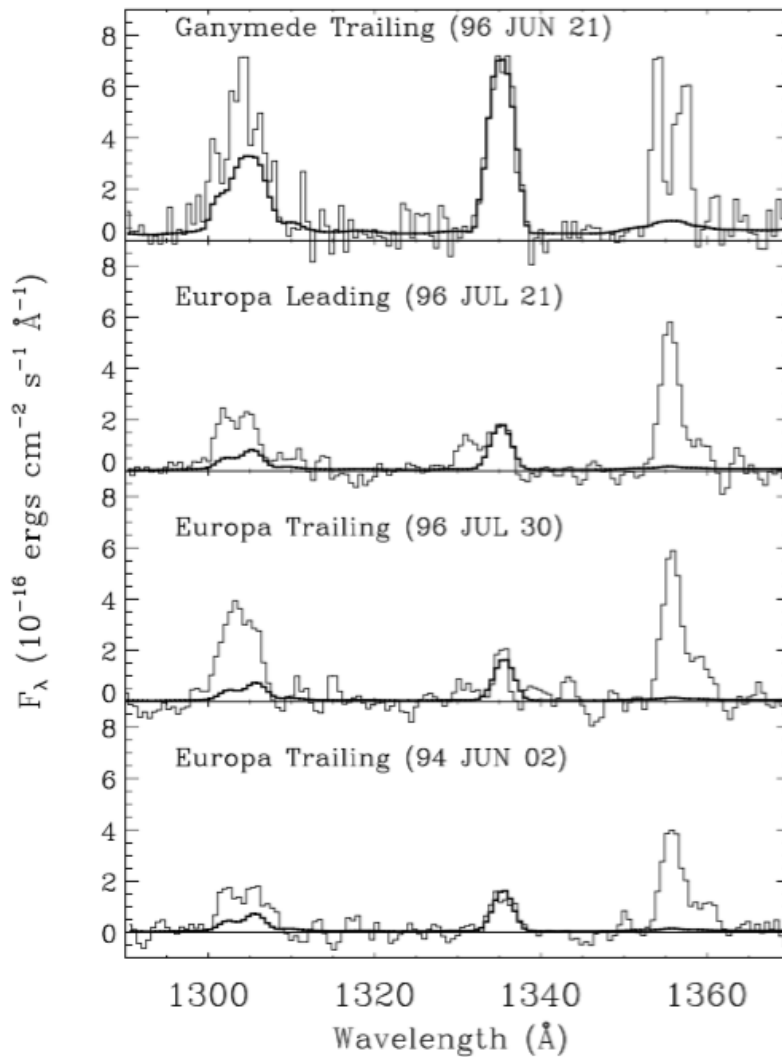


Figure 13 – HST/GHRS FUV spectra of Ganymede (top panel) and Europa (remaining panels) from Hall et al. (1998, their figure 1, reproduced by permission of the AAS; for further details see Appendix S9). The spectrum (thin lines) is taken from Ganymede’s trailing side on June 21, 1996. Also plotted is the modeled solar spectrum reflected from the satellite. After subtracting the solar spectrum (not shown), the emission at OI $\lambda 1304 \text{ \AA}$ and OI $\lambda 1356 \text{ \AA}$ clearly remain.

for the detected emission. O* indicates an oxygen atom in excited state, subsequently emitting a photon (i.e., emitting the wavelength dependent energy hc/λ , where h is Planck’s constant, c is the speed of light and λ is the wavelength). The ratio of the emission at the two oxygen lines, $F(1356 \text{ \AA})/F(1304 \text{ \AA}) = 1.3 \pm 0.3$ (Hall et al. 1998, their table 1), is diagnostic for dissociative electron-impact excitation of O₂ according to Hall et al. (1998).

The HST/GHRS observations provide reliable evidence for Ganymede’s atmosphere and allow rough assumptions about the location of the aurora. However,

the HST/GHRS observations have two disadvantages. First, GHRS is only able to take a spectrum without spatial resolution of the observed emission. Second, in campaign 6758, Ganymede did not fit completely into the slit of HST. The aperture used for the observation was 1.74×1.74 arcsec² large and Ganymede's disk extended 1.72 arcsec in diameter. Due to an acquisition failure, Ganymede was ~ 0.1 arcsec off the aperture center and, thus, not the entire Ganymedeian emission was measured. These observational disadvantages vanished when GHRS was exchanged with the new and improved *Space Telescope Imaging Spectrograph* (HST/STIS) in 1997 (one year after campaign 6758). STIS has the capability of observing with spectroscopic as well as spatial resolution simultaneously, providing two-dimensional resolved images of a target at individual wavelengths. We further explain STIS and its functionality in the next Chapter 3. The first STIS observations of Ganymede's trailing side were made in 1998 (October 30, campaign ID 7939, PI: H. Moos) using the 2 arcsec wide slit of HST. The observations are analyzed by Feldman et al. (2000). Figure 14 shows spatially resolved OI $\lambda 1356$ Å images of Ganymede's oxygen emission taken from Feldman et al. (2000) (each with a 82×82 pixel resolution). The four images correspond to the four orbits of campaign 7939 and show color coded brightness in the unit of Rayleighs from low (dark, 0 R) to high brightness (white, >300 R). The images confirm the previously by Hall et al. (1998) proposed airglow constrained in the polar regions. The emission is auroral, analogous to the auroral ovals at Earth, as the images in Figure 14 show two distinct auroral ovals around the north and south pole at latitudes above $\pm 40^\circ$ (Feldman et al. 2000). Peak brightnesses lie in the range of ~ 100 R to ~ 400 R. Since the individual images of Figure 14 show snapshots during Ganymede's migration through the current sheet, Feldman et al. (2000) notice temporal variation of brightness from one orbit to another due to changing local plasma conditions. They also observe a difference in brightness between the northern and southern hemisphere.

Further HST observations followed. STIS as well as other HST cameras have been used. Table 2 (Chapter 3) lists HST observations of Ganymede's aurora in the FUV range, i.e., auroral emission at the two oxygen lines. STIS and ACS (*Advanced Camera of Survey*) observations until 2007 are analyzed by McGrath et al. (2013). They provide the first comprehensive study of several observations of the aurora on Ganymede. Feldman et al. (2000) notice that the latitudinal locations of the auroral ovals coincides with the intersection line of the OCFB

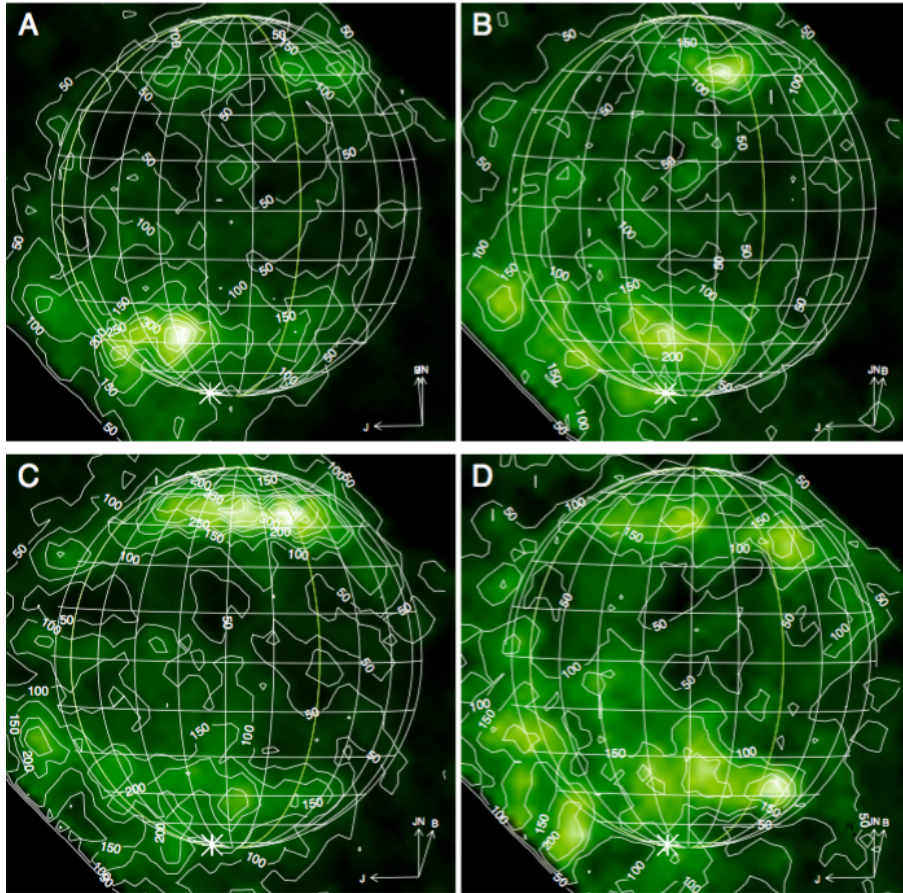


Figure 14 – HST/STIS images of Ganymede’s oxygen emission at OI $\lambda 1356 \text{ \AA}$ (trailing side only) from Feldman et al. (2000, their figure 3, reproduced by permission of the AAS; for further details see Appendix S9).

with Ganymede’s atmosphere (Figure 10). They suggest enhanced conductivity and current in Ganymede’s atmosphere due to magnetic reconnection along the OCFB as a possible acceleration of electrons, which generate the observed auroral emission. This has been analyzed in more detail in theoretical works by several authors, which we discuss in detail in the subsequent Section 2.2.2. As the most important contribution to that discussion, Eviatar et al. (2001a) propose that magnetic field-aligned electric fields cause local acceleration of electrons along the OCFB, which excite neutral atmospheric O_2 . McGrath et al. (2013) take a set of HST campaigns observing Ganymede’s trailing as well as leading side and both hemispheres partially, when Ganymede was in eclipse. They compare the location of the auroral ovals on both hemispheres with the model-predicted OCFB location on Ganymede.

Figure 15 shows the OI $\lambda 1356 \text{ \AA}$ emission images of the HST campaigns cho-

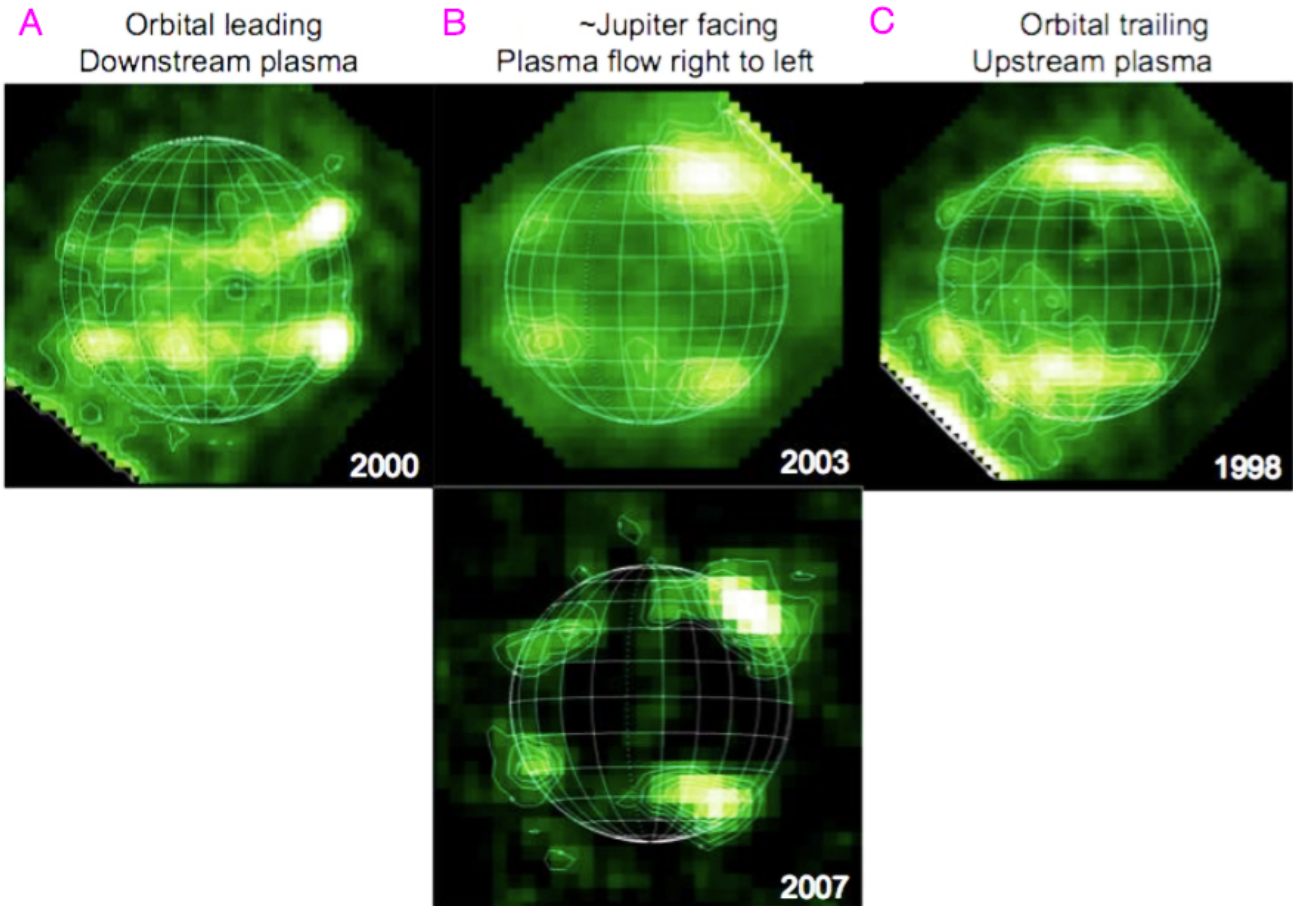


Figure 15 – HST/STIS images of Ganymede’s oxygen emission at OI $\lambda 1356 \text{ \AA}$ from McGrath et al. (2013, their figure 2). Shown is the emission on the leading side (campaign ID 8224, **A**-column), half of the leading and trailing side (campaign ID 9296 and 10871, **B**-column) and the trailing side (campaign ID 7939, **C**-column, superposition of images in Figure 14).

sen by McGrath et al. (2013): leading side (campaign ID 8224 (PI: Melissa M. McGrath), left), half of the leading and trailing side (campaign ID 9296 (PI: Holland Ford) and 10871 (PI: John Spencer), middle) and the trailing side (campaign ID 7939 (PI: H. Moos), right). Note that McGrath et al. (2013) take the superposition of all orbits of a campaign in order to increase the signal-to-noise ratio, e.g., the right image in Figure 15 is a superposition of Feldman et al. (2000)’s images in Figure 14. By extracting the location of peak auroral brightnesses from Figure 15, which is shown in Figure 16, McGrath et al. (2013) find that on the trailing side the brightest emission reaches planetographic latitudes between 40° and 55° on each hemisphere (i.e., in the north and south). This is in agreement with previous findings by Feldman et al. (2000) and Hall et al. (1998). On the leading side, the peak brightness lies between 10° and 30° latitude. The peak

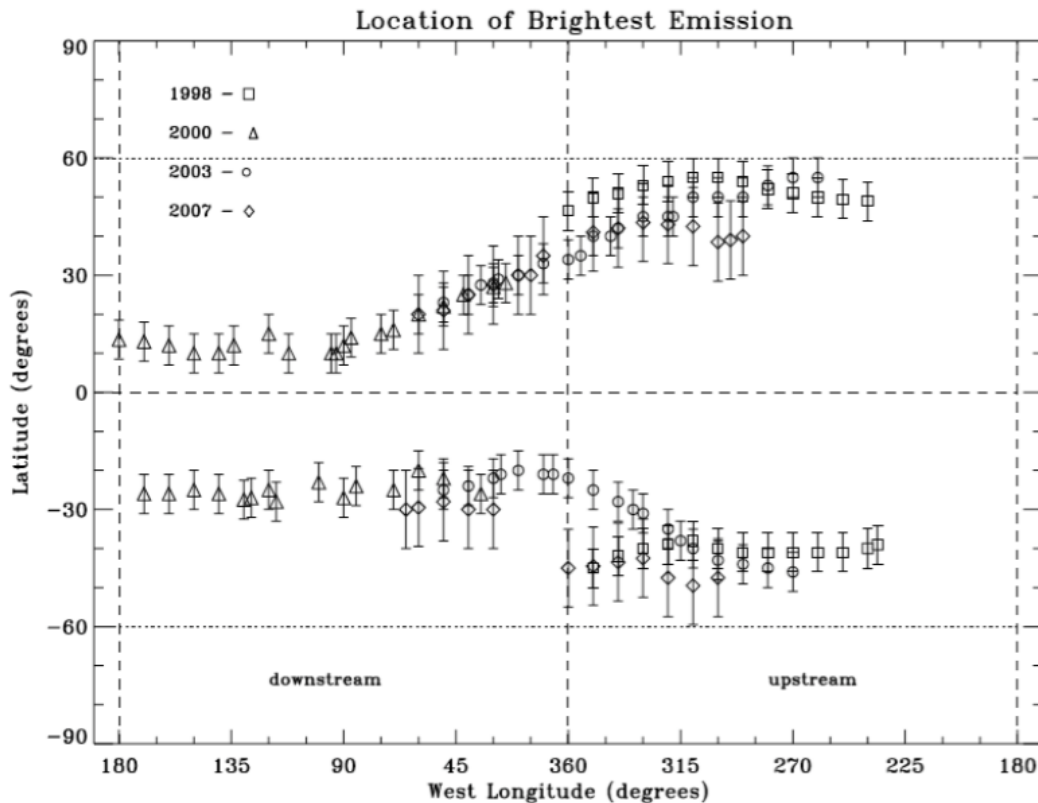


Figure 16 – Location of peak auroral brightnesses from McGrath et al. (2013, their figure 3).

brightnesses lie between 100 to 400 R. The average oval location is long-term stable in time, but significant brightness variations occur from one HST orbit to another (McGrath et al. 2013). The different hemispheric locations of the peak brightnesses indicate a compression of the ovals on the plasma upstream side (trailing side) towards higher planetographic latitudes and a stretching on the downstream side (leading side) towards the planetographic equator. This is in agreement with the compression of the OCFB on both hemispheres as described in Section 2.1.3 and shown in Figure 10 (McGrath et al. 2013). At Earth, as well as at Jupiter, the magnetospheres and the auroral ovals are also compressed on the upstream and stretched on the downstream side due to the impinging solar wind. At Ganymede, it is the magnetospheric plasma impinging on the moon's mini-magnetosphere. McGrath et al. (2013) find a good match between the observed locations of the brightness peaks with the location of the OCFB predicted by the Jia et al. (2008, 2009b) model (see McGrath et al. (2013), their figure 7).

2.2.2 Previous modeling of the aurora and comparison with the observations

The observations discussed in the previous section show a coincidence of the location of the auroral ovals with the intersection line of the OCFB with Ganymede's surface/atmosphere. The comprehensive study by McGrath et al. (2013) verified this coincidence by approving the correlation between the auroral ovals' location and the OCFB modeled by several authors, which we present in this section. However, the actual excitation process of the observed auroral emission is still unclear. As the emission is thought to be generated by electron-impact dissociative excitation (Equation 2.2), Eviatar et al. (2001a) calculate the energy required to generate auroral emission with the observed brightness by this process. They find that magnetospheric plasma at Ganymede's orbit alone has not sufficient energy (20 eV) to generate the observed aurora. Compared to the brightness peaks of 100 to 400 R reported by McGrath et al. (2013), the thermal component of the Jovian magnetospheric plasma is able to generate emission of only 10 to 40 R (Eviatar et al. 2001a). Hence, the authors conclude that a local acceleration is needed to generate an electron population which is characterized by a Maxwellian distribution with temperatures between 75-300 eV. Eviatar et al. (2001a) analyze two possible acceleration mechanisms: First, stochastic acceleration by electrostatic waves, and second, magnetic field-aligned electric fields associated with sufficiently intense field aligned currents (FAC, also called *Birkeland* currents). The authors favor¹² the latter mechanism over the first since the concept of FAC along the OCFB is similar to Birkeland current system at Earth proposed by Straus and Schulz (1976). Furthermore, the location of the aurora coincides with the location of OCFB on Ganymede (Feldman et al. 2000). Eviatar et al. (2001a) state that local acceleration by FAC would be plausible along the OCFB. The Ganymedeian Birkeland current system, on the other hand, is generated by magnetic field reconnection at the upstream magnetopause of Ganymede's mini-magnetosphere (Eviatar et al. 2001a; Ip and Kopp 2002; Kopp and Ip 2002). This reconnection occurs at intersection points of the anti-parallel oriented Jovian and Ganymedeian magnetic field lines as discussed in Section 2.1.3 (Figure 10). The study by Payan et al. (2015) recently confirmed that regions of energetic electrons

¹²Eviatar et al. (2001a) admit that the first suggested mechanism, the collective plasma acceleration through electrostatic waves, could play a role as a (minor) contributing factor for the acceleration process.

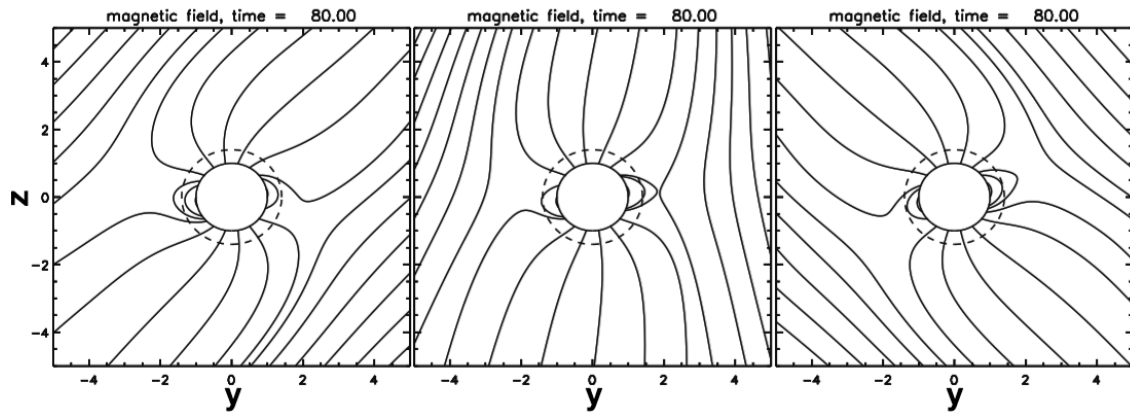


Figure 17 – Results of the Kopp and Ip (2002, their figure 3) MHD model. Shown are selected Ganymede magnetic field lines in the y - z plane for different orientations of the background field. Their MHD model reproduces the G2 (left), G7 (right) and G8 (center) *Galileo* flyby.

accelerated due to parallel electric fields coincide with regions of brightest auroral emission.

The magneto-hydrodynamic (MHD) model by Ip and Kopp (2002) and Kopp and Ip (2002) was one of the first theoretical studies of the mini-magnetosphere interacting with Ganymede's magnetospheric environment. It includes contributions from Ganymede's internal and the external Jovian field as well as magnetic fields caused by the local plasma interaction - but without induction in a subsurface ocean. They use a resistive MHD model to study the variation of Ganymede's magnetosphere under changing Jovian background field orientations. They are able to reproduce the magnetospheric configuration measured during three specific *Galileo* flybys, G2, G7 and G8, shown in Figure 17. During the G2 flyby (left), the background field was oriented $\sim 50^\circ$ outward (positive y -axis points towards Jupiter, same coordinate system as in previous sections). In contrast, during the G7 flyby (right) the background field was oriented inward. During the G8 flyby (center), the background field was oriented nearly parallel to Ganymede's rotation axis (y -axis). The three different flybys roughly represent snapshots of Ganymede's transit through the current sheet, i.e., when Ganymede is above, inside and below the current sheet center. The MHD model confirms the variability of Ganymede's magnetospheric topology under changing background field orientations. Also the intersection line of the OCFB with Ganymede's surface varies accordingly (as sketched in Figure 10). In addition, the Ip and Kopp (2002) MHD model is able to establish a Birkeland current system associated with the OCFB. These

FAC originate at Ganymede's magnetopause and connect to the ionosphere in Ganymede's polar region. Ip and Kopp (2002) furthermore calculate the energy charged particles gain through magnetic reconnection. They find, that the energies are sufficient (max. 2.9 - 48 keV) to produce energetic electrons which are able to generate the enhanced ionization of Ganymede's oxygen atmosphere. Hence, their model supports the acceleration mechanism via FAC proposed by Eviatar et al. (2001a). However, McGrath et al. (2013) compare the calculated location of the OCFB from the Ip and Kopp (2002) model with the measured auroral oval locations and only find a weak correlation between both, indicating that their MHD model does not satisfy all components of Ganymede's mini-magnetosphere and its interaction with its environment.

A three-dimensional multi-fluid model by Paty and Winglee (2004) provided an improved modeling of the currents and electromagnetic fields within the mini-magnetosphere as well as the interaction with the local plasma environment. Unfortunately, McGrath et al. (2013) were not able to compare these model results with the measured oval locations as further quantitative information, e.g., of the location of the OCFB calculated by Paty and Winglee (2004) were unavailable. An additional model of the mini-magnetosphere by Khurana et al. (2007) included only a superposition of the internal and external field without plasma interaction similar to the Kivelson et al. (1997) or Neubauer (1998) models. The model by Khurana et al. (2007) was also not able to reproduce a good match between the location of the OCFB and the auroral ovals (McGrath et al. 2013). However, the model confirms the correlation between the OCFB location and the boundary of Ganymede's polar caps. Due to this correlation, the authors associate the polar caps with charged particle effects.

So far, the best agreement between the theoretical OCFB position from model calculations and the measured oval location is provided by the Jia et al. (2008) resistive MHD model and its subsequent improvements (Jia et al. 2009a, 2010). According to McGrath et al. (2013), the Jia et al. (2008, 2009b) MHD model OCFB appropriately reproduces the location and the shape of the ovals. Another three-dimensional MHD model developed by Duling et al. (2014), which introduced new spherical boundary conditions describing the insulating nature of the moon, also includes Ganymede's internal magnetic field, the Jovian background field, induction in a possible subsurface ocean as well as elastic collisions, and

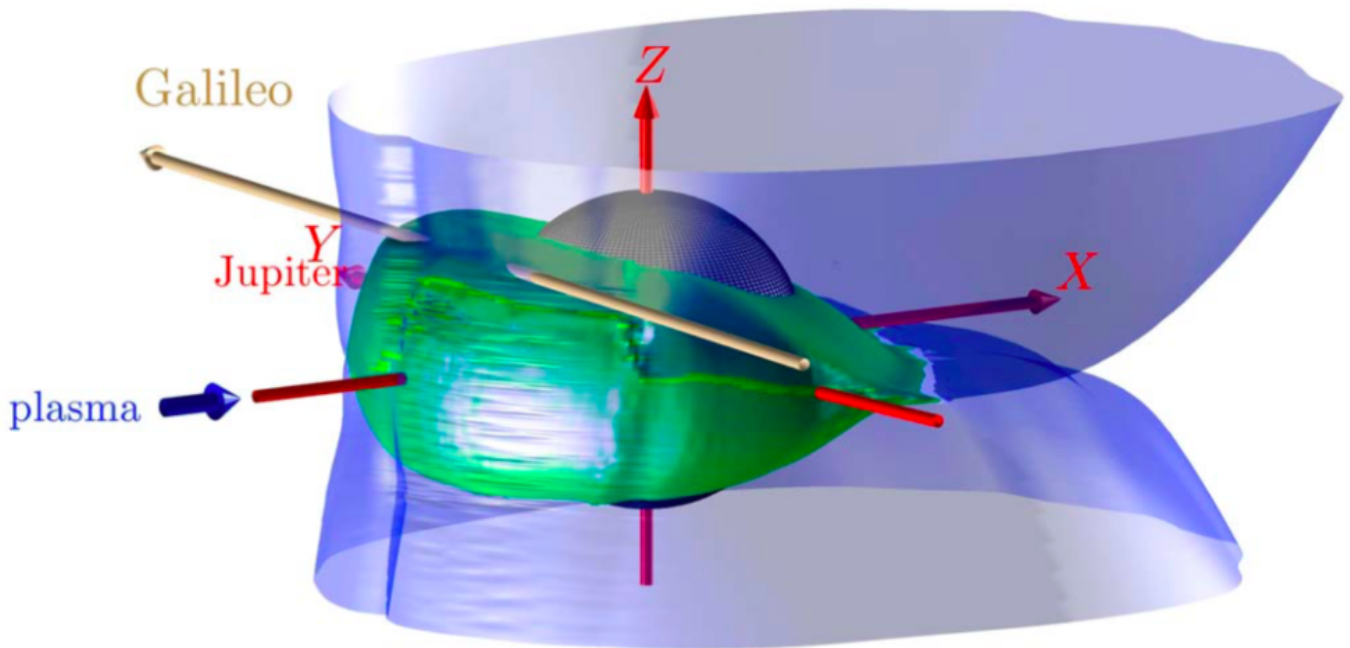


Figure 18 – Results of the Duling et al. (2014, their figure 15) MHD model for the *Galileo* G8 flyby, showing the structure of Ganymede's magnetosphere. Blue surfaces: boundary of field lines connected and not connected with Ganymede. Green surfaces: OCFB. Coordinate system as introduced in the previous sections.

photo-ionization with the moon's atmosphere. The predicted location of the OCFB fits very well with the observed oval locations (Saur et al. 2015) even for changing background field variations, i.e., changing orientation of the Jovian magnetic field during Ganymede's transit through the current sheet. Like the previous authors, Duling et al. (2014) reproduce several *Galileo* flybys. Exemplarily shown for the G8 flyby (also shown in Figure 17 (mid panel) for the Ip and Kopp (2002) MHD model), Figure 18 shows the three-dimensional representation of Ganymede's magnetosphere. The modeled OCFB (represented by the green surface in that figure) reproduces very well the upshifted location of the OCFB near to the poles on the plasma upstream side and its downshifted location on the plasma downstream side towards Ganymede's equator.

Another aspect of the reconnection processes at Ganymede is its intermittence. In their work, Ip and Kopp (2002) already mention the possibility that the FAC projected back to Ganymede's auroral ovals could be highly filamentary. Indeed, the emission pattern of Ganymede's aurora is not that of a constantly emitting ribbon going around both poles (see Figure 14 and 15). Instead, the emission shows patchy, i.e., spot-like structures. The ovals consist of spots of increased brightness,

separated by gaps of lower brightness (McGrath et al. 2013). The correlation between the patchiness of the aurora and the intermittence of the reconnection is still unclear. Jia et al. (2010) analyze the reconnection process at Ganymede in more detail with their improved MHD simulations. They increase the temporal resolution of the dynamic processes at the magnetopause with time-scales shorter than the time the local plasma needs to convect across the mini-magnetosphere. They find that even under the steady upstream plasma conditions at Ganymede (compared to Earth, where the reconnection is coupled to the fluctuating solar wind conditions), the reconnection at Ganymede's upstream magnetopause is intermittent, i.e., it occurs in a bursty manner with periodicities between 20 and 50 seconds (see, e.g., figure 9 in Jia et al. (2010)). The reconnection events they find are impulsive in nature and limited in spatial extent. Unfortunately, HST observations which were available to Jia et al. (2010), had a minimum temporal resolution of 10 minutes. Hence, they were not able to compare their findings to aurora observations. For example at Earth, Panov et al. (2016) most recently find a correlation between the reconnection process at the Earth's magnetotail and brightness fluctuations of the Earth's aurora. They analyze *Themis*¹³ data and identify plasma jets in Earth's magnetotail, triggered by solar wind activity and accelerated towards Earth, impacting Earth's dipolar magnetic field and triggering oscillation of Earth's magnetic field lines. This oscillation, on the other hand, generates electric currents which accelerate electrons towards Earth's atmosphere where they trigger auroral emission. The authors show that both, the oscillation period of the magnetic field lines and the period of aurora brightness fluctuations are identical.

2.3 Summary

Ganymede is the largest moon of the solar system and even larger than the innermost planet, Mercury. It is also the only known moon so far which possesses an intrinsic magnetic field embedded within a planetary magnetic field, similar to Earth's magnetosphere being embedded within the solar wind. Another similarity to Earth are the two distinctive auroral ovals around the north and south pole observed in the FUV with the *Hubble Space Telescope* (HST) at wavelengths

¹³Since 2007, the NASA mission *Themis* investigates Earth's magnetotail with five satellites.

of emitting atomic oxygen. Several HST observations followed after the first detection in order to investigate the overall morphology of the aurora. And several theoretical studies analyzed the generation process(es) behind Ganymede's auroral emission. The morphology of the emission seems to be controlled by the interaction between Ganymede and its surrounding plasma environment, by the variability of its environment, and by the induction in a subsurface ocean. The overall pattern of the ovals is relatively stable. The most likely acceleration mechanism for the energetic electrons, which generate the observed bright aurora, is the acceleration of electrons along the OCFB towards Ganymede by field aligned currents. This acceleration mechanism is consistent with the location of the observed ovals as predicted by numerical modeling being close to the OCFB. The reconnection process at Ganymede's magnetopause is intermittent and bursty in nature.

However, the influence of changing local plasma conditions on the morphology and brightness of Ganymede's aurora has not been sufficiently analyzed yet. Due to the tilt between Ganymede's orbital plane and the Jovian magnetospheric equator, the satellite changes its position relative to the magnetic equator within 5.25 hours and transits through the Jovian current sheet. During that transit, Ganymede experiences a varying orientation of Jupiter's magnetic field lines as well as changing local plasma conditions like ram and thermal pressure of the magnetospheric plasma. The response of the aurora on this change of conditions is still an open research question. In this thesis, we therefore analyze sets of HST campaigns which consecutively observe Ganymede's transit through the Jovian current sheet. We focus on the influence of changing local plasma conditions on the morphology of Ganymede's aurora. Unlike the comprehensive study of HST observations by McGrath et al. (2013), we do not superimpose individual orbits of each HST visit, but we analyze each orbit with its ~ 25 to ~ 40 minutes of observations separately, in order to maintain temporal resolution of the HST visit. This is necessary to cover Ganymede's transit through the current sheet. Another difference is that we use a set of HST observations which was not available to McGrath et al. (2013) at that time. This set consists of two visits observing Ganymede's leading side (HST 12244 (PI: Joachim Saur), see Table 2), each with a ~ 6 hour coverage of Ganymede moving through the current sheet. In the following chapter, we explain the data sets used in our study and our methods to process this data.

Observations and data processing

In this chapter, we discuss the available set of HST campaigns observing Ganymede's aurora in the far ultraviolet (FUV). We present criteria for choosing those HST campaigns that are appropriate for the purpose of our study. As all chosen observations are made by *HST Space Telescope Imaging Spectrograph* (HST/STIS), we outline the principal concept of the instrument. We then explain the single steps of processing HST/STIS data sets in order to study the auroral morphology, brightness and variability.

3.1 Selecting HST campaigns

Table 2 gives a summary of all HST campaigns mentioned in the previous Chapter 2. We further added all other campaigns, whose primary target was the observation of Ganymede’s auroral emission in the FUV range, i.e., focussed on the spectrum containing the two oxygen lines OI $\lambda 1304 \text{ \AA}$ and OI $\lambda 1356 \text{ \AA}$. In the table, we indicate the cameras used and the hemispheres observed, i.e., trailing or leading hemisphere or parts of both hemispheres (i.e., when Ganymede was in eclipse). To monitor changes of Ganymede’s aurora due to changing local plasma conditions, we need to track Ganymede’s transit through the Jovian current sheet. Therefore, we only analyze HST observations where at least two consecutive HST orbits of observations are available. Campaigns 10871 and 13328¹ do not fulfill this condition. We also only use observations where the emission was resolved spatially and spectrally. This limits the set of appropriate HST campaigns to HST/STIS observations as campaigns 6758, 9296, 10871 and 13328 do not fulfill this condition. In order to distinguish between effects due to the plasma interaction on the upstream and downstream side, we only take observations into account which observed Ganymede’s trailing or leading side separately. This condition is not met by campaigns 9296 and 10871. The HST/STIS campaigns 7939 (year 1998), 8224 (year 2000) and 12244 (years 2010 and 2011) meet all conditions mentioned above (indicated as *used* in Table 2).

¹HST campaign 13328 consists of more than two orbits, but they were not obtained consecutively.

Table 2 – Overview of HST campaigns observing Ganymede’s aurora in the FUV.

campaign ID	year	hemisphere	camera	orbits	used
6758	1996	trailing	GHRIS	6	no
7939	1998	trailing	STIS	8	yes
8224	1999/2000	leading	STIS	2	yes
9296	2003	trailing/leading	STIS/ACS	2/3	no
10871	2007	trailing/leading	ACS	1	no
12244	2010/2011	leading	STIS	10	yes
13328	2014	leading	STIS/COS	4/3	no

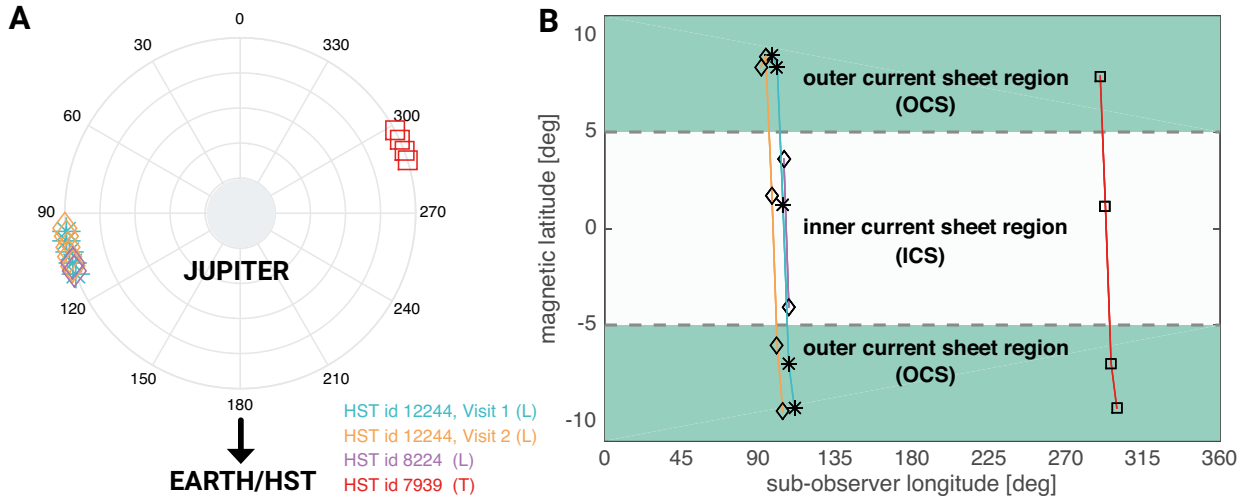


Figure 19 – Orbital coverage of HST campaigns used in this work. **A**: elongations of Ganymede for each orbit of HST (compare with Table 3). Jupiter is in the center, 180° points towards the observer, 90° is the eastern elongation (observing the leading side of Ganymede, indicated by *L*) and 270° is the western elongation (trailing side, *T*). **B**: magnetic latitude and sub-observer longitude of the observations, where 90° and 270° sub-observer longitude are the center of the leading and trailing side, respectively. We define the area between -5° to $+5^\circ$ magnetic latitude as inside the current sheet (ICS), and any latitude above or below as outside the current sheet (OCS). Note that all chosen campaigns have sufficient and consecutive magnetic latitudinal coverage in order to track any auroral variability during a full transit of Ganymede through the current sheet.

Ganymede’s sub-observer longitudes and magnetic latitudes covered by these campaigns are displayed in Figure 19. Figure 19A shows the orbital coverage, i.e., observed orbital elongations of Ganymede for each orbit. At eastern elongation (90°), HST observes the leading hemisphere of Ganymede (indicated by *L*), and at western elongation (270°) the trailing hemisphere (*T*). The chosen HST campaigns cover these hemispheres with twelve and four orbits, respectively. Figure 19B shows the observational coverage of magnetic latitude, ϑ_{mag} , and the sub-observer longitude, λ_{obs} . Almost centered around the leading and trailing side central meridian ($90^\circ/270^\circ$), the chosen HST campaigns provide an adequate coverage of both hemispheres. The magnetic latitude ϑ_{mag} is related to Ganymede’s system III longitude λ_{mag} according to Dessler (1983) and Connerney et al. (1998) by

$$\vartheta_{\text{mag}} = 9.5^\circ \cos(\lambda_{\text{mag}} - 200.8^\circ). \quad (3.1)$$

At $\vartheta_{\text{mag}}=0^\circ$, Ganymede is located in the densest part of the Jovian magnetosphere, the current sheet, and at $|\vartheta_{\text{mag}}| \approx 10^\circ$ at the location, where the upstream plasma density is the smallest (see, e.g., Figure 35). In order to determine any variation of Ganymede's auroral emission as a function of varying plasma conditions, we define the magnetic latitudinal area of $|\vartheta_{\text{mag}}| < 5^\circ$ as inside the current sheet (ICS) and any latitude above or below as outside the current sheet (OCS). Inside the current sheet, the plasma density and thermal pressure are increased (Kivelson et al. 1997; Khurana et al. 2004). Campaign 12244 with its ten orbits provides the best coverage of magnetic latitudes for the leading side (see Table 3). Campaign 8224 complements the leading side observations with two observations when Ganymede was inside the current sheet. Campaign 7939 consists of four consecutive orbits. The three chosen HST campaigns have a sufficient number of consecutively observed magnetic latitudes to monitor Ganymede's movements through and out of the Jovian current sheet.

Detailed information about these campaigns is listed in Table 3. Note that one HST orbit is a superposition of two consecutive exposures, which are not listed separately. Campaign 12244 consists of two visits in 2010 and 2011. The mean diameter of the Ganymede disk for all campaigns is 1.7 arcsec and the observed disks perfectly fit into the 2 arcsec wide slit of HST. The average exposure time of each orbit is 33.3 minutes and the average time between each orbit of a visit lies around 40 minutes which approximately corresponds to half of the time HST takes to complete one orbit around the Earth. During one orbit, which takes 95.8 minutes, HST can observe its target only when HST is inside the shadow of the Earth. This limits each observational part of the orbit (in the following just called *HST orbit*) to a maximum time of around 40 minutes. During each visit, the sub-observer latitude, ϑ_{obs} , shows no significant variation. ϑ_{obs} is overall very small, meaning that HST observed Ganymede's equator nearly perpendicular. During one visit the sub-observer longitude, λ_{obs} , though, varies by around 10° .

The chosen campaigns provide sufficient planetographic as well as magnetic latitude coverage and fulfill the criteria explained above. In the next section, we briefly introduce the concept of HST/STIS and explain in detail our applied data processing.

Table 3 – Observational parameters of HST/STIS campaigns ID 7939, 8224 and 12244. All specifications refer to the center of the exposure time.

ID	V/O ^{a)}	Date	Time ^{b)} (UTC)	$\Delta t^c)$ [s]	$\lambda_{\text{obs}}^d)$ [°]	$\vartheta_{\text{obs}}^d)$ [°]	$\lambda_{\text{s3}}^e)$ [°]	$\vartheta_{\text{mag}}^e)$ [°]	$\lambda_{\text{orb}}^f)$ [°]	$\varphi_{\text{sol}}^g)$ [°]	$\varnothing^h)$ [arcsec]
7939	V1O1	1998-10-30	08:21	1700	289.8	1.7	234.5	7.9	287.7	8.6	1.71
7939	V1O2	1998-10-30	09:40	2410	292.9	1.7	283.8	1.2	291.0	8.6	1.71
7939	V1O3	1998-10-30	11:16	2225	296.2	1.7	338.0	-7.0	294.7	8.6	1.71
7939	V1O4	1998-10-30	12:53	2330	299.5	1.7	32.6	-9.3	298.4	8.6	1.71
8224	V1O1	2000-12-23	03:45	1480	104.8	3.0	268.5	3.6	106.4	5.4	1.75
8224	V1O2	2000-12-23	05:00	2200	107.7	3.0	316.1	-4.1	109.0	5.4	1.75
12244	V1O1	2010-11-19	20:11	1596	98.0	1.9	181.7	9.0	96.0	10.3	1.64
12244	V1O2	2010-11-19	21:25	2358	100.9	1.9	228.8	8.4	99.2	10.3	1.64
12244	V1O3	2010-11-19	23:01	2358	104.2	1.9	283.4	1.2	102.9	10.3	1.64
12244	V1O4	2010-11-20	00:37	2358	107.6	1.9	338.1	-7.0	106.6	10.3	1.64
12244	V1O5	2010-11-20	02:13	2358	110.9	1.9	32.7	-9.3	110.2	10.3	1.64
12244	V2O1	2011-10-01	09:38	1626	91.1	3.4	172.4	8.4	94.7	5.9	1.78
12244	V2O2	2011-10-01	10:55	2388	94.1	3.4	221.2	8.9	97.7	5.9	1.78
12244	V2O3	2011-10-01	12:47	1626	97.8	3.4	280.3	1.7	101.3	5.9	1.78
12244	V2O4	2011-10-01	14:07	2388	100.9	3.4	330.3	-6.0	104.3	5.9	1.78
12244	V2O5	2011-10-01	15:43	2418	104.2	3.4	24.4	-9.5	107.5	5.9	1.78

^{a)} Visit and orbit number.^{b)} Start time of HST-exposure.^{c)} Exposure time.^{d)} Sub-observer longitude (λ_{obs}) and latitude (ϑ_{obs}).^{e)} System III longitude (λ_{s3}) and magnetic latitude (ϑ_{mag}) after Jovian coordinate convention according to Dessler (1983) and Connerney et al. (1998).^{f)} Orbital phase angle, i.e., angle between Ganymede- and Earth-Jupiter line, according to Nelson et al. (1987).^{g)} Solar phase angle, i.e., angle between Jupiter-Earth/observer and Jupiter-Sun line (angle between incident light onto and reflected light from Ganymede), according to Nelson et al. (1987).^{h)} Diameter of observable Ganymede disk.

3.2 Processing of HST/STIS data

All data sets we analyze throughout this thesis are obtained with the *Space Telescope Imaging Spectrograph* on board the *Hubble Space Telescope* (HST/STIS). STIS uses three different high resolving 1024×1024 pixel detectors: a Charge Coupled Device (CCD) with a 52×52 arcsec² field of view (FOV) covering the spectrum between 1640 and 10300 Å and two Multi Anode Multichannel Arrays (MAMA) detectors, each with a FOV of 25×25 arcsec², covering the wavelength range of 1600 to 3100 Å (near ultraviolet, NUV) and 1150 to 1700 Å (far ultraviolet range, FUV), respectively (Ely et al. 2011). The latter MAMA detector is used in the HST campaigns presented in Section 3.1 due to the targeted wavelength range (FUV) of Ganymede’s aurora. A sketch of STIS’ observational concept is shown in Figure 20. Note that this sketch is simplified and not to scale². A speciality of STIS is that the spectrograph is able to obtain spectrally as well as spatially resolved images when operated in the spectroscopic mode. As indicated in Figure 20, the detector coordinate system contains an ordinate axis parallel to the slit, y_d , with spatial resolution (in the unit of pixels), and an abscissa perpendicular to the slit, x_d . While the x_d -axis is in the unit of pixels and has spatial resolution, the same axis can be converted in the unit of wavelengths (i.e., in Angström), λ_d , with spectral resolution (see Equation 3.2 below). The x_d -axis is also called *dispersion axis*, and the y_d -axis *cross-dispersion axis*.

A set of different apertures and gratings is available, each specific for the targeted wavelength range and providing both spatial and spectral resolution. In order to obtain a fully resolved disk of Ganymede, the 52×2 arcsec² aperture slit (called *52X2*) is used for almost all chosen HST/STIS campaigns. Using the *52X2* aperture, the target is positioned in the vertical center of the slit. For campaign 12244, the pseudo aperture *52X2D1* has been applied. STIS’ pseudo apertures are physically identical to the *52X2* aperture, but the target is placed at different locations along the slit (Ely et al. 2011). The *52X2D1* pseudo aperture places the target in the lower part of the slit in order to prevent contamination by dark current counts at the region with large detector noise (also called the “*blotch*”). Note that due to the FOV of the used MAMA detector, the effective length of the slit is limited to

²A technical drawing and further details can be found in Ely et al. (2011) and on <https://www.spacetelescope.org/about/general/instruments/stis>.

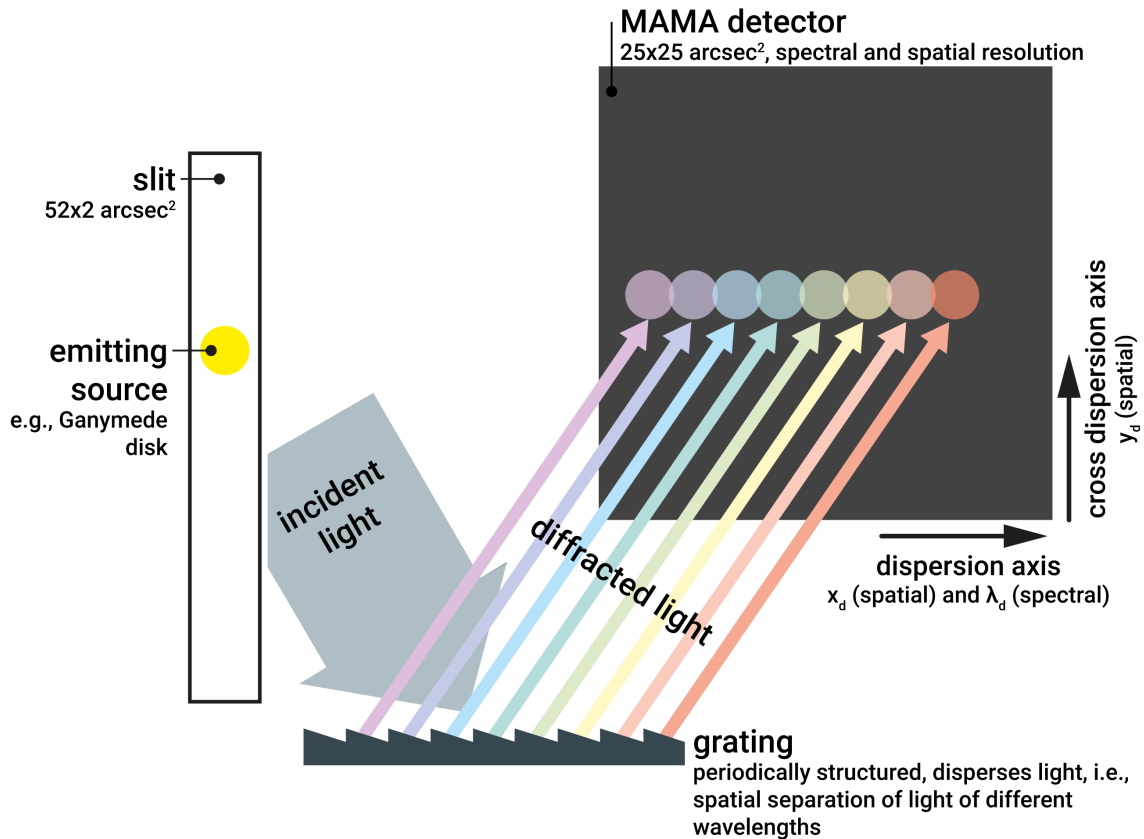


Figure 20 – Sketch of HST/STIS' principle functionality. Note that the content of this sketch is greatly simplified and not to scale.

25 arcsec.

The used HST observations are taken in the first-order spectroscopy mode using the *G140L* grating. As indicated in the sketch in Figure 20, the grating disperses the incident light of the emitting source by spatial separation of the light into its different wavelength components. This is represented by the dispersion of the incident light into different colors in the sketch. The detector records the spatially resolved target, i.e., the Ganymede disk, at each diffracted (and so far emitted) wavelength, representing distinct images of the target for individual emission lines. The individual images may overlap if the separation between the emissions is lower than the target's extent, i.e., the Ganymede disk.

The choice of the detector and aperture mode determines the applicable set of gratings (a complete list of gratings is available in Ely et al. (2011, page 288ff.)). From this set, the *G140L* grating has its throughput maximum at around 1300 Å (Ely et al. 2011, their figure 13.39) and is therefore suitable for the targeted wavelengths at 1304 Å and 1356 Å. The relation between x_d and λ_d is determined

by the dispersion of the grating, which is $\Delta\lambda = 0.584 \text{ \AA}$ per pixel for the *G140L* grating:

$$\begin{aligned}\lambda_d &= \lambda_r + (x_d - x_r)\Delta\lambda \\ \Leftrightarrow x_d &= x_r + \frac{\lambda_d - \lambda_r}{\Delta\lambda},\end{aligned}\tag{3.2}$$

where x_r and λ_r are reference coordinates stored in the scientific header of each HST/STIS data file. In Equation 3.2, x_d determines the horizontal center pixel of the extended target, i.e. the center of the Ganymede disk, at a given wavelength λ_d .

Another speciality of STIS is, that it can be operated in the so-called *time-tag mode*. Operated in that mode, the position (x_d, y_d) and the arrival time t of the photon on any detector pixel is recorded with a temporal resolution of 125 microseconds. One HST orbit consists of two exposures, each usually lasting 15 to 20 minutes. An exposure is the smallest time interval which is available by default. If required, the time-tag mode allows a further temporal splitting of the exposure into shorter time intervals at the expense of reduction of the signal-to-noise ratio (SNR) of a pixel.

The raw data, which consists of the stored electron counts triggered by incoming photons at the detector pixel (x_d, y_d) , is processed by the so-called *calstis* pipeline. Further details of the pipeline software can be found in Bostroem and Proffitt (2011). The general steps of the pipeline procedure are a pixel quality check, subtraction of dark signal and a flat-field correction. The output after these steps is a flat-field corrected data file, called *flt*-file. Each *flt*-file consists of three extensions:

- 1 an array of the stored electron counts for each pixel, $c(x_d, y_d)$,
- 2 an array of the statistical errors for each pixel, $\sigma_0(x_d, y_d)$, and
- 3 a data quality array, flagging suspicious pixels.

Additionally, there is a scientific file header for the entire *flt*-file and for each ex-

tension. Each header contains important keywords and specifications which characterize the observation and its processing (e.g., applied grating and aperture, reference pixels, exposure time, throughput specification). Further details of the file structure can be found in Bostroem and Proffitt (2011, e.g., their figure 2.2 and chapter 2.3.1). The *flt*-files can be further processed by the *calstis* pipeline software, e.g., conversion into photon flux and rectification of the image (then called for example *x2d*-files). Throughout our study, we use *flt*-files in order to operate on the least processed data format. Thus, we are able to process the data step by step on our own (e.g., flux conversion) when they are required, avoiding reverse processing of pipeline steps. In the following, we describe each of our processing steps in detail.

3.2.1 flt-files and background subtraction

The different pipeline processed data files are available through the online *Mikulski Archive for Space Telescopes*³ (MAST). In order to increase the SNR, we superpose the two exposures of each orbit (also see Table 5). During two exposures of one HST orbit (~ 40 minutes), Ganymede travels 0.4% of its entire orbit around Jupiter. This corresponds to a rotation of 1.4° which is very low. Hence, the change of sub-observer longitude from the beginning of the first exposure until the end of the second exposure is negligible. Exemplary for one visit, we show in Figure 21A the image containing electron counts per seconds for the superposition of all orbits of visit 2 of the HST/STIS campaign 12244. The image is generated with the data stored in the corresponding *flt*-file divided by the exposure time for the entire visit. The dispersion-axis is converted into wavelength units according to the dispersion of the *G140L* grating. We indicate the part of the detector where the target is located (*target area*, trace along the dispersion-axis around $y_d = 100$ pixel). The prominent emissions at HI $\lambda 1216 \text{ \AA}$, OI $\lambda 1304 \text{ \AA}$, and OI $\lambda 1356 \text{ \AA}$ are indicated by white dashed lines. The horizontal extent of each emission has the size of the 2 arcsec wide slit. The resolution of a pixel is defined by the plate scale m_s , which is stored in the scientific header of the *flt*-file. For the MAMA detector operated in the FUV range with the *G140L* grating, each pixel has the resolution of $m_s \sim 0.0246$ arcsec per pixel in both detector di-

³<https://archive.stsci.edu/hst/search.php>

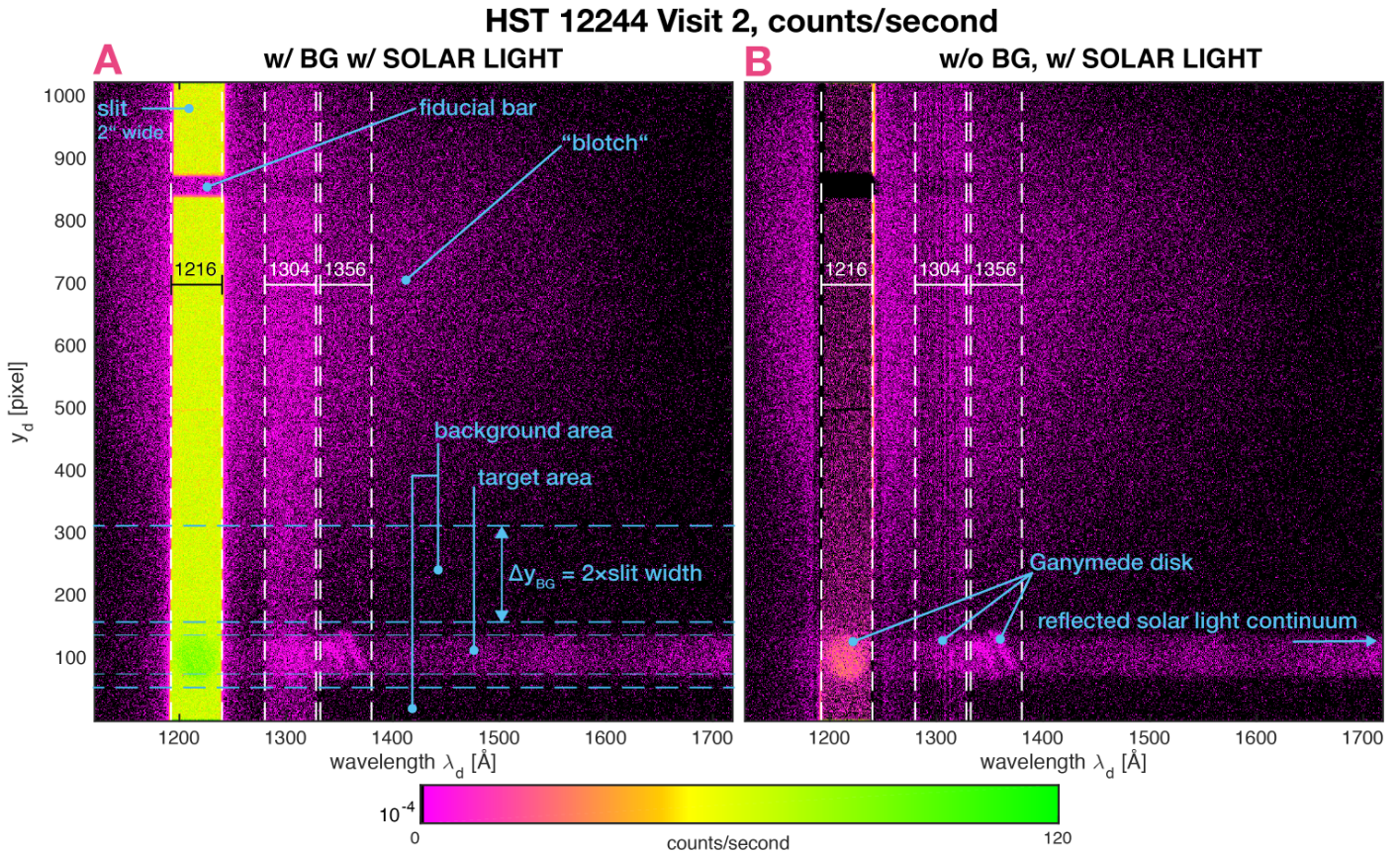


Figure 21 – 1024×1024 detector image containing electron counts per seconds (A) and background subtracted image (B) for the superposition of all orbits of visit 2 from HST/STIS campaign 12244. Emission at HI $\lambda 1216$ Å, OI $\lambda 1304$ Å, and OI $\lambda 1356$ Å are indicated. The *target area* (area on the detector where Ganymede is placed) and the *background area* (used to calculate the background subtracted image in B) are indicated in A.

rections⁴ (Ely et al. 2011). Hence, the slit width corresponds to approximately 82 pixels. Each emission line is interrupted by a blank stripe at around $y_d = 850$ pixel. This stripe is caused by the so-called *fiducial bar*, a physical part of the slit which can be used for occultation experiments. The highest count rate is at HI $\lambda 1216$ Å, which mostly results from the Lyman- α emission in the geocorona. The *blotch* area of faulty counts due to hot pixels is also indicated in the image. As discussed in the previous section, the target, Ganymede, is located below that area in the newer HST campaigns.

The detector image is contaminated by background emission due to the geocoronal scattered light, interplanetary emission, and noise by the detector. We

⁴Hence, one pixel on the detector corresponds on average for all chosen HST campaigns to ~ 76 km \times 76 km on the Ganymede disk. The spatial resolution of a pixel on the moon disk varies from one HST visit to another due to the changing distance between HST and Ganymede.

remove this background emission by summing along pixels above and below the moon disk (*target area* in Figure 21A) in y_d -direction for each x_d/λ_d value. The *background area* in Figure 21A spans two times of the slit width (i.e., 164 pixels) in y_d -direction above and below the *target area*. To avoid contamination of the *background area* by the signal from the *target area*, a buffer area of 10 pixels in y_d -direction separates both areas from each other. When Ganymede is located near the upper or lower edge of the detector image and summing over twice the slit-width is not possible, we take all available pixels up to the physical detector limitation. This is the case, for example, in campaign 12244. We then remove the average of the two sums above and below the target from the disk emission. The resulting background corrected image is shown in Figure 21B, where the emission in shape of the Ganymede disk at the three prominent emission lines becomes more distinct. The background subtraction is provided to all *flt*-files, i.e., for each exposure of each orbit. The background corrected detector image, which becomes the reference for all subsequent calculations, is still superimposed by reflected solar radiation. This effects the disks at the three emission lines as well as the in Figure 21B as *reflected solar light continuum* indicated area along the trace. This area contains no Ganymede emission and is due to reflected solar light. We discuss the subtraction of the solar light in Section 3.2.4.

3.2.2 Locating the Ganymede disk on the detector

The location of Ganymede's disk on the 1024×1024 pixel detector image can be determined by a reference pixel (x_r, y_r) recorded in the scientific header of the data files. Sometimes, there is a discrepancy of up to 10 pixels in both directions, x_d and y_d , between the real disk position and the header reference as will be shown below. In order to obtain the best estimate for the real disk position, we apply two independent methods for locating the Ganymede disk.

With the first method, we identify the center of the disk at 1216 \AA , which we convolve with an artificial idealized disk of the same size as Ganymede. The idea of the first method is to find the disk center by searching for the minimum deviation between the convolved disk from the data and the convolution of two idealized disks using a least squares fit. In all selected HST campaigns, Ganymede's disk diameter is not larger than 73 pixels (Table 3). Under the assumption of the idealized case of homogeneously reflected solar Lyman- α from Ganymede's surface,

we cut out a box around the disk position at 1216 Å (calculated according to the header reference) with edge lengths of 82 pixels, which is slightly larger than Ganymede's disk and which corresponds to the 82 pixel wide slit. Due to systematic and stochastic variability, the Ganymede disk inside this 82×82 pixels data box $D(x, y)$ differs from an ideal disk and a least squares fit with an artificial idealized disk of the same size as Ganymede is not suitable. Instead, we convolve $D(x, y)$ with an artificial idealized disk:

$$C(x, y) = D * K = \int_0^{82} \int_0^{82} D(x', y') K(x - x', y - y') dx' dy'. \quad (3.3)$$

We normalize $D(x, y)$ by dividing the array by its maximum value so that the new maximum value of $D(x, y)$ equals 1. K is the convolution kernel containing the artificial disk:

$$K(x, y) = \{(x, y) \in \mathbb{R}^2 : (x - x_0)^2 + (y - y_0)^2 \leq R_G\}. \quad (3.4)$$

The kernel K has the same size as D . The coordinates $x_0 = y_0 = 41$ pixel determine the center of the disk inside the kernel box. To allow for a comparison with $D(x, y)$, any pixel inside the circle of the radius lower or equal than Ganymede's radius R_G is assigned the value of 1, any pixel outside of R_G the value of 0. Figure 22A and B show the resulting normalized convolution $C(x, y)$ as a two-dimensional and three-dimensional contour plot, respectively, again for the superposition of all orbits of visit 2 of campaign 12244. $C(x, y)$ exhibits a rather oval than circular shape. The emission pattern at 1216 Å is not that of an isolated disk, but it is embedded in a weak residual background noise which is not subtracted by the background calculation method (see Figure 21B). This residual background emission causes the stretching of the convolution result in cross-dispersion direction. We indicate the center of the disk at 1216 Å according to the header reference with two black lines in Figure 22A. A qualitative comparison of the disk center coordinates and the location of the intensity maximum of C suggests a mismatch between them. However, $C(x, y)$ has a distinct intensity

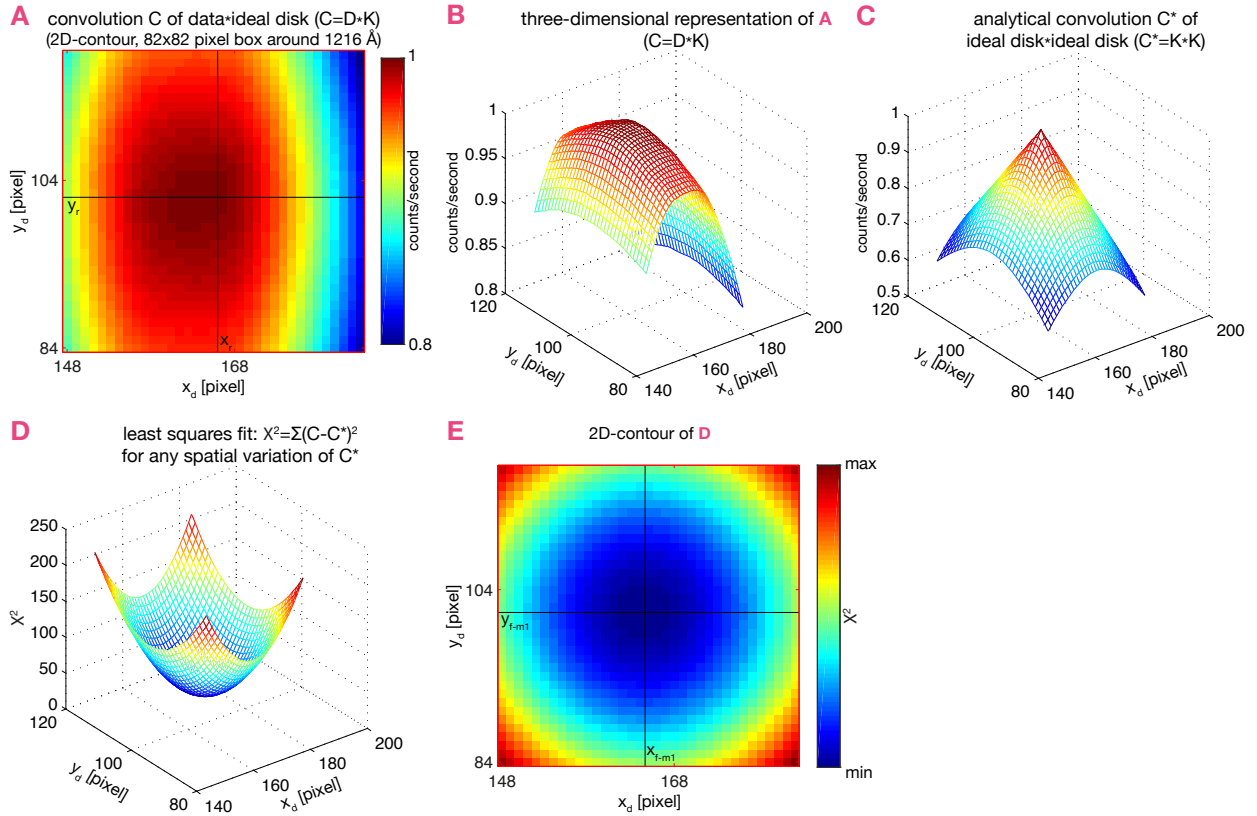


Figure 22 – Disk detection method 1: two-dimensional convolution of the Ganymede disk at 1216 \AA (here: for the superposition of all orbits of campaign 12244, visit 2). **A**: 82×82 pixel cut-out box around the disk center at 1216 \AA according to the header reference, convolved with ideal disk (C). **B**: three-dimensional representation of **A**. **C**: analytical solution of the convolution of two ideal disks ($C^*=K \cdot K$). **D**: resulting Chi-squared (χ^2) of the least squares fit between C and C^* . **E**: two-dimensional contour plot of **D**. Disk center coordinates according to the header reference and the least squares fit are indicated (black lines) in **A** and **E**, respectively.

maximum as shown by the flat peak in the three-dimensional representation of Figure 22B. In order to determine the location of the peak, we calculate the least squares fit between $C(x, y)$ and the convolution $C^*(x, y)$ of two idealized disks of the same size as Ganymede:

$$C^*(x, y) = K * K = \int_0^{82} \int_0^{82} K(x', y') K(x - x', y - y') dx' dy'. \quad (3.5)$$

The convolution between two circles corresponds to the calculation of the overlapping area between two circles of equal radius expressed in terms of the distance

$d = (x'^2 + y'^2)^{\frac{1}{2}}$ between them (Williams and Bocklung 1989, e.g., their figure B.10 and corresponding chapter). Half of this overlapping area corresponds to the segment area A_{sec} of one circle, which can be expressed according to Williams and Bocklung (1989):

$$A_{sec} = R_G^2 \cos^{-1} \left(\frac{d}{2R_G} \right) - \frac{d}{2} \left(R_G^2 - \left(\frac{d}{2} \right)^2 \right)^{\frac{1}{2}} . \quad (3.6)$$

Thus, Equation 3.5 follows:

$$\Rightarrow C^*(x, y) = 2A_{sec} \quad (3.7)$$

$$= 2 R_G^2 \cos^{-1} \left(\frac{\sqrt{x'^2 + y'^2}}{2R_G} \right) - \frac{\sqrt{x'^2 + y'^2}}{2} \left(R_G^2 - \frac{x'^2 + y'^2}{4} \right)^{\frac{1}{2}} . \quad (3.8)$$

C^* is shown in Figure 21C and has a cone shape with a clear peak at the center. The least squares fit is provided by minimizing Chi-squared (χ^2):

$$\chi^2(x_f, y_f) = \sum_{x,y} [C(x, y) - C^*(x_f - x, y_f - y)]^2 \stackrel{!}{=} \min . \quad (3.9)$$

The two fit parameters in Equation 3.9 are x_f and y_f . Geometrically interpreted, we move $C^*(x, y)$ over the entire array $C(x, y)$ by varying x_f and y_f in $C^*(x_f - x, y_f - y)$. For the specific pair of $(x_f = x_{f-m1}, y_f = y_{f-m1})$, where $\chi^2(x_{f-m1}, y_{f-m1})$ has its minimum, C and C^* have the highest correspondence and the peak location, i.e., the disk center, is determined. $\chi^2(x_f, y_f)$ for all variations of (x_f, y_f) is shown in Figure 22D. The coordinates (x_{f-m1}, y_{f-m1}) of the minimum of χ^2 are indicated by the two black lines in Figure 22E, which is the two-dimensional contour plot of D. By setting $x_r = x_{f-m1}$ and $\lambda_d = 1216 \text{ \AA}$, we recalculate the dispersion axis according to Equation 3.2 and correct any existing discrepancy in x_d -direction caused by inadequate header x -references.

The second method is an independent calculation of the reference in y_d -direction using the long wavelength trace. As indicated in Figure 21B, in the trace for wavelengths greater than $\lambda \geq 1450 \text{ \AA}$ we expect no further emission originating from Ganymede's atmosphere but only solar light reflected by the moon disk. The idea of the second method is to integrate the signal $S(\lambda_d, y_d)$ (counts per second) for each y_d inside the trace along the dispersion axis from $\lambda = 1450 \text{ \AA}$ to 1550 \AA :

$$I_{obs}(y_d) = \int_{1450\text{\AA}}^{1550\text{\AA}} S(\lambda_d, y_d) d\lambda_d. \quad (3.10)$$

For the ideal case of a uniform reflecting disk, the resulting profile follows

$$I_{ideal}(y_d) = I_0 \sqrt{1 - \left(\frac{y_d - y_r}{R_G}\right)^2}, \quad (3.11)$$

where y_r is the y -coordinate of the disk center, which we set to y_{f-m1} derived using the first method. I_{ideal} is zero for $|y_d - y_r| > R_G$, i.e., outside the Ganymede disk. In order to compare I_{obs} and I_{ideal} , we set the amplitude I_0 to 1 and normalize I_{obs} so that the maximum value of I_{obs} equals 1. I_{obs} (black line) and I_{ideal} (blue line) are shown in Figure 23A for the same data set as discussed for method 1. Note that for a better illustration of the subsequent convolution we plot I_{ideal} for $y_r = 36$ ($= R_G$ in pixel). We also indicate the extent of the Ganymede disk and the y -center coordinate from method 1 in red. Unfortunately, Ganymede's surface is not uniformly reflecting the solar light and due to additional scattering I_{obs} differs from the profile of I_{ideal} . I_{obs} is irregular and it is not possible to determine a distinct peak maximum. Therefore, we apply the same procedure as in method 1 and convolve I_{obs} with the profile of the idealized Ganymede disk:

$$I_{conv}(y_d) = I_{obs} * I_{ideal} = \int_0^{200} I_{obs}(y') I_{ideal}(y_d - y') dy', \quad (3.12)$$

As can be seen in Figure 23B, the convolution in Equation 3.12 smoothes of the

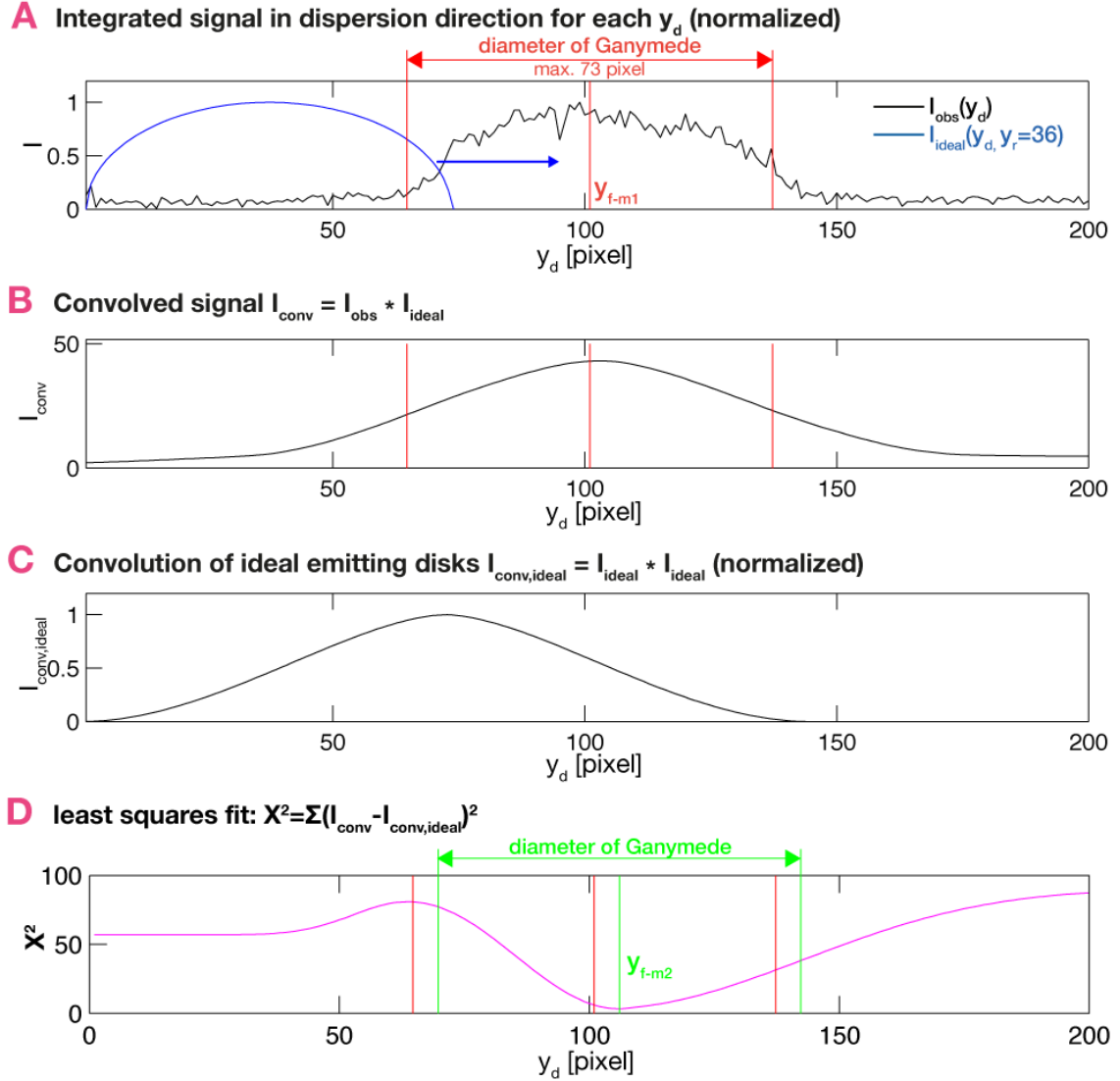


Figure 23 – Disk detection method 2: using the long wavelength trace (same data set as in Figure 22). **A:** integrated signal I_{obs} along λ_d -axis for each y_d inside the long wavelength trace and signal I_{ideal} of an ideal emitting Ganymede disk. **B:** Convolution $I_{conv} = I_{obs}(y_d) * I_{ideal}(y' - y_d)$ (blue arrow in **A** indicates the direction of the convolution). **C:** Convolution $I_{conv,ideal} = I_{ideal}(y_d) * I_{ideal}(y' - y_d)$ of two ideal emitting Ganymede disks. **D:** resulting Chi-squared (χ^2) of the least squares fit between I_{conv} and $I_{conv,ideal}$. y_{f-m2} indicates the minimum of χ^2 and, therefore, the y -coordinate of the disk center.

measured, irregular profile and simultaneously enhances the profile peak. We then convolve the profile of two idealized Ganymede disks,

$$I_{conv,ideal}(y_d) = I_{ideal} * I_{ideal} = \int_0^{200} I_{ideal}(y') I_{ideal}(y_d - y') dy', \quad (3.13)$$

shown in Figure 23C. Similar to method 1, we provide a least squares fit between I_{conv} and $I_{conv,ideal}$ by minimizing $\chi^2(y_f) = \sum_y [I_{conv}(y) - I_{conv,ideal}(y_f - y)]^2$. The resulting $\chi^2(y_f)$ is plotted in Figure 23D, showing a distinct minimum at $y_f = y_{f-m2}$. With the second method, we derive a second y -center coordinate, y_{f-m2} , of the Ganymede disk.

In Figure 23D we also see a discrepancy between y_{f-m2} and y_{f-m1} . The average discrepancy for all analyzed campaigns lies between 2 to 3 pixels. In the *flt*-files, the dispersion is predominantly along the x_d -direction with a slight shift in y_d -direction. This causes the center coordinates to be shifted in y_d -direction as a function of x_d/λ_d . The difference between y_{f-m1} and y_{f-m2} is due to the so-called *trace drift*, as method 1 and method 2 are applied at different wavelengths. In order to compensate the shifting effect we determine the y_d -drift with calibration measurements of the stellar object *WD2126+734* obtained with the HST/STIS campaign 10040 by Proffitt et al. (2003). This reference campaign has a broad coverage of applied aperture and gratings, including those used in the campaigns we selected for our study. The observation with the pseudo aperture *52X2D1* and grating *G140L* (as used, e.g., in HST campaign 12244) is shown in Figure 24A. We limit the area for our calibration to $x_d = 200$ to 1024 pixel due to the gap between $x_d \approx 100$ and ~ 200 pixel. This range also contains a nearly symmetrical distribution of the signal in y_d -direction - except for the mentioned shift in y_d -direction as a function of x_d . We show the signal profile exemplarily for $x_d = 300$ pixel in Figure 24B (cut-out profile indicated with the dashed magenta line in A). The extracted profile (red line) is irregular. To determine the location of the peak maximum, we apply a least squares fit. Since the exact shape of the emitting source is unknown, we use a Gaussian function (blue dashed line) which we fit to the extracted profile. Again, the minimum of the resulting χ^2 determines the peak location of the profile. We repeat this fit for all remaining x_d in the selected calibration range and plot the resulting peak locations in Figure 24C (black line), where the drift in y_d -direction becomes clearly visible. The drift is almost linear for the *52X2D1* aperture and can therefore be determined by fitting a polynomial of first degree⁵ of the form

⁵Note that for the aperture *52X2* (e.g., applied in HST campaign 7939) the drift is not linear. Hence, fits with polynomials of higher order have to be applied (see Figure 49 in the Appendix).

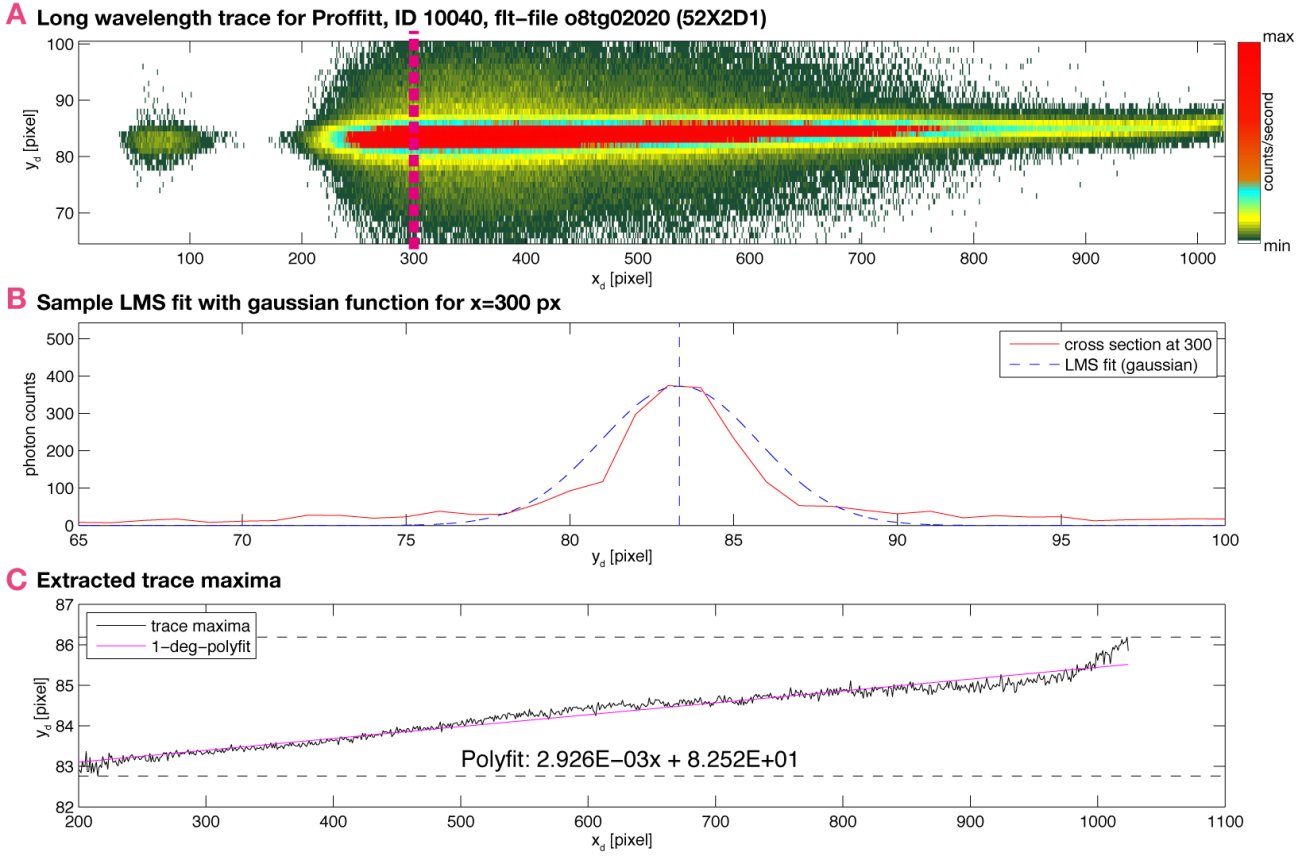


Figure 24 – Determining the trace drift in y -direction using calibration measurements of the stellar object $WD2126+734$ of HST/STIS campaign 10040 (Proffitt et al. 2003) using the pseudo aperture $52X2D1$ and grating $G140L$ (fit-file o8tg02020_fit.fits).

$$y_{\text{drift}}(x_d) = a_0 + a_1 x_d, \quad (3.14)$$

with the two fit parameters a_0 and a_1 . We find $a_0 = 8.25 \times 10^1$ and $a_1 = 2.93 \times 10^{-3}$. The corresponding function $y_{\text{drift}}(x_d)$ is plotted as the magenta line in Figure 24C.

We derive the disk center y -coordinate with method 2, y_{f-m2} , by fitting inside the range of $\lambda_d = 1450 \text{ \AA}$ to 1550 \AA . According to Equation 3.14, the y -drift for a range of 100 \AA (~ 170 pixels) is lower than 1 and therefore negligible. Thus, we assign y_{f-m2} to the center of the fitting range, $x_{f-m2} = x(1450 \text{ \AA}) + (x(1550 \text{ \AA}) - x(1450 \text{ \AA}))/2$ (the notation $x(\lambda_d)$ refers to Equation 3.2 and means taking the x_d value corresponding to the given λ_d). Evaluating Equation 3.14 for $y_{\text{drift}}(x_d = x_{f-m2})$ gives a discrepancy of

Table 4 – Calculated disk-center coordinates of Ganymede at 1356 Å in pixel. Values in brackets display the header reference.

Campaign ID	x_d	y_d
7939	399 (403)	620 (636)
8224	406 (405)	379 (387)
12244-1	404 (404)	102 (98)
12244-2	404 (404)	105 (88)

$$\Delta y = y_{f-m2} - y_{\text{drift}}(x_{f-m2}) \quad (3.15)$$

compared to the fitted disk center y -coordinate. Adding Δy to Equation 3.14 corrects this discrepancy and leads to a modified equation for the trace drift:

$$\begin{aligned} y_{\text{drift-m2}}(x_d) &= y_{\text{drift}}(x_d) + \Delta y \\ &= y_{f-m2} + y_{\text{drift}}(x_d) - y_{\text{drift}}(x_{f-m2}). \end{aligned} \quad (3.16)$$

Now, we evaluate $y_{\text{drift-m2}}(x_d)$ at $x_d = x_{f-m1}$, the disk center x -coordinate from method 1. By averaging y_{f-m1} and $y_{\text{drift-m2}}(x_{f-m1})$ we derive the new disk center y -coordinate y_{f-m12} , which becomes the final y -coordinate for the disk center at 1216 Å. Repeating the steps in Equation 3.15 and 3.16 for x_{f-m1} and y_{f-m12} gives the final function $y_{\text{drift-m12}}(x_d)$, which can be used to calculate the correct disk center y -coordinate for any specific x_d or λ_d coordinate. For comparison, we list in Table 4 the derived disk center coordinates for the Ganymede disk at 1356 Å for each HST campaign together with the corresponding position according to the header reference (values in brackets).

3.2.3 Flux conversion

The counts $n(x_d, y_d)$ stored for each pixel (x_d, y_d) in the *flt*-files represent the electron counts on the *MAMA* detector triggered by incident photons reaching and

passing through HST. For any further physical interpretations we need to convert the electron counts on the detector into the photon flux density ϕ as they arrive in front of the HST mirror. The photon flux density is defined as photons per time per effective area per wavelength (Saleh et al. 1992; Tennyson 2005; Ely et al. 2011):

$$\phi(x_d, y_d) = \frac{n(x_d, y_d)}{\Delta t} \frac{1}{A_{\text{eff}}} \frac{1}{\Delta \lambda} \quad [\text{photons/s/cm}^2/\text{\AA}], \quad (3.17)$$

with the exposure time Δt and the dispersion $\Delta \lambda$. The effective area A_{eff} is defined by the product of the area A of the unobstructed telescope mirror and the instrument specific and wavelength dependent throughput $T(\lambda_d)$ of the telescope:

$$A_{\text{eff}} = AT(\lambda_d). \quad (3.18)$$

We remember that according to Equation 3.2, the i_x -th value of the wavelength $\lambda_d(i_x)$ corresponds to the i_x -th value of the pixel position $x_d(i_x)$ with $i_x = 1, 2, 3, \dots, 1024$. The diameter of HST's mirror is $\varnothing = 2.4$ m. The unobstructed area of the mirror follows $A = \pi(\varnothing/2)^2 \cdot 0.85 = 38,453.095$ cm². The correction factor 0.85 has to be applied in order to obtain the actual unobstructed area of the mirror according to Paul D. Feldman (personal communication, April 1, 2013, Cologne). $T(\lambda_d)$ is unitless and determines the fraction of incoming photons which actually reach the detector after their path through HST. Hence, by dividing $n(x_d, y_d)$ by $T(\lambda_d)$ we convert the detector counts to photon counts in front of the HST mirror. The throughput is stored in calibration tables specified in the header of the *flt*-files. The throughput tables are available via the MAST archive.

The photon flux density ϕ can also be expressed in terms of energy by multiplying Equation 3.17 with the wavelength dependent photon energy $E_p(\lambda_d) = hc/\lambda_d$ in [erg],

$$\begin{aligned}\phi_{E_p}(x_d, y_d, E_p) &= \text{Eq. 3.17} \cdot E_p(\lambda_d) \\ &= \frac{n(x_d, y_d)}{\Delta t} \frac{1}{AT(\lambda_d)} \frac{1}{\Delta\lambda} \frac{hc}{\lambda_d} \quad [\text{photons erg/s/cm}^2/\text{\AA}], \quad (3.19)\end{aligned}$$

where h is Planck's constant and c the speed of light. Throughout our study we use the photon flux density defined in Equation 3.17. The conversion of the photon flux $\phi(x_d, y_d)$ at HST to the surface brightness $L(x_d, y_d)$ at Ganymede follows

$$L(x_d, y_d) = \phi(x_d, y_d) \Delta\lambda d\Omega^{-1} \quad [\text{photons/s/cm}^2/\text{arcsec}^2], \quad (3.20)$$

with $d\Omega = m_{s_x} \times m_{s_y}$ the FOV of a pixel, which is for the *G140L* grating $d\Omega = 0.0246 \times 0.0246 \text{ arcsec}^2$. We multiply by λ_d as $L(x_d, y_d)$ is not expressed in terms of the dispersion. $L(x_d, y_d)$ describes the total amount of photons emitted within a column of unity radius in direction of the line of sight of the pixel (x_d, y_d) . Usually, auroral brightness is expressed in the unit auf *Rayleighs* R with $1 \text{ R} = 10^6 \text{ photons } (4\pi)^{-1} \text{ cm}^{-2} \text{ s}^{-1} \text{ sr}^{-1}$:

$$f(x_d, y_d) = L(x_d, y_d) \frac{4\pi}{10^6} \left(\frac{360 \cdot 3600}{2\pi} \right)^2 \quad [\text{R}]. \quad (3.21)$$

The factor $((360 \cdot 3600)/(2\pi))^2$ is due to the conversion of arcsec^{-2} into Steradian sr^{-1} .

3.2.4 Modeling reflected solar light

As mentioned in Section 3.2.1, the background corrected image is still superimposed by solar light reflected from Ganymede's surface (as exemplarily shown for visit 2 of campaign 12244 in Figure 21B). In order to remove the reflected solar light we use solar spectra $\phi_{\text{sol } 1\text{AU}}(\lambda_d)$ by the *Solar Extreme Ultraviolet Experiment* (SEE) on-board the *Thermosphere Ionosphere Mesosphere Energetics and Dynamics satellite* (TIMED) for the specific day of the observation (Woods et al.

2005). Measured roughly at the orbit of the Earth with the Sun-Earth-distance of $d_{SE} = 1$ AU, we scale $f_{sol\ 1AU}(\lambda_d)$ to the Sun-Ganymede-distance d_{SG} (≈ 5 AU). To calculate the part of the spectrum, which is reflected back to HST, we have to take into account the distance between Ganymede and HST, d_{GH} (≈ 4 AU). By assuming Ganymede as a uniform reflecting disk, the reflected solar flux reaching HST follows

$$\phi_{sol, PS}(\lambda_d) = a f_{sol\ 1AU}(\lambda_d) \left(\frac{d_{SE}}{d_{SG}d_{GH}} \right)^2 R_G^2, \quad (3.22)$$

with the geometric albedo a . $\phi_{sol, PS}(\lambda_d)$ is the one-dimensional reflected solar flux for a point source reaching HST. In order to compare it with the measured photon flux at HST, we express ϕ from Equation 3.17 in terms of wavelengths, $\phi(\lambda_d, y_d)$, and integrate it in cross-dispersion direction y_d at each wavelength λ_d ,

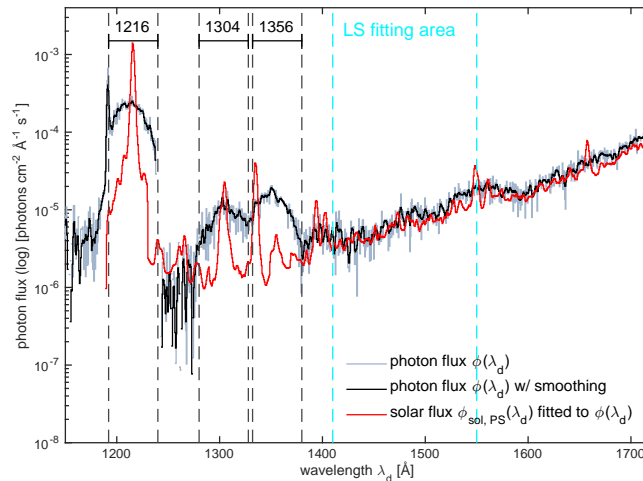
$$\phi(\lambda_d) = \int_{y_{drift-m2}(\lambda_d) - \Delta s}^{y_{drift-m2}(\lambda_d) + \Delta s} \phi(\lambda_d, y_d) dy_d \quad \forall \lambda_d(i_x) \text{ with } i_x = 1, 2, 3, \dots, 1024. \quad (3.23)$$

Δs is the slit width in pixel and $y_{drift-m2}(\lambda_d)$ is the function of the corrected y_d -position of the disk center from Equation 3.16 expressed in terms of wavelength λ_d . We show the integrated flux in Figure 25A as a function of wavelength, again for the same example as in the previous sections (visit 2 of campaign 12244). In grey we show $\phi(\lambda_d)$ and in black $\phi(\lambda_d)$ after applying a smoothing function⁶ for visual enhancement. This integrated one-dimensional flux is characterized by three distinct peaks at 1216 Å, 1304 Å, and 1356 Å, which correspond to the previously detected emission enhancements in the two-dimensional image (Figure 21A and B). At wavelengths greater than ~ 1410 Å, the spectrum increases almost linearly without any further distinct peaks.

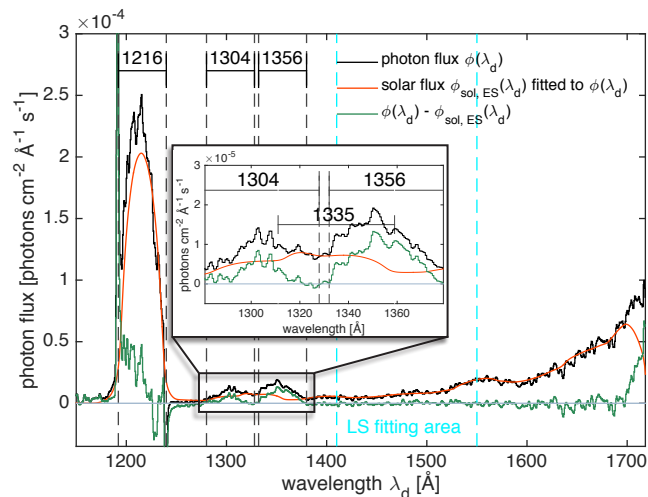
We fit $\phi_{sol, PS}(\lambda_d)$ to $\phi(\lambda_d)$ with a least squares fit with a as the free parameter. We fit between 1410 Å and 1550 Å (area within the dashed turquoise lines in Figure 25A), where we expect that the observed trace to consist only of reflec-

⁶We apply a moving average as defined in Equation 3.26, but only in one dimension. The size of the moving average is set to 5 pixel.

ted solar light. We assume a constant albedo as a function of wavelength for $\lambda_d \leq 1700 \text{ \AA}$. $\phi_{\text{sol, PS}}(\lambda_d)$ for the fitted albedo a_{PS} is shown in red in Figure 25A. Inside the fitting area (1410 \AA to 1550 \AA) and for greater wavelengths, the solar spectrum shows linear behavior, increasing as a function of wavelength, and is in



A Measured and background corrected 1D photon flux ϕ is shown in grey (plotted logarithmically). The black line is the same flux after applying a smoothing function in order to enhance the visibility. The solar flux reflected from Ganymede's surface for a point source reaching HST, $\phi_{\text{sol, PS}}$, is shown in red.



B Modeled reflected solar flux $\phi_{\text{sol, ES}}$ for a uniform emitting moon disk (red line) is subtracted from the background corrected flux (ϕ , black line). The magnification box shows the remaining emission from Ganymede's atmosphere at 1304 \AA and 1356 \AA .

Figure 25 – 1D photon fluxes from Ganymede reaching HST for visit 2 of campaign 12244. The area, where the least squares fit is applied, is inside the two turquoise lines.

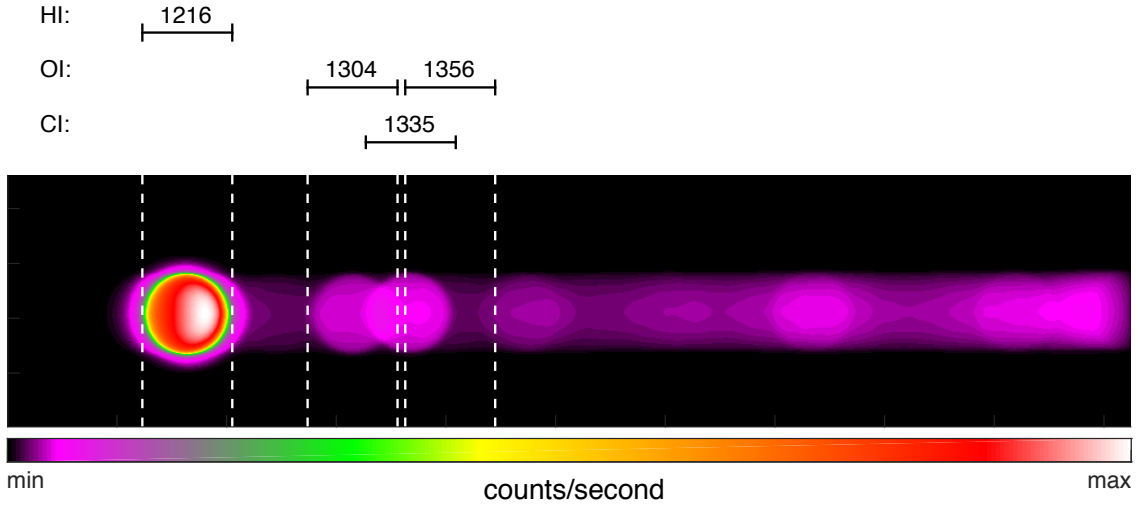


Figure 26 – Modeled disks convolved with the fitted reflected solar flux and with HST's point spread function at each wavelength.

the same range as the measured photon flux ϕ . For the extended emission regions of 1216 Å, 1304 Å, and 1356 Å (indicated by the black lines in Figure 25A; distance between the lines equals the slit width), ϕ is greater than $\phi_{\text{sol, PS}}$ except for three peaks at 1335 Å and at the center of 1216 Å and 1304 Å. However, we must bear in mind that we are comparing the signal from a spatially extended source, the Ganymede disk, with the reflected solar flux for a point source. Thus, under assumption that the fitted $\phi_{\text{sol, PS}}(\lambda_d, a = a_{\text{PS}})$ is uniformly emitted from a disk of the size of Ganymede, we convolve artificially generated disks with radius $r = R_G$ with $\phi_{\text{sol, PS}}$. We then convolve the model disks with the point spread function (PSF) obtained by the *TinyTim* software package (Krist et al. 2011) in order to account for scattering and diffraction of light in the optical systems of HST. The resulting two-dimensional image containing the artificial disks is shown in Figure 26. By integrating the model disks along the y_d -axis for each wavelength, we obtain the one-dimensional model spectrum of a spatial extended source, $\phi_{\text{sol, ES}}(\lambda_d)$. Again, we fit this spectrum to the observed flux $\phi(\lambda_d)$ by a least squares fit, i.e., we minimize the function

$$\chi^2(\tilde{a}) = \sum_{\lambda_d} [\tilde{a}\phi_{\text{sol, ES}}(\lambda_d) - \phi(\lambda_d)]^2 \stackrel{!}{=} \min, \quad (3.24)$$

with \tilde{a} as the free fit parameter. The resulting \tilde{a} is a correction factor to the pre-

viously fitted albedo a_{SP} in order to obtain the final fitted albedo a_{final} with

$$a_{\text{final}} = \tilde{a} a_{\text{SP}}. \quad (3.25)$$

Using a_{final} in Equation 3.22 and repeating all subsequent steps for creating the artificial model disks, we obtain the final two-dimensional model disks which we subtract from the background corrected image. The final resulting image for our example is shown in Figure 27. The integrated one-dimensional fluxes are shown in Figure 25B with the measured photon flux $\phi(\lambda_d)$ in black, the fitted reflected solar flux for an extended disk $\phi_{\text{sol ES}}(\lambda_d)$ in red, and the final corrected spectrum $\phi(\lambda_d) - \phi_{\text{sol ES}}(\lambda_d)$ in green. After both subtractions, background emission and reflected solar light, only the emission originating from Ganymede's atmosphere itself remains. The magnification box in Figure 25B clearly shows this for OI $\lambda 1304$ and OI $\lambda 1356$, indicating auroral emission at these two wavelengths. Prior to the correction for reflected solar light, both emissions were overlapped by reflected solar CII $\lambda 1335$. However, this carbon emission vanishes after the subtraction of reflected solar light and the two oxygen lines are clearly separated from each other as shown. The calculated reflected solar Lyman- α emission at 1216 \AA is slightly overestimated. As described in Section 3.2.1, we subtract the background by measuring above and below the disk under the assumption of an unobstructed line of sight. As neutral hydrogen of the interplanetary medium backscatters solar Lyman- α emission (Ajello et al. 1994), with Ganymede obstructing parts of the Lyman- α emission, we possibly overestimate the Lyman- α background. It is also possible, that the Lyman- α albedo is different from the albedo for the wavelength range which we chose to fit. However, this discrepancy has no implications on the results of our work as we only use Lyman- α for determining the location of the disk.

3.2.5 Generating spectral images

To obtain spatially resolved images of Ganymede's auroral emission for a specific wavelength as shown, e.g., in Figure 14 or Figure 15, we cut out a 82×82 pixel image around the disk center for each desired wavelength from the background

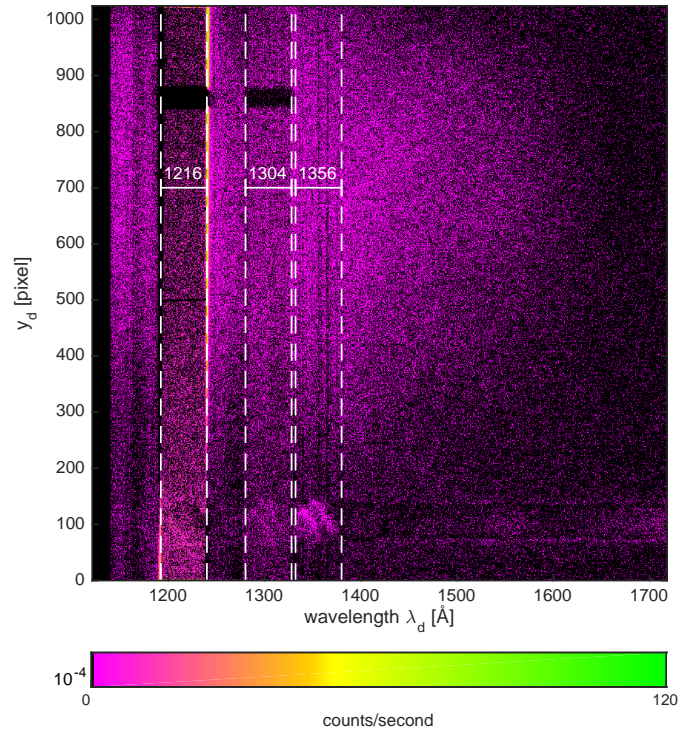


Figure 27 – 2D background emission and reflected solar flux corrected image for visit 2 of campaign 12244.

and reflected solar light corrected and Rayleigh converted detector image. The edge lengths of the new images correspond to the 2 arcsec wide slit which ensures that the entire Ganymede disk of ~ 1.6 to 1.7 arcsec fits into the image. For the transformation of detector frame (x_d, y_d) into a new coordinate system, where the y -axis of the new images is aligned with Jupiter’s rotation axis, we use the software package *SPICE* provided by NASA’s *Navigation and Ancillary Information Facility*⁷ (*NAIF*). Using the reference *ORIENTAT* given in the scientific head of the *flt*-file, which describes the angle between the detector’s cross-dispersion axis (y_d) and Celestial North (Bostroem and Proffitt 2011, their figure 2.6), we align the detector’s y_d -axis with the latter one and transform from the Celestial into the desired coordinate system. We now introduce coordinates to describe the position of each pixel in the new reference frame. The pixel positions in the Jupiter north-south direction, i.e., the y -direction of the images, are indicated by i_y , and the pixel position in the perpendicular direction, i.e., in the x -direction, are indicated by i_x . The corresponding photon flux of each pixel, expressed in terms of Rayleighs, is then described by $f(i_x, i_y)$. In order to increase the visibility

⁷<http://naif.jpl.nasa.gov/naif/>

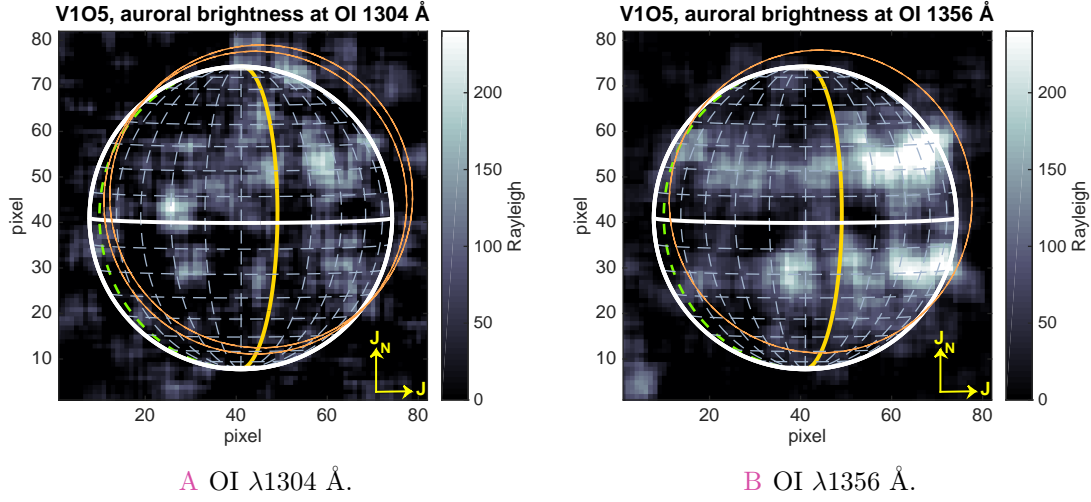


Figure 28 – Spectral images of the oxygen emission for orbit 5, visit 1 of campaign 12244 (2010). Prominent longitudes are indicated: the leading/trailing side central meridian (i.e., $90^\circ/270^\circ$ of planetographic west longitude) is plotted in yellow, and the sub-Jovian/anti-Jovian meridian ($0^\circ/180^\circ$ longitude) is plotted as a dashed green line. The images are centered around the brightest emission line of each multiplet (thick white circle), while the remaining dispersed disks are shown as orange circles. Yellow arrows indicate the Jupiter and Ganymede north direction (J_N) and the direction towards Jupiter (J).

of the auroral structure, we smooth the images (similar to Saur et al. (2015) or Roth et al. (2014a, b, 2015)) by using a two-dimensional moving average filter of the size $(2M+1) \times (2N+1)$ (Glasbey and Horgan 1995; Bevington and Robinson 2003),

$$f_{\text{smoothed}}(i_x, i_y) = \frac{1}{\sum_{k=-M}^M \sum_{l=-N}^N w_{kl}} \sum_{k=-M}^M \sum_{l=-N}^N w_{kl} f(i_x + k, i_y + l), \quad (3.26)$$

where N and M determine the size of the smoothing box. We set $N = M = 3$ pixel, i.e., we apply a 3×3 moving average filter to the photon flux $f(i_x, i_y)$ of the pixel (i_x, i_y) . w_{kl} is the weighting factor, which we set to 1 for all $k = -M, \dots, M$ and $l = -N, \dots, N$, i.e., all accounted pixels are equally weighted. $f_{\text{smoothed}}(i_x, i_y)$ is the resulting smoothed flux of the pixel (i_x, i_y) . Note that Equation 3.26 is applicable for $i_x = (M + 1), \dots, (M_x - M)$ and $i_y = (N + 1), \dots, (N_y - N)$, where $M_x = N_y = 1024$ is the size of the 1024×1024 pixel image, i.e., we apply the smoothing prior to cutting out the 82×82 images. The reason for applying the

filter to the entire detector image is that we assign to the pixels at the borders of $f_{\text{smoothed}}(i_x, i_y)$ the same values as those of $f(i_x, i_y)$, i.e., the borders are not smoothed (Glasbey and Horgan 1995). As the finally cut-out 82×82 images are far away from these borders, they are not affected by the chosen border definition. Note again, that smoothing the images is just for enhancement of visibility and for a basic qualitative analysis of the spectral images, while all calculations in this work refer to unsmoothed data.

The resulting image is exemplarily shown for orbit 5, visit 1 of campaign 12244 in Figure 28. We indicate the Ganymede disk with the thick white circle and plot the corresponding planetographic coordinate system as dashed longitude and latitude lines. We indicate the leading/trailing side central meridian (i.e., $90^\circ/270^\circ$ of planetographic west longitude) by the yellow line, and the sub-Jovian/anti-Jovian meridian ($0^\circ/180^\circ$ longitude) as the dashed green line. Due to the low offset of the sub-observer longitude from the leading/trailing meridian, the sub-Jovian/anti-Jovian meridian is hardly visible. Ganymede's planetographic equator is indicated by the thickest latitude line. The yellow arrows in the lower right corner of each image indicate the Jupiter and Ganymede north direction (J_N) and the direction towards Jupiter (J). J points to the right for leading side campaigns and to the left for trailing side campaigns. We show spectral images for both oxygen emissions at 1304 \AA (A) and 1356 \AA (B), respectively. Auroral emission is apparent in both images. Both emissions are multiplets of atomic oxygen. The emission at 1304 \AA is the OI $\lambda 1304 \text{ \AA}$ triplet ($2s^2 2p^4 \text{ } ^3P \leftarrow 2s^2 2p^3 3s \text{ } ^3S^0$) with wavelengths at 1302.2 , 1304.9 and 1306.0 \AA , while the emission at 1356 \AA is the spin forbidden OI $\lambda 1356 \text{ \AA}$ doublet ($2s^2 2p^4 \text{ } ^3P \leftarrow 2s^2 2p^3 2s \text{ } ^5S^0$) with wavelengths at 1355.6 and 1358.65 \AA (Hall et al. 1998; Meier 1991). The intensity ratios of the OI $\lambda 1304 \text{ \AA}$ triplet are $f(1302.2 \text{ \AA})/f(1304.9 \text{ \AA})/f(1306.0 \text{ \AA}) = 5:3:1$ (Meier 1991). In Figure 28A, we show the dispersed emissions of each multiplet as orange circles, while the image is centered around the disk with the strongest emission, 1302.2 \AA , which is plotted as the thick white circle. The spectral images throughout this work are always centered around the brightest emission of the specific multiplet. Note that due to the rotation of the images, also the dispersion axis is rotated (for the chosen example HST orbit by around 45°), which places the remaining dispersed disks of the multiplet into the upper right direction of both cut-out images in Figure 28. Due to the dispersion $\Delta\lambda$ of the applied *G140L* grating, the dispersed disks in Figure 28A are only ~ 5 and ~ 6 pixels apart and the disper-

sed disks overlap. Together with the intensity ratio of $f(1302.2 \text{ \AA})/f(1304.9 \text{ \AA}) = 5:3$, the emission at 1304 \AA is partially blurred. The dispersed disks of the OI $\lambda 1356 \text{ \AA}$ doublet are also just ~ 5 pixels apart. Due to the intensity ratio of $f(1355.6 \text{ \AA})/f(1358.5 \text{ \AA}) = 3.76:1$ (Meier 1991), though, the brightness contrast of the dispersed disks is higher which reduces the blur. Hence, auroral emission patterns are more distinct in the OI $\lambda 1356 \text{ \AA}$ images, making them more preferable over the OI $\lambda 1304 \text{ \AA}$ images for studying the oxygen aurora at Ganymede.

Another reason for giving preference to the OI $\lambda 1356 \text{ \AA}$ images is the brightness ratio between the emission at 1304 and 1356 \AA . Approximately half of the emission at OI $\lambda 1304 \text{ \AA}$ induced by reflected solar light (compare magnification box in Figure 25B). After subtracting the reflected solar radiation, the averaged brightness at OI $\lambda 1304 \text{ \AA}$ is two times weaker than at OI $\lambda 1356 \text{ \AA}$ (Feldman et al. 2000; Saur et al. 2015). Additionally, the signal-to-noise ratio is higher at OI $\lambda 1356 \text{ \AA}$ due to lower geocoronal background (see Table 5). Hence, even though Ganymede's auroral ovals are visible in both images of Figure 28, they are more pronounced in the image of OI $\lambda 1356 \text{ \AA}$. This also accounts for all orbits of the chosen HST campaigns. Therefore, we focus our analysis on the OI $\lambda 1356$ emission.

To enhance the visibility, we introduce a polynomial fit to the observed ovals. For all subsequent quantitative analysis of the location of the auroral ovals in Chapter 4 we do not use this polynomial fit but apply different calculation methods. Similar to Saur et al. (2015), we determine the y -component $y_{\text{oval}}(i_x)$ of the location of the ovals for a given i_x by using the brightest pixel of each column in north-south direction of the spectral image:

$$y_{\text{oval}}(i_x) = \frac{\sum_{i_y} i_y f(i_x, i_y)^\kappa}{\sum_{i_y} f(i_x, i_y)^\kappa}, \quad (3.27)$$

where the exponent κ allows to differently weight the brightest pixels. We use a very high $\kappa = 30$, taking the brightest pixel into account as the major contributor for the oval localization, but still preserving the contribution of the pixels around that pixel as co-contributor. The effective width of the oval follows

$$\sigma_{\text{oval}}(i_x) = \left(\frac{\sum_{i_y} (i_y - y_{\text{oval}}(i_x))^2 f(i_x, i_y)}{\sum_{i_y} f(i_x, i_y)} \right). \quad (3.28)$$

To compensate the stochastic and systematic variability, we additionally fit the resulting jagged line of $y_{\text{oval}}(i_x)$ by a second order polynomial,

$$y_{\text{oval, fit}}(i_x) = a_0 + a_1 i_x + a_2 i_x^2, \quad (3.29)$$

where a_i are the fit parameters. The fit is performed by taking into account the error of every data point in $y_{\text{oval}}(i_x)$, i.e., we weight every data point by the factor $w(i_x) = \frac{1}{\sigma_{\text{oval}}^2(i_x)} \left(1/N \sum \frac{1}{\sigma_{\text{oval}}^2(i_x)} \right)^{-1}$ (Bevington and Robinson 2003), where N is the number of data points. The resulting polynomial fits are shown in the spectral images of Figure 32 in the following Chapter 4.

3.2.6 Error propagation

We remove from the observed signal $S_{\text{obs}}(i_x, i_y) = n_{\text{obs}}(i_x, i_y)/\Delta t$ (expressed in terms of counts per seconds) the background counts, $S_{\text{bg}}(i_x, i_y)$ (described in Section 3.2.1), and the counts of the reflected solar radiation, $S_{\text{sol}}(i_x, i_y)$ (described in Section 3.2.4), for each pixel (i_x, i_y) , i.e.,

$$S_{\text{clear}} = S_{\text{obs}} - S_{\text{bg}} - S_{\text{sol}}. \quad [\text{counts/s}] \quad (3.30)$$

The statistical error of the counts associated with auroral photons on a pixel is given by

$$\begin{aligned} \sigma_{\text{clear}} &= \sqrt{\sigma_{\text{obs}}^2 + \sigma_{\text{bg}}^2 + \sigma_{\text{sol}}^2} \\ &= \sqrt{(S_{\text{obs}} + S_{\text{bg}} + S_{\text{sol}})\Delta t}, \end{aligned} \quad [\text{counts}] \quad (3.31)$$

where σ_{obs} corresponds to the square root of the detected and Poisson distributed counts at the specific pixel, i.e., $\sigma_{\text{obs}} = \sqrt{S_{\text{obs}} \Delta t}$. $\sigma_{\text{sol}} = \sqrt{S_{\text{sol}} \Delta t}$ and $\sigma_{\text{bg}} = \sqrt{S_{\text{bg}} \Delta t}$ correspond to the square root of the counts of reflected sunlight and background emission, respectively. The propagated total error σ_{clear} is subsequently converted to spectral flux and brightness as described in Section 3.2.3. The signal-to-noise ratio SNR follows

$$\text{SNR}(i_x, i_y) = \frac{S_{\text{clear}}(i_x, i_y) \Delta t}{\sigma_{\text{clear}}(i_x, i_y)}. \quad (3.32)$$

In Table 5, we calculate the SNR for all pixels inside the Ganymede disk inside the spectral images of both oxygen lines averaged for every visit of each campaign. Even though the SNR for both emissions is generally greater than 1 for each visit, we have to bear in mind that the calculated SNR accounts for the average of the total disk. The SNR for individual disk parts may vary from the values listed in Table 5 (see, e.g., Figure 39). Averaged over all visits, the average SNR (SNR=17.5) of the spectral images at OI $\lambda 1356 \text{ \AA}$ is three times better than the average SNR (SNR=5.6) of the spectral images at OI $\lambda 1304 \text{ \AA}$.

3.2.7 Flux integration

The brightness values B discussed in this work are calculated by the integration of the photon flux $f(i_x, i_y)$ converted in Rayleighs inside the moon disk or specific area A :

Table 5 – SNR averaged for the Ganymede disk in the spectral images of the OI $\lambda 1304 \text{ \AA}$ and OI $\lambda 1356 \text{ \AA}$ emission for each visit.

HST campaign	average SNR	
	OI $\lambda 1304 \text{ \AA}$	OI $\lambda 1356 \text{ \AA}$
7939	5.2	12.5
8224	5.9	21.2
12244-1	6.8	15.5
12244-2	4.4	20.8

$$B = \int_A f(i_x, i_y) di_x di_y. \quad (3.33)$$

In numerical practice, we evaluate this integral by summing over the flux of all pixels inside the integration area:

$$B \approx \frac{1}{N_x N_y} \sum_{x=1, y=1}^{N_x, N_y} f(i_x, i_y) \quad \forall i_x, i_y \text{ in } A, \quad (3.34)$$

with the number of pixels in x - and y -direction, N_x and N_y , inside the integration area A . We normalize the sum by the total number of pixels inside A similar to previous works (e.g., Feldman et al. (2000), Roth et al. (2014b) or Saur et al. (2015)) in order to obtain the average brightness inside A and to compare it with averaged brightnesses of integration areas of different sizes.

Due to the discrete nature of the image array, i.e., the coordinate system is related to the pixel position on the detector and, therefore, based on integer division, no further sub-division of the x - and y -axis is possible. Integrating over pixels inside the area, e.g., of a circle or the moon disk, causes problems as area borders overlap pixels. We demonstrate this problem on the basis of a simplified example. In Figure 29A, we show an artificial 5×5 pixel image (*random signal*), where we assigned random numbers as counts to each pixel. We plotted a circle of the radius $r = 1.5$ pixel in red as the desired integration area $A = \pi r^2$. Inside that circle, only the pixel $(5, 5)$ is fully inside A , while pixels at the borders of the circle are overlapped by the integration area. Without further sub-division of these pixels, the corresponding counts would be accounted for the weight of 1 by the averaging method in Equation 3.34. In A, we also plotted the corresponding mask (*imprecise weights*) including the weighting factor of each pixel for calculating the average inside A . Unfortunately, the weights are of binary nature and only have the value 0 or 1. For example, pixel $(2, 4)$ with the weight of 1 would be fully accounted in the average calculation, even though this pixel is only nearly half inside A . For a large radius r (or generally speaking, for a large integration area), the impact of this distortion effect by pixels overlapped by the border of A on the

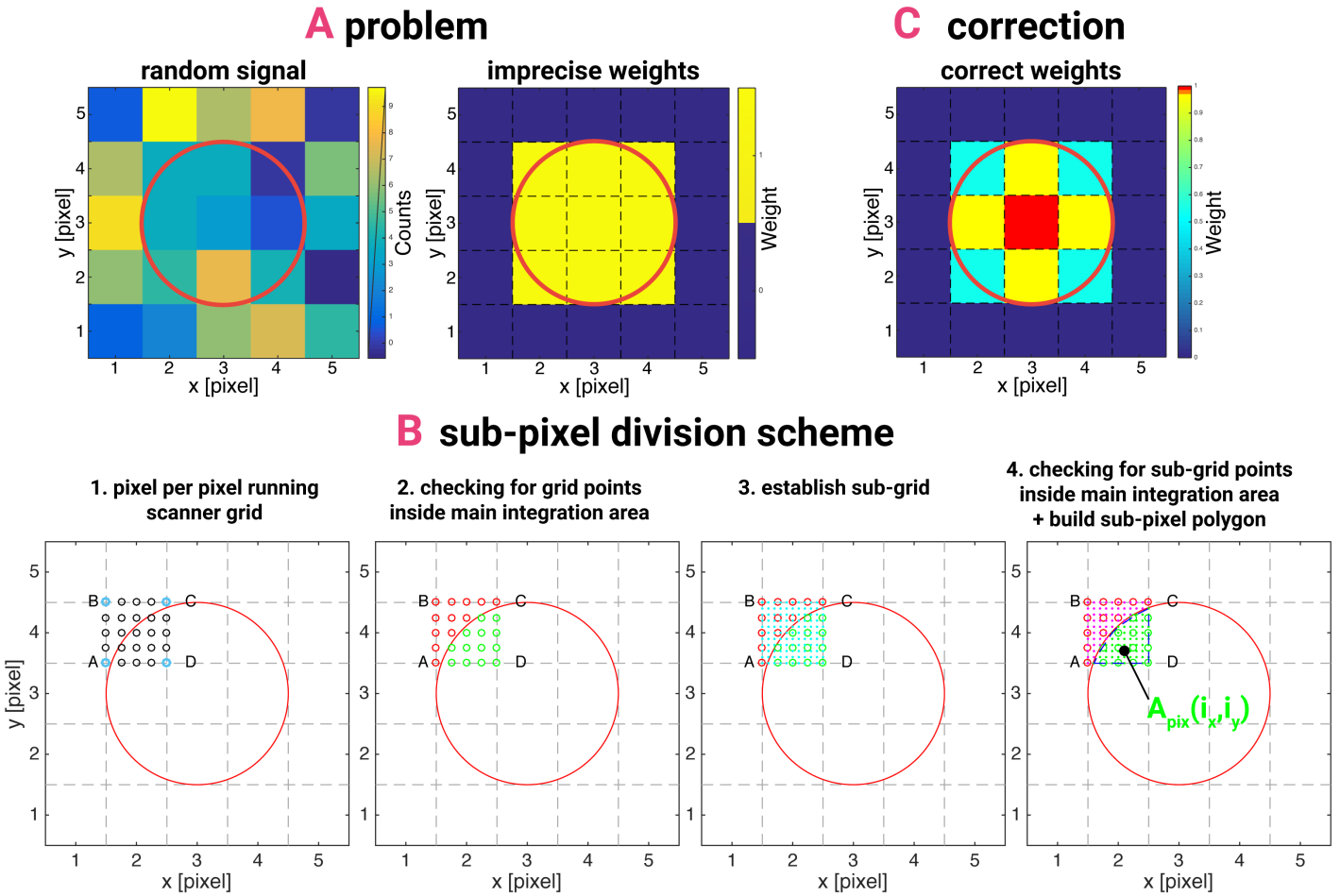


Figure 29 – Sub-pixel division scheme for a simplified example of an artificial 5×5 pixel image. **A**: problem description (incorrect weight assignment at the edges of the integration area (red circle)). **B**: problem solution (searching for parts of the pixels inside the integration area by implementing a moving scanner grid). **C**: image showing the correct weights for each pixel.

average calculation becomes negligible. For small integration areas, however, the impact is not negligible anymore.

We solve this problem by scanning the signal image pixel per pixel with a scanner grid of the size of one pixel. The grid only consists of four points at the edges, indicated by *A*, *B*, *C* and *D* in the first panel of Figure 29B. Note that the grid shown in that panel contains additional grid points lying between the edge points, but here we only discuss the four edge points⁸. The panel shows the grid for pixel (2, 4). By checking if at least one of the grid points is not inside *A* as shown in the second panel of **B** (here: grid points *A*, *B* and *C* are outside *A*, only *D* is inside),

⁸We actually also use these internal grid points in order to increase the sensitivity of our scanning method.

we establish a grid with higher resolution inside the scanner grid (blue dots in the third panel of **B**). We use a grid point distance of $\Delta_{\text{grid}}=0.025$ pixel in both directions for the higher resolved grid (for visual enhancement we show in the third panel of **B** a grid with a higher grid point distance of 0.1). Again, we check which grid points are inside A . In the fourth panel in **B**, we color grid points inside A in green, outside in magenta. By using the outer edges of the area covered by the green dots, we build a new, so-called sub-pixel polygon, which we use to calculate the actual area $A_{\text{pix}}(i_x, i_y)$ covered by the current pixel ($i_x = 2, i_y = 4$) inside A . A_{pix} may have values between 0 and 1. For numerical reasons, we do not start with the high-resolution scanner grid. In order to save computational time, we establish such a grid only for the case, when at least one edge point of the four-point scanner grid is outside A . For example for pixel (3, 3), all four edge points lie inside A , hence, no sub-grid is established and the pixel area $A_{\text{pix}}(3, 3)$ is assigned to 1. By repeating this scan for each pixel, we calculate a new mask of weights as shown in Figure 29C. Pixel (3, 3) has the correct weight of 1, while pixel (2, 4) is assigned the weight of ~ 0.5 . By accounting for the calculated weights, we correct Equation 3.34 according to Bevington and Robinson (2003) to

$$B = \sum_{x=1, y=1}^{N_x, N_y} f(i_x, i_y) \frac{A_{\text{pix}}(i_x, i_y)}{A_0} \left(\sum_{x=1, y=1}^{N_x, N_y} \frac{A_{\text{pix}}(i_x, i_y)}{A_0} \right)^{-1}, \quad (3.35)$$

with A_0 as the reference area of a full covered pixel with $A_0=1$.

3.2.8 Spot detection method

To study the distribution of individual brightness peaks along the auroral ovals disk, we now present a method to detect individual auroral spots. The main principle of this method is to define a brightness threshold, remove any auroral emission below this threshold from the spectral image, and detect the remaining emission and identify individual auroral spots. In the following, we explain each step of this method, exemplarily applied to the spectral image at 1356 Å of the first orbit of visit 1 of campaign 12244.

The chosen 82×82 pixel spectral image $f(i_x, i_y)$ is shown in Figure 30A, pro-

cessed as described in Section 3.2.5 and converted into Rayleigh. We show the contour lines of auroral brightness in steps of 100 R. Individual bright spots with brightnesses >100 R are apparent in the image. For our example and as the first step of our method, we set an adequate⁹ threshold of $f_{\text{lim}}=120$ R. In the second step, we duplicate the spectral image into a new image, $b(i_x, i_y) = f(i_x, i_y)$. Pixels of b , which have a brightness below the threshold, are assigned to the value 0, pixels with a higher brightness are assigned to the value 1,

$$b(i_x, i_y) = \begin{cases} 0 & \text{for } f(i_x, i_y) < f_{\text{lim}} \\ 1 & \text{for } f(i_x, i_y) \geq f_{\text{lim}} \end{cases} \quad \text{with } i_x = 1, \dots, 82, i_y = 1, \dots, 82. \quad (3.36)$$

The resulting binary image is shown in Figure 30B. In that figure, the previously detected bright spots from Figure 30A are represented as binary masks (yellow areas).

In the third step, we detect the outer perimeters of the yellow areas in Figure 30B. We apply the function `bwboundaries`, which is implemented in MATLAB®. `bwboundaries` is based on the *Moore-Neighbor tracing algorithm* (Gonzalez et al. 2004). The basic principle of this algorithm can be described (simplified) by the following scheme according to Gonzalez et al. (2004) and Toussaint (2010):

1. Motivation: Search the contour of the area of interest inside an image. Pixels inside the area of interest are assigned to the value of 1, any other pixels of the image to 0.
2. Starting from the pixel in one edge of the underlying image, search row-by-row and column-by-column for the first pixel, which has the value 1.
3. Set the identified pixel as the new start pixel, $P_{\text{start}}(i_{x,\text{start}}, i_{y,\text{start}})$, and go around that pixel, i.e., search in the neighboring eight pixels around the new start pixel for the next pixel with the value 1. The direction for searching around the new start pixel is not important (clockwise or counter-clockwise). Once chosen, the direction should be kept for all subsequent steps.

⁹We discuss in Section 4.5 how to choose an adequate brightness threshold.

4. When the next pixel with the value of 1 is found, $P_{\text{match}}(i_{x,\text{match}}, i_{y,\text{match}})$, backtrack to the previous pixel (with the value 0).
5. Search around the newly found pixel (with value 1) by repeating steps 2 and 3.
6. The algorithm stops, when $P_{\text{start}}(i_{x,\text{start}}, i_{y,\text{start}})$ is found for a second time.

spot detection scheme

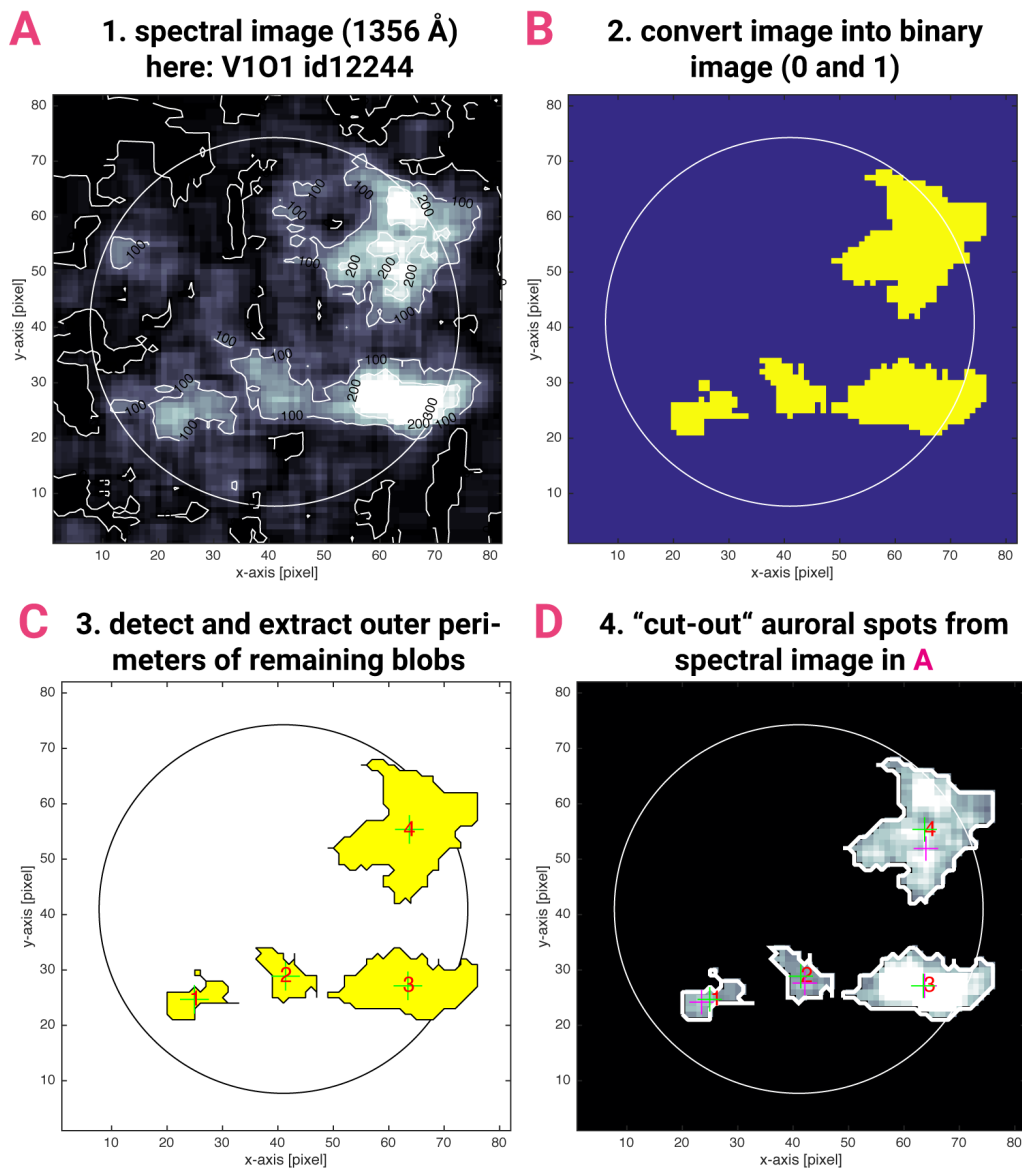


Figure 30 – Spot detection scheme (exemplarily shown for orbit 1 of visit 1 of campaign 12244).

The trace $(i_{x,\text{match}}, i_{y,\text{match}})$ of pixels P_{match} with values of 1 defines the contour of the area of interest in the image (here: the yellow areas in Figure 30B). Since there is more than one area of interest (i.e., spots) in the spectral images, the *Moore-Neighbor tracing algorithm* is applied multiple times (every time the algorithm stops, the currently detected area of interest is excluded from the search in later iterations, and we re-apply the algorithm until no further spots are detected). With the extracted contours of the yellow areas (Figure 30C) we are finally able, to locate and isolate the bright spots in the spectral image as shown in Figure 30D. This enables us to calculate size, brightness, amount (red numbers in Figure 30C), geometric (green crosses in Figure 30D) or brightness weighted centroids (magenta crosses in Figure 30D) of the spot.

Results

In this chapter, we present and discuss the main findings of our study. We first discuss the derived FUV albedo and compare it with the known albedo at other wavelengths. Then, we present the spectral images of the 1356 Å oxygen emission generated as described in the previous chapter. We compare the auroral brightnesses of each campaign and for different locations of Ganymede within the Jovian plasma sheet for the total disk averaged brightness. By analyzing the latitudinal distribution of the auroral emission we are able to separate auroral oval brightness from the residual disk brightness. We analyze the brightness of the ovals and the residual disk for dependencies on Ganymede's changing magnetic latitudes. We introduce a method for determining the location of the auroral ovals for tracking any variation of the oval locations during Ganymede's transit through the Jovian current sheet. We then compare the derived oval locations with the magnetic equator of Ganymede's dipole magnetic field derived by *Galileo* magnetic field measurements. Finally, we study the patchiness of the aurora by separating individual bright spots along the auroral ovals.

4.1 Ganymede's albedo in the FUV range

A convenient *by-product* of the least squares fit, which we apply in Section 3.2.4 when we model the reflected solar light, is the geometric albedo a of Ganymede in the FUV range. As described in that section, we assume the FUV albedo to be constant over the wavelength range covering the two oxygen lines at 1304 and 1356 Å. We summarize all fitted albedos in Table 6 and additionally add the albedo derived by Hall et al. (1998) for the trailing side. With $2.7 \pm 0.4 \%$, the albedo for the trailing side campaign 7939 derived by our fitting method is in good agreement with the albedo of $2.3 \pm 0.2 \%$ previously derived by Feldman et al. (2000) for this campaign. As already noticed by Feldman et al. (2000), the albedo of campaign 7939 in 1998 is also in good agreement with the albedo derived by Hall et al. (1998) for campaign 6758 in 1996. Being two years apart and observing the same hemisphere, both derived albedos show no indication for a significant variation which supports our initial assumption of a constant albedo in the FUV range, at least for our chosen fitting range between 1410 Å and 1550 Å (Section 3.2.4 or see, e.g., Figure 25). This is also true for the leading side, where all derived albedos for the three visits of the leading side campaigns 8224 (2000) and 12244 (2010/11) do not significantly vary over a period of roughly ten years as their errorbars overlap. All trailing side campaigns show a significant higher albedo than the leading side (except for campaign 8224). Compared to Europa, where no pronounced albedo difference between both hemispheres in the FUV has been observed so far (Roth et al. 2014a), the average albedo of $2.7 \pm 0.4 \%$ on Ganymede's trailing side and $1.8 \pm 0.4 \%$ on the leading side indicate a hemispheric albedo dichotomy for the FUV range, instead.

The mid ultraviolet range (MUV) from $2000 \text{ \AA} \leq \lambda \leq 3400 \text{ \AA}$ is already known for the presence of a leading-trailing side albedo dichotomy (Hendrix et al. 1999). Hendrix et al. (1999) confirmed this MUV dichotomy by using the *Galileo Ultraviolet Spectrometer* (UVS). In Figure 31, we show the albedos for the MUV range derived by Nelson et al. (1987) together with the FUV albedo derived from our study. In the MUV range, the leading hemisphere (blue line) is much more reflective than the trailing hemisphere (red line) with increasing difference as a function of increasing wavelength. As discussed in Section 2.1.1, the albedo is also high-

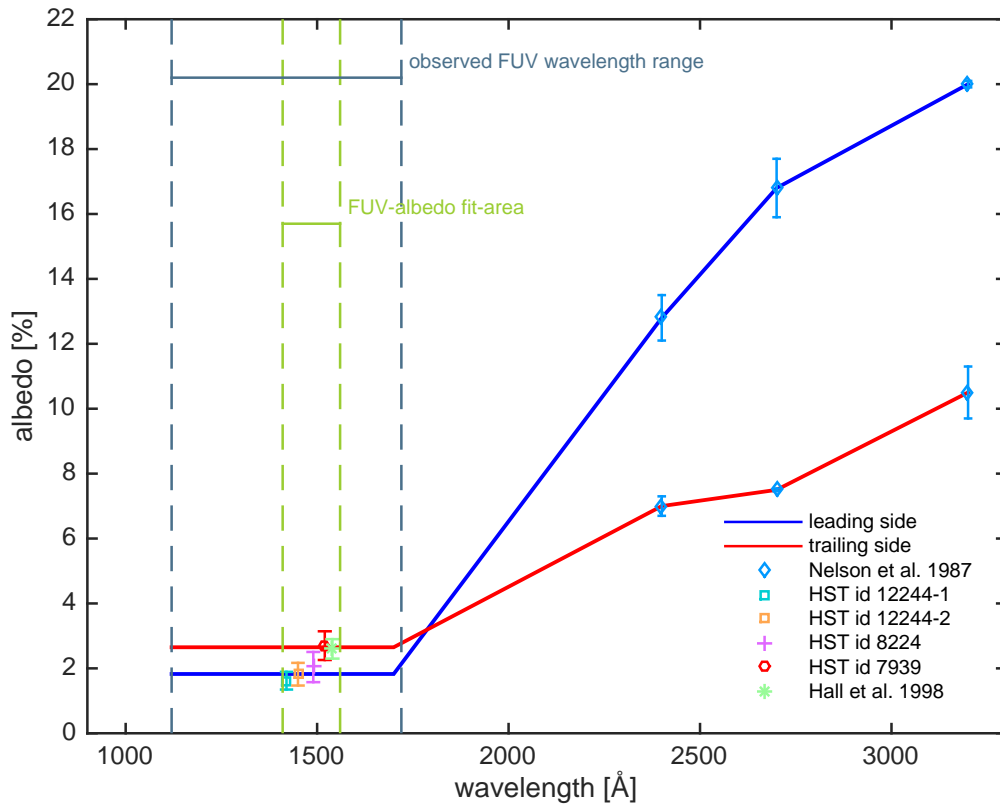


Figure 31 – Albedo for the observed FUV (1100 Å to 1700 Å) and MUV range (2000 Å to 3400 Å) on the leading and trailing side. Note that the derived FUV albedos apply for the entire region inside the dashed green lines, i.e., the FUV fitting area.

her on the leading side than on the trailing side at the visible wavelength of 5600 Å (Figure 5; Pappalardo et al. (2004)). Furthermore, bright surface material is correlated to locally increased albedo values at visible wavelengths, while dark material correlates to lower albedo values (Pappalardo et al. 2004; Squyres and

Table 6 – Albedo in the FUV range. Summarized are all fitted albedo values for the wavelength range observed by the chosen HST/STIS campaigns. Additionally, the albedo derived by Hall et al. (1998) using HST/GHRS is also listed (HST campaign 6758). Letters *T* and *L* denote trailing and leading side observations.

Campaign ID	Hemisphere	Albedo [%]
6758	T	2.6 ± 0.3
7939	T	2.7 ± 0.4
8224	L	2.0 ± 0.5
12244-1	L	1.6 ± 0.3
12244-2	L	1.8 ± 0.3

Veverka 1981). In the FUV range, though, the opposite case is indicated, i.e., bright and dark surface material are anticorrelated compared to the albedo in the FUV range, since we observe the lower FUV albedo on the leading hemisphere.

4.2 Spectral images and general morphology of Ganymede's FUV aurora

In Figure 32, we show spectral images of the emission at 1356 Å for each HST campaign processed as described in Section 3.2. Each panel shows the emission converted in Rayleigh. The campaigns are grouped in columns, where we assign the color red to campaign 7939, blue to visit 1 of campaign 12244, orange to visit 2 of campaign 12244, and violet to campaign 8224 (compare color shadings in Figure 32). We keep this color assignment throughout this work. The spectral images of each orbit are ordered from top to bottom by magnetic latitude ϑ_{mag} . As introduced in Section 3.1, for all observations where Ganymede's magnetic latitude was below $|\vartheta_{\text{mag}}| < 5^\circ$, Ganymede was inside the Jovian current sheet (ICS). For $|\vartheta_{\text{mag}}| > 5^\circ$, Ganymede was outside the current sheet (OCS). As described in Section 3.2.5, the yellow arrows in each panel indicate the direction to Jupiter North (J_N) and towards Jupiter (J). White numbers in the upper right corner of each image show the corresponding HST orbit number of the visit. The red lines represent the polynomial fits to the locations of the auroral ovals as described in Section 3.2.5. The color scale is limited to 240 R and each pixel with higher brightness is colored in white. We smoothed the images (see Equation 3.26) in order to increase the visibility of the auroral ovals. However, all quantitative analysis within this work is done with unsmoothed data.

Each image shows two distinct auroral ovals surrounding the northern and southern hemisphere, respectively. On the leading side, the ovals are located near to Ganymede's planetographic equator at low latitudes. On the trailing side, the ovals are located near the poles at higher latitudes. This is in full agreement with previous findings presented in Chapter 2. Along these ovals, the auroral emission is not distributed homogeneously but shows stochastic and systematic variability. The reconnection process at the open-closed field line boundary is expected to be intermittent (Eviatar et al. 2001a; Jia et al. 2010) and causes together with

the low photon counting rates stochastic variability. Hence, the auroral emission along each oval is of spotty or patchy nature rather than a continuously emitting band.

Campaigns 12244 (leading side) and 7939 (trailing side) cover a full 5.25 hour transit of Ganymede through the Jovian plasma sheet (also see Table 3). Campaign 8224 (leading side) additionally covers two orbits when Ganymede was inside the current sheet. Qualitatively, we can observe already two major characteristics of the aurora at Ganymede in the panels shown:

- 1 The change of auroral brightness with changing magnetic latitude.
- 2 The change of the location of the aurora with changing magnetic latitude.

Starting from $\vartheta_{\text{mag}} > 5$, i.e., above the current sheet, on the leading side (panels 2A, 2B and 3A, 3B) auroral brightness increases, when Ganymede is inside the current sheet ($-5 < \vartheta_{\text{mag}} < 5$, panels 2C, 3C, 4A and 4B). Simultaneously, the fitted auroral ovals move towards the planetographic equator. When Ganymede is below the current sheet, i.e., for $\vartheta_{\text{mag}} < -5$, auroral brightness decreases again and the ovals move to their previous planetographic position (panels 2D, 2E and 3D, 3E). On the trailing side, the opposite seems to be the case with decreasing brightness inside the current sheet (compare panels 1A, 1C and 1D with 1B). Also, the auroral ovals are located at inclined planetographic latitudes nearer to the poles, when Ganymede is inside the current sheet. In the subsequent sections of this chapter we examine both effects quantitatively, the variation of brightness and the moving of the auroral ovals as a function of magnetic latitude.

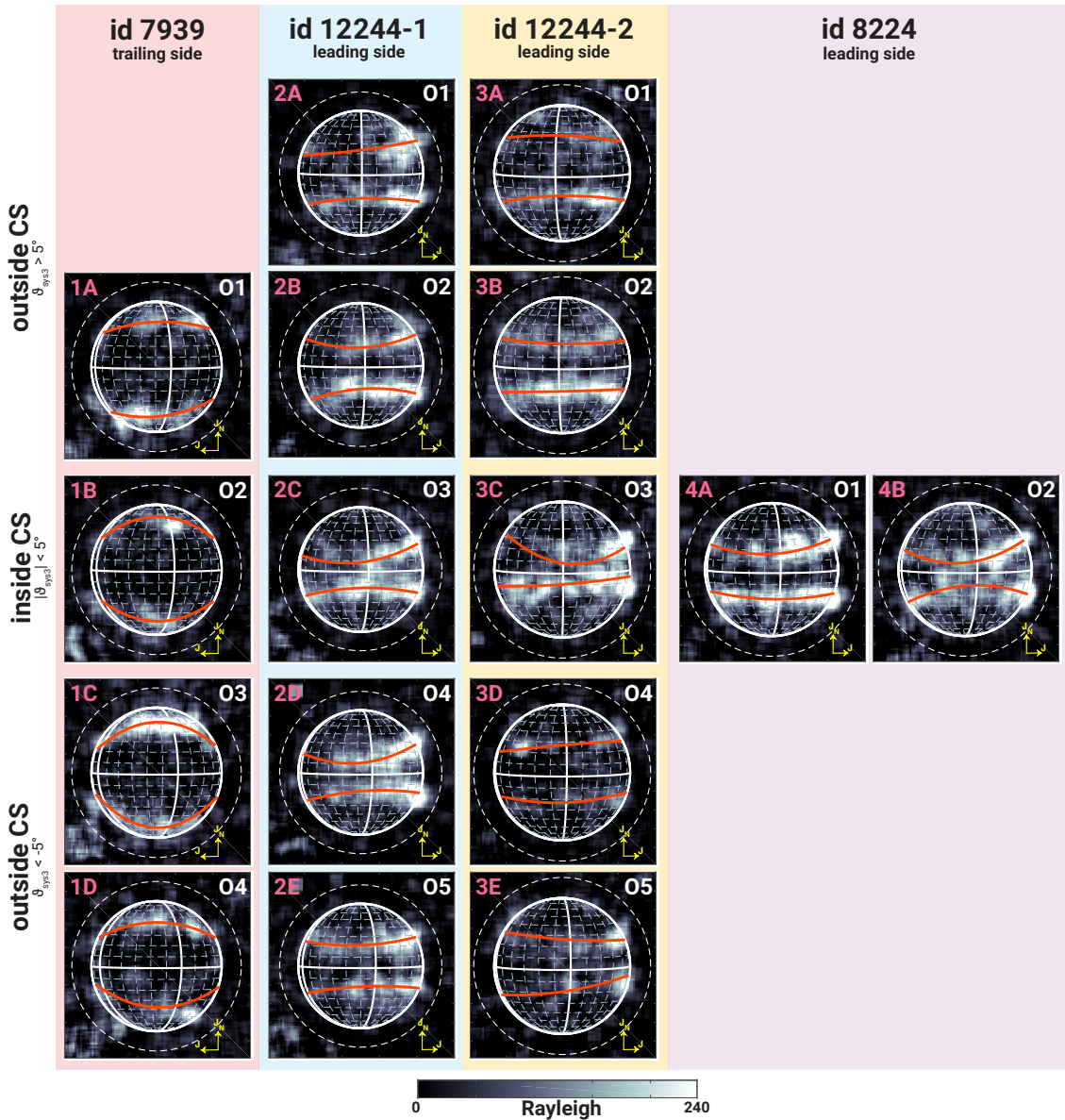


Figure 32 – Spectral images (82×82 pixels) of OI $\lambda 1356 \text{ \AA}$ oxygen emission in Rayleigh. Panels of column 1 show all orbits of campaign 7939 (1998, trailing side), panels of columns 2 and 3 show both visits of campaign 12244 (2010/2011, leading side), and panels of column 4 show the two orbits of campaign 8224 (2000, leading side). All panels are ordered from top to bottom by magnetic latitude ϑ_{mag} . Orbit numbers according to Table 3 are indicated in the right upper corner of each panel. Yellow arrows indicate the orientation of Jovian North (J_N) and direction to Jupiter (J). Red lines are polynomial fits to the auroral ovals (see Section 3.2.5). Dashed circles indicate the off-limb area. The color scale is limited to 240 R (pixels with higher brightness are white). Images are smoothed to increase the visibility of the auroral ovals.

4.3 Total disk averaged brightness

In this section, we analyze the integrated and averaged brightness for total moon disk and we describe the general distribution of aurora along the disk.

4.3.1 Hemispheric brightness asymmetries

The spectral images in Figure 32 show both, auroral emission on the disk of Ganymede and off-limb emission around that disk inside a radius of roughly $1.3 R_G$, indicated by the dashed circles in each panel. Outside the dashed circles, there are additional bright areas, mostly in the lower left corner of each image, originating from the neighboring OI $\lambda 1304 \text{ \AA}$ emission. Since there are no other known sources (so far), the origin of the off-limb emission can only be Ganymede's atmosphere itself and is, therefore, also part of the OI $\lambda 1356 \text{ \AA}$ auroral emission. In order to account for all auroral emission at 1356 \AA on the disk as well as in the off-limb area, we calculate the disk-normalized total brightness (Equation 3.35) by integrating the flux over all pixels inside the area $A = \pi(1.3 R_G)^2$. The chosen radius of $1.3 R_G$ is limited by the size of the cut-out spectral images and by the borderline to the OI $\lambda 1304 \text{ \AA}$ emission. We normalize the integrated flux to the size of the actual disk of Ganymede, i.e., to the number of pixels inside πR_G^2 similar to previous studies (e.g., Hall et al. (1998), Roth et al. (2014b) or Saur et al. (2015)). The total disk averaged brightness for each orbit of all campaigns is shown in Figure 33A as a function of magnetic latitude. Visit 1 and 2 of campaign 12244 are combined due to similar magnetic latitudinal coverage. The grey vertical dashed lines separate the observations in the current sheet (ICS) from the region of higher magnetic latitudes (OCS).

Both leading side campaigns 8224 (year 2000) and 12244 (years 2010 and 2011) are roughly 10 years apart, providing two independent temporal snapshots of Ganymede's aurora. The latitudinal coverage of campaign 8224 only allows a comparison of observations inside the current sheet. The total disk brightnesses averaged for all ICS observations, $120.5 \pm 4.0 R$ for campaign 8224 and $108.9 \pm 3.7 R$ for campaign 12244, also show no overlap (see also Figure 34). However, the two measurements alone, taken 10 years apart, are not sufficient to

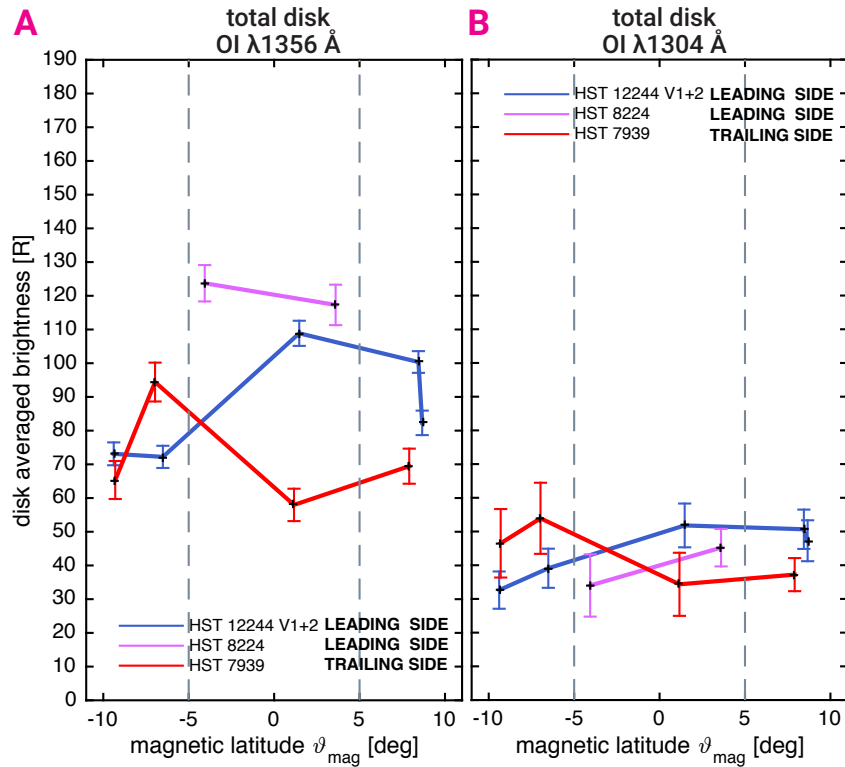


Figure 33 – Total disk averaged brightnesses of the OI $\lambda 1356 \text{ \AA}$ (A) and OI $\lambda 1304 \text{ \AA}$ (B) emission. Grey dashed lines separate the region inside (ICS) and outside the current sheet (OCS). We average the brightness by integrating over the on-disk and off-limb area (the emission inside the dashed white circles in Figure 32) and normalizing it to the size of Ganymede’s disk (solid white circles in Figure 32).

draw a clear conclusion on the long term variability of the auroral emission. Turc et al. (2014) expect energy variations of the Jovian plasma of one order of magnitude as they have been found by Paranicas et al. (2002) for Europa on time-scales for different *Galileo* flybys at Europa. In their three-dimensional test-particle model, Turc et al. (2014) study the influence of varying local plasma conditions on Ganymede’s neutral atmosphere. They find, that for a decrease of Jovian plasma energy, the sputtering on Ganymede’s icy surface decreases as well. For a weaker surface sputtering, also the amount of H_2O , H_2 and H in the atmosphere decreases (Turc et al. 2014). Hence, the production of molecular oxygen as described in Section 2.1.2 would also be affected. There exists no study yet, on how a reduced amount of oxygen in Ganymede’s atmosphere would impact the complex process of aurora generation at Ganymede. The comprehensive study of HST observations of Ganymede’s aurora by McGrath et al. (2013) gives hints for a long-term stability of auroral emission on time-scales of the HST campaigns that were analyzed by the authors (~ 10 years).

Due to the lack of latitudinal coverage of campaign 8224, we focus on campaigns 12244 and 7939 to compare the total disk averaged brightness between the leading and the trailing side. By averaging the total disk brightnesses for individual orbits of both campaigns shown in Figure 33, we see that the leading side with a mean brightness of 95.4 ± 2.1 R is by a factor of 1.42 ± 0.07 significantly brighter than the trailing side which has a mean brightness of 67.2 ± 2.9 R. A possible explanation for the observed hemispheric brightness asymmetry between the upstream and downstream side might be that more field aligned electric currents (FAC) driven in Ganymede's magnetosphere is closed in Ganymede's downstream ionosphere compared to the upstream part of the ionosphere. The high-energetic electrons, which generate the auroral emission, are approximately aligned with the magnetic field lines, which carry the FAC into Ganymede's ionosphere (Eviatar et al. (2001a), also see Section 2.2.2). Stronger ionospheric currents on the ionospheric downstream (leading) side compared to the upstream (trailing) side might, therefore, cause brighter auroral ovals on the leading side. On the other hand, the observed brighter downstream aurora does not imply that currents, which are coupled to the ionosphere and generate the aurora, are completely driven on Ganymede's magnetospheric downstream side.

For comparison, we also calculate the total disk averaged brightness for the OI $\lambda 1304$ Å emission¹, shown in Figure 33B. As discussed in Section 3.2.4 and quantitatively shown in Section 4.3.4, the OI $\lambda 1304$ Å total disk averaged brightness is two times weaker than the brightness at OI $\lambda 1356$ Å. Furthermore, the trends for changing magnetic latitudes identified in the OI $\lambda 1356$ Å emission also seem to be apparent in the OI $\lambda 1304$ Å, but they are less pronounced. The brightness slightly increases on the leading side (campaign 12244, blue line) and slightly decreases on the trailing side (campaign 7939, red line), when Ganymede is inside the current sheet. But, due to the lower SNR of the OI $\lambda 1304$ Å images compared to the OI $\lambda 1356$ Å (see Table 5), individual orbit values of the total disk averaged brightness overlap due to large errorbars, making it impossible to identify any trend as a function of magnetic latitude. Hence, we focus on the brightnesses of the OI $\lambda 1356$ Å oxygen line only.

¹The corresponding spectral images of the emission at 1304 Å are shown in Figure 50 in Appendix S4.

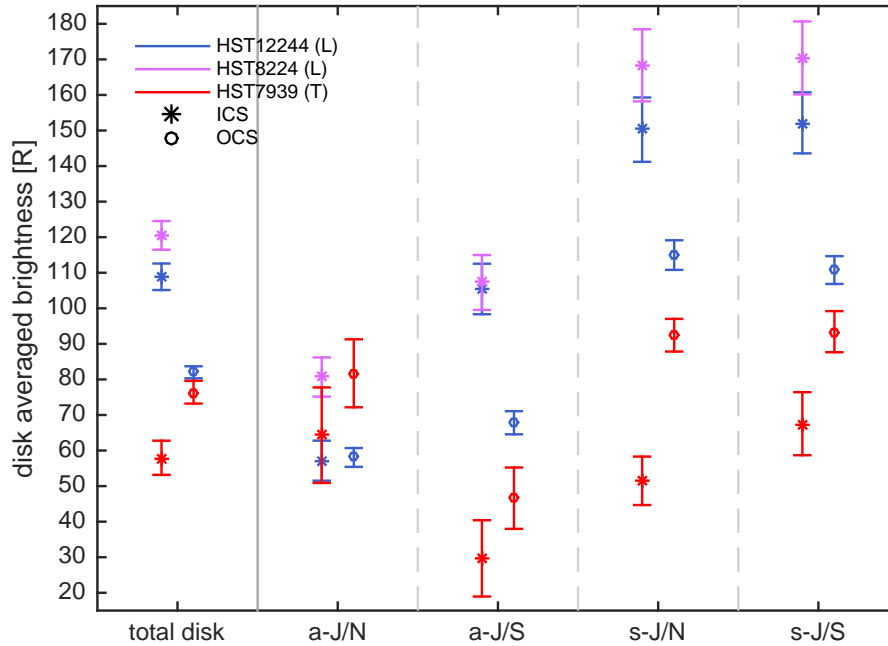


Figure 34 – Average ICS and OCS brightness for the total disk and anti-Jovian (a-J)/sub-Jovian (s-J) northern (N) and southern (S) quadrant in addition to Figure 33 and 38.

4.3.2 Magnetic latitude dependency of total disk averaged brightness

In Figure 33, we also see variability of the emission on time scales of Jupiter’s rotation period. During half a rotation period (5.25 hours), Ganymede transits different regions within the Jovian plasma sheet. During this transit on the leading side (campaign 12244), brightness is highest when Ganymede is inside the current sheet and decreases for elevated magnetic latitudes ($|\vartheta_{mag}| > 5^\circ$). Due to similar local plasma conditions at high elevated magnetic latitudes, i.e., in northern and southern direction, we bin all observations outside the current sheet (OCS) and compare them with the observations inside the current sheet (ICS) in Figure 34. Outside the current sheet (circles), the average of the total emission within the disk (*total disk* in that figure) on the leading side (campaign 12244 in blue, 82.0 ± 1.7 R) and trailing side (campaign 7939 in red, 76.4 ± 3.2 R) are relatively similar, although not identical as the errorbars do not overlap. Inside the current sheet (stars), there is a large difference between both hemispheres as the total disk averaged brightness increases by a factor of 1.33 ± 0.05 to 108.9 ± 3.7 R on the leading side, while the brightness on the trailing side decreases by a factor of 0.76 ± 0.07 to 58.0 ± 4.8 R.

The variability of the auroral emission with magnetic latitude coincides with changes of the local plasma conditions at Ganymede. We calculated the radial density and scale height profile of the Jovian magnetospheric plasma in the equatorial plane after Bagenal and Delamere (2011), shown in Figure 35A, and the radial plasma temperature profile (not shown in the figure). At Ganymede's orbit, we find a plasma density of $n_0 = 1.65 \text{ cm}^{-3}$, a scale height of $H = 10.4^\circ$ magnetic latitude (or $2.8 R_G$) and a temperature for thermal ions of $T = 390.8 \text{ eV}$. For these values, we calculate the plasma density $n(z)$ and pressure profile $P(z)$ as a function of magnetic latitude,

$$n(z) = n_0 \exp(-(z/H)^2), \quad P(z) = n(z)k_B T, \quad (4.1)$$

respectively, where k_B is Boltzmann's constant (see Appendix on page 161). Both profiles are shown in Figure 35B. By comparing values at 10° and 0° of magnetic latitude, we find a low/high altitude-ratio of 2.5 for both quantities. When Ganymede moves into the current sheet, its magnetosphere is exposed to a much larger plasma ram pressure, resulting into a higher compression of the magnetosphere on the upstream/trailing side and a broader stretching on the downstream/leading side. The effects of increased plasma pressure inside the current sheet possibly drive larger currents (also see, e.g., Jia et al. (2009a)), which likely leads to a stronger auroral emission.

The increase of total disk averaged brightness inside the current sheet is only observed on the downstream side, while the brightness on the upstream side decreases (Figure 33 and Figure 34). In Figure 32.1B, we see that the auroral ovals on the trailing side are shifted to larger planetographic latitudes inside the current sheet compared to outside of the current sheet (Figure 32.1, A, C and D). This indicates that the ovals could be partially shifted towards the downstream side when Ganymede is at the center of the current sheet and, as a result, a larger fraction of the magnetospheric current closes in the downstream ionosphere of Ganymede than in the upstream ionosphere.

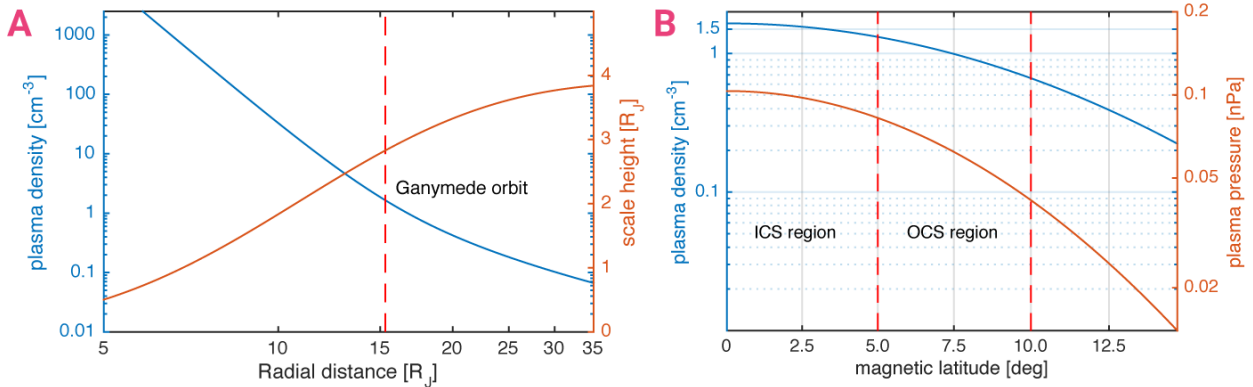


Figure 35 – Jovian magnetospheric scale height and plasma density at Ganymede.

A: Jovian plasma density and scale height as a function of radial distance (in units of Jovian radii R_J) after Bagenal and Delamere (2011). **B:** Jovian plasma density and pressure at Ganymede’s orbit. Dashed red lines in **B** separate inner current sheet region (ICS) from the outer region (OCS).

4.3.3 Off-Limb emission and comparison with the emission on the moon disk

The increase of total disk averaged brightness inside the current sheet is only observed on the leading side. Additionally to the given reasons in Section 4.3.2 for the absence of increased auroral brightness on the trailing side, we now compare the on-disk and off-limb auroral emission. As introduced in the previous section, we define the off-disk area (i.e., area between the thick solid and dashed circles in Figure 32) as the annulus from 1.0 to 1.3 R_G . The integrated and averaged brightness is shown in Figure 36A as a function of magnetic latitude ϑ_{mag} . We averaged again both visits of campaign 12244. In general, the off-limb emission is lower than the total disk averaged emission discussed in the previous section. Even though individual bright spots inside the off-disk area can reach brightnesses of up to 100 R (see Figure 32), the averaged off-limb emission ranges between 12.0 ± 4.9 R and 33.5 ± 4.6 R (minimum and maximum values from Figure 36A), which is consistent with the brightnesses derived by (Feldman et al. 2000).

We now average the off-limb emission specifically for each hemisphere. On the leading side, the average off-limb emission of all orbits outside the current sheet is with 17.8 ± 1.8 R significantly lower than inside the current sheet with 26.8 ± 2.7 R. On the trailing side, the off-limb emission is almost constant as the average off-limb emission of all orbits outside the current sheet, 25.6 ± 5.2 R, overlaps with the emission inside the current sheet, 24.9 ± 3.5 R.

The average off-limb emission over all magnetic latitudes on the leading side, 20.8 ± 1.5 R, overlaps with the overall averaged off-limb emission on the trailing side, 25.1 ± 3.0 R. Hence, there is no significant difference between the off-limb emission of the leading and trailing side. In general, the off-disk emission is independent of the observed hemisphere, since we observe the same emission just from a different point of view. However, we also compare the off-limb emission ratio for different time periods when we compare campaigns 7939 and 12244, which are 12-13 years apart. In the following, we assume only weak temporal variations of auroral brightness for each observed hemisphere on time-scales of a single decade (also see Section 4.3.1).

By comparing the off-limb emission to the emission on the disk, the decrease of auroral brightness on the trailing side inside the current sheet again becomes apparent. With exceptions, the ratio of the off-limb/on-disk emission in Figure 36B is almost constant over the observed range of magnetic latitude. The average off-limb/on-disk emission ratio on the leading side, 0.26 ± 0.05 , is lower than on the trailing, 0.48 ± 0.11 , which indicates a higher on-disk emission on the leading side compared to the trailing side. On the trailing side, there is also a significant increase of the off-limb/on-disk ratio inside the current sheet, which is consistent with the previously observed decrease of total disk brightness inside the current sheet on that hemisphere (see, e.g., Figure 33 or Figure 34).

4.3.4 Abundance of atomic and molecular oxygen in Ganymede's atmosphere from 1356/1304 Å brightness ratios

As known from laboratory tests, the ratio of the auroral brightnesses at $\text{OI } \lambda 1356 \text{ \AA}$ and $\text{OI } \lambda 1304 \text{ \AA}$ is diagnostic for the abundance of atomic and molecular oxygen in Ganymede's atmosphere (Meier 1991). In Figure 37A, we show the $\text{OI } \lambda 1356 \text{ \AA} / \text{OI } \lambda 1304 \text{ \AA}$ ratios of total disk averaged brightnesses for each orbit of the chosen HST campaigns as a function of magnetic latitude. Note that we average the ratios of the two visits of campaign 12244. The brightness ratio averaged over all orbits of each campaign is plotted as a dashed line (same color code as the campaign). The averaged ratio of 2.0 ± 0.2 for campaign 12244 (blue dashed line) and 1.7 ± 0.2 for campaign 7939 (red dashed line) indicate

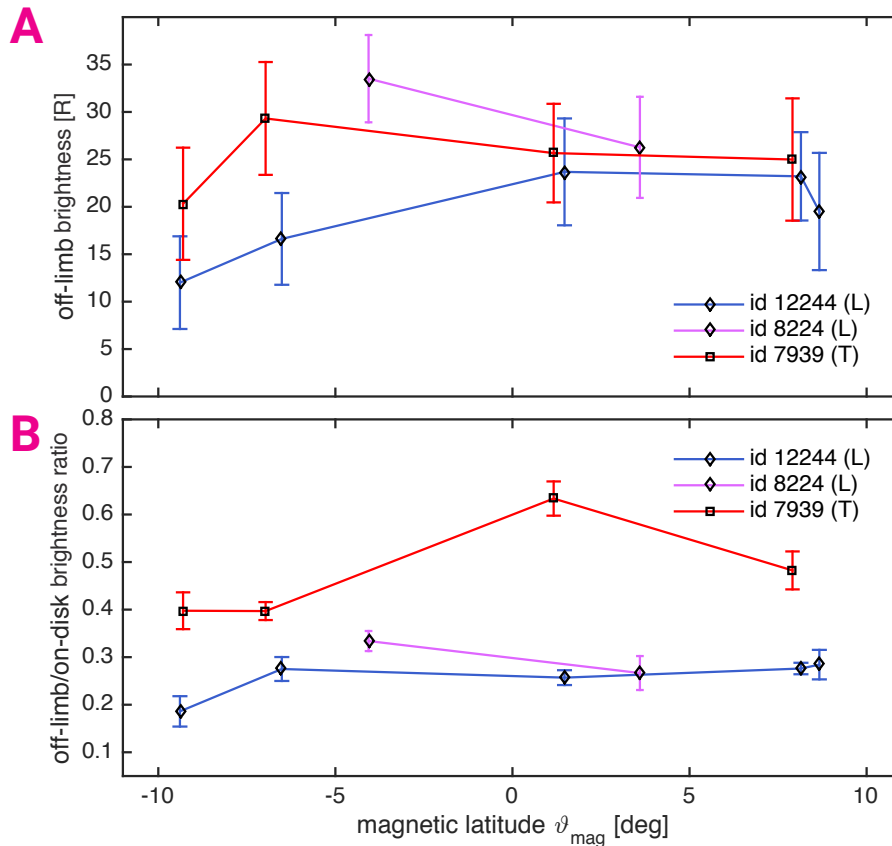


Figure 36 – Off-limb emission (A) and off-limb/on-disk brightness ratio (B).

that the abundance of molecular oxygen exceeds the abundance of atomic oxygen (Meier 1991), which is consistent with previous findings by Hall et al. (1998) and Feldman et al. (2000). The ratio for dissociative electron impact excitation of O_2 from laboratory tests is 2 (Meier 1991), which is consistent with our derived ratio. Due to the overlapping errorbars, there is no indication for an atmospheric leading/trailing side asymmetry of Ganymede’s oxygen atmosphere.

Unlike Feldman et al. (2000), who identify an orbit-to-orbit variation of the brightness ratios of campaign 7939, we do not find such an indication as the errorbars of individual orbits in Figure 37A overlap. This might be caused by a different integration method² for calculating the brightnesses at $\text{OI } \lambda 1304 \text{ \AA}$ and $\text{OI } \lambda 1356 \text{ \AA}$, by differences in the model of the reflected solar light (as discussed in Section 4.1, the derived albedo by Feldman et al. (2000) overlaps with the albedo derived by our method within the errorbars, but they are not identical), or by

²Feldman et al. (2000) do not exactly specify how they calculate the brightness ratios summarized in their table 1. We use the brightnesses integrated and averaged for the total moon disk as described in the Data Processing Section 3.2.

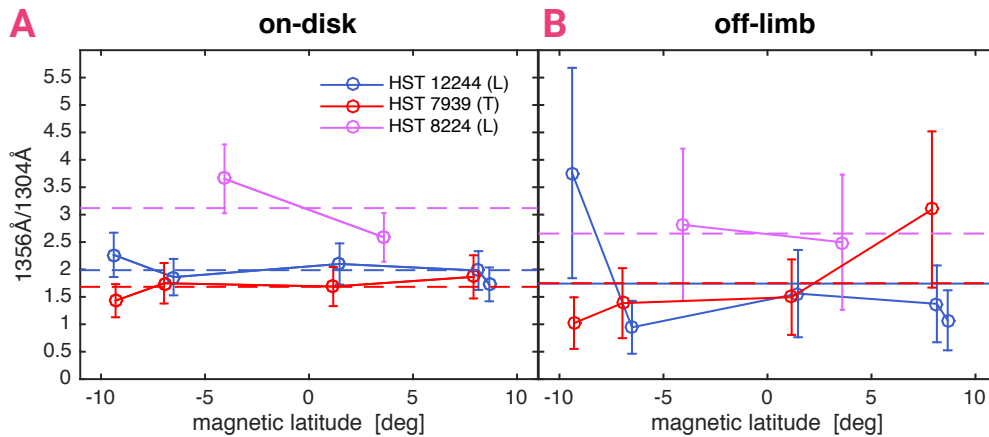


Figure 37 – OI $\lambda 1356 \text{ \AA}$ /OI $\lambda 1304 \text{ \AA}$ brightness ratio. The two visits of campaign 12244 are averaged. Dashed lines indicate the average ratio of each orbit. Panel **A** shows on-disk ratio, **B** the off-limb-ratio. Note that the average ratios of campaigns 12244 and 7939 in panel **B** overlap.

the fact, that Feldman et al. (2000) argue with the ratios calculated for individual exposures instead of their superpositions to orbits, which increases the statistical variability due to a lower SNR. However, also for campaign 12244, there are no indications for an orbit-to-orbit variability of the oxygen mixing ratio in Ganymede's atmosphere due to the overlapping errorbars. Also, in contrast to Feldman et al. (2000), who derive individual brightness ratios lower than 2 and refer this to a possible contribution from electron impact on atomic oxygen, which increases the abundance of the OI $\lambda 1304 \text{ \AA}$ emission and simultaneously reduces the OI $\lambda 1356 \text{ \AA}$ /OI $\lambda 1304 \text{ \AA}$ ratio, we cannot confirm this for both campaigns 7939 and 12244, again, due to the overlapping errorbars.

For campaign 8224, the ratio of the orbit at positive magnetic latitude overlaps with the ratios of the two other campaigns for several orbits and for their averages over all orbits. On the other hand, the orbit of campaign 8224 at negative magnetic latitude exceeds the averaged ratios with a ratio of 3.7 ± 0.5 and shifts the entire average for 8224 up to 3.1 ± 0.8 . However, the higher averaged ratio of campaign 8224 still overlaps with the averaged ratios of campaigns 7939 and 12244 within the errorbars, making it difficult to determine any temporal variation of atmospheric abundance over the period of the discussed HST campaign, i.e., from 1998 to 2011.

In order to analyze spatial variations of the brightness ratio and accordingly of the abundance of atomic and molecular oxygen in Ganymede's atmosphere, we

calculate the $\text{OI } \lambda 1356 \text{ \AA} / \text{OI } \lambda 1304 \text{ \AA}$ ratio just within the off-limb area, shown in Figure 37B, in order to compare it with the ratio on the moon disk (Figure 37A). The ratios in the off-limb area show a broader variability and larger errorbars due to the decreased SNR in the off-limb area compared to the SNR on the moon-disk. Although campaign 12244 and 7939 have nearly identical mean ratios, 1.7 ± 1.2 and 1.8 ± 0.9 , respectively, individual orbit values scatter a lot. Campaign 8224 has a mean ratio of 2.7 ± 1.7 . Due to overlapping errorbars, a variation of oxygen abundance in the off-limb area compared to the on-disk area is uncertain and cannot be determined by the available sets of HST observations alone.

4.3.5 General on-disk distribution of auroral brightness

As mentioned in Section 4.2, auroral emission in the spectral images of Figure 32 is not distributed homogeneously along the ovals but has a spot-like structure. Furthermore, some of these *spots* appear brighter than others. For example, in the spectral image in Figure 32.2A there is a concentration of bright auroral emission on the right part of the moon disk, i.e., on the Jupiter-facing side, while the other side is darker. While other images (e.g., Figure 32.2B to Figure 32.2E) show a similar distribution of brightness, for some images it is not clear which side is the predominantly brighter hemisphere. In order to systematically analyze the on-disk distribution of auroral brightness, we divide the disk into four quadrants: the northern and the southern anti- and sub-Jovian quadrant determined by the leading/trailing side central meridian and the planetographic equator. For each quadrant, we calculate the integrated and averaged brightness similar to the total disk brightness in the previous section. In Figure 38A and B, we show these brightnesses for the sub- (stars) and anti-Jovian (squares) quadrant in the northern (solid lines) and southern hemisphere (dashed lines). The two leading side campaigns are plotted together in A, the trailing side campaign in B.

First, we average both sub-Jovian as well as both anti-Jovian quadrants in order to compare the brightness between the two hemispheres. On the leading side, the sub-Jovian hemisphere ($128.7 \pm 2.5 \text{ R}$) is 1.81 ± 0.06 times brighter than the anti-Jovian hemisphere ($71.2 \pm 1.8 \text{ R}$) calculated as an average over all campaigns and over all magnetic latitudes. On the trailing side, the sub-Jovian

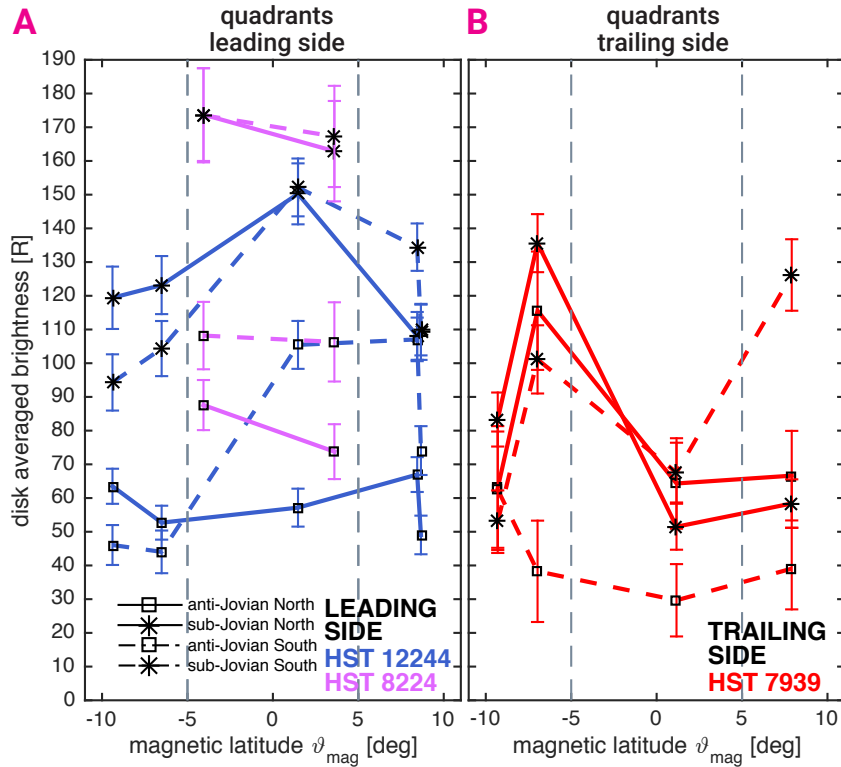


Figure 38 – Averaged brightnesses of OI $\lambda 1356$ emission \AA emission for individual quadrants on the moon disk on the leading side (A) and trailing side (B), as a function of magnetic latitude φ_{mag} (similar to Figure 33). Dashed grey lines separate the region inside (ICS) and outside the current sheet (OCS).

hemisphere (84.6 ± 3.1 R) is 1.41 ± 0.14 times brighter than the anti-Jovian hemisphere (59.9 ± 5.3 R). We note that during campaign 7939, Ganymede was not observed at maximum western elongation but between $\sim 290^\circ$ and $\sim 300^\circ$ (Table 3). Thus, a fraction of the leading side was visible and a fraction of the trailing side was blocked to the view of HST which might slightly bias the result for the trailing side. However, McGrath et al. (2013) also identify the Jupiter-facing hemisphere to be the brighter one which is consistent with our findings.

Besides this hemispheric variability there are also differences in brightness between individual quadrants. On the leading side in campaign 12244 (Figure 38A), both sub-Jovian quadrants and the southern anti-Jovian quadrant show variable auroral brightness as a function of Ganymede's magnetic latitude. These quadrants follow the trend of increased brightness inside the current sheet compared to the average of observations at higher magnetic latitudes. The northern anti-Jovian quadrant with a mean brightness of 57.9 ± 2.4 R is the darkest quadrant on the leading side. This quadrant has also the lowest variability during Gany-

mede's transit through the current sheet and the brightness is nearly constant within the errorbars. Similar to the total disk brightness in Section 4.3.2, we average all observations inside and outside the current sheet separately, shown in Figure 34 for individual quadrants (anti-Jovian (a- J)/sub-Jovian (s-J) northern (N) and southern (S) quadrant). Nearly all quadrants of campaign 12244 vary significantly with Ganymede's magnetic latitude and have increased brightness in the current sheet. Only the northern anti-Jovian quadrant again shows no variation and simultaneously has the lowest emission. It is also the northern anti-Jovian quadrant in campaign 8224 with the lowest brightness (see Figure 38A and Figure 34). The other three quadrants are comparable to the observations of campaign 12244 inside the current sheet, which implies that there was no significant temporal change between the observations. The individual quadrants of campaign 7939 repeat the total disk trend of a decreased brightness inside the current sheet on the trailing side (Figure 38B). Here, it is the southern anti-Jovian quadrant with the lowest average brightness of 42.4 ± 7.0 R and less latitudinal variation compared to the other quadrants. A comparison of the averaged brightnesses in Figure 34 shows, that inside the current sheet, the brightness of this quadrant is also the lowest one among all quadrants of all campaigns.

The observed variability of Ganymede's auroral emission occurs on various time scales and has different reasons. The time scales between the observations, i.e., from one HST visit to another, are months or years (see Table 3). Due to variability in the Jovian magnetosphere on these time scales (see, e.g., Bagenal and Delamere (2011); Frank and Paterson (2000)), auroral emission might vary from each visit to another (compare the two leading side campaigns in Figure 33). At Europa, for example, Roth et al. (2016) detect a significant brighter aurora in 1999 than between 2012 and 2015.

The time scales within a visit, i.e., from one HST orbit to another, are hours. Apart from changing local plasma and magnetic conditions during one current sheet transit of Ganymede, variability within one visit can also be caused by intermittent reconnection causing stochastic orbit-to-orbit variability. From Figure 38, A and B, we see variability between observations at low and high magnetic latitudes, i.e., auroral brightness before and after passing through the current sheet is not always the same. This is for example the case for the southern sub-Jovian quadrant of campaign 12244.

The reasons for the observed spatial brightness asymmetries are not clear. Local anomalies induced by inhomogeneities in Ganymede's icy surface might cause the atmosphere to be asymmetric which could be one reason for the observed emission inhomogeneity. The brightness asymmetry between the sub- and anti-Jovian side might also be explained by an asymmetric interaction due to the ionospheric Hall effect as suggested for Io (Saur et al. 1999, 2000). Dorelli et al. (2015) recently showed in their Hall magnetohydrodynamics (MHD) simulations for Ganymede that the Hall effect in the magnetospheric plasma causes both, significant asymmetries in the plasma convection as well as in the patterns of field aligned currents. They find that the Jovian magnetospheric plasma predominantly flows around the sub-Jovian flank on its way into Ganymede's wake region, which generates a new FAC system. This new FAC system peaks right at the sub- and anti-Jovian flanks of the open-closed field line boundary on the upstream as well as on the downstream side.

4.4 Latitudinal distribution of auroral brightness

In the previous Section 4.3, we studied the morphology and brightness of the aurora by calculating the brightness averages for the total disk or individual quadrants. In order to better understand the spatial structure of the auroral distribution, we integrate the auroral disk brightness as a function of planetographic latitude. We now bin the moon disk into 60 latitudinal anuli with equal width of $\Delta\vartheta = 3^\circ$. The resolution of the chosen binning ensures an adequate SNR for the latitudinal regions where the main auroral emission is located. We calculate the SNR according to Equation 3.32 for each anulus and campaign, shown in the SNR maps of Figure 39. The upper image of each panel in that figure shows the two-dimensional representation of the latitudinal anuli, color coded according to the SNR of each anulus. The lower panel shows the SNR of each anulus as a function of the latitudinal bins ϑ_{bin} with $\text{bin} = 1, 2, 3, \dots, 60$. On the trailing side (Figure 39A), the anuli at elevated latitudes around $|\vartheta| = 45^\circ$ have an $\text{SNR} \gg 1$. This latitudinal region coincides with the expected location of the ovals on that hemisphere (compare, e.g., with panels 1, A to D in Figure 32). The SNR decreases

towards lower latitudes and especially towards the poles. The decrease of SNR around the planetographic equator is due to the weaker signal at low planetographic latitudes on the trailing side. At the poles, the anuli bins become very small as the size of an annulus decreases in width and height with increasing planetographic latitude ϑ . Hence, with our applied integration method we are not able to detect an adequate amount of photon counts in the bins near to the poles and the SNR becomes virtually zero. On the leading side (Figure 39, B and C), the anuli with an SNR $\gg 1$ are located around the planetographic equator which again coincides with the expected location of the ovals on this hemisphere (compare, e.g., with panels 2,A to E in Figure 32). Again, the SNR decreases towards the poles.

We integrate the brightness $I(\vartheta_{\text{bin}})$ inside each annulus bin³ ϑ_{bin} . Similar to the previous sections, we normalize the brightness of each annulus by the number of pixels inside each bin. Hence, we rather calculate the disk brightness than a surface brightness. E.g., the integration of $I(\vartheta_{\text{bin}})$ over all ϑ_{bin} reproduces the total disk averaged brightnesses I_{tot} ,

$$I_{\text{tot}} = \frac{2}{\pi} \int_{-\pi/2}^{\pi/2} I(\vartheta_{\text{bin}}) \cos^2(\vartheta_{\text{bin}}) d\vartheta_{\text{bin}}. \quad (4.2)$$

Note that I_{tot} accounts for the averaged total disk brightness integrated only for the pure moon disk without the off-disk area since the latitude anuli only cover the on-disk parts. For instance, we calculate the total averaged disk brightness by integrating over the moon disk only for each campaign and show in Figure 51 (in Appendix S5) the resulting I_{tot} (solid lines in that figure) together with I_{tot} derived by Equation 4.2 (dashed lines with circles). I_{tot} derived by both integration methods overlap with small discrepancies which are caused by difficulties of the sub-pixel division method introduced in Section 3.2.7 for very small and/or curvy integration areas close to the poles.

From Equation 4.2 we see, that the contribution $I(\vartheta_{\text{bin}})$ of each annulus to the total disk averaged brightness I_{tot} decreases as a function of planetographic latitu-

³Note that ϑ_{bin} with bin=1, 2, 3, ..., 60 has only discrete values ranging from -90° to $+90^\circ$ with a step-size of 3° .

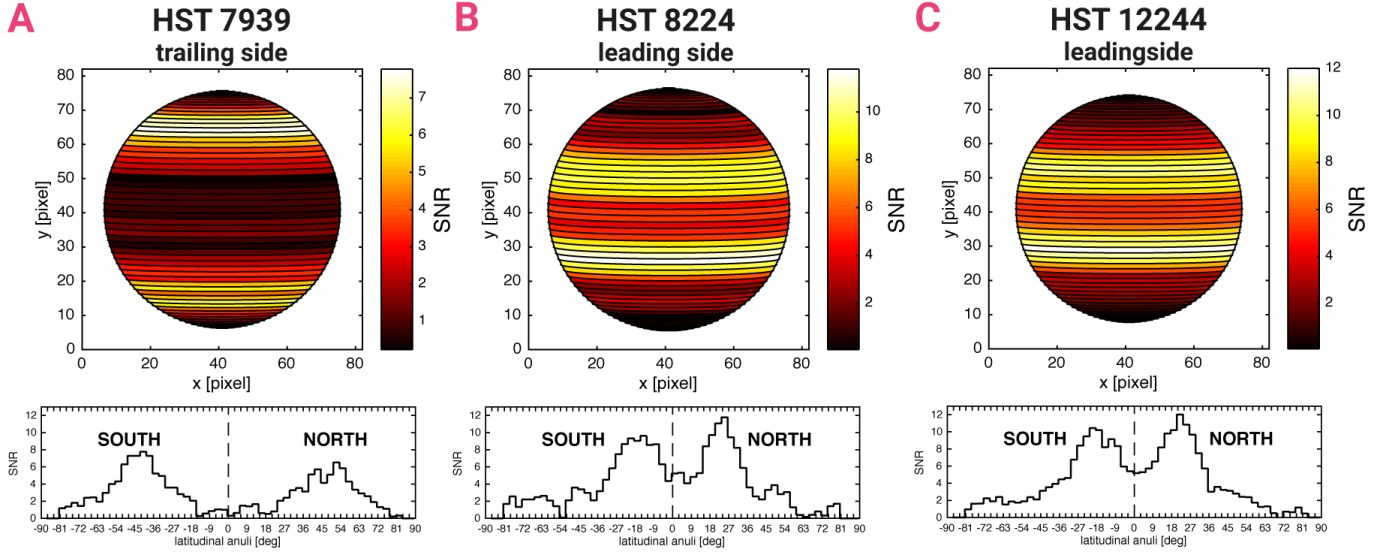


Figure 39 – SNR maps of the latitude anuli. Upper image of each panel shows a two-dimensional representation of the anuli on the disk, color coded according to their SNR. The lower images show the SNR as a function of the planetographic latitudinal bins.

de ϑ_{bin} . Therefore, high latitudinal bins contribute less to the total disk averaged brightness I_{tot} than the emission at more equatorial latitudes.

The averaged brightness of each latitudinal anulus is shown in Figure 40 as a function of planetographic latitude for each campaign and visit. We calculate the anuli brightnesses for the superposition of all orbits, when Ganymede was inside the current sheet (ICS, upper panels in Figure 40) and outside the current sheet (OCS, lower panels). The auroral ovals are represented by the two clearly distinguishable peaks in each panel. In order to determine these brightness peaks quantitatively, we fit a Gaussian function $G_{\mu,\sigma}(\vartheta)$ to the data in the northern and southern hemisphere,

$$G_{\mu,\sigma}(\vartheta) = \frac{1}{\sqrt{2\pi}\sigma} e^{-((\vartheta-\mu)^2/2\sigma^2)}, \quad (4.3)$$

where the location of the maximum, μ , and the width of the function, σ , are the two fit parameters. The resulting values are listed in Table 7, each for the northern and southern ovals, separated into ICS and OCS observations. The corresponding fitted $G_{\mu,\sigma}(\vartheta)$ are plotted as solid black curves (ϑ) in the panels of Figure 40. In the following sections, we analyze the overall latitudinal distribution of auroral

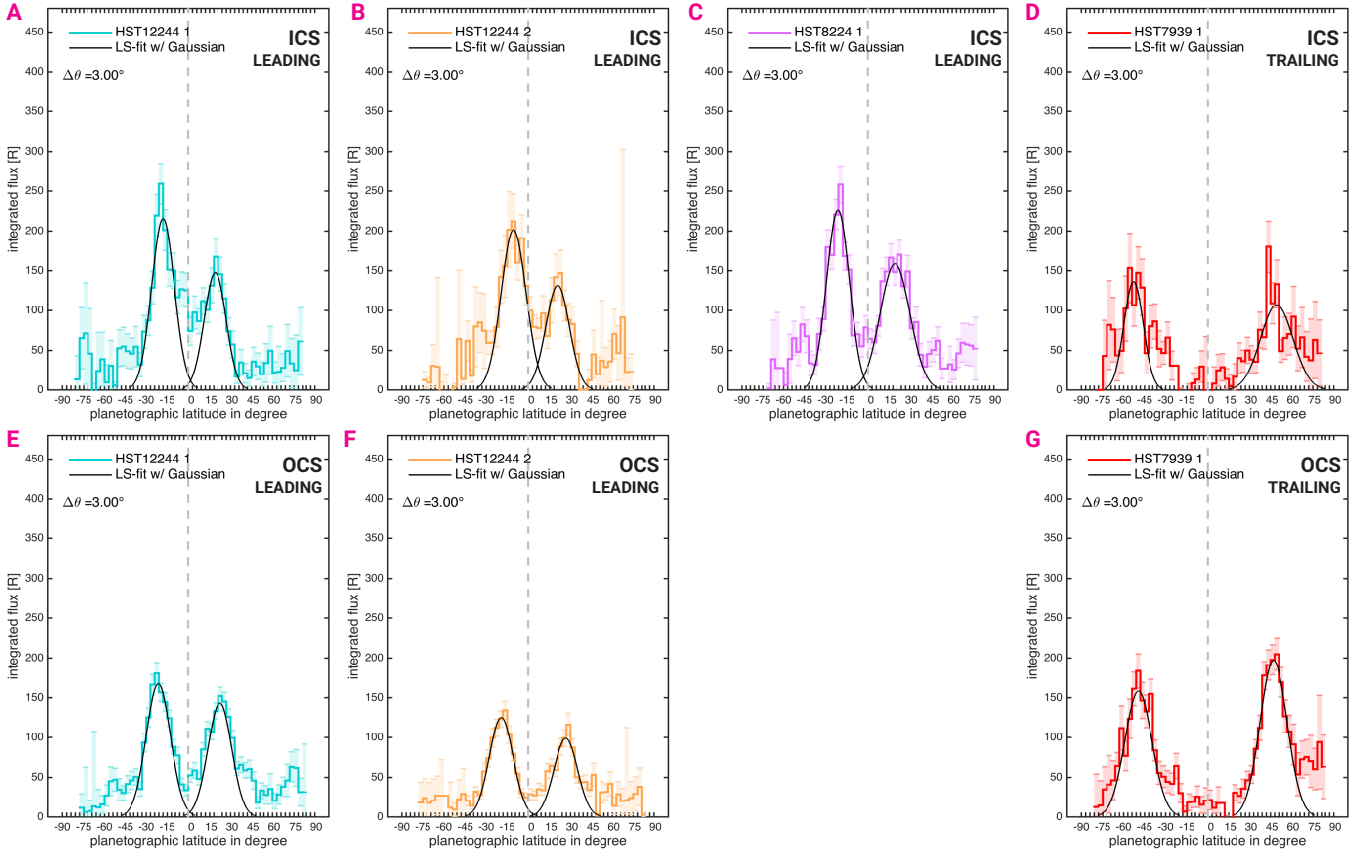


Figure 40 – Latitudinal anuli-averaged OI $\lambda 1356$ brightness. The average of each latitudinal anulus of width 3° is plotted as a function of planetographic latitude ϑ . The equator is indicated by the dashed grey line. Top panels **A** to **D** show averaged brightness when Ganymede is in the current sheet (ICS), bottom panels **E** to **G** when Ganymede is outside that region (OCS). Note that for campaign 8224, no OCS data are available. A least squares fit with a Gaussian function is provided for the two auroral oval peaks for each campaign (black line).

emission, i.e., we first separate pure auroral oval from residual auroral emission, and, then, study the brightness and morphology in detail.

Table 7 – Resultant location of the maximum, μ , and width, σ , of the fitted Gaussian function in Figure 40. All values are given in the unit of planetographic latitude.

		id 12244-1	id 12244-2	id 8224	id 7939
		μ/σ [°]	μ/σ [°]	μ/σ [°]	μ/σ [°]
ICS	northern oval	20.5 / 7.7	22.2 / 8.4	20.9 / 10.7	51.0 / 11.6
	southern oval	16.5 / 8.1	8.9 / 8.9	19.8 / 8.0	51.3 / 7.0
OCS	northern oval	23.8 / 8.5	28.0 / 8.5	-	48.7 / 9.7
	southern oval	19.9 / 8.8	17.8 / 8.6	-	47.8 / 9.8

4.4.1 Separating oval and rest-disk emission

The resulting Gaussian functions $G_{\mu,\sigma}(\vartheta)$ give a good fit of the observed brightness peaks in Figure 40. Fitting a Gaussian function to the auroral brightness peaks therefore provides an appropriate approximation for phenomenologically describing the brightness distribution shown in Figure 40. This allows us to quantitatively distinguish between auroral emission originating from the ovals and emission from the rest of the disk. Hence, we now distinguish between the two individual ovals and separate their emission from the residual disk emission by integrating the emission under the fitted Gaussian curves. The integration area of each oval is determined by taking thrice the width σ around the fitted μ from Table 7 which ensures a coverage of approximately 99.7% of the area under the fitted Gaussian curves (Bevington and Robinson 2003), which we account to the oval emission. We calculate the residual disk brightness by subtracting the brightness of the emission determined by the Gauss fits for the two ovals from the total disk brightness. In order to study brightness variations between these different disk parts, we show in Figure 41 the integrated brightnesses of the northern (right tick, **N**) and southern oval (left tick, **S**) together with the average between both (middle tick, **Av**) for each campaign. The residual disk brightness is shown in the grey area. In order to study brightness variations as a function of Ganymede's varying magnetic latitude, we distinguish again between observations inside (ICS, solid lines and stars) and outside the current sheet (OCS, dashed lines and circles).

Comparing the residual disk brightness with the brightnesses of the northern and southern ovals, we see that the auroral ovals are indeed the main contributor to the total disk averaged brightness as their average brightness is by a higher factor of 2.7 ± 0.2 to 5.9 ± 0.7 than the residual disk emission. Even though for the residual disk area the uncertainties are high due to the lower SNR in this dim area (see Figure 39), the high brightness contrast compared to the average oval brightness for each campaign is far beyond their errorbars.

The increase of brightness on the leading side within the total disk and within the quadrants for low magnetic latitudes discussed in Section 4.3 and shown in Figure 33 and 34 is also reflected in Figure 41 when we compare the averages between the northern and southern ovals (**Av**) for ICS and OCS data.

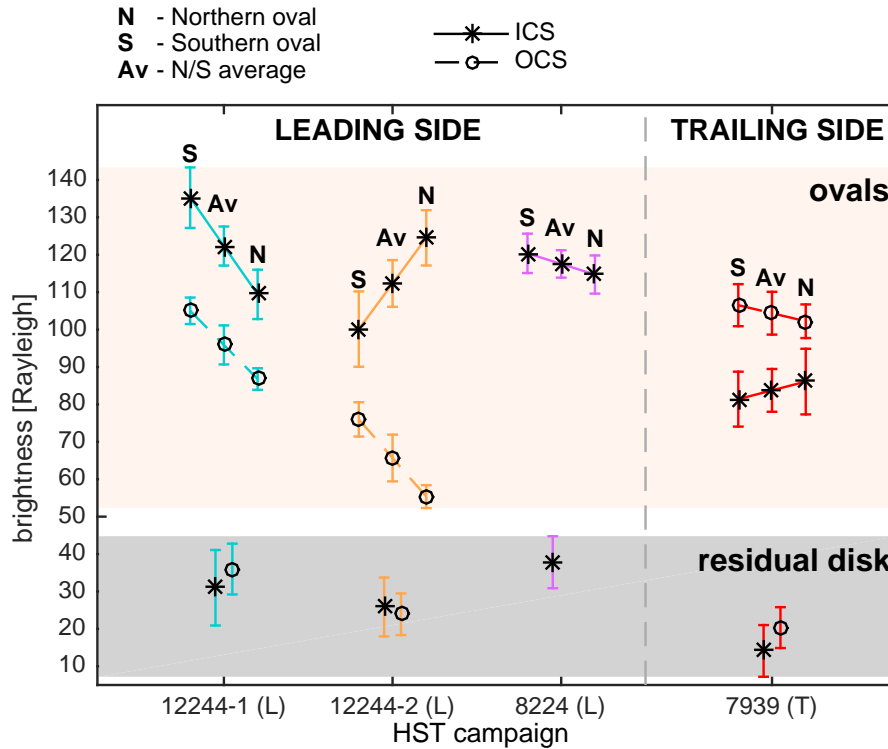


Figure 41 – Auroral brightness distinguished between oval and residual disk emission for each HST campaign. In the light red area, average auroral brightness for the southern oval (left tick, **S**), the northern oval (right tick, **N**) and the average between both (middle tick, **Av**) of each campaign are compared between observations inside (ICS, stars) and outside the current sheet (OCS, circles). Residual disk brightness is indicated by the grey area. (L) and (T) denote whether the leading or trailing side was observed.

The average north/south oval brightness is increased inside the current sheet (117.4 ± 1.1 R, average oval emission for all leading side visits) compared to outside the current sheet (80.8 ± 0.9 R). As already shown for the total disk averaged emission in Section 4.3.1, the average north/south oval brightnesses of the two leading side campaigns are again almost identical, i.e., there is no significant brightness variation from 2000 (campaign 8224) to 2010/2011 (campaign 12244). The average north/south oval brightness on the trailing side repeats the trend of decreased brightness inside the current sheet, i.e., the northern and southern oval are brighter outside (on average 104.4 ± 1.6 R) than inside the current sheet (83.8 ± 2.0 R). Inside the current sheet, the leading side ovals are on average 1.40 ± 0.04 times brighter than on the trailing side, while outside the current sheet, in contrast, the trailing side ovals are 1.29 ± 0.02 times brighter than on the leading side. To quantify how dynamically the brightness of the ovals changes during Ganymede's transit through the current sheet, we calculate the

ratio between the average oval emission inside and outside the current sheet on the leading and trailing side, respectively. We find that the average brightness of the auroral ovals on the leading side increases by a factor of 1.45 ± 0.02 and decreases on the trailing side by a factor of 0.80 ± 0.02 when Ganymede transits into the current sheet.

The residual disk brightness varies between 14.1 ± 6.9 R and 37.8 ± 6.9 R with an average of 27.0 ± 1.9 R. Unlike for the oval emission, we cannot determine with certainty a variability of the residual disk brightness between the observations inside and outside the current sheet due to overlapping errorbars. The errorbars even overlap among all campaigns and the residual disk brightness is only weakly time-variable. The dimmer residual disk brightness on the trailing side mainly originates from the inter-oval region below planetographic latitudes $|\vartheta| < 30^\circ$ (see Figure 40, D and G). This region is connected to closed field lines of Ganymede's magnetic field, where measurements of the *Energetic Particles Detector (EPD)* on-board the *Galileo* spacecraft revealed the existence of trapped energetic ions (Williams et al. 1997; Williams et al. 1997; Williams 2001; Kivelson et al. 1998). On the leading side, the residual disk brightness mainly originates from Ganymede's mid-latitude regions above $|\vartheta| > 30^\circ$ (see Figure 40, A to C, and E to F). This is the region of open field lines, which have one end on Ganymede and the other in Jupiter's ionosphere (Kivelson et al. 2004). Energetic electrons are trapped on these open field lines and bounce between the mirror-points of Jupiter and Ganymede (Williams et al. 1998). It has not been sufficiently investigated yet if and to what extent trapped particles inside Ganymede's magnetosphere or on open field lines co-contribute to the generation of auroral emission besides the most-likely acceleration process for the main ovals as described by Eviatar et al. (2001a). On the other hand, Eviatar et al. (2001a) and Eviatar et al. (2001b) calculate, that without the additional acceleration mechanism by FAC along the OCFB as described in Section 2.2.2, local thermal electrons are indeed energetic enough to create a continuous aurora with a steady background emission of ~ 20 R. This suggested background emission fits into the range of the rest-disk emission we find.

4.4.2 Brightness synchronicity between the northern and southern oval

From Figure 41 we see that the brightnesses of the ovals in some cases show a north-south asymmetry. Outside the current sheet, this is the case for both visits of campaign 12244, where the southern oval is significantly brighter than the northern oval. When Ganymede is inside the current sheet, the ovals of visit 2 of campaign 12244 show asynchronous behavior as the brightness of the northern oval increases and becomes the brightest one. This is not reflected by visit 1 of campaign 12244, where the brightness of the ovals increase synchronously inside the current sheet and the southern oval remains the brightest one. Due to the lack of observations outside the current sheet during campaign 8224 and due to overlapping errorbars in campaign 7939, a systematic behavior cannot be derived.

4.4.3 Location of the auroral ovals

We see qualitatively from the brightness peaks in Figure 40 and quantitatively from the derived σ in Table 7, that the width of each oval does not vary much and lies around $\sigma \approx 9^\circ$ planetographic latitude. In contrast, the fitted locations of the maximum of auroral oval brightness (the μ in Table 7) show variations depending on Ganymede's magnetic latitude. On the leading side, the auroral ovals are closer to the planetographic equator inside the current sheet (compare Figure 40, A to E, and B to F). There is also an increase of brightness around the planetographic equator between the northern and southern oval, when Ganymede transits into the current sheet, making the ovals less distinguishable from each other (see, e.g., Figure 40B). On average on the leading side, the northern oval moves from $25.9^\circ \pm 0.6^\circ$ down (i.e., equatorward) to $21.2^\circ \pm 0.5^\circ$ planetographic latitude, while the southern oval moves from $-18.8^\circ \pm 0.4^\circ$ to $-15.1^\circ \pm 0.4^\circ$. On the trailing side (compare Figure 40, D and G), the opposite is the case and the ovals are located closer to the poles inside the current sheet. On average, the northern and southern oval nearly synchronously shift up (i.e., poleward) from $\pm(47.9^\circ \pm 1.0^\circ)$ to $\pm(51.3^\circ \pm 1.3^\circ)$. The mean oval movement on the leading side is slightly higher with $4.2^\circ \pm 0.2^\circ$ than on the trailing side with $2.9^\circ \pm 0.7^\circ$.

As mentioned in Section 4.2, the auroral emission shows a patchy structure, i.e., the emission pattern is rather that of a spot-like structure along the ovals than being a continuous emitting ribbon. At the flanks of the observed disks in Figure 32, the auroral spots show increased brightness and shift up to higher planetographic latitudes on the leading side compared to the emission at the disk center. On the trailing side, the opposite is the case as the spots at the flanks shift towards lower latitudes compared to the spots around the leading/trailing side central meridian. In general, the locations of the ovals are not expected to lie along constant planetographic latitudes due to the plasma interaction and due to Ganymede's inclined field (see, e.g., McGrath et al. (2013), Saur et al. (2015, figure 9), or Figure 10). Hence, the average oval position calculated by averaging along all planetographic longitudes as applied by fitting the Gaussian function to the peaks in Figure 40 (and generating the results shown in Table 7) is biased by these bright and up and down shifted spots. To avoid this effect, we further separate the anuli into three longitudinal regions:

- a mid-region defined by $\pm 25^\circ$ around the leading/trailing side central-meridian, i.e., $\lambda = 90^\circ$ and 270° planetographic longitude, respectively,

and from the remaining left and right disk parts, respectively,

- the sub-Jovian and
- the anti-Jovian part.

As the classification of the sub- and anti-Jovian side depends on the observed he-

Table 8 – Classification of the longitudinal bins introduced in Section 4.4.3 for each campaign. Values in brackets show the center longitude of each bin.

ID	left bin 0°-65° (32.5°)	mid-bin 65°-115° (90°)	right bin 115°-180° (147.5°)	left bin 180°-245° (212.5°)	mid-bin 245°-295° (270°)	right bin 295°-360° (327.5°)
12244-1	sub-Jovian	mid-region	anti-Jovian	-	-	-
12244-2	sub-Jovian	mid-region	anti-Jovian	-	-	-
8224	sub-Jovian	mid-region	anti-Jovian	-	-	-
7939	-	-	-	anti-Jovian	mid-region	sub-Jovian

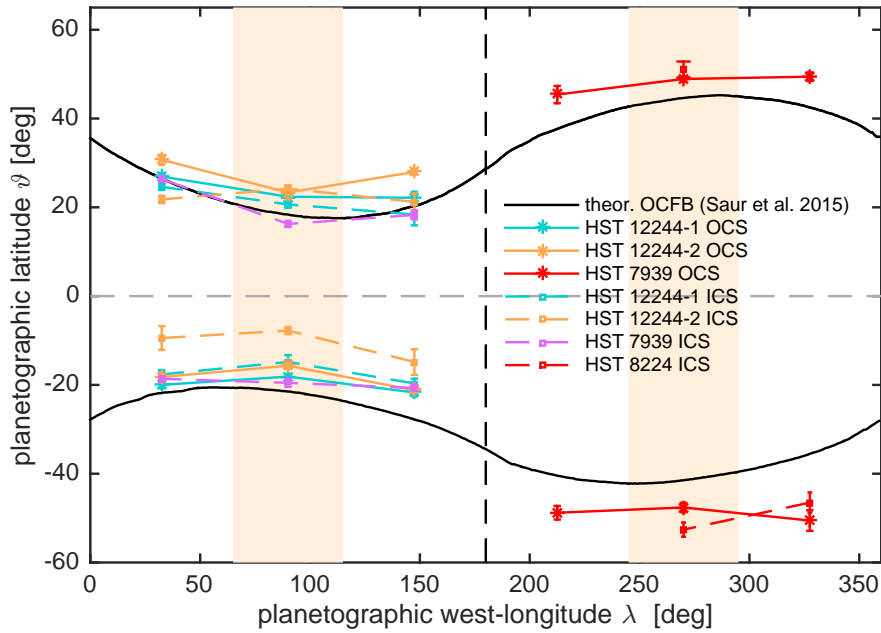


Figure 42 – Average oval locations as a function of planetographic west-longitude with 0° pointing towards Jupiter. Shown are the locations of the northern and southern ovals for three different longitudinal disk-regions: the anti- and sub-Jovian side and a mid-region around the trailing/leading side center-meridian (i.e., $\lambda = 90^\circ$ or 270°). Shaded areas indicate the longitudinal extent of each region. For the OCS region the theoretical oval locations, i.e., the intersection-line between the OCFB and Ganymede’s surface from Saur et al. (2015) are plotted as a solid black line.

misphere, we show for clarification the classification of the longitudinal disk parts for each campaign in Table 8. Again, we fit the location of the peak emissions by a Gaussian function to the latitudinal anuli integrated brightnesses for each longitudinal region. The resulting peak locations μ and oval widths σ are summarized in Table 11 in Appendix S6 and plotted in Figure 42. In that figure, the resulting peak locations are plotted as a function of planetographic west-longitude λ . The orange shaded areas indicate the extent of the mid-longitudinal region and the dashed black line separates the leading ($\lambda = 0^\circ$ to 180°) from the trailing side ($\lambda = 180^\circ$ to 360°). Simultaneously, the dashed black line marks the central anti-Jovian meridian, while $\lambda = 0^\circ$ and $\lambda = 360^\circ$ mark the sub-Jovian meridian. ICS observations are plotted with squares and dashed lines, OCS observations with stars and solid lines. Please note that we were not able to fit the location of the ovals for every longitudinal region due to a too low SNR in the specific regions. This is the case for the anti- and sub-Jovian region of the northern oval and the anti-Jovian region of the southern oval inside the current sheet of campaign 7939.

To analyze how the fitted location of the ovals correspond to the theoretical locati-

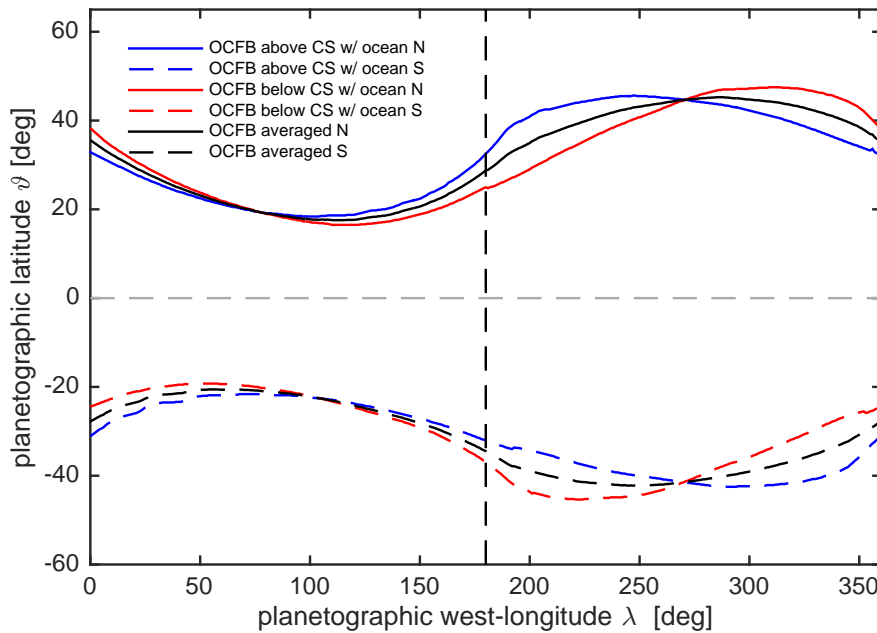


Figure 43 – Theoretical locations of the OCFB from Saur et al. (2015). Blue lines show the OCFB on the northern and southern hemisphere (solid and dashed lines, respectively), when Ganymede is above the current sheet. The red lines show the OCFB, when Ganymede is below the current sheet. The black lines are the averages between both magnetic latitudes, which approximately averages out the effects of induction in the subsurface ocean.

on of the open-closed field lines boundary (OCFB), we compare them with calculated OCFBs from the MHD model results shown in figure 9 in Saur et al. (2015), who used the MHD model introduced in Duling et al. (2014). The MHD model includes Ganymede’s internal dynamo field which is tilted by 176° with the dipole axis rotated by -24° planetographic west-longitude in the southern hemisphere (Kivelson et al. 2002). It includes plasma interaction with the Jovian magnetosphere and induction in a conductive subsurface ocean located between 150 km to 250 km depth. The resultant locations of the OCFBs are shown in Figure 43, when Ganymede is above (blue lines) and below the current sheet (red lines) for the northern (solid lines) and southern hemisphere (dashed lines), respectively. For further analysis and comparison with our observations, we average out the time variability of the orientation of Jupiter’s magnetospheric field by averaging the OCFBs for the two different magnetic latitudes on each hemisphere (black lines). We show the averaged OCFB from the model calculations also in Figure 42 as the black solid line in the northern and southern hemisphere.

We now compare in Figure 42 our fitted oval locations to the theoretical locations

predicted by the averaged model OCFB. The positions of the ovals in all three longitudinal regions are similar to the theoretically expected OCFB locations, i.e., they lie at low latitudes around $\pm 20^\circ$ on the leading side and at high latitudes around $\pm 50^\circ$ on the trailing side. The ovals' positions are in general agreement with the upstream-downstream asymmetries predicted from the numerical models by Jia et al. (2008, 2009a) and Saur et al. (2015) (also see Section 2.2.2 and Figure 10). For campaign 8224, the consistency of the observed locations of the auroral ovals and the locations of the OCFB from the MHD model of Jia et al. (2008, 2009a) has been shown previously in McGrath et al. (2013). On the leading side, the ovals in the mid-longitudinal region tend to be located at lower latitudes than in the other two longitudinal regions, while on the sub-Jovian side they are slightly at higher latitudes than on the anti-Jovian side. This trend is also predicted by the theoretical OCFB. On the trailing side, not all observations follow the prediction of the theoretical OCFB. A key reason for the discrepancy is that the locations of the ovals depend on the upstream plasma pressure at Ganymede (Saur et al. 2015). The plasma pressures are unknown for the time intervals when the HST observations were taken. The theoretical curve in Figure 42 only represents the expected location for one possible set of upstream plasma conditions, representing a case when Ganymede is outside of the current sheet. Additionally, it is not clear whether the location of the auroral ovals corresponds exactly to the location of the OCFB intersection with Ganymede's atmosphere. At Earth, for example, discrepancies are also observed between the location of observed UV auroral oval emission and the boundaries of electron precipitation (Eviatar et al. 2001a; McGrath et al. 2013).

In Figure 42, also the shift of the auroral ovals as a function of Ganymede's magnetic latitude becomes even more apparent in all three longitudinal regions. On the trailing side, the ovals are pushed towards higher latitudes into the polar region, when Ganymede is inside the current sheet. At the same time on the leading side, the southern ovals are located near the planetographic equator for all longitudinal regions, while the northern ovals show nearly no variation. The largest variation shows visit 2 of campaign 12244 where the southern oval has the smallest distance to the equator among all observations inside the current sheet.

Overall, we see that the northern and southern oval are not symmetrically aligned with respect to the planetographic equator. Hence, we further study the oval

symmetries in the following section.

4.4.4 Symmetry study of the northern and southern oval

As the location of the auroral ovals primarily depends on the local magnetic environment, we now further analyze the symmetry between the ovals with respect to Ganymede's magnetic equator. We first analyze the general symmetry of the theoretical OCFB between the northern and southern hemisphere. The varying strength of the local plasma interaction causes the ovals to shift up and down in planetographic latitude (Saur et al. 2015). In order to average out the effects of the plasma interaction, we subtract the OCFB in the northern hemisphere, ϑ_N , from the southern hemisphere, ϑ_S ,

$$\vartheta_c = \frac{(\vartheta_N + \vartheta_S)}{2}, \quad (4.4)$$

with ϑ_N assuming positive and ϑ_S negative values. We also approximately remove the effects of induction in a subsurface ocean (Saur et al. 2015) by averaging observations above and below the current sheet. Thus, ϑ_c characterizes the average center position between the northern and southern OCFBs. Figure 44 shows the modeled ϑ_c of the OCFBs, when Ganymede is above the current sheet (blue line), below the current sheet (red line) and the average between both (black line). ϑ_c is primarily determined by Ganymede's intrinsic dynamo magnetic field. Thus, we compare ϑ_c of the averaged OCFB (black line in Figure 44) with the theoretical magnetic equator for Ganymede's dipolar magnetic field (green line in Figure 44) using the dipole coefficients taken from Kivelson et al. (2002). Note with the presence of an ocean, Ganymede's dynamo magnetic field is essentially dominated by its dipole components and the quadrupole coefficients can be neglected for our analysis (Kivelson et al. 2002; Saur et al. 2015). Both, ϑ_c of the averaged OCFB and the theoretical magnetic equator in Figure 44, are almost perfectly aligned. This demonstrates that the centers ϑ_c of the averaged OCFBs are a good measure for the magnetic equator. Because the observed auroral ovals are located where the OCFBs intersect Ganymede's atmosphere, we use the observed

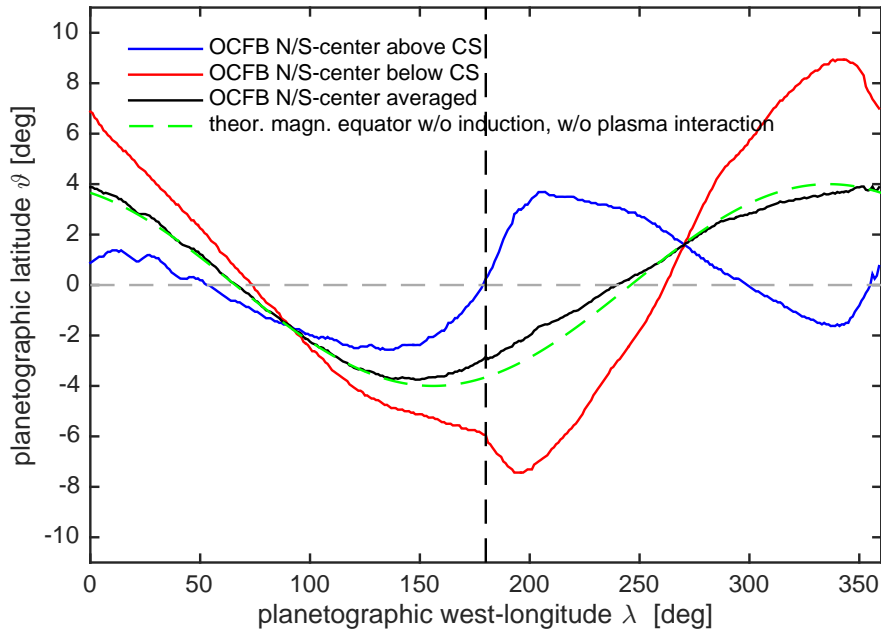


Figure 44 – Centers ϑ_c according to the expression in Equation 4.4 between northern and southern OCFB from MHD simulations. The blue line shows the center of the OCFB, when Ganymede is above the current sheet. The red line shows the center, when Ganymede is below the current sheet. Black line is the average between both, which approximately averages out the effects of the local plasma interaction (see text). The green line shows the theoretical magnetic equator for a dipolar magnetic field without plasma interaction and without internal induction.

ovals to constrain Ganymede’s dipole dynamo field. Therefore, we calculate the centers of the auroral ovals by applying Equation 4.4 to the measured locations of the auroral ovals shown in Figure 42 and Table 11. In Figure 45, we show the derived oval centers ϑ_c appropriately averaged for all observations outside (solid lines with stars) and inside the current sheet (dashed lines with diamonds, color coded for each HST campaign) together with the planetographic (dashed gray line) and theoretically calculated magnetic equator (dashed green line).

4.4.4.1 Comparing ϑ_c to the planetographic equator

Compared to the planetographic equator, the measured oval centers ϑ_c on the leading side clearly lie above the planetographic equator with the exception of three data points (mid- ($\lambda = 90^\circ \pm 25^\circ$) and anti-Jovian region ($\lambda = 147.5^\circ \pm 32.5^\circ$) of ICS and OCS data of campaigns 12244, visit 1 and 8224). This means that the southern ovals are located at lower planetographic latitudes than the northern ovals, which shifts ϑ_c into the northern hemisphere on the lea-

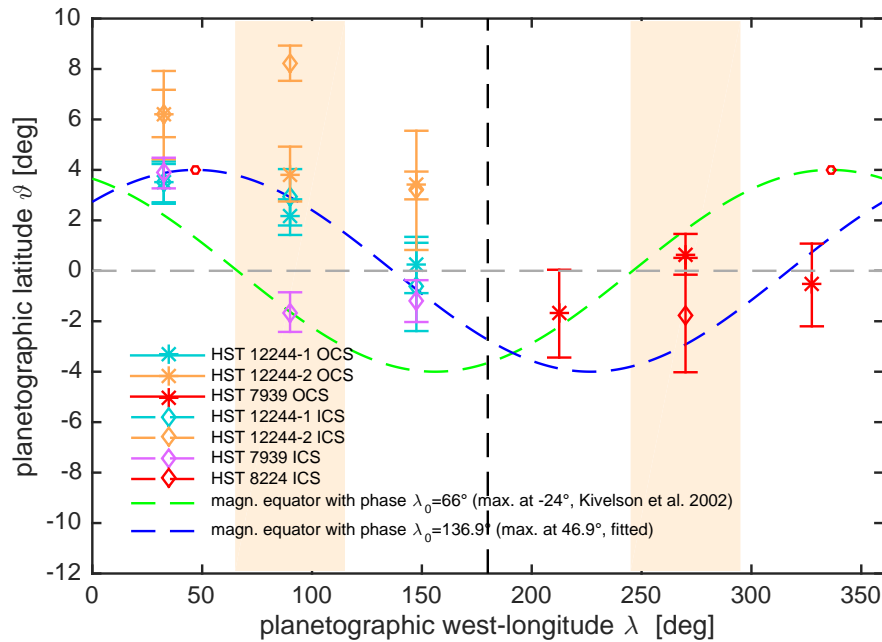


Figure 45 – Measured centers ϑ_c between each northern and southern oval compared to Ganymede’s magnetic equator with dipole coefficients from Kivelson et al. (2002) (dashed green line). the dashed blue line represents the magnetic equator with a shifted magnetic moment. The shifted magnetic moment is characterized by a phase of 136.9° , i.e., the maximum extent of the magnetic equator lies at $+46.9^\circ$ west-longitude. Shaded areas indicate the extent of each longitudinal region.

ding side. On the trailing side, with the exception of a single⁴ data point (mid-region ($\lambda = 270^\circ \pm 25^\circ$) of OCS data of campaign 7939), the opposite is the case and the centers are located below the planetographic equator, which means that the southern ovals are located at higher latitudes than the northern ovals on that hemisphere. Our findings disagree with findings of McGrath et al. (2013), who find the exactly opposite case for both hemispheres in their study (McGrath et al. (2013), see, e.g., their figure 3, also shown Figure 16). The following reasons might explain the discrepancy.

First, we use a different HST data set than McGrath et al. (2013). In our study, especially the leading side is resolved higher due to the good magnetic latitude coverage of campaign 12244, which was not available and therefore not included in the study of McGrath et al. (2013). McGrath et al. (2013) use HST campaigns with only 1 or 2 orbits observing the leading side (campaigns 8224, 9296 and 10871, listed in Table 2). Two of these campaigns observed only half of the leading side and simultaneously half of the trailing side (observations in eclipse, 9296

⁴actually, for two data points when we also account the uncertainty due to the large errorbar of the OCS data point in the sub-Jovian region ($\lambda = 327.5^\circ \pm 32.5^\circ$).

and 10871), which additionally reduces the coverage of the leading (and trailing) side. The reduced coverage, i.e., the reduced amount of HST orbits on the leading side compared to our analyzed data set might have biased the statistics of McGrath et al. (2013) regarding the location of the ovals. For example, taking campaign 8224 alone, we would come to the same conclusions as McGrath et al. (2013) for the mid- and anti-Jovian longitudinal regions.

Second, the method for determining the location of the auroral ovals by McGrath et al. (2013), shown in their figure 3 (Figure 16), is different to ours. McGrath et al. (2013) detect the peak locations of individual bright spots in the spectral images. As mentioned in Section 4.2 and 2.2.2, the auroral oval emission at Ganymede has a patchy structure, most likely due to the intermittence of the reconnection process at the OCFB causing stochastic variability (Eviatar et al. 2001a; Jia et al. 2010). The locations of the peak brightness of individual bright spots might be therefore influenced by this variability. Averaging over all spots by integrating over the latitudinal annuli in longitudinal direction, we slightly average out this stochastic variability with our method.

The third reason might be another major difference of our method regarding the planetographic longitudinal binning for detecting the oval locations compared to the method by McGrath et al. (2013). It is not clear, if and how McGrath et al. (2013) bin the observed moon disk in longitudinal direction λ . In their figure 3 (Figure 16) oval locations for many λ are shown, indicating a very tight longitudinal binning. The oval locations derived by our method as shown in Figure 42 account for the longitudinal binning into three different longitudinal regions as introduced in Section 4.4.3, i.e., we chose a larger longitudinal bin size compared to Figure 16. This significantly increases the SNR in each longitudinal bin leading to smaller errorbars in Figure 42 compared to Figure 16. Accounting for the larger errorbars in Figure 16, one could interpret the latitudinal locations of the auroral ovals in that figure rather as more balanced between the northern and southern oval instead of giving preferences to one hemispheric direction, i.e., to the north or to the south.

However, we should bear in mind that the method for locating the auroral ovals by McGrath et al. (2013) and by our method as described in Section 4.4.3 is different. Thus, results from both methods might not be directly comparable.

4.4.4.2 Comparing ϑ_c to the magnetic equator

The magnetic equator in Figure 45 (dashed green line) varies as a function of planetographic longitude due to the tilt of Ganymede's intrinsic magnetic field. For the mid-longitudinal region around the leading/trailing side central meridian (orange shaded areas in that figure and see definition of the longitudinal regions in Table 8), the magnetic equator is predicted to lie below the planetographic equator (dashed grey line) on the leading side and above the equator on the trailing side. On the anti-Jovian side ($\lambda = 135^\circ$ to 225° west-longitude), the magnetic equator is predicted to lie below the planetographic equator on both hemispheres, while on the sub-Jovian side ($\lambda = 315^\circ$ to 45° west-longitude) it lies above the equator. Only for campaign 8224, the oval centers ϑ_c in all three longitudinal regions follow these predictions and have the lowest offset to the theoretical magnetic equator (also shown by McGrath et al. (2013, e.g., their figure 9)). The ovals' centers of the mid-regions of campaign 12244 lie far above the magnetic equator. On the anti-Jovian side, only visit 1 of campaign 12244 follows the theoretical prediction within the errorbars. On the sub-Jovian side, in contrast, all measured locations of the ovals' centers lie in the predicted northern hemisphere. The ovals' centers of the mid-region of both visits of campaign 12244 show a variation, i.e., a shift of the centers further into the north when Ganymede is inside the current sheet, while visit 2 shows the highest displacement of ϑ_c to the magnetic and planetographic equator. On the other hand and with the exception of three points from visit 2 of campaign 12244, the oval centers of all campaigns do not exceed the planetographic latitude of $\pm 4^\circ$, which is consistent with the 176° tilt of Ganymede's magnetic dipole (Kivelson et al. 2002).

Overall, the longitudinal locations of all ϑ_c show a clear offset from the magnetic equator, indicating an additional shift to the orientation of Ganymede's dipole axis. We estimate this shift by applying a least squares fit of the magnetic equator to the observed oval centers. The planetographic latitudinal location $\vartheta_{\text{eq}}(\lambda)$ of Ganymede's magnetic equator can be described as a function of planetographic longitude λ ,

$$\vartheta_{\text{eq}}(\lambda) = A \sin \left((\lambda - \lambda_0) \frac{2\pi}{360^\circ} \right), \quad (4.5)$$

where $\lambda_0 = (-24^\circ + 90^\circ) = 66^\circ$ is the value of the phase and $A = -4^\circ$ is the tilt of the magnetic dipole derived by Kivelson et al. (2002). We constrain λ_0 to the measured oval centers $\vartheta_c(\lambda_i)$ by minimizing the reduced Chi-squared:

$$\chi_{\text{red}}^2 = \frac{1}{(N - p)} \sum_{i=1}^N \frac{(\vartheta_c(\lambda_i) - \vartheta_{\text{eq}}(\lambda_i))^2}{\sigma_{\text{eff}}^2(\lambda_i)}, \quad (4.6)$$

where λ_0 is the free fit parameter of the least squares fit. N is the number of measured oval centers and $N - p$ is the degree of freedom of the fit. The error $\sigma_{\text{eff}}(\lambda_i)$ is the effective error of each $\vartheta_c(\lambda_i)$:

$$\sigma_{\text{eff}}^2(\lambda_i) = \sigma_{\text{stat}}^2(\lambda_i) + \sigma_{\lambda^*}^2(\lambda_i) + \text{Var}(\vartheta_c(\lambda_i)), \quad (4.7)$$

where we consider three statistically independent sources of error. The error $\sigma_{\text{stat}}(\lambda_i)$ of each $\vartheta_c(\lambda_i)$ is propagated from the statistical uncertainties of the fitted oval locations, which result from the Gaussian fits in the Section 4.4.3 and which are shown as errorbars in Figure 45. The error $\sigma_{\lambda^*}(\lambda_i)$ is due to the uncertainty $\sigma_\lambda(\lambda_i)$ of the exact longitudinal location of $\vartheta_c(\lambda_i)$. With $\sigma_\lambda(\lambda_i) = \pm 25^\circ$ (mid-regions around $90^\circ/270^\circ$ planetographic west-longitude, orange shaded areas in Figure 45) and $\pm 32.5^\circ$ (remaining regions, white areas in Figure 45), $\sigma_{\lambda^*}(\lambda_i)$ follows after Bevington and Robinson (2003):

$$\begin{aligned} \sigma_{\lambda^*}^2(\lambda_i) &= \left(\sigma_\lambda(\lambda_i) \frac{d\vartheta_{\text{eq}}(\lambda_i, \lambda_0)}{d\lambda_i} \right)^2 \\ &= \left[\sigma_\lambda(\lambda_i) \left(\frac{2\pi}{360^\circ} A \cos \left((\lambda_i - \lambda_0) \frac{2\pi}{360^\circ} \right) \right) \right]^2. \end{aligned} \quad (4.8)$$

$\text{Var}(\vartheta_c(\lambda_i))$ is the variance of all $\vartheta_c(\lambda_i)$ at the same planetographic longitude due to stochastic variability of the oval centers from one HST campaign to another likely caused by intermittent reconnection. We list the individual components of $\sigma_{\text{eff}}^2(\lambda_i)$ in Table 12 in Appendix S7.

We obtain the best fit⁵ for $\lambda_{0,\min} = 136.9^\circ$ with a minimum $\chi_{\text{red},\min}^2 = 0.5$. Note that fits with reduced Chi-squared values of ~ 1 and smaller are considered adequate fits to observations (Bevington and Robinson 2003). For the phase suggested by Kivelson et al. (2002), $\lambda_0 = 66^\circ$, we achieve a larger χ_{red}^2 of 3.8. We do not reach $\chi_{\text{red}}^2 = 1$ until we add an additional phase of $\Delta\lambda = +58.4^\circ$ or -42.5° to $\lambda_{0,\min}$. Our fit result indicates a westward orientation of Ganymede's magnetic south pole at $136.9^\circ - 90^\circ = +46.9^\circ$ planetographic west-longitude. We have to bear in mind the uncertainty of the fit and the values of the derived $\chi_{\text{red},\min}^2$, which are largely due to the large fluctuations of the locations of the oval centers. In Figure 45, we show the magnetic equator for such a shifted orientation as a dashed blue line. Visit 1 of campaign 12244 and two longitudinal regions of campaign 8224 have a better alignment to this shifted magnetic equator than compared to the magnetic equator with an orientation at -24° (Kivelson et al. 2002) (dashed green line in the same figure). The offsets for visit 2 of campaign 12244 are also reduced. The trailing side campaign 7939 does not show a better fit to the shifted magnetic equator.

Our redirection of $\lambda_{0,\min}$ into positive planetographic west-longitudinal direction is in agreement with previous findings by Jia (2009). In his fit of the internal Gauss coefficient, Jia (2009) additionally includes Ganymede's plasma magnetic field contributions using a MHD model. Note that Kivelson et al. (2002) did not explicitly include the plasma magnetic fields near Ganymede. Jia (2009) calculated a phase of $\lambda_0 \sim 94^\circ$ (which results in a χ_{red}^2 of 1.1) into positive west-longitudinal direction (i.e., the orientation of the dipole axis lies at $+4^\circ$ west-longitude). Even though our calculated phase does not match this value in detail, it is still remarkable that we derive an offset into the same direction independently derived from an analysis of magnetometer measurements.

⁵We show the corresponding χ_{red}^2 as a function of planetographic west-longitude in Figure 52 in Appendix S8.

4.5 Longitudinal distribution of brightest spots

Similar to, e.g., Feldman et al. (2000), McGrath et al. (2013) and Saur et al. (2015), we find that the pattern of the emission along the auroral ovals is patchy as discussed in Section 4.2. In the spectral images of Figure 32 we see, that the emission along the ovals contains individual spots of increased brightness. These spots have an inhomogeneous pattern and generally a broader extent into longitudinal than in latitudinal direction. They occur isolated from each other (e.g., the bright spot in the northern hemisphere in Figure 32.1B) or are more or less connected to each other (e.g., the two bright spots in the southern hemisphere in Figure 32.2B). In order to further characterize the distribution of these spots, we now detect individual bright spots with the spot detection method described in Section 3.2.8.

We define an auroral spot as the closed region on the moon disk with a peak brightness higher than the total disk averaged brightness B_{LT} of the leading (L) and trailing side (T) presented in Section 4.3.1 in order to distinguish between individual spots. The size of a spot is limited by the necessary condition that the SNR of the auroral emission inside a spot is greater than 1. From empirical tests, we find an adequate brightness threshold of $f_{lim\ LT} = 120\% \cdot B_{LT}$ (i.e., ~ 115 R on the leading side and ~ 85 R on the trailing side). Hence, we define an auroral spot by any emission within the area enclosed by the isoline of $f_{lim\ LT}$. After applying the steps described in Section 3.2.8, we obtain the auroral spots for each spectral image. We show in Figure 46 the extracted spots as binary images, i.e., any pixel inside the spots is assigned to the value 1 (yellow areas) and any pixel outside to the value 0 (white area). The panels of the figure are ordered from top to bottom by Ganymede's magnetic latitude similar to Figure 32. In each panel, we see spots of irregular shape, structured along two ovals in the northern and southern hemisphere. As initially noticed, the width in longitudinal direction of the spots is larger than their height in latitudinal direction. The height of the spots shows no clear dependency on Ganymede's magnetic latitude. For example, inside the current sheet on the trailing side (Figure 46.1B), the ovals are smaller in latitudinal direction compared to the third orbit outside the current sheet (Figure 46.1C), but

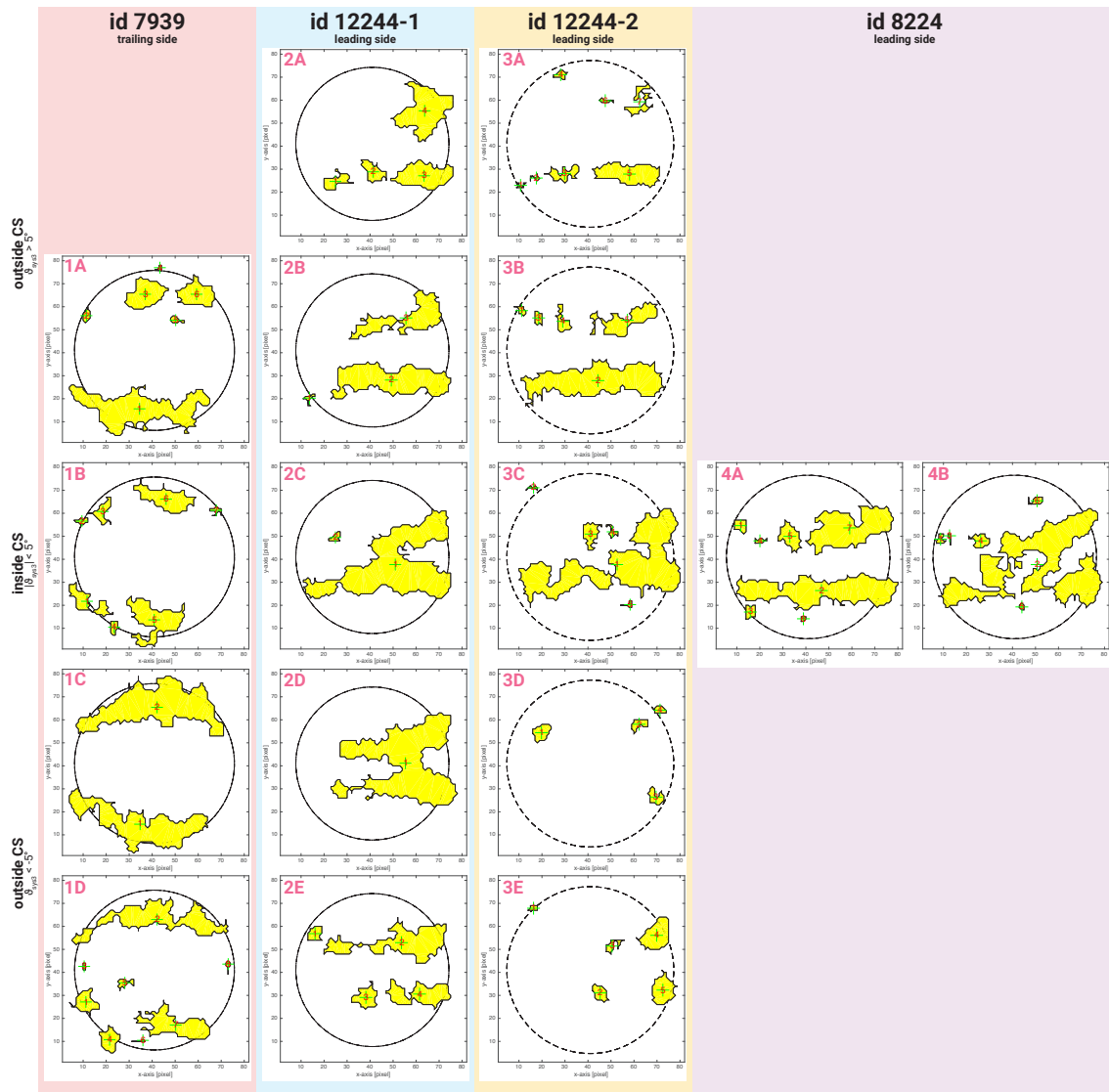


Figure 46 – Detected spots in the spectral images of OI $\lambda 1356 \text{ \AA}$ (shown as binary masks). Yellow areas have the value 1, white areas have the value 0. The circle indicates the Ganymede disk.

not in the remaining orbits (Figure 46.1A and Figure 46.1D). On the leading side, the first orbit outside the current sheet shown in Figure 46.2A has one spot in the northern hemisphere with a larger extent in latitudinal direction compared to the spots in the southern hemisphere, while the subsequent orbit in Figure 46.2B (still outside the current sheet) shows no clear differences in height of the detected bright spots. This indicates a random component in the structure of the spots.

We again see the shift of the ovals towards the planetographic equator on the leading side, when Ganymede is inside the current sheet (e.g., Figure 46.2C) compared to outside of the current sheet (Figure 46.2A, 46.2B and Figure 46.2D,

46.2E) as discussed in the previous sections. Inside the current sheet on the leading side, the spots of the northern and southern oval merge into one big and several small sized spots (Figure 46.2C, 46.3C and 46.4B). For one orbit of campaign 8224 (Figure 46.4A), in contrast, the emission pattern is still that of two distinct ovals. On the trailing side, we see that simultaneous with the previously discussed decrease of total disk averaged brightness inside the current sheet, also the spot sizes decrease (compare Figure 46.4B with 46.4A, 46.4C and 46.4D). In Figure 46.4C (outside the current sheet), the spots merge into one big spot on each hemisphere.

4.5.1 Occurrence of bright spots

In order to further investigate the distribution of the bright spots, we count the number of detected spots during each HST orbit shown as green lines in Figure 47 (with the corresponding y -axis on the right side of each panel). The color coded shaded areas in each panel of Figure 47 separate individual orbits from each other. We show the orbit number (in brackets) together with the corresponding magnetic latitude in the x -axis labels. The number of detected spots varies from orbit to orbit in each campaign. The lowest spot count is 1 (campaign 12244, Figure 47A, orbit 4), and the highest count is 8 (campaign 7939, Figure 47D, orbit 4). We cannot determine any systematic behavior in the occurrence of the spots. For example, in visit 1 of campaign 12244 (A) and in campaign 7939 (D), the number of spots decreases inside the current sheet but remains high in the other two visits of the leading side (B and C) for low magnetic latitudes. Hence, on time scales of an HST orbit (on average 33.3 minutes), the number of detectable bright spots is rather of stochastic nature than systematic organized, e.g., by magnetic latitude.

Such variability also accounts for the size of the spots. In Figure 47, we also plot the size of each detected spot as dots (color coded for each orbit) in the unit of pixels (with the corresponding y -axis on the left side of each panel). While the majority of detected spots in visit 2 of campaign 12244 (B) and in campaign 7939 (D) is of small size of less than 100 pixels (which corresponds to a coverage of less than 3% of the moon disk), in visit 1 of the same campaign (A) the distribution between small sized and larger spots is more or less balanced. On the other hand, while inside the current sheet in visit 1 of campaign 12244 (orbit 3 in A) the spots

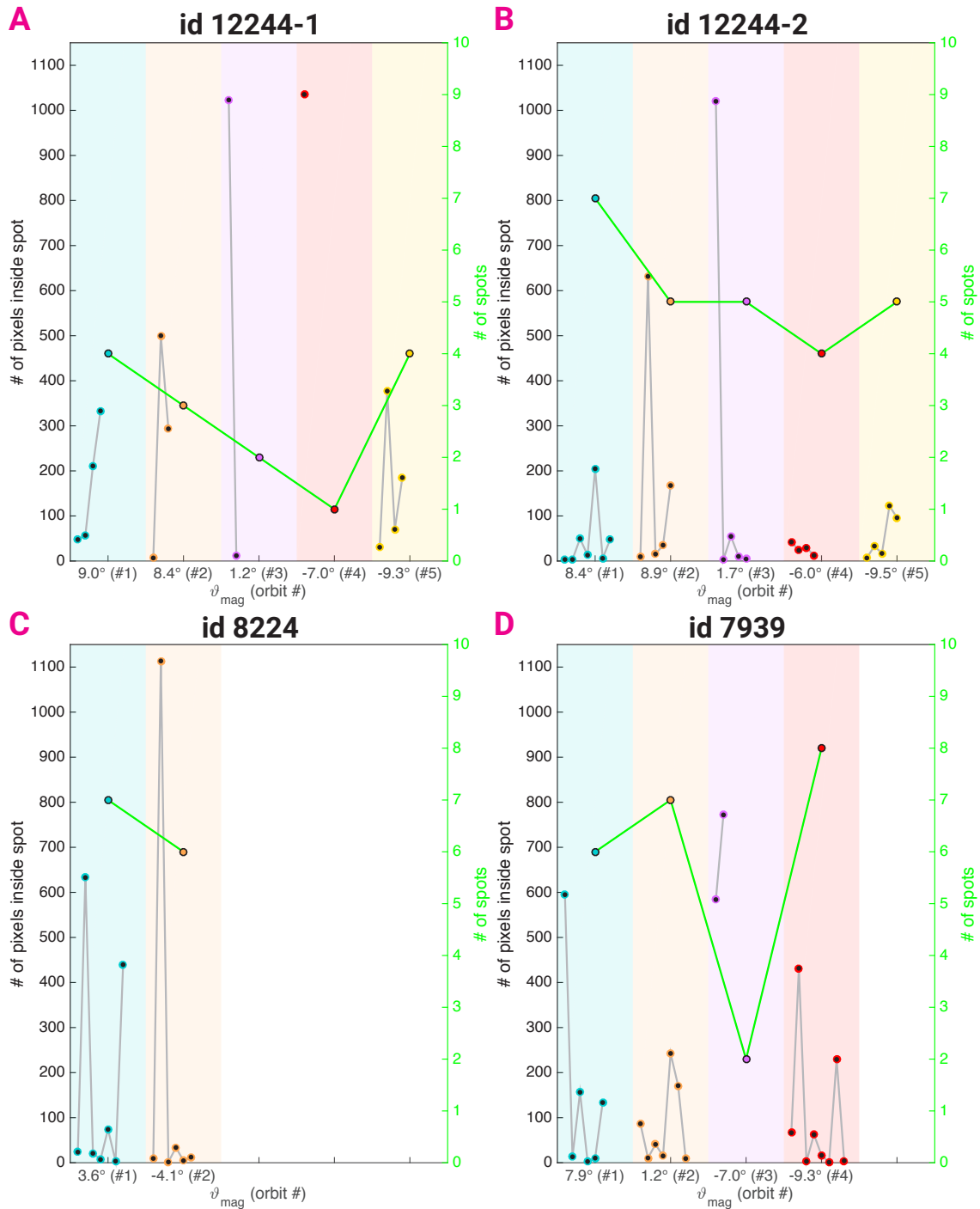


Figure 47 – Number of spots in each panel of Figure 46 (green lines, corresponding y -axis on the right side of each panel) plotted together with the size of each spot (color coded dots, corresponding y -axis on the left side of each panel). The color codes of the dots and shaded areas separate one orbit from each other. On the x -axis, the first value shows the magnetic latitude and in brackets the number of the corresponding HST orbit.

merge into one big spot (>1000 pixels, which covers $\sim 30\%$ of the moon disk) and one small sized spot. In campaign 8224 (C), for the same magnetic latitude the

big sized spots are accompanied by several small sized spots. Overall, there is a large variability of spot size from one HST orbit to another.

The variable amount of spots and spot size from one HST orbit to another indicates that the auroral spots underlay a steady rearrangement. Small spots merge into bigger spots and vice versa. Spots vanish and new spots occur or their brightness decreases so that they fall below the brightness threshold $f_{\text{lim } L/T}$ and are not detected any more by our method. Also, the opposite can be the case and their brightness exceeds $f_{\text{lim } L/T}$ from one orbit to another and they are additionally detected by our method. Unfortunately, due to the concept of our spot detection method we are not able to record the *history* of individual spots, i.e., how one spot develops from one orbit to another. For example, if we track two spots over two orbits and one of these spots vanishes in the second orbit, we cannot determine whether the remaining spot is the first or the second spot from the previous orbit. However, our spot detection method gives an overview of the overall variability and the stochastic nature of the spot size and spot occurrence.

4.5.2 Longitudinal distribution of the centroids of the spots

In order to investigate the longitudinal variability of the auroral spots, we calculate the longitudinal component of the brightness weighted centroid M of each spot (Bevington and Robinson 2003),

$$M = \sum_{i_x} \left(\frac{\sum_{i_y} i_y f(i_x, i_y)^\kappa}{\sum_{i_y} f(i_x, i_y)^\kappa} \right), \quad (4.9)$$

with the corresponding error σ_M

$$\sigma_M = \sqrt{\sum_{i_y} \frac{\sum_{i_x} f(i_x, i_y)^\kappa (i_x - M)^2}{\sum_{i_x} f(i_x, i_y)^\kappa}}. \quad (4.10)$$

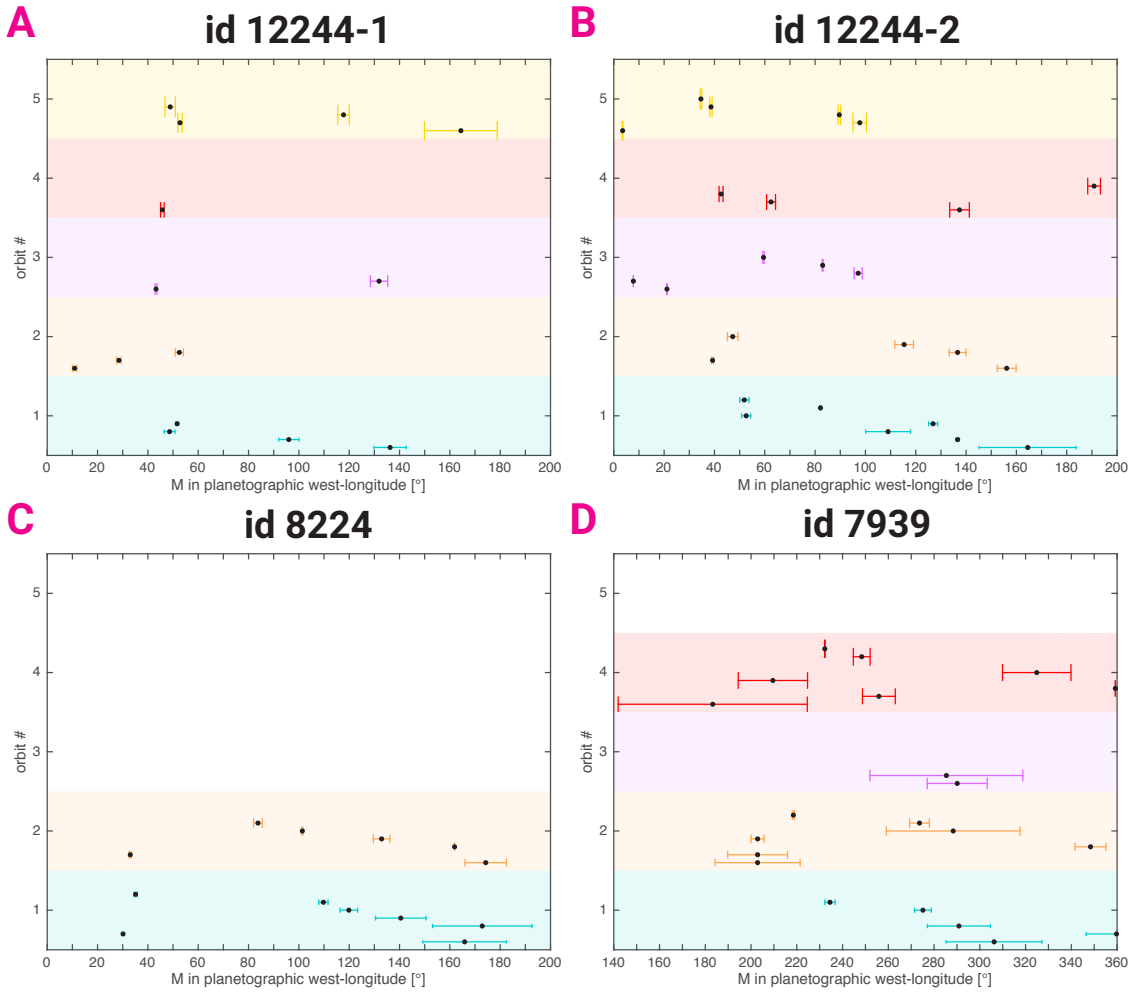


Figure 48 – Planetographic longitudinal component of brightness weighted centroids M (Equation 4.10) of the bright auroral spots. Similar to Figure 47, color coded points and shaded areas separate individual orbits from each other (ordered along the y -axis).

κ is a weighting factor for the flux $f(i_x, i_y)$. We use again a very high $\kappa = 30$ to account for the brightest pixel inside each spot. The resulting centroid coordinates are shown in the panels of Figure 48 for each campaign. The centroids are plotted together with their error as a function of planetographic west-longitude λ (in degree, x -axis) and are ordered by HST orbits (y -axis, again color coded to distinguish between individual orbits). Note that in cases where M lies outside the Ganymede disk (occurs when the majority of the spot emission is located in the off-limb area), we set the corresponding planetographic longitude on the limb of the disk. Also note that we neglect the latitudinal distribution of the centroids and, hence, we do not distinguish between spots of the northern and southern oval. For both reasons, setting off-limb centroids on the limb of the disk and the

lack of latitudinal dependency, centroids in Figure 48 may overlap in some cases during one orbit.

As shown in Figure 47, there are fewer spots in campaign 12244, visit 1 (Figure 47A), than in visit 2 of the same campaign (Figure 47B). Hence, there are accordingly fewer brightness centroids in visit 1 (A) than in visit 2 (B) of campaign 12244 in Figure 48. While the spot centroids of visit 1 roughly show a preference for the Jupiter-facing side (summarized over all orbits, 9 centroids lie below 90° planetographic longitude compared to 5 centroids lying above 90°), this preference is not reflected by the second visit. In visit 2 of campaign 12244, the brightness centroids are randomly distributed along all planetographic longitudes of the leading side for each orbit. Furthermore, their longitudinal distribution also varies from one orbit to another, i.e., there are barely centroids which overlap with centroids in a preceding orbit. This finding is contradictory to the findings of McGrath et al. (2013), who identify the brightest spot in the northern hemisphere to be located at roughly the same planetographic latitude and longitude over several campaigns, i.e., in the northern sub-Jovian quadrant (*NW* quadrant in their work). The difference between our findings and that of McGrath et al. (2013) might be due to differences in the spot detection methods. The principal difference in the study of McGrath et al. (2013) and ours is that McGrath et al. (2013) analyze the superposition of all orbits of one visit and neglect the temporal evolution of the spots from one orbit to another. Hence, they calculate the position of the superposition of individual spots into one (or few) large and longitudinal broadened spot(s), while we analyze individual spots of each orbit.

In contrast to campaign 12244, the centroids of the other leading side campaign (campaign 8224, C) actually show a preference for the anti-Jovian side (summarized over both orbits of campaign 8224, 3 centroids lie below 90° and 10 centroids lie above 90°). This is remarkable, since we observe in Section 4.3.5 a higher amount of auroral brightness on the Jupiter-facing side for both leading side campaigns. On the other hand, we have to bear in mind that the spots detected by our method have brightnesses far above the total disk averaged brightnesses. Hence, we neglect a majority of the auroral brightness. We also do not directly compare the actual brightness of a spot, but its brightness weighted centroids. Also, the tendency on the leading side of larger errorbars for longitudes greater than 90° in Figure 48A to C indicate a lower SNR of spot brightness on the anti-Jovian

hemisphere.

The centroids of the trailing side campaign 7939 (Figure 48D) show, similar to the second visit of campaign 12244, a random distribution along all planetographic longitudes covered by that hemisphere. For example, in the first orbit a majority of centroids lie on the Jupiter-facing side ($>270^\circ$), while in the last orbit the distribution is completely the opposite. In orbit 3 and 4, the distribution is indifferent due to a balanced distribution in orbit 2 and large errorbars in orbit 3.

4.5.3 Summary

Overall, we cannot identify any dependency of the distribution of the spot centroids, e.g., for changing magnetic latitudes. Also, the detected preference for the sub-Jovian side in visit 1 of campaign 12244 might be biased due to the low number of detected spots. In all remaining visits the amount of spots is higher and the centroids tend to be (more or less) randomly distributed along all planetographic longitudes. Further HST observations and a larger amount of orbits would be required in order to determine, whether the centroids' longitudinal distribution is randomly ordered or if there are preferences for a specific hemisphere.

McGrath et al. (2013) relate the occurrence of individual bright spots along the auroral ovals to localized electrojets associated with the OCFB. Electrojets are related to regions in the ionosphere, where currents are driven by parallel electric fields through the ionospheric resistance (McGrath et al. 2013). According to McGrath et al. (2013), the spot-like structure of the auroral emission and accordingly the localized character of the electrojets indicate a rather localized than global ionosphere at Ganymede. Our finding of a randomly organized structure, occurrence and longitudinal distribution of auroral spots additionally indicates a stochastic variability of the currents along the OCFB which generate the bright auroral spots. A reason for this variability might be the intermittence of the reconnection process as discussed in Section 2.2.2. Jia et al. (2010) find that the reconnection events are impulsive and limited in spatial extent. This corresponds to the unordered distribution of the spot centroids along all planetographic longitudes and to the isolated occurrence of individual spots along the ovals. Jia et al. (2010) also find, that the reconnection at Ganymede's upstream magnetopause occurs in a bursty manner with periodicities between 20 and 50 seconds. We

cannot analyze the auroral emission on such time scales due to the decreasing SNR for shorter exposure times. For instance, we applied our spot detection method also to the two exposures of each orbit (not shown here). This increases the temporal resolution to approximately lower than 20 minutes. Even though the detected auroral spots in each exposure indicate an increased occurrence of spots, i.e., more smaller sized spots are detected within one exposure compared to one orbit, the average SNR of a spot decreases to 1 or even lower. This allows no reliable further investigation of the auroral spots on time scales of one exposure (or lower). However, the bursty, i.e., intermittent character of the reconnection might still be reflected by the random behavior of the spots analyzed on time scales of one orbit.

Summary and Conclusions

In the final chapter of this thesis we summarize our study by presenting and discussing our main findings and by drawing our main conclusions. At the end, we give a short outlook on possible further investigations of the aurora on Ganymede.

In this thesis, we present a detailed analysis of a comprehensive set of observations by the *Space Telescope Imaging Spectrograph* on-board the *Hubble Space Telescope* (HST/STIS) of the auroral emission originating from the tenuous atmosphere of the Galilean satellite Ganymede. Electron-impact dissociative excitation of oxygen in Ganymede's atmosphere generates auroral emission in the far ultraviolet (FUV) wavelength range (Hall et al. 1998; Feldman et al. 2000). The auroral emission on Ganymede is not homogeneously distributed on the moon disk, but is concentrated along two distinct ovals in the northern and southern hemisphere (Feldman et al. 2000). The ovals are located between 10° and 30° planetographic latitude on the plasma downstream side (leading hemisphere) and between 40° and 55° on the plasma upstream side (trailing hemisphere) (McGrath et al. 2013). The location of the ovals coincides with the theoretically predicted intersection line of the open-closed magnetic field lines boundary (OCFB) with Ganymede's atmosphere (Feldman et al. 2000; Eviatar et al. 2001a; McGrath et al. 2013). Ganymede is so far the only known moon in the solar system, which possesses an intrinsic magnetic field (Kivelson et al. 1996). This magnetic field is embedded within the magnetic field of Jupiter. The intrinsic magnetic field of Ganymede is strong enough, to maintain a region of closed magnetic field lines shielding the moon from the impinging Jovian magnetospheric plasma flow. Hence, Ganymede's magnetic field is able to form a so-called mini-magnetosphere embedded within the gigantic planetary magnetosphere of Jupiter. As the orbital velocity of Ganymede is slower than the impinging Jovian magnetospheric plasma flow, the mini-magnetosphere underlies the steady stream of the Jovian plasma, which compresses the mini-magnetosphere on the upstream side. On the downstream side, the mini-magnetosphere is stretched and a magnetotail develops (Kopp and Ip 2002; Ip and Kopp 2002; Jia et al. 2008, 2009b; Duling et al. 2014). The resulting bullet-like/cylindrical shape of the mini-magnetosphere is similar to the magnetosphere of Earth, which is exposed to and influenced by the solar wind. As the Ganymede and Jovian magnetic fields are oriented in anti-parallel direction, reconnection might occur at points of intersection between both fields (Neubauer 1998; Eviatar et al. 2001a). The magnetic reconnection most likely triggers field aligned electric currents (FAC), which accelerate electrons along the OCFB towards Ganymede's atmosphere (Eviatar et al. 2001a). These energetic electrons trigger the FUV aurora in Ganymede's atmosphere. Due to the compression and stretching on the upstream and downstream side, respectively, the OCFB and accordingly the auroral ovals are shifted to elevated planetographic latitudes on

the trailing side and to lower latitudes on the leading side as observed by several HST campaigns (e.g., Feldman et al. (2000) and McGrath et al. (2013)).

We analyze a set of HST observations which were obtained between 1998 and 2011 and which cover the satellite at eastern and western elongation, observing Ganymede's leading (plasma upstream) and trailing (plasma downstream) side. The aurora on Ganymede is expected to be time-variable since the moon is exposed to the time-periodic plasma and magnetic field of Jupiter's magnetosphere. The periodic variability is due to the tilt of $\sim 10^\circ$ between Ganymede's orbital plane and Jupiter's magnetic equator. Ganymede's magnetic latitudes therefore oscillate with Ganymede's synodic rotation period of 10.5 hours between approximately 10° and -10° . As the influence of periodically changing local plasma conditions on the morphology and brightness of Ganymede's aurora has not been analyzed yet, we systematically analyze the spatial structure and the temporal variability of Ganymede's auroral ovals as a function of its time-variable magnetospheric environment. In the following we summarize and discuss our main findings.

1 Albedo dichotomy between the leading and trailing side

We find a hemispheric albedo dichotomy between the leading and trailing side. With an average of 2.7 ± 0.4 % the geometric FUV albedo on the trailing side is higher than on the leading side with an average of 1.8 ± 0.4 %. This is remarkable for two reasons. First, an albedo dichotomy between both hemispheres is also apparent at higher wavelength ranges in the MUV and at visible light, but in the opposite direction. While we assume the albedo to be constant for the fitted wavelength range (1410 Å to 1550 Å), the albedo increases as a function of wavelength above that fitting range with the albedo on the leading side increasing faster than on the trailing side (Figure 31). Second, while such albedo dichotomy for higher wavelength ranges has also been observed for Ganymede's neighboring moon, Europa (Saur et al. 2011, see, e.g., their figure 6), a pronounced difference between the albedo of the leading and trailing side in the FUV has not been observed so far (Roth et al. 2014a). The reasons for the observed dichotomies (in the FUV and MUV) at Ganymede are still not well understood. The surface reflectivity in the FUV is lower than the reflectivity of 5.5 % of pure H₂O frost obtained from laboratory measurements (Hall et al. 1998), indicating that Ganymede's icy surface contains FUV darkening materials similar to, e.g.,

Europa. Unlike at Europa, where the hemispheric difference in the UV darkening contaminants are related to the bombardment by magnetospheric ions on the trailing side (Hendrix et al. 2005), the situation at Ganymede is more complex. Orbiting at $15 R_J$, the flux of charged particles at Ganymede is lower than the flux at Europa's orbit at $9 R_J$ (Hendrix et al. 2005). The plasma particles at Ganymede's orbit are not energetic enough to pass through the region of closed field lines in Ganymede's mini-magnetosphere and are deflected around the moon or they hit magnetic unshielded parts of Ganymede's surface, i.e., the polar regions (Hendrix et al. 1999). Thus, the reasons for the observed albedo dichotomy and its change of direction from the FUV to the MUV range are still an open research question.

2 Brightness dichotomy of total disk averaged brightness between the leading and trailing side

The brightness of Ganymede's aurora is not distributed equally along the moon's hemispheres. The total disk averaged brightness is 1.42 ± 0.07 times brighter on the leading side ($95.4 \pm 2.1 R$) compared to the trailing side ($67.2 \pm 2.9 R$). This indicates that more field aligned electric currents, which are associated with auroral electron acceleration (Eviatar et al. 2001a), are closed in the downstream ionosphere compared to the upstream side. Further MHD and plasma modeling are required to better understand the overall distribution of the currents in Ganymede's mini-magnetosphere and their relation to the auroral structures. Future remote-sensing and in-situ measurements, e.g., by ESA's *JUICE* mission (see below), within the mini-magnetosphere will also greatly help our understanding of Ganymede's current system and auroral oval acceleration processes.

3 Dependency of total disk averaged brightness on Ganymede's magnetic latitude

The total disk averaged brightness is dependent on Ganymede's position within the Jovian plasma sheet on both, the leading and trailing side. Inside the current sheet, the total disk averaged brightness on the leading side ($108.9 \pm 3.7 R$) is increased by a factor of 1.33 ± 0.05 compared to outside the current sheet ($82.0 \pm 1.7 R$). The increase of the auroral brightness for low magnetic latitudes is indicative for the influence of the plasma interaction on the generation of

the aurora and, thus, on Ganymede's magnetic field. As the plasma density increases at the center of the current sheet (Bagenal and Delamere (2011) and see Figure 35), the increased upstream ram pressure possibly generates larger magnetic stresses, which imply larger electric currents near the OCFB in Ganymede's ionosphere. On the trailing side, the total disk averaged brightness does not reflect this prediction and the average of total disk averaged brightness decreases by a factor of 0.76 ± 0.07 inside the current sheet (from 58.0 ± 4.8 R to 76.4 ± 3.2 R). A possible reason for the difference between the leading and trailing side might be, that, when Ganymede is inside the current sheet, the auroral ovals and the associated electric current systems might be partially shifted towards the downstream (leading) hemisphere due to stronger plasma interaction and thus could result in a decreased emission on the upstream (trailing) side.

4 Inhomogeneous distribution of auroral brightness along the moon disk

In addition to the global brightness asymmetry between the leading and trailing side, the aurora on Ganymede is also inhomogeneously distributed within each hemisphere. Regardless of the observed hemisphere, the sub-Jovian side is always brighter than the anti-Jovian side. Furthermore, individual quadrants of the observed disk (Figure 38) follow the general trend of increased brightness inside the current sheet on the leading side except for the northern anti-Jovian quadrant, which shows nearly no variation as a function of changing magnetic latitude and has the lowest emission compared to the remaining quadrants. On the trailing side, it is the southern anti-Jovian quadrant with the lowest brightness and lowest variation. The reasons for these spatial asymmetries are unclear. Asymmetries in Ganymede's oxygen atmosphere induced by surface inhomogeneities might be an explanation. An additional current system due to the Hall effect in the ionosphere as it is the case at Io (Saur et al. 2000) or at the magnetopause, as recently proposed by Dorelli et al. (2015), might also explain the observed on-disk brightness asymmetries.

5 Movement of the auroral ovals as a function of changing magnetic latitude

After studying the general distribution of the aurora on Ganymede, we analyze

the latitudinal distribution of the auroral emission by dividing the moon disk into 60 equidistant latitudinal anuli and by integrating the photon flux of each anulus. The general location of the auroral ovals has been measured in previous studies (e.g., by Feldman et al. (2000) or McGrath et al. (2013)), i.e., the ovals are located near the planetographic equator on the leading side and near the poles on the trailing side. The location of the auroral ovals is most likely controlled by the location of the OCFB and, hence, by the interaction between the Ganymede-an magnetic field with the impinging plasma flow and the Jovian magnetic field. In our study, we find an additional dependency of the morphology of the aurora on Ganymede's position relative to the Jovian current sheet. When Ganymede is inside the Jovian current sheet, the auroral ovals shift to the planetographic equator on the leading side and towards the poles on the trailing side. On average for the northern and southern hemisphere, the ovals shift on the leading side from $22.3^\circ \pm 0.5^\circ$ to $18.2^\circ \pm 0.5^\circ$ planetographic latitude and on the trailing side from $48.3^\circ \pm 0.5^\circ$ to $51.2^\circ \pm 1.4^\circ$. The average displacement of the ovals is in opposite direction on each hemisphere, but similar in amplitude, i.e., $-4.1^\circ \pm 0.7^\circ$ on the leading side and $+2.9^\circ \pm 1.5^\circ$ on the trailing side. Possible reasons for the movement of the ovals are changing local plasma conditions in vicinity of Ganymede. Inside the current sheet, Ganymede's magnetosphere is exposed to a stronger interaction with the local Jovian plasma flow. An increased upstream ram and plasma pressure generates a higher compression of Ganymede's magnetosphere on the plasma upstream side. The resultant magnetic stresses push the OCFB and the auroral ovals accordingly towards higher planetographic latitudes. At the same time on the plasma downstream side, the magnetosphere gets stretched which results in a shift of the OCFB towards the planetographic equator. The effect of higher compression and stretching of the magnetosphere inside the current sheet is, similar to the increase of auroral brightness at low magnetic latitudes, a result of plasma interaction between the Jovian and Ganymede's magnetosphere, which becomes directly visible by the movement of the auroral ovals.

6 Asynchronous brightness variation of the northern and southern auroral oval

By integrating along the latitudinal anuli, we are able to separate the emission of the auroral ovals from the remaining emission on the moon disk. We detect both, an asymmetry between the brightness of the northern and southern oval

and an asynchronous behavior of both ovals when Ganymede transits into the current sheet. For instance, the southern ovals of both visits of campaign 12244 (leading side, Figure 41) are brighter than the northern ovals outside the current sheet. When Ganymede is inside the current sheet, the brightness of both ovals of the first visit increases simultaneously. On visit 2, the brightness of both ovals also increases, but the northern oval becomes the brighter one. Additional HST observations are required to figure out if there is any systematic behavior of the increase of auroral oval brightness or if the increase of brightness includes a random component induced by intermittent reconnection.

7 Dim residual disk brightness compared the bright auroral oval emission

The remaining disk emission, i.e., total disk brightness minus the oval brightness, shows no dependency on Ganymede's position within the Jovian plasma sheet as the auroral ovals do. With an average brightness of 27.0 ± 1.9 R, the residual disk brightness is significantly dimmer than the oval brightness, which ranges between 80.8 ± 0.9 R (OCS) and 117.4 ± 1.1 R (ICS) on the leading side and between 83.8 ± 2.0 R (ICS) and 104.4 ± 1.6 R (OCS) on the trailing side. The behavior of the residual disk brightness might be indicative for the existence of an additional source of energetic electrons which is not directly related to the acceleration mechanism near the OCFB and which is less sensitive to variations of local plasma conditions.

8 Offsets between the measured location and theoretical calculated location of Ganymede's magnetic equator

Under the assumption that the auroral ovals are symmetrically aligned around Ganymede's magnetic equator, we find an offset of the center of the northern and southern auroral oval to the theoretical magnetic equator. This offset might be indicative for an additional phase of the orientation of Ganymede's magnetic dipole axis. Independently from Jia (2009), who calculated an additional phase to the orientation into positive west-longitudinal direction by analyzing Galileo magnetic field measurements, we find that an orientation of Ganymede's dipole magnetic moment at $+46.9^\circ$ planetary west-longitude fits best to our observations. We thus demonstrate with our study that the analysis of the location of the ovals and their

asymmetries can be used to further constrain Ganymede's magnetic field environment. For instance, Saur et al. (2015) used the observations of Ganymede's auroral ovals to deduce the presence of induction magnetic fields within an ocean. In our study, we find that HST observations of Ganymede's auroral ovals can also be used to derive further constraints to the intrinsic dynamo magnetic field of the moon.

9 Patchiness of the aurora

The aurora at Ganymede is characterized by its bright auroral emission along the two auroral ovals in the northern and southern hemisphere. Along these ovals, several isolated brightness peaks occur with brightnesses far above the total disk average. To further investigate the spot-like structure of the aurora, we separate the individual brightness peaks. By counting the spots and measuring their brightness weighted centroids in planetographic longitudinal direction, we identify a random occurrence and distribution of the spots. Unlike the brightness of the disk quadrants, which show significant preferences for an increased brightness on the Jupiter-facing hemisphere compared to the anti-Jovian hemisphere, the spots show no favored location in longitudinal direction. The spots are randomly distributed along all planetographic longitudes. Furthermore and unlike the total disk averaged and separated oval brightnesses, the locations of the spots show no dependency on Ganymede's position relative to the Jovian current sheet. The amount of detected bright spots varies randomly from orbit to orbit. The stochastic character of the bright spots corresponds to the intermittent nature of the reconnection process at Ganymede's upstream magnetosphere predicted by Jia et al. (2010).

Final conclusions

Our study demonstrates the variable character of Ganymede's aurora and its dependency on Ganymede's time-variable magnetospheric environment. We detect a change of auroral brightness when Ganymede changes its position relative to the Jovian current sheet. At the same time, the planetographic latitudinal locations of Ganymede's auroral ovals also change during Ganymede's transit through the Jovian current sheet. We measure both, the increase and decrease of au-

roral brightness on the plasma downstream and upstream side, respectively, and the variation of the ovals' location when Ganymede moves into the current sheet. We relate the brightness and spatial variation of the auroral ovals to changing local plasma conditions in Ganymede's environment, i.e., both variations are a response to an increased ram and thermal pressure of the Jovian magnetospheric plasma inside the current sheet. We also detect inhomogeneities of auroral brightness distribution along the sphere of Ganymede, which indicates local inhomogeneities in the current systems associated with the generation of the aurora. We analyze the stochastic character of the occurrence and planetographic longitudinal distribution of bright auroral spots, which might be related to the intermittent nature of the reconnection process as proposed by Jia et al. (2010). Even though we do not analyze measurements of the magnetic fields in Ganymede's vicinity (e.g., from observations by the *Galileo* spacecraft), we derive further constraints to Ganymede's intrinsic magnetic field. Therefore, we measure the location of Ganymede's magnetic equator derived from the location of the auroral ovals. We compare our findings with the location derived from magnetic field measurements by Kivelson et al. (2002) and we find differences to that reference. Overall, we demonstrate that studying the auroral brightness and its distribution is a valuable diagnostic tool for exploring Ganymede's atmosphere, surface properties and magnetospheric environment. By investigating the aurora of Ganymede we gain a better understanding of the moon's intrinsic magnetic field, as the properties of the aurora on Ganymede are likely to be controlled by the interaction between the moon's dipole magnetic field and the surrounding Jovian magnetospheric plasma.

Outlook

The work described in this thesis contributes key issues to the understanding of the aurora on Ganymede. Furthermore, our study leads to other interesting, but still unanswered questions. The assumption of a spatial constant albedo along the Ganymede disk for the wavelength range analyzed in this study (1304 Å and 1356 Å) does possibly not account for the Lyman- α emission, which is indicated by the slightly overestimated reflected solar flux at 1216 Å (Section 3.2.4, Figure 25). As the surface of Ganymede consists of both, water ice (bright regions in Figure 4) and carbonaceous contaminants (dark regions in Figure 4), and as both surface materials are expected to have different albedos at Lyman- α

(McGrath and Hendrix 2013), the surface reflectivity at 1216 Å might be locally inhomogeneous. Local albedo variations are also apparent at other wavelengths, e.g., at visible light (Figure 5). We therefore suggest a further analysis of the reflectivity at 1216 Å.

Turc et al. (2014) find in their model calculations of Ganymede's atmosphere, that the peak of H₂O in the sub-solar region due to sublimation could disappear within one hour, when this region is not illuminated by sunlight any more. Unfortunately, there is only a weak coverage of Ganymede by HST observations in eclipse. Further observations by HST (or equivalent space telescope) of Ganymede in the shadow of Jupiter or spacecraft observations of Ganymede's nightside could investigate a possible dayside/nightside variability of the FUV oxygen aurora. The next opportunity for spacecraft observations may be provided by the *European Space Agency's JUpiter ICy moons Explorer* (JUICE), which is equipped with the *Ultraviolet Spectrograph* instrument (UVS) and which presumably arrives the Jovian system in 2030.

One aspect that is not addressed by our study, is the electrodynamic coupling of Ganymede with Jupiter's ionosphere by Alfvén wings (see, e.g., Jia et al. (2010)), resulting into the so-called auroral footprint of Ganymede in the Jovian ionosphere (see, e.g., Figure 2B). In their recent study, Payan et al. (2015) suggest a correlation between the variability of the auroral morphology and brightness at Ganymede and variations of Ganymede's auroral footprint. A simultaneous observation of Ganymede's auroral footprint in Jupiter's ionosphere and the aurora on Ganymede (e.g., by a combination of spacecraft and space telescope observations) could address the question of such a correlation. With a simultaneous spectroscopic observation of Jupiter and Ganymede it could be investigated, if and how the auroral footprint in Jupiter's ionosphere responds to the variation of the OCFB and accordingly of the auroral ovals when Ganymede transits into the center of the current sheet. Periodical variations (e.g., in location and brightness) of the footprint on time-scales of Ganymede's transit through the current sheet (5.25 hours) might be an indication for such a response.

List of Figures

1	Galileo Galilei's sketches of Jupiter and the Galilean satellites (1610) (Galilei 1610)	3
2	Auroral ovals at Earth (A), Jupiter (B), Uranus (C) and Ganymede (D). Note that additionally to the main oval at Jupiter the so-called footprints (indicated as "spots" in the image) of the Galilean satellites are also visible, caused by magnetic flux tubes which connect Jupiter's ionosphere to the moons. The two FUV auroral ovals at Ganymede go around the moon's north and south pole as they do at Earth, but at lower planetographic latitudes.	4
3	Surface of Ganymede	12
4	Mosaic of spherical projected photographs of Ganymede	13
5	Albedo map at visible wavelengths (Pappalardo et al. 2004)	14
6	Sketch of Ganymede's interior after the Bland et al. (2008) model.	16
7	Sketch of the "rocking" auroral ovals at Ganymede (taken from Saur et al. (2015))	18
8	Heating map of Ganymede's dayside (Orton et al. 1996)	19
9	Vacuum-superposition of Ganymede's dipole field and Jovian background field (Neubauer 1998)	22
10	Schematic view of Ganymede's magnetic field (Kivelson et al. (2004), modified)	23
11	Jovian magnetic field lines after Engle (1992) (their figures 2 and 3)	26
12	Schematic view of the Jovian current sheet (Khurana et al. 2004)	26
13	HST/GHRS FUV spectra of Ganymede and Europa from Hall et al. (1998) (their figure 1).	29
14	HST/STIS images of Ganymede's oxygen emission at OI $\lambda 1356 \text{ \AA}$ from Feldman et al. (2000) (their figure 3)	31
15	HST/STIS images of Ganymede's oxygen emission at OI $\lambda 1356 \text{ \AA}$ from McGrath et al. (2013) (their figure 2).	32
16	Location of peak auroral brightnesses from McGrath et al. (2013) (their figure 3).	33
17	Results of the Kopp and Ip (2002) (their figure 3) MHD model.	35

18	Structure of Ganymede's magnetosphere after the Duling et al. (2014) (their figure 15) MHD model.	37
19	Orbital coverage of HST campaigns used in this work	43
20	Sketch of HST/STIS' principle functionality.	47
21	1024×1024 detector image containing electron counts per seconds and background subtracted image.	50
22	Disk detection method 1: two-dimensional convolution of the Ganymede disk at 1216 Å.	53
23	Disk detection method 2: using the long wavelength trace.	56
24	Determining the trace drift.	58
25	1D photon fluxes from Ganymede reaching HST	63
26	Modeled disks convolved with the fitted reflected solar flux and with HST's point spread function at each wavelength.	64
27	2D background emission and reflected solar flux corrected image.	66
28	Spectral images of the oxygen emission for orbit 5, visit 1 of campaign 12244 (2010).	67
29	Sub-pixel division scheme.	73
30	Spot detection scheme.	76
31	Albedo for the observed FUV (1100 Å to 1700 Å) and MUV range (2000 Å to 3400 Å) on the leading and trailing side	81
32	Spectral images of OI λ 1356 Å oxygen emission in Rayleigh	84
33	Total disk averaged brightnesses of the OI λ 1356 Å and OI λ 1304 Å emission	86
34	Average ICS and OCS brightness	88
35	Jovian magnetospheric scale height and plasma density at Ganymede.	90
36	Off-limb brightness and off-limb/on-disk brightness ratio.	92
37	OI λ 1356 Å/OI λ 1304 Å brightness ratio.	93
38	Averaged brightnesses of OI λ 1356 Å emission for individual quadrants on the moon disk	95
39	SNR maps of the latitude anuli.	99
40	Latitudinal anuli-averaged OI λ 1356 brightness.	100
41	Auroral brightness distinguished between oval and residual disk emission.	102

42	Average oval locations as a function of planetographic west-longitude with 0° pointing towards Jupiter.	106
43	Theoretical locations of the OCFB from Saur et al. (2015).	107
44	Centers ϑ_c between northern and southern OCFB from MHD simulations.	110
45	Measured centers ϑ_c between each northern and southern oval compared to Ganymede's magnetic equator.	111
46	Detected spots in the spectral images of OI $\lambda 1356 \text{ \AA}$	117
47	Number of spots in each panel of Figure 46 plotted together the size of each spot.	119
48	Planetographic longitudinal component of brightness weighted centroids of the bright auroral spots.	121
49	Determining the trace drift.	162
50	Spectral images of OI $\lambda 1304 \text{ \AA}$ oxygen emission in Rayleigh . . .	163
51	Comparison between total disk averaged brightnesses I_{tot}	164
52	Reduced χ^2 of Section 4.4.4.	167
53	Figure 4 rotated by 90°	169

List of Tables

1	Orbital and physical parameters of Jupiter and the Galilean satellites. (Bagenal et al. 2004)	11
2	Overview of HST campaigns observing Ganymede’s aurora in the FUV.	42
3	Observational parameters of HST/STIS campaigns ID 7939, 8224 and 12244. All specifications refer to the center of the exposure time.	45
4	Calculated disk-center coordinates of Ganymede at 1356 Å	59
5	SNR averaged for the Ganymede disk in the spectral images of the OI $\lambda 1304$ Å and OI $\lambda 1356$ Å emission for each visit.	71
6	Albedo in the FUV range	81
7	Resultant location of the maximum, μ , and width, σ , of the fitted Gaussian function in Figure 40	100
8	Classification of the longitudinal bin on the moon disk for each campaign	105
11	Resultant location of the maximum, μ , and width, σ , of the fitted Gaussian function for the latitudinal anuli integrated brightnesses, each for the three longitudinal regions on the disk.	165
12	Individual values of the effective error σ_{eff} in Equation 4.7 introduced in Section 4.4.4.	166

References

Ajello et al. 1994

AJELLO, J. M. ; PRYOR, W. R. ; BARTH, C. A. ; HORD, C. W. ; STEWART, A. I. F. ; SIMMONS, K. E. ; HALL, D. T.: Observations of interplanetary Lyman-alpha with the Galileo Ultraviolet Spectrometer: Multiple scattering effects at solar maximum. In: *Astronomy and Astrophysics* 289 (1994), September, p. 283–303

Anderson et al. 1996

ANDERSON, J. D. ; LAU, E. L. ; SJOGREN, W. L. ; SCHUBERT, G. ; MOORE, W. B.: Gravitational constraints on the internal structure of Ganymede. In: *Nature* 384 (1996), Dezember, p. 541–543. <http://dx.doi.org/10.1038/384541a0>. – DOI 10.1038/384541a0

Bagenal and Delamere 2011

BAGENAL, Fran ; DELAMERE, Peter A.: Flow of mass and energy in the magnetospheres of Jupiter and Saturn. In: *Journal of Geophysical Research* 116 (2011), Mai, Nr. A5, 1–17. <http://dx.doi.org/10.1029/2010JA016294>. – DOI 10.1029/2010JA016294. – ISSN 0148–0227

Bagenal et al. 2004

BAGENAL, Fran ; DOWLING, Timothy E. ; MCKINNON, William B.: *Jupiter: The Planet, Satellites and Magnetosphere*. Cambridge University Press, 2004. – 732 S. <http://www.amazon.com/Jupiter-Satellites-Magnetosphere-Cambridge-Planetary/dp/0521035457>. – ISBN 0521035457

Bar-Nun et al. 1985

BAR-NUN, A. ; HERMAN, G. ; RAPPAPORT, M. L. ; MEKLER, Y.: Ejection of H₂O, O₂, H₂ and H from water ice by 0.5-6 keV H⁺ and Ne⁺ ion bombardment. In: *Surface Science* 150 (1985), Februar, p. 143–156. [http://dx.doi.org/10.1016/0039-6028\(85\)90215-8](http://dx.doi.org/10.1016/0039-6028(85)90215-8). – DOI 10.1016/0039–6028(85)90215–8

Barker 2004

BARKER, Peter: *Galileo Galilei's Sidereus Nuncius, A page by page translati-*

on. Byzantium Press, Oklahoma City, 2004

Barth et al. 1997

BARTH, C. A. ; HORD, C.W. ; STEWART, A. Ian F. ; PRYOR, Wayne R. ; SIMMONS, K. E.: Galileo ultraviolet spectrometer observations of atomic hydrogen in the atmosphere of Ganymede. In: *Geophysical Research Letters* 24 (1997), Nr. 17, p. 2147–2150

Bevington and Robinson 2003

BEVINGTON, Philip R. ; ROBINSON, D. K.: *Data reduction and error analysis for the physicals science*. 3rd. McGraw-Hill, 2003. – 330 S. – ISBN 0072472278

Bland et al. 2008

BLAND, Michael T. ; SHOWMAN, Adam P. ; TOBIE, Gabriel: The production of Ganymede's magnetic field. In: *Icarus* 198 (2008), Dezember, Nr. 2, 384–399. <http://dx.doi.org/10.1016/j.icarus.2008.07.011>. – DOI 10.1016/j.icarus.2008.07.011. – ISSN 00191035

Bostroem and Proffitt 2011

BOSTROEM, K. A. ; PROFFITT, Charles: *STIS Data Handbook, Version 6.0*. STScI, Baltimore, Md., 2011

Broadfoot et al. 1981

BROADFOOT, A. L. ; SANDEL, B. R. ; SHEMANSKY, D. E. ; MCCONNELL, J. C. ; SMITH, G. R. ; HOLBERG, J. B. ; ATREYA, S. K. ; DONAHUE, T. M. ; STROBEL, D. F. ; BERTAUX, J. L.: Overview of the Voyager ultraviolet spectrometry results through Jupiter encounter. In: *Journal of Geophysical Research: Space Physics* 86 (1981), Nr. A10, 8259–8284. <http://dx.doi.org/10.1029/JA086iA10p08259>. – DOI 10.1029/JA086iA10p08259. – ISSN 2156–2202

Brown et al. 2015

BROWN, Dwayne ; NEAL-JONES, Nancy ; SCOTT, Jim ; NASA, Sarah Ramsey /. (Edit.): *NASA Spacecraft Detects Aurora and Mysterious Dust Cloud around Mars*. <http://www.nasa.gov/press/2015/march/nasa-spacecraft-detects-aurora-and-mysterious-dust-cloud-around-mars>. Version:2015, Last checked: March 18, 2015

Budzien et al. 1994

BUDZIEN, S. A. ; FESTOU, M. C. ; FELDMAN, P. D.: Solar flux variability and the lifetimes of cometary H₂O and OH. In: *Icarus* 107 (1994), Januar, p. 164. <http://dx.doi.org/10.1006/icar.1994.1014>. – DOI 10.1006/icar.1994.1014

Calvin et al. 1995

CALVIN, W. M. ; CLARK, R. N. ; BROWN, R. H. ; SPENCER, J. R.: Spectra of the icy Galilean satellites from 0.2 to 5 μ m: A compilation, new observations, and a recent summary. In: *Journal of Geophysical Research* 100 (1995), September, p. 19041–19048. <http://dx.doi.org/10.1029/94JE03349>. – DOI 10.1029/94JE03349

Carlson et al. 1973

CARLSON, R. W. ; BHATTACHARYYA, J. C. ; SMITH, B. A. ; JOHNSON, T. V. ; HIDAYAT, B. ; SMITH, S. A. ; TAYLOR, G. E. ; O'LEARY, B. ; BRINKMANN, R. T.: An Atmosphere on Ganymede from Its Occultation of SAO 186800 on 7 June 1972. In: *Science* 182 (1973), Oktober, p. 53–55. <http://dx.doi.org/10.1126/science.182.4107.53>. – DOI 10.1126/science.182.4107.53

Christensen 2015

CHRISTENSEN, U. R.: Iron snow dynamo models for Ganymede. In: *Icarus* 247 (2015), Februar, p. 248–259. <http://dx.doi.org/10.1016/j.icarus.2014.10.024>. – DOI 10.1016/j.icarus.2014.10.024

Clarke et al. 2004

CLARKE, John T. ; GRODENT, Denis ; COWLEY, Stan W. H. ; BUNCE, Emma J.: 26 Jupiter's Aurora. In: BAGENAL, Fran (Edit.): *Jupiter: The Planet, Satellites and Magnetospheres*. 1st edition. Cambridge University Press, 2004. – ISBN 9780521035453, Chapter 26

Connerney et al. 1998

CONNERNEY, J. E. P. ; ACUÑA, M. H. ; NESS, N. F. ; SATOH, T.: New models of Jupiter's magnetic field constrained by the Io flux tube footprint. In: *Journal of Geophysical Research* 103 (1998), Juni, 11929–11940. <http://dx.doi.org/10.1029/97JA03726>. – DOI 10.1029/97JA03726

Crary and Bagenal 1998

CRARY, Frank J. ; BAGENAL, Fran: Remanent ferromagnetism and the interior structure of Ganymede. In: *Journal of Geophysical Research* 103 (1998), Nr. 773, p. 757–25

Delitsky and Lane 1998

DELITSKY, M. L. ; LANE, A. L.: Ice chemistry on the Galilean satellites. In: *Journal of Geophysical Research* 103 (1998), Dezember, p. 31391–31404. <http://dx.doi.org/10.1029/1998JE900020>. – DOI 10.1029/1998JE900020

Dessler 1983

DESSLER, A. J.: Appendix: Coordinate Systems. Version: 1983. http://www.amazon.de/Physics-Magnetosphere-Cambridge-Planetary-Science/dp/0521520061/ref=sr_1_fkmr1_1?ie=UTF8&qid=1366880224&sr=8-1-fkmr1&keywords=dessler+1983%2C+magnetosphere+of+jovian. In: *Physics of the Jovian Magnetosphere*. 1983, Chapter Appendix

Domingue et al. 1996

DOMINGUE, D. ; LANE, A. ; MOTH, P.: Evidence from IUE for Spatial and Temporal Variations in the Surface Composition of the Icy Galilean Satellites. In: *AAS Division for Planetary Sciences Meeting Abstracts Bd. 28*, 1996 (Bulletin of the American Astronomical Society), p. 1070

Domingue et al. 1998

DOMINGUE, D. L. ; LANE, A. L. ; BEYER, R. A.: IUE's detection of tenuous SO₂ frost on Ganymede and its rapid time variability. In: *Geophysical Research Letter* 25 (1998), p. 3117–3120. <http://dx.doi.org/10.1029/98GL02386>. – DOI 10.1029/98GL02386

Dorelli et al. 2015

DORELLI, J. C. ; GLOCER, A. ; COLLINSON, G. ; TÓTH, G.: The role of the Hall effect in the global structure and dynamics of planetary magnetospheres: Ganymede as a case study. In: *Journal of Geophysical Research* 120 (2015), p. 5377–5392. <http://dx.doi.org/10.1002/2014JA020951>. – DOI 10.1002/2014JA020951

Duling et al. 2014

DULING, S. ; SAUR, J. ; WICHT, J.: Consistent boundary conditions at non-conducting surfaces of planetary bodies: Applications in a new Ganymede

MHD model. In: *Journal of Geophysical Research (Space Physics)* 119 (2014), Juni, 4412-4440. <http://dx.doi.org/10.1002/2013JA019554>. – DOI 10.1002/2013JA019554

Ely et al. 2011

ELY, Justin ; ALOISI, A. ; BOHLIN, R. ; BOSTROEM, A. ; DIAZ, R. ; DIXON, V. ; GOUDFROOIJ, P. ; HODGE, P. ; LENNON, D. ; LONG, C. ; NIEMI, S. ; OSTEN, R. ; PROFFITT, C. ; WALBORN, N. ; WHEELER, T. ; WOLFE, M. ; YORK, B. ; ZHENG, W.: *STIS Instrument Handbook for Cycle 20, Version 11.0*. STScl, Baltimore, Md., 2011

Engle 1992

ENGLE, Irene M.: Diurnal Variation in Jovian Subsolar Magnetopause Position. In: *Journal of Geophysical Research* 97 (1992), Nr. A11, p. 169–172. <http://dx.doi.org/10.1029/92JA02036>. – DOI 10.1029/92JA02036

Eviatar et al. 2001a

EVIATAR, Aharon ; STROBEL, Darrell F. ; MCGRATH, Melissa A. ; WILLIAMS, Donald J. ; FELDMAN, Paul D.: Excitation of the Ganymede Ultraviolet Aurora. In: *Astrophysical Journal* (2001), Nr. 555, p. 1013–1019

Eviatar et al. 2001b

EVIATAR, Aharon ; VASYLIUNAS, Vytenis M. ; GURNETT, Donald A.: The ionosphere of Ganymede. In: *Planetary and Space Science* 49 (2001), p. 327–336

Falck-Ytter and Torbjorn 1999

FALCK-YTTER, H. ; TORBJORN, L.: *Aurora: The Northern Lights in Mythology, History and Science*. Bell Pond Books, 1999 <https://books.google.de/books?id=Poxcz5AbrpcC>. – ISBN 9780880104685

Feldman et al. 2000

FELDMAN, Paul D. ; MCGRATH, Melissa A. ; STROBEL, Darrell F. ; MOOS, H W. ; RETHERFORD, Kurt D. ; WOLVEN, Brian C.: HST/STIS ultraviolet imaging of polar aurora on Ganymede. In: *The Astrophysical Journal* 535 (2000), Nr. 2, 1085-1090. <http://dx.doi.org/10.1086/308889>. – DOI 10.1086/308889

Frank and Paterson 2000

FRANK, L. A. ; PATERSON, W. R.: Return to Io by the Galileo spacecraft: Plas-

ma observations. In: *Journal of Geophysical Research* 105 (2000), November, p. 25363–25378. <http://dx.doi.org/10.1029/1999JA000460>. – DOI 10.1029/1999JA000460

Galilei 1610

GALILEI, Galileo: *Sidereus Nuncius*. 1610. <http://dx.doi.org/10.3931/e-rara-695>. <http://dx.doi.org/10.3931/e-rara-695>

Glasbey and Horgan 1995

GLASBEY, C. A. ; HORGAN, G. W. ; 1ST (Edit.): *Image Analysis for the Biological Sciences*. New York, NY, USA : Wiley Publishing Inc., 1995 <http://dl.acm.org/citation.cfm?id=208252>. – ISBN 0–471–93726–6

Gonzalez et al. 2004

GONZALEZ, R. C. ; WOODS, R. E. ; EDDINS, S. L.: *Digital Image Processing Using MATLAB*. Pearson Prentice Hall, 2004

Hall et al. 1998

HALL, D. T. ; FELDMAN, Paul D. ; MCGRATH, Melissa A. ; STROBEL, Darrell F.: The far-ultraviolet oxygen airglow of Europa and Ganymede. In: *The Astrophysical Journal* 499 (1998), Nr. 1, 475-481. <http://dx.doi.org/10.1086/305604>. – DOI 10.1086/305604

Hallinan et al. 2015

HALLINAN, G. ; LITTLEFAIR, S. P. ; COTTER, G. ; BOURKE, S. ; HARDING, L. K. ; PINEDA, J. S. ; BUTLER, R. P. ; GOLDEN, A. ; BASRI, G. ; DOYLE, J. G. ; KAO, M. M. ; BERDYUGINA, S. V. ; KUZNETSOV, A. ; RUPEN, M. P. ; ANTONOVA, A.: Magnetospherically driven optical and radio aurorae at the end of the stellar main sequence. In: *Nature* 523 (2015), Juli, p. 568–571. <http://dx.doi.org/10.1038/nature14619>. – DOI 10.1038/nature14619

Hendrix et al. 1999

HENDRIX, Amanda R. ; BARTH, C. A. ; HORD, C. W.: Ganymede's ozone-like absorber: Observations by the Galileo ultraviolet spectrometer. In: *Journal of Geophysical Research* 104 (1999), Juni, Nr. E6, 14169. <http://dx.doi.org/10.1029/1999JE900001>. – DOI 10.1029/1999JE900001. – ISSN 0148–0227

Hendrix et al. 2005

HENDRIX, Amanda R. ; DOMINGUE, Deborah L. ; KING, Kimberly: The icy Galilean satellites: ultraviolet phase curve analysis. In: *Icarus* 173 (2005), Januar, Nr. 1, 29–49. <http://dx.doi.org/10.1016/j.icarus.2004.06.017>. – DOI 10.1016/j.icarus.2004.06.017. – ISSN 00191035

Ip and Kopp 2002

IP, Wing H. ; KOPP, Andreas: Resistive MHD simulations of Ganymede's magnetosphere - 2. Birkeland currents and particle energetics. In: *Journal of Geophysical Research* 107 (2002), Nr. A12, 1–7. <http://dx.doi.org/10.1029/2001JA005072>. – DOI 10.1029/2001JA005072. – ISSN 0148–0227

Jia 2009

JIA, Xianzhe: *Ganymede's Magnetosphere: Observations and Modeling*, University of California, Los Angeles, Diss., 2009

Jia et al. 2009a

JIA, Xianzhe ; KIVELSON, Margaret G. ; KHURANA, Krishan K. ; WALKER, Raymond J.: Magnetic Fields of the Satellites of Jupiter and Saturn. In: *Space Science Reviews* 152 (2009), April, Nr. 1-4, 271–305. <http://dx.doi.org/10.1007/s11214-009-9507-8>. – DOI 10.1007/s11214-009-9507-8. – ISSN 0038–6308

Jia et al. 2009b

JIA, Xianzhe ; WALKER, Raymond J. ; KIVELSON, Margaret G. ; KHURANA, Krishan K. ; LINKER, Jon A.: Properties of Ganymede's magnetosphere inferred from improved three-dimensional MHD simulations. In: *Journal of Geophysical Research* 114 (2009), September, Nr. A9, 1–19. <http://dx.doi.org/10.1029/2009JA014375>. – DOI 10.1029/2009JA014375. – ISSN 0148–0227

Jia et al. 2010

JIA, Xianzhe ; WALKER, Raymond J. ; KIVELSON, Margaret G. ; KHURANA, Krishan K. ; LINKER, Jon A.: Dynamics of Ganymede's magnetopause: Intermittent reconnection under steady external conditions. In: *Journal of Geophysical Research* 115 (2010), Dezember, Nr. A12, 1–14. <http://dx.doi.org/10.1029/2010JA015771>. – DOI 10.1029/2010JA015771. – ISSN 0148–0227

Jia et al. 2008

JIA, Xianzhe ; WALKER, Raymond J. ; KIVELSON, Margaret G. ; KHURANA, Krishan K. ; LINKER, Jon a.: Three-dimensional MHD simulations of Ganymede's magnetosphere. In: *Journal of Geophysical Research* 113 (2008), Juni, Nr. A6, 1–17. <http://dx.doi.org/10.1029/2007JA012748>. – DOI 10.1029/2007JA012748. – ISSN 0148–0227

Johnson 1996

JOHNSON, R. E.: Sputtering of ices in the outer solar system. In: *Reviews of Modern Physics* 68 (1996), Januar, p. 305–312. <http://dx.doi.org/10.1103/RevModPhys.68.305>. – DOI 10.1103/RevModPhys.68.305

Kao et al. 2016

KAO, M. M. ; HALLINAN, G. ; PINEDA, J. S. ; ESCALA, I. ; BURGASSER, A. ; BOURKE, S. ; STEVENSON, D.: Auroral Radio Emission from Late L and T Dwarfs: A New Constraint on Dynamo Theory in the Substellar Regime. In: *Astrophysical Journal* 818 (2016), Februar, p. 24. <http://dx.doi.org/10.3847/0004-637X/818/1/24>. – DOI 10.3847/0004-637X/818/1/24

Khurana 1997

KHURANA, Krishan K.: Euler potential models of Jupiter's magnetospheric field. 102 (1997)

Khurana et al. 2004

KHURANA, Krishan K. ; KIVELSON, Margaret G. ; VASYLIUNAS, Vytenis M. ; KRUPP, Norbert ; WOCH, Joachim ; LAGG, Andreas ; MAUK, Barry H. ; KURTH, William S.: 24 The Configuration of Jupiter's Magnetosphere. In: BAGENAL, Fran (Edit.): *Jupiter: The Planet, Satellites and Magnetospheres*. 1st. Cambridge University Press, 2004, Chapter 24, p. 593–616

Khurana et al. 2007

KHURANA, Krishan K. ; PAPPALARDO, Robert T. ; MURPHY, N. ; DENK, T.: The origin of Ganymede's polar caps. In: *Icarus* 191 (2007), November, Nr. 1, 193–202. <http://dx.doi.org/10.1016/j.icarus.2007.04.022>. – DOI 10.1016/j.icarus.2007.04.022. – ISSN 00191035

Kivelson et al. 1997

KIVELSON, Margaret G. ; KHURANA, Krishan K. ; CORONITI, F. V. ; JOY, S. ; RUSSELL, Christopher T. ; WALKER, Raymond J. ; WARNECKE, J. ; BENNETT,

C. L. ; POLANSKEY, C.: The magnetic field and magnetosphere of Ganymede. In: *Geophysical Research Letters* 24 (1997), Nr. 17, p. 2155–2158

Kivelson et al. 1996

KIVELSON, Margaret G. ; KHURANA, Krishan K. ; RUSSELL, Christopher T. ; WALKER, R. J. ; WARNECKE, J. ; CORONITI, F. V. ; POLANSKEY, C. ; SOUTHWOOD, D. J. ; SCHUBERT, Gerald: Discovery of Ganymede's magnetic field by the Galileo spacecraft. In: *Nature* 384 (1996), p. 537–541. <http://dx.doi.org/doi:10.1038/384537a0>. – DOI doi:10.1038/384537a0

Kivelson et al. 2002

KIVELSON, Margaret G. ; KHURANA, Krishan K. ; VOLWERK, M.: The Permanent and Inductive Magnetic Moments of Ganymede. In: *Icarus* 157 (2002), Juni, Nr. 2, 507–522. <http://dx.doi.org/10.1006/icar.2002.6834>. – DOI 10.1006/icar.2002.6834

Kivelson et al. 2004

KIVELSON, Margaret G. ; KURTH, William S. ; NEUBAUER, Fritz M. ; PARANICAS, Chris ; SAUR, Joachim: 21 Magnetospheric Interactions with Satellites. In: BAGENAL, Fran (Edit.): *Jupiter: The Planet, Satellites and Magnetospheres* Bd. m. 1st. Cambridge University Press, 2004, Chapter 21, p. 513–536

Kivelson et al. 1998

KIVELSON, Margaret G. ; WARNECKE, J. ; BENNETT, L. ; JOY, S. ; KHURANA, Krishan K. ; LINKER, J. A. ; RUSSELL, Christopher T. ; WALKER, Raymond J. ; POLANSKEY, C.: Ganymede's magnetosphere: Magnetometer overview. In: *Journal of Geophysical Research* 103 (1998), p. 963–972

Kopp and Ip 2002

KOPP, Andreas ; IP, Wing H.: Resistive MHD simulations of Ganymede's magnetosphere - 1. Time variabilities of the magnetic field topology. In: *Journal of Geophysical Research* 107 (2002), Nr. A12, 1–5. <http://dx.doi.org/10.1029/2001JA005071>. – DOI 10.1029/2001JA005071. – ISSN 0148–0227

Krist et al. 2011

KRIST, John E. ; HOOK, Richard N. ; STOEHR, Felix: 20 years of Hubble Space Telescope optical modeling using Tiny Tim John. In: *SPIE Digital Library* 8127 81270 (2011), September. <http://dx.doi.org/10.1117/12.892762>. – DOI

10.1117/12.892762

Krupp et al. 2004

KRUPP ; VASYLIUNAS, V. M. ; WOCH, Joachim ; LAGG, Andreas ; KURTH, William S. ; FRANK, L. A. ; PATERSON, W. R.: 25 Dynamics of the Jovian Magnetosphere. In: BAGENAL, Fran (Edit.): *Jupiter: The Planet, Satellites and Magnetospheres*. 1st. Cambridge University Press, 2004, Chapter 25

Kurth et al. 2009

KURTH, W. S. ; BUNCE, E. J. ; CLARKE, J. T. ; CRARY, F. J. ; GRODENT, D. C. ; INGERSOLL, A. P. ; DYUDINA, U. A. ; LAMY, L. ; MITCHELL, D. G. ; PERSON, A. M. ; PRYOR, W. R. ; SAUR, J. ; STALLARD, T.: 12 Auroral Processes. In: DOUGHERTY, M. K. (Edit.) ; ESPOSITO, L. W. (Edit.) ; KRIMIGIS, S. M. (Edit.): *Saturn from Cassini-Huygens*. Springer, 2009, Chapter 12, p. 333–374

Lamy et al. 2012

LAMY, L. ; PRANGÉ, R. ; HANSEN, K. C. ; CLARKE, J. T. ; ZARKA, P. ; CECCONI, B. ; ABOUDARHAM, J. ; ANDRÉ, N. ; BRANDUARDI-RAYMONT, G. ; GLADSTONE, R. ; BARTHÉLÉMY, M. ; ACHILLEOS, N. ; GUIO, P. ; DOUGHERTY, M. K. ; MELIN, H. ; COWLEY, S. W. H. ; STALLARD, T. S. ; NICHOLS, J. D. ; BALLESTER, G.: Earth-based detection of Uranus' aurorae. In: *Geophysical Research Letter* 39 (2012), April, p. L07105. <http://dx.doi.org/10.1029/2012GL051312>. – DOI 10.1029/2012GL051312

Leblanc and Chicarro 2008

LEBLANC, Francois ; CHICARRO, Agustin: Mars Express observes aurorae on the red planet. (2008). http://www.esa.int/Our_Activities/Space_Science/Mars_Express/Mars_Express_observes_aurorae_on_the_Red_Planet, Last checked: April 15, 2016

Marazzini 2005

MARAZZINI, C: The names of the satellites of Jupiter: from Galilio to Simon Marius. In: *LETTERE ITALIANE* 57 (2005), Nr. 3, p. 391–407

McCord et al. 1998

MCCORD, T. B. ; HANSEN, G. B. ; CLARK, R. N. ; MARTIN, P. D. ; HIBBITTS, C. A. ; FANALE, F. P. ; GRANAHAN, J. C. ; SEGURA, M. ; MATSON, D. L. ; JOHNSON, T. V. ; CARLSON, R. W. ; SMYTHE, W. D. ; DANIELSON, G. E.: Non-

water-ice constituents in the surface material of the icy Galilean satellites from the Galileo near-infrared mapping spectrometer investigation. In: *Journal of Geophysical Research* 103 (1998), April, p. 8603–8626. <http://dx.doi.org/10.1029/98JE00788>. – DOI 10.1029/98JE00788

McGrath and Hendrix 2013

MCGRATH, M. ; HENDRIX, A.: The Ultraviolet Albedo of Ganymede. In: *AAS/Division for Planetary Sciences Meeting Abstracts Bd. 45, 2013* (AAS/Division for Planetary Sciences Meeting Abstracts), p. 501.04

McGrath et al. 2013

MCGRATH, Melissa A. ; RETHERFORD, Kurt D. ; FELDMAN, Paul D. ; STROBEL, Darrell F. ; SAUR, Joachim: Aurora on Ganymede. In: *Journal of Geophysical Research* 118 (2013), Nr. 5, p. 2043–2054. <http://dx.doi.org/10.1002/jgra.50122>. – DOI 10.1002/jgra.50122

Meier 1991

MEIER, R. R.: *Ultraviolet spectroscopy and remote sensing of the upper atmosphere*. Hulburt Center for Space Research, Naval Research Laboratory, Washington : Kluwer Academic Publisher, 1991

NASA 1998

NASA: *Jupiter's aurorae in November 1998. The image made by HST. The main auroral oval and polar ovals are marked with dash lines. Satellite spots and other features are also shown. (modified by author)*. <http://apod.nasa.gov/apod/ap001219.html>. Version: 1998, Last checked: 19 April 2016

NASA 2005

NASA: *False-colour image of ultraviolet Aurora australis captured by NASA's IMAGE satellite and overlaid onto NASA's satellite-based Blue Marble image*. <http://earthobservatory.nasa.gov/IOTD/view.php?id=6226>. Version: 2005, Last checked: 19 April 2016

NASA 2012

NASA: *Aurora at Uranus (composite image)*. <http://www.universetoday.com/94565/hubble-reveals-curious-auroras-on-uranus/>. Version: 2012, Last checked: 19 April 2016

Nelson et al. 1987

NELSON, Robert M. ; LANE, Arthur L. ; MATSON, Dennis L. ; VEEDER, Glenn J. ; BURATTI, Bonnie J. ; TEDESCO, Edward F.: Spectral Geometric Albedos of the Galilean Satellites from 0 . 24 to 0 . 34 Micrometers : Observations with the International Ultraviolet Explorer. In: *Icarus* 72 (1987), p. 358–380

Neubauer 1998

NEUBAUER, Fritz M.: The sub-Alfvénic interaction of the Galilean satellites with the Jovian magnetosphere. In: *Journal of Geophysical Research* 103 (1998), p. 843–866

Orton et al. 1996

ORTON, G. S. ; SPENCER, J. R. ; TRAVIS, L. D. ; MARTIN, T. Z. ; TAMPARI, L. K.: Galileo Photopolarimeter-Radiometer Observations of Jupiter and the Galilean Satellites. In: *Science* 274 (1996), Oktober, p. 389–391. <http://dx.doi.org/10.1126/science.274.5286.389>. – DOI 10.1126/science.274.5286.389

Panov et al. 2016

PANOV, E. V. ; BAUMJOHANN, W. ; WOLF, R. A. ; NAKAMURA, R. ; ANGELOPOULOS, V. ; WEYGAND, J. M. ; KUBYSHKINA, M. V.: Magnetotail energy dissipation during an auroral substorm. In: *Nature Physics* advance online publication (2016), 09. <http://dx.doi.org/10.1038/nphys3879>. ISBN 1745–2481

Pappalardo et al. 2004

PAPPALARDO, Robert T. ; COLLINS, Geoffrey C. ; HEAD, James W. ; HELFENSTEIN, Paul ; MCCORD, Thomas B. ; PROCKTER, Loiuise M. ; MOORE, Jeffrey M. ; SPENCER, John R.: 16 Geology of Ganymede. In: BAGENAL, Fran (Edit.): *Jupiter: The Planet, Satellites and Magnetospheres*. 1st. Cambridge University Press, 2004, Chapter 16

Pappalardo et al. 1998

PAPPALARDO, Robert T. ; HEAD, James W. ; COLLINS, Geoffrey C. ; KIRK, Randolph L. ; GREELEY, Ronald ; CHAPMAN, Clark R. ; HELFENSTEIN, Paul ; MOORE, McEwen A. Jeffrey M.A M. Jeffrey M.A ; TUFTS, B. R. ; SENSKE, David A. ; BRENNEMAN, H. Herbert H. ; KLAASEN, Ken: Grooved Terrain on Ganymede: First Results from Galileo High-Resolution Imaging. 302 (1998),

p. 276–302

Paranicas et al. 1999

PARANICAS, C. ; PATERSON, W. R. ; CHENG, a. F. ; MAUK, B. H. ; McENTIRE, R. W. ; FRANK, L. a. ; WILLIAMS, D. J.: Energetic particle observations near Ganymede. In: *Journal of Geophysical Research* 104 (1999), Nr. A8, 17459. <http://dx.doi.org/10.1029/1999JA900199>. – DOI 10.1029/1999JA900199. – ISSN 0148–0227

Paranicas et al. 2002

PARANICAS, C. ; RATLIFF, J. M. ; MAUK, B. H. ; COHEN, C. ; JOHNSON, R. E.: The ion environment near Europa and its role in surface energetics. In: *Geophysical Research Letter* 29 (2002), März, p. 18–1. <http://dx.doi.org/10.1029/2001GL014127>. – DOI 10.1029/2001GL014127

Paty and Winglee 2004

PATY, Carol S. ; WINGLEE, Robert: Multi-fluid simulations of Ganymede's magnetosphere. In: *Geophysical Research Letters* 31 (2004), Nr. 24, 1–5. <http://dx.doi.org/10.1029/2004GL021220>. – DOI 10.1029/2004GL021220. – ISSN 0094–8276

Payan et al. 2015

PAYAN, A. P. ; PATY, C. S. ; RETHERFORD, K. D.: Uncovering local magnetospheric processes governing the morphology and variability of Ganymede's aurora using three-dimensional multifluid simulations of Ganymede's magnetosphere. In: *Journal of Geophysical Research (Space Physics)* 120 (2015), Januar, p. 401–413. <http://dx.doi.org/10.1002/2014JA020301>. – DOI 10.1002/2014JA020301

Phillips 2015

PHILLIPS, Tony ; NASA, Tony Phillips /. (Edit.): *Auroras on Mars*. http://science.nasa.gov/science-news/science-at-nasa/2015/11may_aurorasonmars/. Version: 2015, Last checked: May 11, 2015

Proffitt et al. 2003

PROFFITT, C. R. ; BROWN, T. M. ; MOBASHER, B. ; DAVIES, J.: *Absolute Flux Calibration of STIS MAMA Imaging Modes*. 2003

Roth et al. 2016

ROTH, L. ; SAUR, J. ; RETHERFORD, K. D. ; STROBEL, D. F. ; FELDMAN, P. D. ; MCGRATH, M. A. ; SPENCER, J. R. ; BLÖCKER, A. ; IVCHENKO, N.: Europa's far ultraviolet oxygen aurora from a comprehensive set of HST observations. In: *Journal of Geophysical Research (Space Physics)* 121 (2016), März, p. 2143–2170. <http://dx.doi.org/10.1002/2015JA022073>. – DOI 10.1002/2015JA022073

Roth et al. 2014a

ROTH, Lorenz ; RETHERFORD, Kurt D. ; SAUR, Joachim ; STROBEL, Darrell F. ; FELDMAN, Paul D. ; MCGRATH, Melissa A. ; NIMMO, Francis: Orbital apocenter is not a sufficient condition for HST/STIS detection of Europa's water vapor aurora. In: *Proceedings of the National Academy of Sciences* 111 (2014), December, Nr. 48, p. E5123–E5132

Roth et al. 2015

ROTH, Lorenz ; SAUR, Joachim ; RETHERFORD, K. D. ; STROBEL, Darrell F. ; FELDMAN, Paul D. ; MCGRATH, Melissa A. ; SPENCER, John R. ; BLOECKER, Aljona ; IVCHENKO, Nickolay: Europa's far-ultraviolet oxygen aurora. In: *Journal of Geophysical Research (Space Physics)* (2015)

Roth et al. 2014b

ROTH, Lorenz ; SAUR, Joachim ; RETHERFORD, Kurt D. ; STROBEL, Darrell F. ; FELDMAN, Paul D. ; MCGRATH, Melissa A. ; NIMMO, Francis: Transient Water Vapor at Europa's South Pole. In: *Science* 343 (2014), January, p. 171–174

Saleh et al. 1992

SALEH, Bahaa ; TEICH, Malvin ; SLUSHER, Richard E.: *Fundamentals of Photonics*. 1992. – 87 S. <http://dx.doi.org/10.1063/1.2809878>. <http://dx.doi.org/10.1063/1.2809878>. ISSN 00319228

Saur et al. 2015

SAUR, J. ; DULING, S. ; ROTH, L. ; JIA, X. ; STROBEL, D. F. ; FELDMAN, P. D. ; CHRISTENSEN, U. R. ; RETHERFORD, K. D. ; MCGRATH, M. A. ; MUSACCHIO, F. ; WENNMACHER, A. ; NEUBAUER, F. M. ; SIMON, S. ; HARTKORN, O.: The search for a subsurface ocean in Ganymede with Hubble Space Telescope observations of its auroral ovals. In: *Journal of Geophysical Research (Space Physics)* 120 (2015), März, 1715-1737. <http://dx.doi.org/10.1002/2014JA020648>

[//dx.doi.org/10.1002/2014JA020778](http://dx.doi.org/10.1002/2014JA020778). – DOI 10.1002/2014JA020778

Saur et al. 2011

SAUR, Joachim ; FELDMAN, Paul D. ; ROTH, Lorenz ; NIMMO, Francis ; STROBEL, Darrell F. ; RETHERFORD, Kurt D. ; MCGRATH, Melissa A. ; SCHILLING, Nico ; GÉRARD, Jean-Claude ; GRODENT, Denis: Hubble Space Telescope / Advanced Camera for Surveys Observations of Europa's Atmospheric Ultraviolet Emission At Eastern Elongation. In: *The Astrophysical Journal* 738 (2011), Nr. 2, 153. <http://dx.doi.org/10.1088/0004-637X/738/2/153>. – DOI 10.1088/0004-637X/738/2/153

Saur et al. 1999

SAUR, Joachim ; NEUBAUER, Fritz M. ; STROBEL, Darrell F. ; SUMMERS, Michael E.: Three-dimensional plasma simulation of Io's interaction with the Io plasma torus: Asymmetric plasma flow. In: *Journal of Geophysical Research* 104 (1999), Nr. A11, 25105–25126. <http://dx.doi.org/10.1029/1999JA900304>. – DOI 10.1029/1999JA900304. – ISSN 0148–0227

Saur et al. 2000

SAUR, Joachim ; NEUBAUER, Fritz M. ; STROBEL, Darrell F. ; SUMMERS, Michael E.: Io's ultraviolet aurora: Remote sensing of Io's interaction. In: *Geophysical Research Letters* 27 (2000), Nr. 18, 2893. <http://dx.doi.org/10.1029/2000GL003824>. – DOI 10.1029/2000GL003824. – ISSN 0094–8276

Schubert et al. 1996

SCHUBERT, G. ; ZHANG, K. ; KIVELSON, M. G. ; ANDERSON, J. D.: The magnetic field and internal structure of Ganymede. In: *Nature* 384 (1996), Dezember, p. 544–545. <http://dx.doi.org/10.1038/384544a0>. – DOI 10.1038/384544a0

Schubert et al. 2004

SCHUBERT, Gerald ; ANDERSON, John D. ; SPOHN, T.: 13 Interior Composition, Structure and Dynamics of the Galilean Satellites. In: BAGENAL, Fran (Edit.): *Jupiter: The Planet, Satellites and Magnetospheres*. 1st edition. Cambridge University Press, 2004, Chapter 13

Showman and Malhotra 1999

SHOWMAN, Adam P. ; MALHOTRA, Renu: The Galilean Satellites. In:

Science 286 (1999), Oktober, Nr. 5437, 77–84. <http://dx.doi.org/10.1126/science.286.5437.77>. – DOI 10.1126/science.286.5437.77

Showman et al. 1997

SHOWMAN, Adam P. ; STEVENSON, David J. ; MALHOTRA, Renu: Coupled Orbital and Thermal Evolution of Ganymede. 383 (1997), p. 367–383

Siscoe 1978

SISCOE, George L.: An historical footnote on the origin of "aurora borealis". In: *EOS Transactions* 59 (1978), p. 994–997. <http://dx.doi.org/10.1029/E0059i012p00994>. – DOI 10.1029/E0059i012p00994

Squyres and Veverka 1981

SQUYRES, Steven W. ; VEVERKA, Joseph: Voyager photometry of surface features on Ganymede and Callisto. In: *Icarus* 46 (1981), Mai, Nr. 2, 137–155. [http://dx.doi.org/10.1016/0019-1035\(81\)90203-7](http://dx.doi.org/10.1016/0019-1035(81)90203-7). – DOI 10.1016/0019-1035(81)90203-7. – ISSN 00191035

Straus and Schulz 1976

STRAUS, J. M. ; SCHULZ, M.: Magnetospheric convection and upper atmospheric dynamics. In: *Journal of Geophysical Research* 81 (1976), Dezember, p. 5822–5832. <http://dx.doi.org/10.1029/JA081i034p05822>. – DOI 10.1029/JA081i034p05822

Tennyson 2005

TENNYSON, Jonathan: *Astronomical Spectroscopy - An introduction to the atomic and molecular physics of astronomical spectra*. Imperial College Press, 2005. – 203 S. – ISBN 1860945139

Toussaint 2010

TOUSSAINT, Godfried: *Grids, connectivity, and contour-tracing*. <http://dx.doi.org/http://www-cgri.cs.mcgill.ca/~godfried/teaching/mir-reading-assignments/>. Version: February 2010

Turc et al. 2014

TURC, L. ; LECLERCQ, L. ; LEBLANC, F. ; MODOLO, R. ; CHAUFRAY, J.-Y.: Modelling Ganymede's neutral environment: A 3D test-particle simulation. In: *Icarus* 229 (2014), Februar, 157–169. <http://dx.doi.org/10.1016/j.icarus>.

2013.11.005. – DOI 10.1016/j.icarus.2013.11.005. – ISSN 00191035

USGS 2003

USGS: *Controlled Color Photomosaic Map of Ganymede; Jg 15M CMNK*. <http://pubs.usgs.gov/imap/i2762/>. Version: 2003, Last checked: April 15, 2016

Vance et al. 2014

VANCE, S. ; BOUFFARD, M. ; CHOUKROUN, M. ; SOTIN, C.: Ganymede's internal structure including thermodynamics of magnesium sulfate oceans in contact with ice. In: *Planetary and Space Science* 96 (2014), Juni, p. 62–70. <http://dx.doi.org/10.1016/j.pss.2014.03.011>. – DOI 10.1016/j.pss.2014.03.011

Williams and Bocklung 1989

WILLIAMS, Chales S. ; BOCKLUNG, Orville A.: *Introduction to the Optical Transfer Function*. 1989 (x). – 362–386 S.

Williams 2001

WILLIAMS, D. J.: Ganymede's ionic radiation belts. In: *Geophysical Research Letter* 28 (2001), p. 3793–3796. <http://dx.doi.org/10.1029/2001GL013353>. – DOI 10.1029/2001GL013353

Williams et al. 1997

WILLIAMS, D. J. ; MAUK, B. ; MCENTIRE, R. W.: Trapped electrons in Ganymede's magnetic field. In: *Geophysical Research Letter* 24 (1997), December, p. 2953–2956. <http://dx.doi.org/10.1029/97GL03003>. – DOI 10.1029/97GL03003

Williams et al. 1998

WILLIAMS, D. J. ; MAUK, B. ; MCENTIRE, R. W.: Properties of Ganymede's magnetosphere as revealed by energetic particle observations. In: *Journal of Geophysical Research* 103 (1998), August, p. 17523–17534. <http://dx.doi.org/10.1029/98JA01370>. – DOI 10.1029/98JA01370

Williams et al. 1997

WILLIAMS, D. J. ; MAUK, Barry H. ; MCENTIRE, Richard W. ; ROELOF, E. C. ; ARMSTRONG, Thomas P. ; WILKEN, B. ; ROEDERER, J. G. ; KRIMIGIS, Stama-

tios M. ; FRITZ, S. M. ; LANZEROTTY, L. J. ; MURPHY, N: Energetic particle signatures at Ganymede: Implications for Ganymede's magnetic field. In: *Geophysical Research Letters* 24 (1997), September, Nr. 17, p. 2163–2166

Woods et al. 2005

WOODS, Thomas N. ; EPARVIER, Frank G. ; BAILEY, Scott M. ; CHAMBERLIN, Phillip C. ; LEAN, Judith ; ROTTMAN, Garry J. ; SOLOMON, Stanley C. ; TOBISKA, W. K. ; WOODRASKA, Donald L.: Solar EUV Experiment (SEE): Mission overview and first results. In: *Journal of Geophysical Research* 110 (2005), Nr. A1, 1–24. <http://dx.doi.org/10.1029/2004JA010765>. – DOI 10.1029/2004JA010765. – ISSN 0148–0227

Zahnle et al. 1998

ZAHNLE, K. ; DONES, L. ; LEVISON, H. F.: Cratering Rates on the Galilean Satellites. In: *Icarus* 136 (1998), Dezember, p. 202–222. <http://dx.doi.org/10.1006/icar.1998.6015>. – DOI 10.1006/icar.1998.6015

Zhan and Schubert 2012

ZHAN, X. ; SCHUBERT, G.: Powering Ganymede's dynamo. In: *Journal of Geophysical Research* 117 (2012), August, Nr. E8, E08011. <http://dx.doi.org/10.1029/2012JE004052>. – DOI 10.1029/2012JE004052. – ISSN 0148–0227

Supplementary Material

S1 List of abbreviations

ACS	HST's Advanced Camera of Survey
CCD	charge coupled device
CS	current sheet
EPD	<i>Galileo's</i> Energetic Particles Detector
EUV	extreme ultraviolet
FAC	field aligned currents
FOV	field of view
FUV	far ultraviolet
GHRS	HST's Goddard High Resolution Spectrograph
HST	Hubble Space Telescope
IAU	International Astronomical Union
ICS	inside the current sheet
JUICE	JUperiter ICy moons Explorer
MAMA	Multi-Anode Multichannel Arrays
MAST	Mikulski Archive for Space Telescopes
MHD	magneto-hydrodynamic(s)
MUV	mid ultraviolet
NAIF	NASA's Navigation and Ancillary Information Facility
NUV	near ultraviolet
OCFB	open-closed field lines boundary
OCS	outside the current sheet
PI	principal investigator
PSF	point spread function
SEE	TIMED's Solar Extreme Ultraviolet Experiment
SNR	signal-to-noise ratio
SSI	<i>Galileo's</i> Solid State Imaging system
STIS	HST's Space Telescope Imaging Spectrograph
TIMED	Thermosphere Ionosphere Mesosphere Energetics and Dynamics satellite
UTC	Universal Time Coordinated
UVS	Galileo or JUICE Ultraviolet Spectrometer

S2 List of quantities and units

Symbol	Explanation/Name	Value/Definition
Å	Angstrom	10^{-1} nm
AU	Astronomical Unit	149,597,870.7 km
c	speed of light	$2.99 \cdot 10^8$ m s ⁻¹
erg	energy	10^{-7} J = 10^{-7} kg m ² s ⁻² , or in cgs units: 1 g cm ² s ⁻²
eV	electron Volt	$1.6021761 \times 10^{-19}$ J
h	Planck's constant	$6.6261 \cdot 10^{-34}$ J s, or in cgs units: $6.6261 \cdot 10^{-27}$ erg s
J	Joule	kg m ² s ⁻² = 1 Nm
K	Kelvin	with 0 K = 273.15 °C
k_B	Boltzmann's constant	$8.62 \cdot 10^{-5}$ eV K ⁻¹ or $1.38 \cdot 10^{-23}$ J K ⁻¹
Pa	Pascal	N m ⁻²
R	Rayleigh	10^6 photons $(4\pi)^{-1}$ cm ⁻² s ⁻¹ sr ⁻¹
R_C	radius of Callisto	2,410 km
R_E	radius of Europa	1,560 km
R_G	radius of Ganymede	2,634 km
R_I	radius of Io	1,820 km
R_J	radius of Jupiter	71,492 km
T	Tesla	1 kg s ⁻² A ⁻¹

S3 Trace drift calibration for the 52X2 aperture

In addition to the trace drift calibration for the pseudo aperture *52X2D1* in Chapter 3.2.2, Figure 49 shows the calibration for the aperture *52X2*. We apply a fit with a polynomial of fourth order. The resulting polynomial is displayed in panel C.

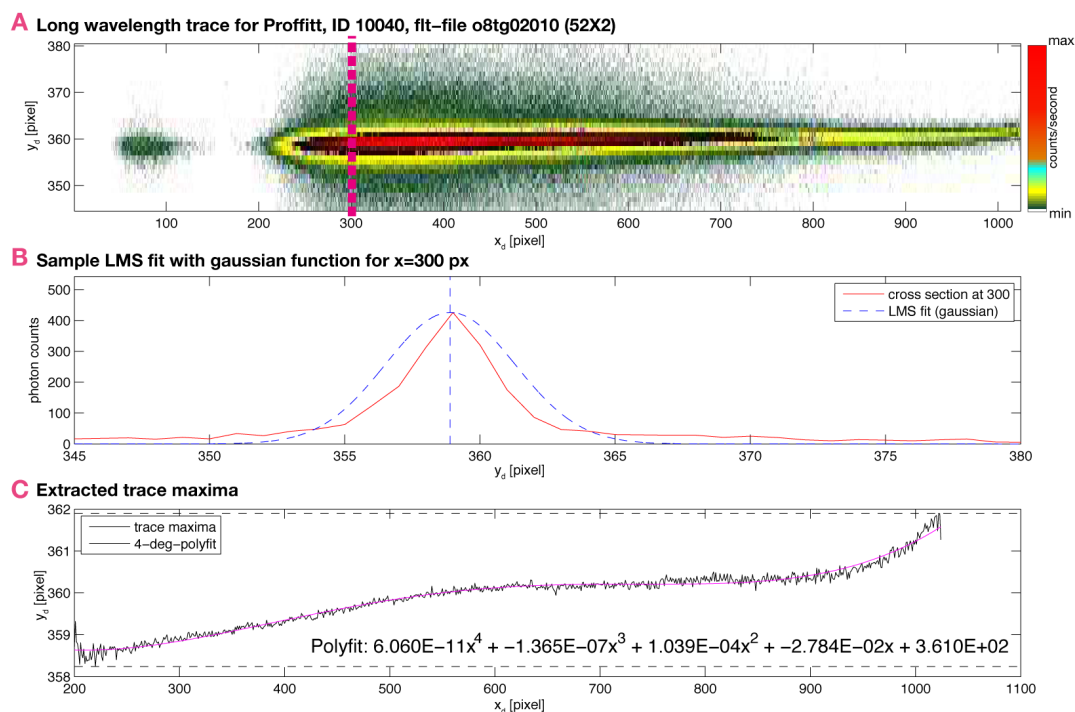


Figure 49 – Determining the trace drift in y -direction using calibration measurements of the stellar object *WD2126+734* of HST/STIS campaign 10040 (Proffitt et al. 2003) using the aperture *52X2* and grating *G140L* (fit-file o8tg02010_fit.fits).

S4 Spectral images of OI $\lambda 1304 \text{ \AA}$

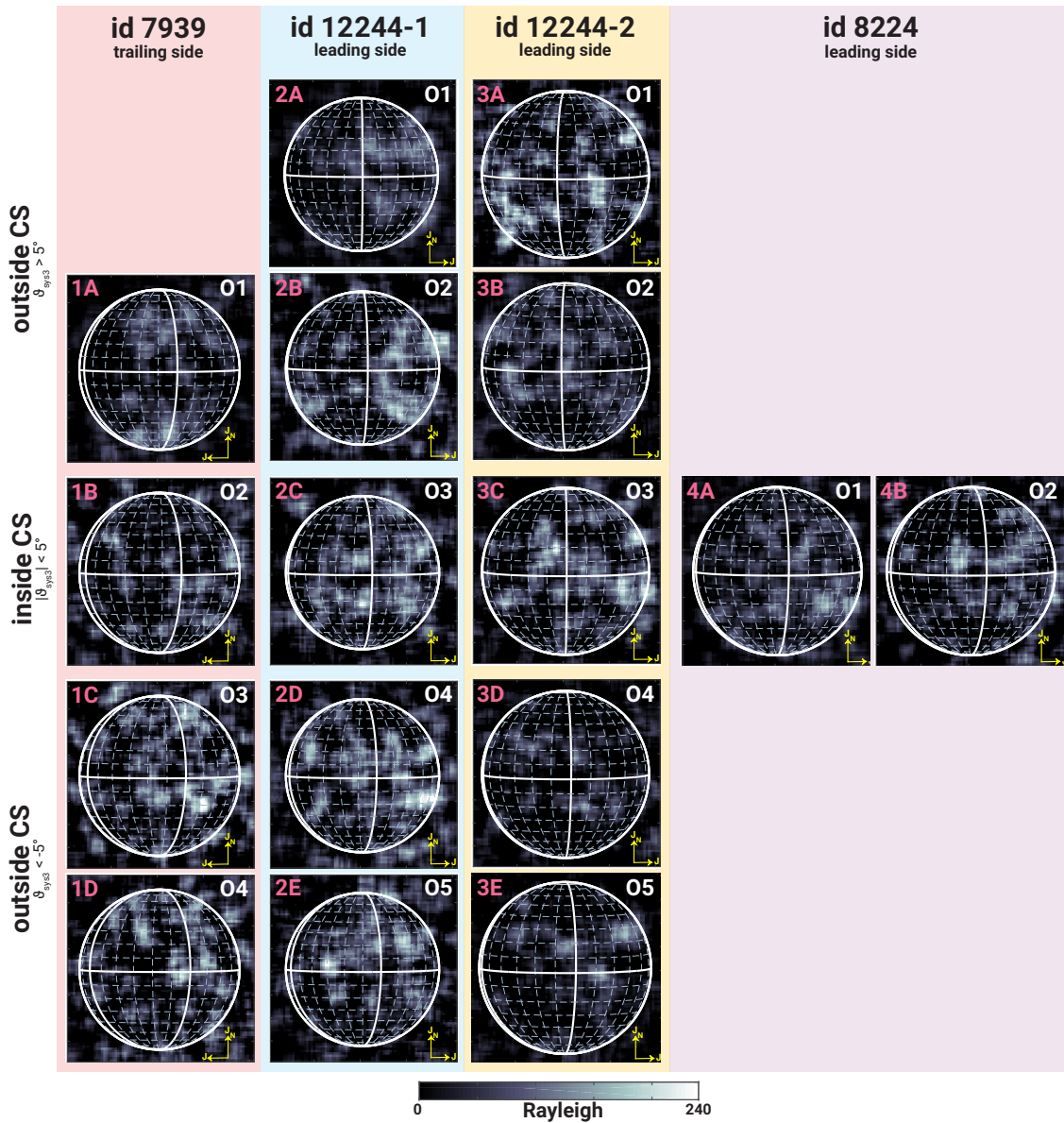


Figure 50 – Spectral images (82×82 pixels) of OI $\lambda 1304 \text{ \AA}$ oxygen emission in Rayleigh. Panels of column 1 show all orbits of campaign 7939 (1998, trailing side), panels of columns 2 and 3 show both visits of campaign 12244 (2010/2011, leading side), respectively, and column 4 shows the two orbits of campaign 8224 (2000, leading side). All panels are ordered by magnetic latitude ϑ_{mag} . Orbit numbers according to Table 3 are indicated in the right upper corner of each panel. Yellow arrows indicate the orientation of Jovian North (J_N) and direction to Jupiter (J). The color scale is limited to 240 R (pixel with higher brightness are white). Images are smoothed to increase the visibility of the auroral ovals.

S5 Comparison of total disk averaged brightnesses and brightnesses derived by the anuli integration

Comparison between averaged total disk brightnesses I_{tot} calculated by integrating and averaging the brightness over the entire disk without the off-limb area similar to Section 4.3 (solid lines) and by integrating over the latitude anuli brightnesses $I(\vartheta_{bin})$ according to Equation 4.2 (dashed lines).

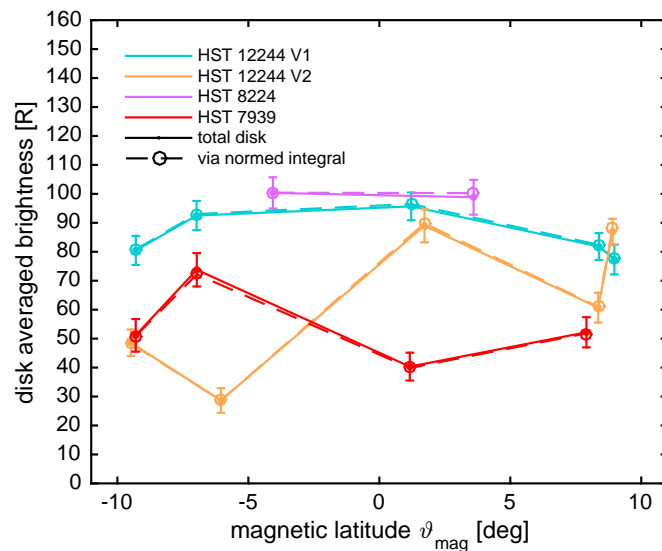


Figure 51 – Comparison between averaged total disk brightnesses I_{tot} . Dashed lines with circles show I_{tot} calculated according Equation 4.2, i.e., by integrating over the latitude anuli brightnesses $I(\vartheta_{bin})$. Solid lines show I_{tot} integrated and averaged directly over the entire disk without off-limb area similar to Section 4.3.

S6 Gaussian fit results for latitudinal anuli integrated brightness peaks in three longitudinal regions on the moon disk

Table 11 – Resultant location of the maximum, μ , and width, σ , of the fitted Gaussian function for the latitudinal anuli integrated brightnesses, each for the three longitudinal regions on the disk as introduced in Section 4.4.3, Table 8. Mid longitudinal region expands $\pm 25^\circ$ longitude around the leading/trailing side center-meridian ($90^\circ/270^\circ$). Left and right longitudinal regions account for the remaining sub- and anti-Jovian disk part on the trailing side, respectively, and for the remaining anti- and sub-Jovian disk part on the leading side, respectively. All values are given in the unit of planetographic latitude.

		id 12244-1	id 12244-2	id 8224	id 7939
		μ/σ [°]	μ/σ [°]	μ/σ [°]	μ/σ [°]
left longitudinal region					
ICS	northern oval	18.4 / 7.3	21.2 / 4.9	18.3 / 6.4	-
	southern oval	19.7 / 9.2	14.8 / 11.8	20.7 / 7.3	46.5 / 11.8
OCS	northern oval	22.2 / 9.1	28.0 / 6.7	-	49.4 / 11.2
	southern oval	21.7 / 8.4	21.2 / 8.9	-	50.5 / 12.1
mid longitudinal region					
ICS	northern oval	20.7 / 4.6	24.2 / 5.5	16.3 / 6.5	49.1 / 8.8
	southern oval	14.8 / 7.1	7.8 / 6.4	19.5 / 9.3	52.6 / 5.8
OCS	northern oval	22.4 / 8.5	23.3 / 10.5	-	48.9 / 8.4
	southern oval	18.1 / 8.9	15.7 / 8.0	-	47.6 / 7.7
right longitudinal region					
ICS	northern oval	24.6 / 6.2	21.8 / 5.5	26.4 / 5.9	-
	southern oval	17.6 / 5.5	9.4 / 5.2	18.6 / 7.3	-
OCS	northern oval	26.9 / 6.5	30.7 / 7.5	-	45.4 / 10.4
	southern oval	20.0 / 8.1	18.2 / 6.4	-	48.8 / 6.7

S7 Effective error of Section 4.4.4

Table 12 – Individual values of the effective error σ_{eff} in Equation 4.7 introduced in Section 4.4.4. All values are given in unit of planetographic latitude (in degree).

λ_i	campaign		$\vartheta_c(\lambda_i)$	$\sigma_{\text{stat}}(\lambda_i)$	$\sigma_{\lambda^*}(\lambda_i)$	$\text{Var}(\vartheta_c(\lambda_i))^{-\frac{1}{2}}$	σ_{eff}
32.5	12244	OCS-R	3.48	0.76	-2.14	1.43	2.68
32.5	12244	ICS-R	3.50	0.84	-2.14	1.43	2.70
32.5	12244	OCS-R	6.24	0.94	-2.14	1.43	2.74
32.5	12244	ICS-R	6.17	1.75	-2.14	1.43	3.11
32.5	8224	ICS-R	3.88	0.61	-2.14	1.43	2.64
90.0	12244	OCS-M	2.13	0.71	-1.38	3.55	3.87
90.0	12244	ICS-M	2.91	1.12	-1.38	3.55	3.96
90.0	12244	OCS-M	3.84	1.09	-1.38	3.55	3.96
90.0	12244	ICS-M	8.23	0.70	-1.38	3.55	3.87
90.0	8224	ICS-M	-1.64	0.79	-1.38	3.55	3.88
147.5	12244	OCS-L	0.23	1.12	0.21	2.16	2.44
147.5	12244	ICS-L	-0.64	1.75	0.21	2.16	2.78
147.5	12244	OCS-L	3.38	0.55	0.21	2.16	2.24
147.5	12244	ICS-L	3.19	2.36	0.21	2.16	3.21
147.5	8224	ICS-L	-1.20	0.83	0.21	2.16	2.32
212.5	7939	OCS-R	-1.70	1.74	2.14	0.00	2.76
270.0	7939	OCS-M	0.65	0.81	1.38	1.70	2.33
270.0	7939	ICS-M	-1.75	1.69	1.38	1.70	2.77
327.5	7939	OCS-L	-0.56	1.64	-0.21	0.00	1.65

S8 Resulting reduced χ^2 of Section 4.4.4

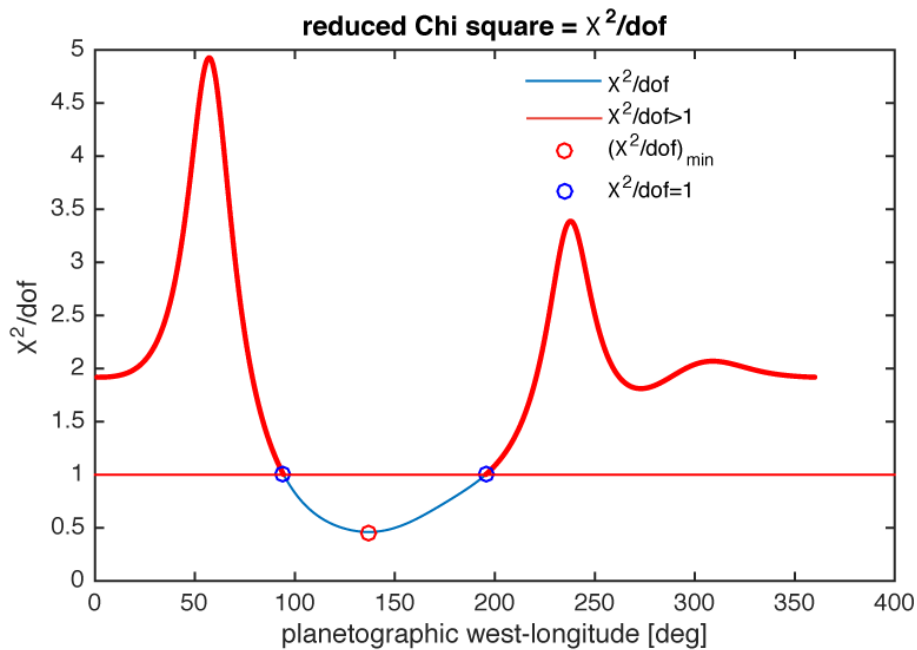


Figure 52 – Reduced χ^2_{red} ($=\chi^2/\text{dof}$, with $\text{dof} = \text{degree of freedom or } N - p$) of the least squares fit (Equation 4.6) in Section 4.4.4 as a function of planetographic west-longitude λ . We obtain the best fit for $\lambda_{0,\text{min}}=136.9^\circ$, i.e., where χ^2/dof has its minimum (indicated by the red circle). According to Bevington and Robinson (2003), fits with reduced Chi-squared values of ~ 1 and smaller are considered adequate fits to observations. Therefore, we estimate the error of $\lambda_{0,\text{min}}$ by searching for the first longitudes around $\lambda_{0,\text{min}}$, for which χ^2/dof becomes greater than one (indicated by the blue circles).

S9 USGS surface map

In Figure 53 we show the same image as shown in Figure 4. The image in Figure 53 is rotated and scaled to a larger size. The original image can be downloaded from <http://pubs.usgs.gov/imap/i2762/>.

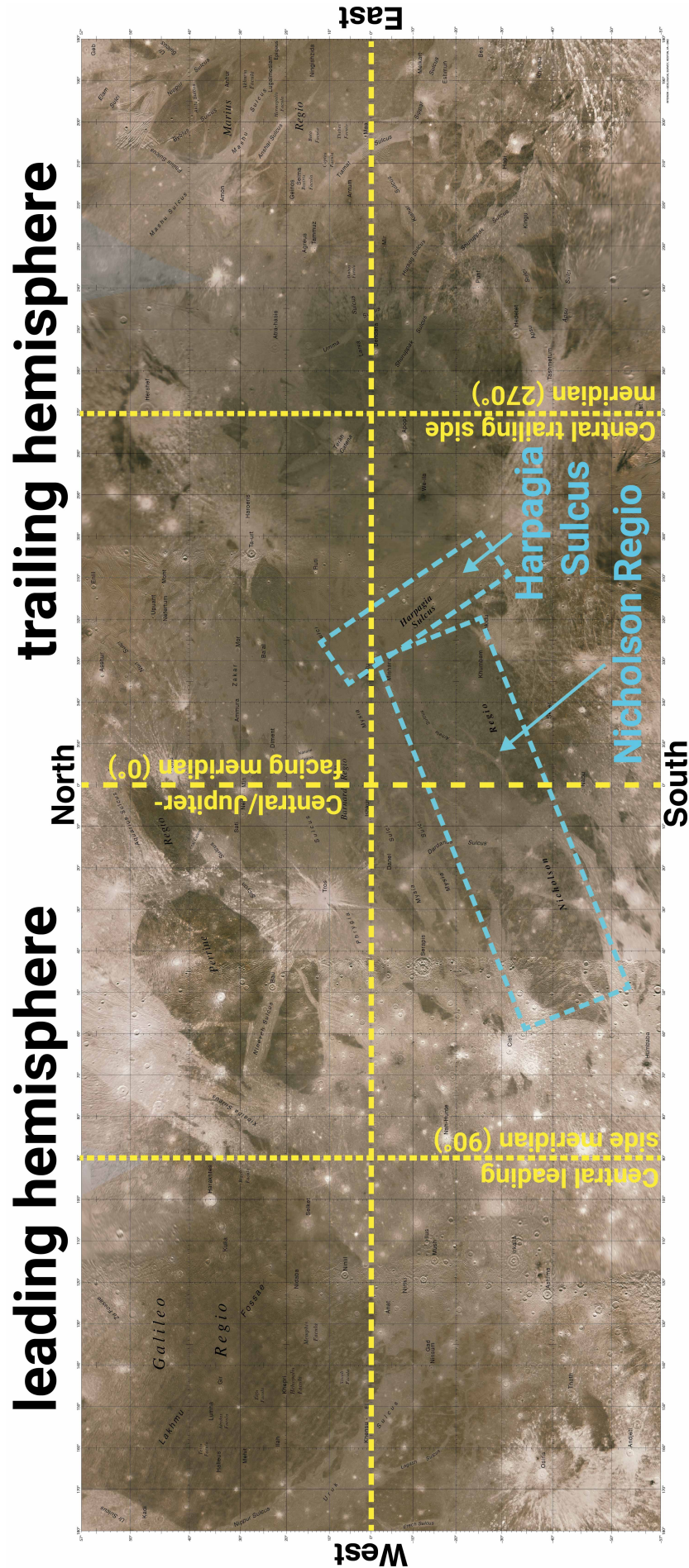


Figure 53 – Figure 4 rotated by 90° (see caption there). (USGS 2003)

Permissions for external material used in this thesis

In the following we list all existing or granted permissions for material used in this thesis, which is extracted and cited from external sources.

Special permissions for academic work

The following publishers allow a reuse of material included in their publications for academic work:

American Geophysical Union (AGU) Journals

Permission for content published in its journals granted for reuse in academic works. Excerpt of the permission guidelines (<http://publications.agu.org/author-resource-center/usage-permissions/>, visited on Sep. 27, 2016):

"[...] AGU grants permission for individuals to use figures, tables, and short quotes from AGU journal and books for republication in academic works and to make single copies for personal use in research, study, or teaching provided full attribution is included. There is no need to request this permission from AGU. This permission does not extend to public posting of the PDF or HTML created by AGU for publication. AGU journal content after 1996 is now freely available 24 months after publication; AGU encourages linking to this content directly. There is no charge or additional permissions needed for any of these uses, but

the material must be cited appropriately. [...]

Cambridge Academic Press: book or journal

Permission for short extracts, single figure or table granted. Excerpt of the permission guidelines (<http://www.cambridge.org/about-us/rights-permissions/permissions>, visited on Sep. 27, 2016):

"[...] Cambridge University Press grants permission freely for the reproduction in another work of a short prose extract (less than 400 words), a single figure or a single table in which it holds rights (see the important caveat in the Notes below). In such cases a request for permission need not be submitted, but the reproduced material must be accompanied by a full citation of the original source. [...]"

Science

Permission for content published in its journals granted for reuse in a dissertation. Excerpt of the permission guidelines (<http://www.sciencemag.org/help/reprints-and-permissions>, visited on Sep. 27, 2016):

"[...] AAAS permits the use of content published in its journals Science, Science Immunology, Science Robotics, Science Signaling, and Science Translational Medicine, but only provided the following criteria are met:

- 1. If you are using figure(s)/table(s), permission is granted for use in print and electronic versions of your dissertation or thesis.*
- 2. A full-text article may be used only in print versions of a dissertation or thesis. AAAS does not permit the reproduction of full-text articles in electronic versions of theses or dissertations.*
- 3. The following credit line must be printed along with the AAAS material: "From [Full Reference Citation]. Reprinted with permission from AAAS."*

4. *All required credit lines and notices must be visible any time a user accesses any part of the AAAS material and must appear on any printed copies that an authorized user might make.*
5. *The AAAS material may not be modified or altered except that figures and tables may be modified with permission from the author. Author permission for any such changes must be secured prior to your use.*
6. *AAAS must publish the full paper prior to your use of any of its text or figures.*
7. *If the AAAS material covered by this permission was published in Science during the years 1974–1994, you must also obtain permission from the author, who may grant or withhold permission, and who may or may not charge a fee if permission is granted. See original article for author's address. This condition does not apply to news articles.*
8. *If you are an original author of the AAAS article being reproduced, please refer to your License to Publish for rules on reproducing your paper in a dissertation or thesis.*

Permission covers the distribution of your dissertation or thesis on demand by a third party distributor (e.g. ProQuest / UMI), provided the AAAS material covered by this permission remains in situ and is not distributed by that third party outside of the context of your thesis/dissertation. [...]"

Explicit granted permissions

The following publishers allow a reuse of material included in their publications after obtaining permission from the authors or publisher:

American Astronomical Society (AAS) Journals

Permission for content published in its journals *The Astronomical Journal* or *The Astrophysical Journal* granted after requesting permission from the author or AAS. (<https://aas.org/publications/aas-copyright-policy>, visited on Sep. 27, 2016). AAS material used in this thesis and the corresponding permission:

- Figure 3 from: Feldman, P. D., McGrath, M. A., Strobel, D. F., Moos, H. W., Retherford, K. D., and Wolven, B. C., 2000, 'HST/STIS ultraviolet imaging of polar aurora on Ganymede', *The Astrophysical Journal*, Volume 535, 2, p. 1085-1090, <http://stacks.iop.org/0004-637X/535/i=2/a=1085>, DOI: <http://dx.doi.org/10.1086/308889> (used as Figure 14 in this thesis)
- Figure 1 from: Hall, D. T., Feldman, P. D., McGrath, M. A., and Strobel, D. F., 1998, 'The far-ultraviolet oxygen airglow of Europa and Ganymede', *The Astrophysical Journal*, Volume 499, 1, p. 475-481, <http://stacks.iop.org/0004-637X/499/i=1/a=475>, DOI: <http://dx.doi.org/10.1086/305604> (used as Figure 13 in this thesis)

Von: Permissions permissions@iop.org 
Betreff: Re: Permission for reuse of two figures from two ApJ papers
Datum: 29. September 2016 um 12:41
An: Fabrizio Musacchio musacchio@geo.uni-koeln.de

P

Dear Fabrizio Musacchio,

Thank you for providing confirmation that you have received the consent of the authors to reproduce content from AAS journals in your thesis.

Regarding:

Figure 3 (Paul D. Feldman et al 2000 ApJ 535 1085)

Figure 1 (D. T. Hall et al 1998 ApJ 499 475)

I am happy to confirm that permission is granted and you need take no further action.

Please include the following alongside the material:

- the source of the material, including author, article title, title of journal, volume number, issue number (if relevant), page range (or first page if this is the only information available) and date of first publication. This material can be contained in a footnote or reference.
- for material being published electronically, a link back to the article (via DOI)
- if practical and IN ALL CASES for works published under any of the Creative Commons licences the words "© AAS. Reproduced with permission".

This permission does not apply to any material/figure which is credited to another source in the AAS publication or has been obtained from a third party. Express permission for such materials/figures must be obtained from the copyright owner.

If you have any questions, please feel free to contact our Permissions team at this address.

Kind regards,

Kathryn Shaw

Copyright & Permissions Team

Gemma Alaway – Rights & Permissions Adviser
 Kathryn Shaw - Editorial Assistant

Contact Details

E-mail: permissions@iop.org

For further information: <http://iopscience.iop.org/page/copyright>

Please see our Author Rights Policy <http://iopublishing.org/author-rights/>

Please note: We do not provide signed permission forms as a separate attachment. Please print this email and provide it to your institution as proof of permission.

Please note: Any statements made by IOP Publishing to the effect that authors do not need to get permission to use any content are not intended to constitute any sort of legal advice. Authors must make their own decisions as to the suitability of the content they are using and whether they require permission for it to be published within their article.

From: Fabrizio Musacchio <musacchio@geo.uni-koeln.de>
 To: permissions@iop.org,
 Cc: "Feldman Paul D." <pfeldman@jhu.edu>
 Date: 29/09/2016 10:19
 Subject: Permission for reuse of two figures from two ApJ papers

Dear IOP team,

I am Fabrizio Musacchio from the University of Cologne, Germany. Currently I am working on my dissertation and I'd like to include two figures from two *The Astrophysical Journal* (ApJ) papers:

- **Figure 3** from: Feldman, P. D., McGrath, M. A., Strobel, D. F., Moos, H. W., Retherford, K. D., & Wolven, B. C., 2000, 'HST/STIS ultraviolet imaging of polar aurora on Ganymede', *The Astrophysical Journal*, Volume 535, 2, p. 1085-1090, <http://stacks.iop.org/0004-637X/535/i=2/a=1085>, DOI:10.1086/308889

Figure 54 – AAS permission for academic reuse (part 1)

- **Figure 1** from: Hall, D. I., Feldman, P. D., McGrath, M. A., & Strobel, D. F., 1998, 'The far-ultraviolet oxygen airglow of Europa and Ganymede', *The Astrophysical Journal*, Volume 499, 1, p. 475-481, <http://stacks.iop.org/0004-637X/499/i=1/a=475>, DOI:10.1086/305604

By this email I inform you, that Paul D. Feldman, one of the authors of these papers, granted me permission for reuse the figures in my thesis (see attached email below).

Can you send me a formal indication of this permission?

Thank you very much,
Fabrizio Musacchio

Anfang der weitergeleiteten Nachricht:

Von: Paul Feldman <pfeldman@jhu.edu>
Betreff: Aw: Permission for reuse of two figures from your papers
Datum: 28. September 2016 um 18:47:16 MESZ
An: Fabrizio Musacchio <musacchio@geo.uni-koeln.de>

Dear Fabrizio,

I am pleased to grant you permission to reproduce the two figures cited below in your PhD thesis.

Best wishes for a speedy completion of this work.

Sincerely,
Paul D. Feldman

On 9/28/16 12:29 PM, Fabrizio Musacchio wrote:
Hi Paul,

I hope you are doing well. Our paper is still in revision and I keep you updated as soon as I get a reply from JGR.

Currently I'm working on my PhD thesis. For the introductory part of the thesis I'd like to include two figures from two of your papers:

- * Figure 3 from "HST/STIS ultraviolet imaging of polar aurora on Ganymede" (Feldman et al. 2000, *The Astrophysical Journal*)
- * Figure 1 from "The far-ultraviolet oxygen airglow of Europa and Ganymede" (Hall et al., 1998, *The Astrophysical Journal*).

I checked the copyright guidelines <<https://aas.org/publications/aas-copyright-policy>> from *The Astrophysical Journal* // AAS/ and I have to ask one of the authors of these papers in order to obtain consent for the reuse of the figures in my dissertation. Would you give me that permission to use these figures in my thesis?

Best regards,
Fabrizio

This email (and attachments) are confidential and intended for the addressee(s) only. If you are not the intended recipient please notify the sender, delete any copies and do not take action in reliance on it. Any views expressed are the author's and do not represent those of IOP, except where specifically stated. IOP takes reasonable precautions to protect against viruses but accepts no responsibility for loss or damage arising from virus infection. For the protection of IOP's systems and staff emails are scanned automatically.

IOP Publishing Limited Registered in England under Registration No 467514. Registered Office: Temple Circus, Bristol BS1 6HG
England Vat No GB 461 6000 84.

Please consider the environment before printing this email

Figure 55 – AAS permission for academic reuse (part 2)

Danksagung

An dieser Stelle möchte ich all jenen danken, die mich durch ihren fachlichen sowie persönlichen Beistand bei der Erstellung dieser Arbeit unterstützt haben.

Ich bedanke mich ganz besonders bei dem Betreuer meiner Arbeit, Professor Dr. Joachim Saur. Die vergangenen vier Jahre waren mir eine außerordentliche Schule wissenschaftlichen Arbeitens gewesen. Er brachte mir das sorgfältig und verantwortungsvoll wissenschaftliche Arbeiten bei, was für die in dieser Arbeit vorgestellten Methoden und Ergebnisse Grundvoraussetzung war. Seine kompetente Betreuung und Unterstützung bei Verständnisproblemen brachte mich bei Problemen stets voran. Darüberhinaus hinaus ermutigte er mich zu eigenen Anregungen und ließ mir genug Spielraum für eigene Ideen. Dank seines Engagements hatte ich im Laufe meines Promotionsstudiums zahlreiche Möglichkeiten, meine Ergebnisse auf nationalen und internationalen Tagungen und Konferenzen vorzustellen und mit führenden Wissenschaftler auf meinem Gebiet zu diskutieren. Darunter zählen auch meine beiden Aufenthalte bei Dr. Lorenz Roth an der Kungliga Tekniska Högskolan (KTH) in Schweden. Ich weiß, dass das keine Selbstverständlichkeit ist und bedanke mich deshalb besonders dafür.

Professor Bülent Tezkan danke ich für die Übernahme des Korreferats, aber auch für die mehr als angenehme und gute Zusammenarbeit bei verschiedenen Angelegenheiten in den vergangenen Jahren.

Ganz besonderen Dank spreche ich an Dr. Lorenz Roth aus. Er hat mich zu Beginn meiner Promotion in die technischen Details meines Promotionsthemas eingeführt. Außerdem stand er mir während der gesamten Zeit meines Promotionsstudiums immer mit guten Ratschlägen zur Seite.

Dr. Lex Wennmacher danke ich für die sachlichen und stets kompetenten Antworten auf meine Fragen. Sein fachliches Wissen, was die Himmelsmechanik angeht, hat mir bei vielen Problemen weitergeholfen.

Speziell danke ich Aljona Blöcker, Christoph Fuchs, Oliver Hartkorn und Anne Schreiner für das Korrekturlesen meiner Arbeit und für den hilfreichen Input, den ich von ihnen erhalten habe.

Danken will ich auch all meinen Bürokollegen, die ich Laufe meines Master- und Promotionsstudiums am Institut für Geophysik und Meteorologie hatte: Bastian Körtgen, Laura Pascharat, Sudha, Pritam Yogeschwar, Daniel Steinbach, Moritz Feyerabend, Natalie Pickartz. Aber ich danke auch all meinen anderen Kollegen, die, dank der stets offenen Türen innerhalb unseres Institutes, zu einem Klima beigetragen haben, was mir die Arbeit an meinem Promotionsthema enorm erleichtert hat. Spaß und ein freundschaftliches Auskommen sind für mich eine Grundvoraussetzung für eine gute Arbeit gewesen.

Schließlich verdanke ich aber das Gelingen dieser Doktorarbeit vor allem Christoph Fuchs. Er hat mich in der ganzen Zeit meiner Arbeit über unterstützt und mir über schwierige Momente hinweggeholfen.

Versicherung

Ich versichere, dass ich die von mir vorgelegte Dissertation selbständig angefertigt, die benutzten Quellen und Hilfsmittel vollständig angegeben und die Stellen der Arbeit - einschließlich Tabellen, Karten und Abbildungen -, die anderen Werken im Wortlaut oder dem Sinn nach entnommen sind, in jedem Einzelfall als Entlehnung kenntlich gemacht habe; dass diese Dissertation noch keiner anderen Fakultät oder Universität zur Prüfung vorgelegen hat; dass sie - abgesehen von unten angegebenen Teilpublikationen - noch nicht veröffentlicht worden ist sowie, dass ich eine solche Veröffentlichung vor Abschluss des Promotionsverfahrens nicht vornehmen werde. Die Bestimmungen der Promotionsordnung sind mir bekannt. Die von mir vorgelegte Dissertation ist von Professor Joachim Saur betreut worden.

Köln, den

Fabrizio-Michele Musacchio

Teilpublikationen / Publications

Parts of our study in this thesis have been presented in the following publication,

- Musacchio, F., Saur, J., Roth, L., Retherford, K. D., McGrath, M. M., Feldman, P. D., and Strobel, D. F., *Morphology of Ganymede's FUV auroral ovals*, unpublished (submitted to Journal of Geophysical Research),

and at the following conferences and seminars:

- **Magnetospheres off the Outer Planets (MOP)**, Athens, Greece, June 27, 2013
- **European Geosciences Union (EGU)**, Vienna, Austria, April 29, 2014
- **Graduate School of Geosciences (GSGS) Research Conference**, Cologne, Germany, July 4, 2014
- **American Geophysical Union (AGU) Fall Meeting**, San Francisco, California, USA, December 11, 2014
- **Graduate School of Geosciences (GSGS) Research Conference**, Cologne, Germany, January 23, 2015
- **Deutsche Physikalische Gesellschaft (DPG) Tagung**, Wuppertal, Germany, March 12, 2015
- **KTH Royal Institute of Technology**, Seminar, Stockholm, Sweden, March 17, 2015
- **Magnetospheres off the Outer Planets (MOP)**, Atlanta, Georgia, USA, June 3, 2015
- **Division for Planetary Sciences (DPS) Meeting**, Washington, D.C., USA, November 12, 2015